

MECHANISTIC UNDERSTANDING OF EXTRACELLULAR ELECTRON TRANSPORT:  
MODELING MEASUREMENTS OF SINGLE-CELL ACTIVITY

by

Xiaojia He

(Under the Direction of Christof Meile)

ABSTRACT

Microorganisms harness biochemical energy from their surroundings and shuttle electrons out of cells to external terminal electron acceptors. Extracellular electron transport (EET) can take place via diffusive exchange of a dissolved electron donor (e.g., H<sub>2</sub>, formate, acetate) between microbes (i.e. mediated electron transfer) and direct electron transfer, which requires physical contact between microbes and the terminal electron acceptors. There is increasing evidence for the important role of direct EET in many microbial communities; yet the exact biophysical mechanisms remain not fully resolved. A primary goal of this dissertation is to investigate the mechanisms underlying EET in the process of anaerobic oxidation of methane as well as anode respiration carried out by *Geobacter sulfurreducens* biofilms. In light of high-resolution metabolic activity acquired using FISH and nanoSIMS, in this thesis I have developed reactive transport models that provide mechanistic understanding of the EET process that can be adapted to a broader microbial community.

INDEX WORDS: Extracellular Electron Transfer, Anaerobic Oxidation of Methane,  
*Geobacter sulfurreducens*, nanoSIMS, Bioenergetics, Thermodynamics,  
Electron Hopping, Reactive Transport Modeling

MECHANISTIC UNDERSTANDING OF EXTRACELLULAR ELECTRON TRANSPORT:  
MODELING MEASUREMENTS OF SINGLE-CELL ACTIVITY

by

XIAOJIA HE

B.E., Ocean University of China, China, 2011

M.S., Jackson State University, 2014

A Dissertation Submitted to the Graduate Faculty of The University of Georgia in Partial  
Fulfillment of the Requirements for the Degree

DOCTOR OF PHILOSOPHY

ATHENS, GEORGIA

2020

© 2020

Xiaojia He

All Rights Reserved

MECHANISTIC UNDERSTANDING OF EXTRACELLULAR ELECTRON TRANSPORT:  
MODELING MEASUREMENTS OF SINGLE-CELL ACTIVITY

by

XIAOJIA HE

Major Professor: Christof Meile

Committee: Chris Kempes  
Suchendra M. Bhandarkar  
Samantha B. Joye  
Patricia M. Medeiros

Electronic Version Approved:

Ron Walcott  
Interim Dean of the Graduate School  
The University of Georgia  
December 2020

## DEDICATION

I dedicate my dissertation work to my wife, Canjingjing Cui, and my family.

## ACKNOWLEDGEMENTS

I owe thanks to my committee members who have helped me along the way towards finishing my PhD. A special thanks to Christof Meile, my academic adviser and committee chairman for his full support and guidance throughout the entire process. I am grateful to have Chris Kempes, Mandy Joye, Suchi Bhandarkar, Patricia Medeiros on my committee. I would like to acknowledge Gray Chadwick and Victoria Orphan at Caltech for providing data and their stimulating conversations on my dissertation topics. Special thanks goes to Yimeng Shi for initiating the first project.

I would like to thank my labmates Jurjen Rooze, Yu Wang, David Miklesh (passed away in 2018), Kadir Bice, and Heewon Jung for their countless discussions. I would also like to thank Adrian Burd, Lorraine Fuller, Frank Ferrer-Gonzalez, Linqun Mu, Yawei Shen, Yu Wang for practicing Kashima Shinryu over the past five years together. Thank you Catherine Teare Ketter for guiding and supporting during my TA. Special thanks to many friends, collaborators, faculty and staff members at Marine Science department for their encouragement and continued support.

## TABLE OF CONTENTS

	Page
ACKNOWLEDGEMENTS .....	v
LIST OF TABLES .....	ix
LIST OF FIGURES .....	x
CHAPTER	
1 INTRODUCTION .....	1
Overview .....	2
History of EET Research .....	3
Current Knowledge on Mechanisms of EET .....	6
Aim and Outline of This Dissertation .....	13
Reference .....	13
2 MICROBIAL INTERACTIONS UNDERLYING ANAEROBIC OXIDATION OF METHANE: CONSTRAINTS ON MECHANISMS FROM PROCESS RATES, ACTIVITY PATTERNS AND MODELING .....	25
Abstract .....	26
Introduction .....	26
Modeling Procedure .....	29
Results and Discussion .....	38
Conclusions .....	57
Acknowledgements .....	57

Reference .....	58
3 CONTROLS AND SIZE LIMITATIONS OF ANAEROBIC METHANE OXIDIZING CONSORTIA METABOLISM .....	67
Abstract.....	68
Introduction.....	68
Materials and Methods.....	70
Results and Discussion .....	81
Conclusions .....	92
Acknowledgements .....	94
Reference .....	94
4 SPATIALLY RESOLVED ELECTRON TRANSPORT THROUGH ANODE- RESPIRING <i>GEOBACTER</i> BIOFILMS: CONTROLS AND CONSTRAINTS .....	102
Abstract.....	103
Introduction.....	104
Materials and Methods.....	106
Results and Discussion .....	115
Implications .....	127
Acknowledgements .....	128
Reference .....	129
5 REGISTERING FISH AND NANOSISM IMAGES USING CNN .....	143
Abstract.....	144
Introduction.....	145
Related Work .....	147

Methods.....	149
Results and Discussion .....	162
Conclusions .....	176
Acknowledgements .....	177
Reference .....	177
6 CONCLUSIONS .....	185
APPENDICES .....	188
A CHAPTER 2 SUPPLEMENTARY MATERIAL .....	188
B CHAPTER 3 SUPPLEMENTARY MATERIAL.....	207
C CHAPTER 4 SUPPLEMENTARY MATERIAL.....	227
D CHAPTER 5 SUPPLEMENTARY MATERIAL .....	235

## LIST OF TABLES

	Page
Table 1.1: Reduction potential ( $E^\circ$ ) of common redox couples under standard conditions (pH = 7, T = 25 °C) .....	8
Table 2.1: Parameterization of reactions .....	37
Table 3.1: Summary of parameters used in model implementation .....	79
Table 4.1: Model parameter and description .....	114
Table 5.1: Selected examples using pretrained CNN architecture for image registration .....	148

## LIST OF FIGURES

	Page
Figure 1.1: Schematic representation of three types of extracellular electron transfer (EET) .....	4
Figure 2.1: Model representation with three distinct mechanisms for the electron transport within archaeal-bacterial consortia .....	32
Figure 2.2: Average cell-specific AOM rates, normalized to the value for the smallest aggregates vs. aggregate radius .....	43
Figure 2.3: Intra-aggregate variation of archaeal and bacterial activity .....	45
Figure 2.4: Average cell-specific AOM rate with varying $k_A$ and $k_B$ for DIET .....	48
Figure 2.5: Simulations of AOM by DIET with varying model parameters .....	51
Figure 3.1: Overview of AOM consortia structure, nanoSIMS data acquisition, analysis, and model geometry .....	77
Figure 3.2: Measured and modeled cell-specific activity in aggregate with a radius of 20 $\mu\text{m}$ ...	83
Figure 3.3: Cell-specific activity vs. distance from syntrophic partner for archaea and bacteria .	85
Figure 3.4: Factors controlling cell activity as a function of the distance from the archaea- bacteria interface at aggregate radius of 60 $\mu\text{m}$ for archaea and bacteria .....	86
Figure 3.5: Changes of activation loss, ohmic resistance loss and net available potential due to a change in total redox active molecules, number of conductive connections, conductivity, cell redox active factor, cell rate constants .....	88
Figure 3.6: The Gibbs free energy change ( $\Delta G$ ) against the change of electron conduction via DIET .....	91
Figure 4.1: Model validation with $^{15}\text{N}$ observations using nanoSIMS at high (+0.24V) and low (- 0.1V) anode potentials .....	116

Figure 4.2: The modeled effects of activation ( $\phi_{act}$ ) and ohmic resistance ( $\phi_{om}$ ) losses on net effective electric potential ( $\phi_{net}$ ) through the biofilm, and the resulting potential constraints on metabolic activity ( $F\theta$ ) .....118

Figure 4.3: The impact of bicarbonate buffering capacity on activity patterns at high anode potential for the early activity peak near electrode .....121

Figure 4.4: Sensitivity analysis of model parameters and their impact on cell specific activity and current density .....127

Figure 5.1: Workflow of registering FISH images and nanoSIMS images .....149

Figure 5.2: Preprocessing FISH and nanoSIMS images .....150

Figure 5.3: Schematic representation of the non-rigid image registration using CNN with VGG16 .....152

Figure 5.4: Schematic representation of the non-rigid image registration using CNN with VGG19 .....152

Figure 5.5: Schematic representation of the non-rigid image registration using CNN with GoogLeNet.....154

Figure 5.6: Schematic representation of the non-rigid image registration using CNN with ShuffleNet .....154

Figure 5.7: Schematic representation of the non-rigid image registration using CNN with ResNet18 .....155

Figure 5.8: Schematic representation of the non-rigid image registration using CNN with ResNet101 .....156

Figure 5.9: Workflow of feature matching and inlier selection after extracting features from CNN models.....157

Figure 5.10: Image registration for a moderately deformed FISH image onto nanoSIMS image using binary and RGB as input with TPS and similarity registration .....	164
Figure 5.11: Feature extraction for a moderately deformed FISH image onto nanoSIMS image using binary and RGB registration .....	165
Figure 5.12: Feature mapping before final thresholding for a moderately deformed FISH image onto nanoSIMS image using binary and RGB registration .....	165
Figure 5.13: Feature mapping after final thresholding for a moderately deformed FISH image onto nanoSIMS image using binary and RGB registration .....	166
Figure 5.14: Image registration accuracy for a moderately deformed FISH image .....	167
Figure 5.15: Image registration for a significantly deformed FISH image onto nanoSIMS image using binary and RGB as input with TPS and similarity registration .....	168
Figure 5.16: Feature extraction for a significantly deformed FISH image onto nanoSIMS image using binary and RGB registration .....	168
Figure 5.17: Feature mapping before final thresholding for a significantly deformed FISH image onto nanoSIMS image using binary and RGB registration .....	169
Figure 5.18: Feature mapping after final thresholding for a significantly deformed FISH image onto nanoSIMS image using binary and RGB registration .....	170
Figure 5.19: Image registration accuracy a significantly deformed FISH image .....	171
Figure 5.20: Image registration for a deformed FISH image with multiple components onto nanoSIMS image using binary and RGB as input with TPS and similarity registration .....	172
Figure 5.21: Feature extraction for a deformed FISH image with multiple components onto nanoSIMS image using binary and RGB registration .....	173

Figure 5.22: Feature mapping before final thresholding for a deformed FISH image with multiple components onto nanoSIMS image using binary and RGB registration .....174

Figure 5.23: Feature mapping after final thresholding for a deformed FISH image with multiple components onto nanoSIMS image using binary and RGB registration .....175

Figure 5.24: Image registration accuracy a deformed FISH image with multiple components .176

## CHAPTER 1

### INTRODUCTION

#### Overview

“*Life is nothing but an electron looking for a place to rest,*” said Albert Szent-Györgyi (Nobel Prize Laureate in Physiology or Medicine, 1937) (1). Although I would prefer using *biology* than *life*, electrons are produced and moved from place to place, and molecule to molecule, in all biological processes, from unicellular to intelligent life. Indeed, electrons are the essence of respiration – a process in which life forms pick up substrates, organic or inorganic, from the environment, and oxidize these substrates via redox reactions, aerobically or anaerobically, to acquire energy, maintain metabolic functions, generate biomass and eventually reproduce. These substrates are also referred to electron donors, ranging from most organic molecules such as methane and glucose to many inorganic matters such as hydrogen and ammonia. The redox potential – a measure of the tendency to gain or lose electrons – is often determining which chemicals a cell can use as electron acceptor to oxidize substrates in a redox reaction. That being said, energy generated from the redox reactions must be sufficient to at least create an electrochemical proton gradient ( $\Delta pH$ ) across a membrane that can drive the synthesis of adenosine triphosphate (ATP) to maintain cell metabolism (2). Humans and many other life forms, for example, use molecular oxygen as electron acceptors and oxidize glucose in form of aerobic

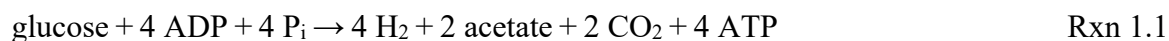
respiration, whereas many microorganisms must rely on other electron acceptors such as sulfate in the absence of oxygen.

However, resources in natural environments can be limited, including electron acceptors in anoxic environments. In a scenario of extracellular soluble electron acceptors are limited or even inaccessible to cells, electrons must be moved outside of cells in searching for terminal electron acceptors. Therefore, extracellular electron transfer (EET) may have acted as one of the most important players to carry out cell functions in early life forms emerged (3, 4). In this process, electrons are moved outside of cells in order to respire extracellular electron acceptors such as solid mineral oxides that are spatially distant (5-7), or alternatively supply electrons to its partners in multispecies community (7-9). The emergence of such EET strategies opens up vast opportunities for microbes to utilize extracellular electron acceptors and enable the formation of a spatially structured multicellular community sharing electron sources (10). The prevalence of EET via mobile redox shuttles has been recognized in a wide variety of environments ranging from deep-sea sediments and groundwater (11, 12) to anaerobic gut (13). More recent studies suggest that direct EET (as opposed to diffusive exchange) between the same or different microbial species takes place in a diverse group of microbes, including methanogens (14, 15), acetogens (16), anaerobically methane oxidizing consortia (17-19) and electroactive biofilms (20-25). Such direct EET overcomes limitations inherent in the diffusive exchange of electron carrying molecules that lead to the build-up of reaction products making the reaction energetically unfavorable, and the subsequent shut-down of metabolism (19, 26). Consequently, large microbial communities are able to form even under circumstances in which electron acceptors are found only at distances too large for efficient delivery by chemical diffusion. As a result, EET is increasingly being recognized as a critical step in a wide range of microbially-mediated processes in environmental and

geological settings (27), as well as in the performance of engineered electrochemical systems such as microbial fuel cells (28).

### History of EET Research

Early discovery of chemicals that are involved in the EET can be traced back to 1930s-1960s when rumen fermentation was extensively studied. Early studies on gas production by ruminants showed that there was a very low concentrations of hydrogen being observed produced, along with considerable amount of methane (29-31), suggesting hydrogen served as intermediate and important precursor of methane in the rumen (32, 33). Later investigations revealed a new concept of interspecies hydrogen transport, in which hydrogen was produced by fermenters (e.g. Rxn 1.1) and directly transferred to methanogens (Rxn 1.2) (34).



The redox coupling between the electron donor, electron shuttle and extracellular electron acceptor can be generalized as



where  $ED_{red}$  and  $ED_{ox}$  are reduced and oxidized electron donors (e.g. acetate/ $\text{CO}_2$  in Table 1.1),  $B_{red}$  and  $B_{ox}$  are reduced and oxidized electron shuttles (e.g.  $\text{FMNH}_2/\text{FMN}$  in Table 1.1), and  $EEA_{ox}$  and  $EEA_{red}$  are oxidized and reduced extracellular electron acceptors (e.g.  $\text{Fe}^{3+}/\text{Fe}^{2+}$  in Table 1.1). Some other redox chemicals may also be involved in Rxn 1.3 and 1.4, for instance,  $\text{NAD}^+/\text{NADH}$ ,  $\text{GSSG}/\text{GSH}$  and membrane bound cytochromes (e.g.  $\text{Cyt } c_{ox}/\text{Cyt } c_{red}$  in Table 1.1). Altogether, the complete reaction between electron donors and extracellular electron acceptors involves a series of redox reactions intracellularly and extracellularly.

Such a mechanism is referred to as mediated interspecies electron transfer (MIET), one of the EET pathways (Fig. 1.1A). Besides hydrogen, many small reduced molecules, including formate (35), acetate (36) and methyl compounds (37) have also been shown to be as intermediates shuttling electrons to methanogens in ruminants. Similar electron shuttling pathways were also found in methanogenic syntrophic microbial communities isolated from sewage sludge, freshwater and marine sediments (38).

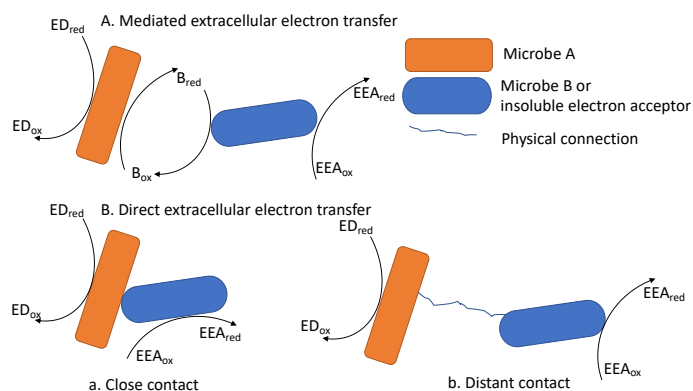


Fig. 1.1 Schematic representation of three types of extracellular electron transfer (EET). A. mediated EET. (B) direct EET: a. close contact, b. distant contact.

In addition, studies on azo dye biodegradation were first to show flavin could act as extracellular electron shuttle (39, 40). In 1967, Roxon and coworkers (39) showed that soluble flavin were essential for reducing azo food coloring, tartrazine, in whole-cell suspensions of *Proteus vulgaris*. They isolated the cell-free extracts and demonstrated extracellular soluble flavin was nearly 60% of the total flavins in *P. vulgaris* that accounted for tartrazine reduction. In 1971, Gingell and Walker (40) further examined the role of soluble flavin in the reducing Red 2G in *Streptococcus faecalis*, and suggested that soluble flavin can act as an electron shuttle between the dye and a reducing enzyme produced by bacteria. A series of experimental exploration on soluble flavins further led to the proposed mechanism that extracellular electron shuttle mediates electron

transfer between microorganism and extracellular electron acceptors such as azo dyes in those studies (39-41).

The study of extracellular electron shuttling was fueled by the discovery of *Geobacter* and *Shewanella* species. In 1987, it was reported that the bacterium *Geobacter metallireducens* can reduce ferric oxide extracellularly in anaerobic sediments (42). Later in 1994, *G. sulfurreducens*, a close relative of *G. metallireducens*, was isolated and shown to be able to reduce Fe(III) (43). In 1988, it was reported that *Alteromonas putrefaciens* (*Shewanella putrefaciens*) was able to use minerals such as manganese and iron oxides as terminal electron acceptors (44). Initially, it was generally thought that these metal-respiring microorganisms must establish direct contact with the insoluble minerals (44-46) (Fig. 1.1B.a). Though it was also demonstrated that soluble chelated metal oxides (47, 48) and naturally occurring humic substances can act as electron shuttles (49, 50) to facilitate metal reduction, it was not clear whether metal reduction can be realized via mobile electron shuttle produced by those bacteria. In 2000, Newman and Kolter (51) were the first to show that *S. putrefaciens* can produce menaquinone-related redox-active small molecules as extracellular electron shuttle to reduce AQDS, a humic substance analogue. Later in 2002, Nevin and Lovley (52) reported that *S. alga* strain BrY released *some chemical(s)* as electron shuttle that promoted electron transfer to iron oxides. Many new evidences have shown that *Shewanella* species can secrete flavin (53, 54) and ACNQ (2-amino-3-carboxyl-1,4-napthoquinone) (55) molecules as extracellular electron shuttles to extracellular electron acceptors. It was not until 2005 that a completely new concept of direct EET via conductive pili was revealed in Fe(III) oxide reducing *G. sulfurreducens* (56) (Fig. 1.1B.b). Later, more biogenic conductive structures were also found in methanogens (14, 15), acetogens (16), anaerobically methane oxidizing consortia

(17-19) and electroactive biofilms (20-25), suggesting the potential ecological and physiological role of direct EET in nature.

Newer data shows that microbial communities have developed the capability to harness energy from environment, in which mediated- and direct- EET may coexist (57). In a *G. metallireducens* and *G. sulfurreducens* coculture, riboflavin was secreted to 1) establish the syntrophic growth between *Geobacter* species prior to the formation of any direct conductive connections, and 2) provide additional EET alongside the DIET, though only at a minor fraction (57). Model simulation from Renslow and coworkers showed that dual EET pathways in *S. oneidensis* biofilms may have a metabolic advantage over biofilms that can use only a single mechanism (58).

#### Current Knowledge on Mechanisms of EET

From a thermodynamic point of view, the removal of product from electron donor oxidation must be fast enough to counter its accumulation. In an environmental setting without advection flow, diffusion is the dominant force for the removal of metabolite, and the distribution of a metabolite ( $B_{red}$ ) can be described by:

$$\frac{\partial B_{red}}{\partial t} = R_{rxn1.1} + \nabla \cdot (D \nabla B_{red}) \quad \text{Eq. (1.1)}$$

where reaction rate  $R_{rxn1.1}$  is a function of reaction kinetics  $F_k$  and thermodynamics  $F_T$ ,

$$R_{rxn1.1} = F_k F_T, \quad \text{Eq. (1.2)}$$

In such a rate expression,  $F_k$  may, for example, be represented as product of a cell-specific rate constant  $k$ , the cell density  $B$  (cells per volume), and the abundance of substrate  $S$  using a Monod expression with half-saturation constant  $K_m^S$ :

$$F_k = kB \frac{S}{K_m^S + S} \quad \text{Eq. (1.3)}$$

Following Jin and Bethke (59, 60)  $F_T$  may be expressed as a function of Gibbs free energy

$\Delta G_{rxn1.1}$  from reaction Rxn1.1,

$$F_T = \max \left( 0, 1 - e^{-\frac{-\Delta G_{rxn1.1} - \Delta G_{ATP}}{\chi R_{gas} T}} \right) \quad \text{Eq. (1.4)}$$

where  $\chi$  is the number of ATP synthesized per reaction,  $\Delta G_{ATP}$  represents a minimum energy required for ATP synthesis.  $\Delta G_{rxn1.1}$  is calculated as

$$\Delta G_{rxn1.1} = \Delta G_{rxn1.1}^\circ + R_{gas} T \ln Q_{rxn1.1} \quad \text{Eq. (1.5)}$$

whereas  $Q_{rxn1.1}$  is the reaction quotient of Rxn 1.3

$$Q_{rxn1.1} = \frac{a_{Bred}^\gamma a_{EDox}^\delta}{a_{Box}^\alpha a_{EDred}^\beta} \quad \text{Eq. (1.6)}$$

where  $a_{Bred}$ ,  $a_{EDox}$ ,  $a_{Box}$ ,  $a_{EDred}$  are activity of each chemical,  $\alpha$ ,  $\beta$ ,  $\gamma$ ,  $\delta$  are stoichiometric coefficient of each chemical and are set to 1 in Rxn 1.3 for demonstration purpose.

Thermodynamic factor  $F_T$  ( $0 \leq F_T \leq 1$ ) is an index that reflects that  $\Delta G_{rxn1.1}$  must be sufficiently negative to counter the minimum energy requirement for cell metabolism  $\Delta G_{ATP}$ . In other words, metabolite products must be consumed at a certain rate in order to keep the microbial metabolism thermodynamically favorable. Otherwise, a drastically declining metabolic activity may occur as the distance from the external electron acceptors increases.

Table 1.1 Reduction potential ( $E^{\circ}$ ) of common redox couples under standard conditions (pH = 7, T = 25 °C) (61-64)

Redox pairs	Half reaction	$E^{\circ}$ (mV)
O <sub>2</sub> /H <sub>2</sub> O	O <sub>2</sub> + 4e <sup>-</sup> + 4H <sup>+</sup> → 2H <sub>2</sub> O	+820
Fe <sup>3+</sup> /Fe <sup>2+</sup>	Fe <sup>3+</sup> + e <sup>-</sup> → Fe <sup>2+</sup>	+771
NO <sub>3</sub> <sup>-</sup> /N <sub>2</sub>	NO <sub>3</sub> <sup>-</sup> + 6e <sup>-</sup> + 6H <sup>+</sup> → 0.5N <sub>2</sub> + 3H <sub>2</sub> O	+750
MnO <sub>2</sub> /Mn <sup>2+</sup>	MnO <sub>2</sub> + 2e <sup>-</sup> + 4H <sup>+</sup> → /Mn <sup>2+</sup> + 2H <sub>2</sub> O	+600
NO <sub>3</sub> <sup>-</sup> /NO <sub>2</sub> <sup>-</sup>	NO <sub>3</sub> <sup>-</sup> + 2e <sup>-</sup> + 2H <sup>+</sup> → NO <sub>2</sub> <sup>-</sup> + H <sub>2</sub> O	+420
NO <sub>3</sub> <sup>-</sup> /NH <sub>4</sub> <sup>-</sup>	NO <sub>3</sub> <sup>-</sup> + 6e <sup>-</sup> + 8H <sup>+</sup> → NH <sub>4</sub> <sup>-</sup> + H <sub>2</sub> O	+360
Cyt a <sub>ox</sub> /Cyt a <sub>red</sub>	Cyt a <sub>ox</sub> + e <sup>-</sup> → Cyt a <sub>red</sub>	+290
Cyt c <sub>ox</sub> /Cyt c <sub>red</sub>	Cyt c <sub>ox</sub> + e <sup>-</sup> → Cyt c <sub>red</sub>	+250
CH <sub>3</sub> OH/CH <sub>4</sub>	CH <sub>3</sub> OH + 2 H <sup>+</sup> + 2e <sup>-</sup> → CH <sub>4</sub> + H <sub>2</sub> O	+170
Cyt b <sub>ox</sub> /Cyt b <sub>red</sub>	Cyt b <sub>ox</sub> + e <sup>-</sup> → Cyt b <sub>red</sub>	+80
ubiquinol/ubiquinone	ubiquinone + 2e <sup>-</sup> + 2H <sup>+</sup> → ubiquinol	+40
fumarate/succinate	fumarate + 2e <sup>-</sup> + 2H <sup>+</sup> → succinate	+30
FAD/FADH <sub>2</sub>	FAD + 2e <sup>-</sup> + 2H <sup>+</sup> → FADH <sub>2</sub>	+30
H <sup>+</sup> /H <sub>2</sub> (pH = 0)	2H <sup>+</sup> + 2e <sup>-</sup> → H <sub>2</sub> O	0
pyruvate/lactate	pyruvate + 2e <sup>-</sup> + 2H <sup>+</sup> → lactate	-190
acetaldehyde/ethanol	acetaldehyde + 2 H <sup>+</sup> + 2 e <sup>-</sup> → ethanol	-197
SO <sub>4</sub> <sup>2-</sup> /HS <sup>-</sup>	SO <sub>4</sub> <sup>2-</sup> + 8e <sup>-</sup> + 9H <sup>+</sup> → HS <sup>-</sup> + 4H <sub>2</sub> O	-220
GSSG/GSH	GSSG + 2e <sup>-</sup> + 2H <sup>+</sup> → 2GSH	-240
CO <sub>2</sub> /CH <sub>4</sub>	CO <sub>2</sub> + 8e <sup>-</sup> + 8H <sup>+</sup> → CH <sub>4</sub> + 2H <sub>2</sub> O	-240
CO <sub>2</sub> /acetate	2CO <sub>2</sub> + 8e <sup>-</sup> + 8H <sup>+</sup> → acetate + 2H <sub>2</sub> O	-290
FMN/FMNH <sub>2</sub>	FMN + 2e <sup>-</sup> + 2H <sup>+</sup> → FMNH <sub>2</sub>	-300
NAD <sup>+</sup> /NADH	NAD <sup>+</sup> + 2e <sup>-</sup> + H <sup>+</sup> → NADH	-320
NADP <sup>+</sup> /NADPH	NADP <sup>+</sup> + 2e <sup>-</sup> + H <sup>+</sup> → NADPH	-320
Cystine/Cysteine	Cystine + 2H <sup>+</sup> + 2e <sup>-</sup> → 2Cysteine	-340
H <sup>+</sup> /H <sub>2</sub> (pH = 7)	2H <sup>+</sup> + 2e <sup>-</sup> → H <sub>2</sub> O	-420

To illustrate the potential buildup of reaction products in a diffusion dominated environment, we consider a simple geometry of two concentric spheres occupied by two distinct interacting groups of microorganisms. If the microbes inhabiting the volume represented by the inner sphere produce a metabolic intermediate at a constant rate and those occupying the surrounding sphere consume that intermediate at a constant rate, then the concentration dynamics are given by

$$\frac{\partial C}{\partial t} = \frac{D}{r^2} \frac{\partial}{\partial r} \left( r^2 \frac{\partial C}{\partial r} \right) - \gamma \quad \text{Eq. (1.5)}$$

where  $C$  is the concentration of the intermediate,  $r$  is the radial distance,  $D$  is the diffusivity of the intermediate, and  $\gamma$  is the consumption rate of the intermediate. Solving for the steady state concentration of  $C$ , with a no-flux boundary condition at the outer edge of the larger sphere,

$\frac{\partial C}{\partial r} \Big|_{r=r_{ou}} = 0$ , and a constant value of  $C_{in}$  at the surface of the inner sphere gives

$$C = C_{in} + \frac{\gamma(2r_{in}r_{ou}^3 - r(r_{in}^3 + 2r_{ou}^3) + r_{in}r^3)}{6Dr_{in}r} \quad \text{Eq. (1.6)}$$

where  $r_{in}$  and  $r_{ou}$  are the inner and outer sphere radii respectively, and  $C_{in}$  is the concentration at the surface of the inner sphere. The concentration profiles for a wide range of  $\gamma$  and  $C_{in}$  are shown in Fig 1.2, showing that the delivery of the intermediate to the microbial community in the outer domain can be limited for molecular diffusion only. Considering effective diffusion coefficient in direct EET is much faster than that of mediated EET (21, 65), it is clear that for a given concentration  $C_{in}$  and consumption rate  $\gamma$ , direct EET allows microbes to reach out to resources at a much greater distance than mediated EET.

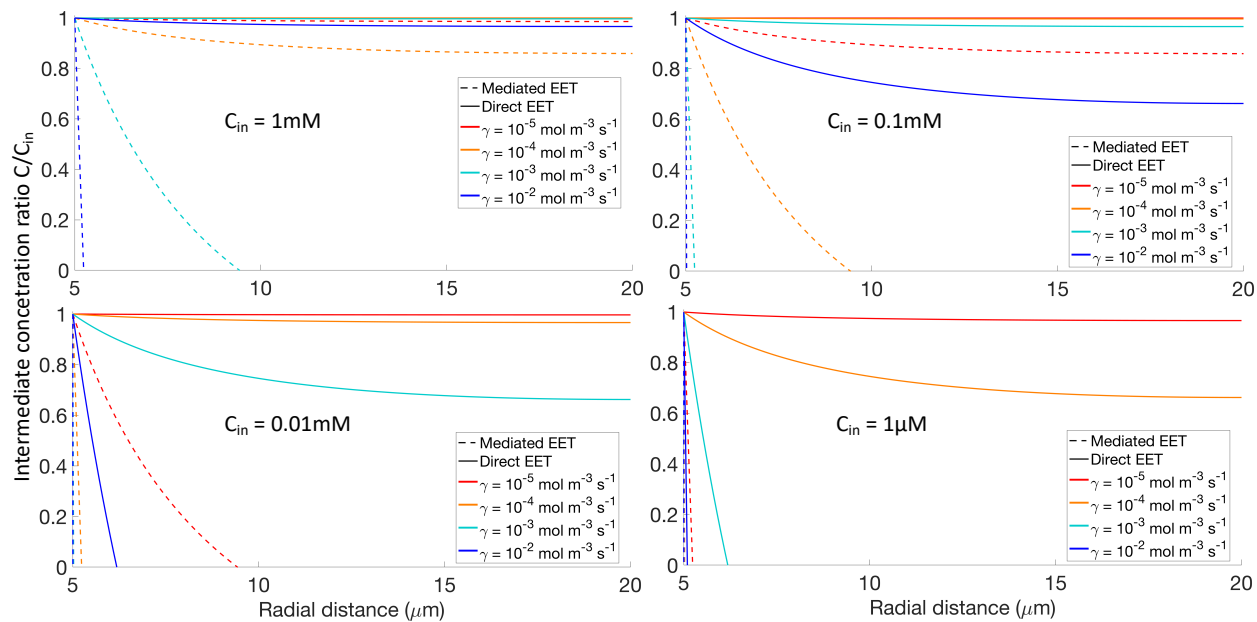


Fig. 1.2 Substrate concentration across the outer sphere ( $C/C_{in}$ ) via mediated and direct EET, at various substrate concentration ( $C_{in}$ ) and consumption rate of the intermediate ( $\gamma$ ). In situ intermediate diffusivity ( $D$ ) was set to  $2.4 \times 10^{-10} \text{ m}^2 \text{ s}^{-1}$  considering typical diffusion coefficient ( $D_{aq}$ ) for small chemicals at  $10^{-9} \text{ m}^2 \text{ s}^{-1}$ , a reducing factor ( $f_{eps}$ ) at 0.6 and tortuosity factor ( $\theta^2$ ) at 2.5, giving  $D = f_{eps} D_{aq} / \theta^2$  (26). Effective direct transfer diffusivity was set to  $1 \times 10^{-7} \text{ m}^2 \text{ s}^{-1}$ .

Although many details have been unveiled in the past decade, the study of direct EET is still in its infancy. There are currently two main hypotheses proposed as fundamental mechanisms underlying direct EET: 1). Metal-like conduction and 2). Electron hopping. Metal conduction is characterized by the presence of free-moving valence electrons. Similarly, valence electrons are required for a polymer to be conductive. This is usually realized by forming a conjugated system in which  $\pi$ -orbitals overlap with one another in a chain of molecules (66). Thus, the conjugated  $\pi$ -orbitals generally lower the overall energy of the molecule by lowering the HOMO-LUMO energy gap, thus making electrons mobile when it is partially emptied (67). The first highly conductive

polymer was reported in the 1950s, in which charge transfer complexes between polycyclic aromatic compounds and halogens showed electrical conductivity as low as  $0.01 \Omega \text{ m}$  (i.e.  $100 \text{ S m}^{-1}$ ) (68). A half century later, metal-like conduction mechanism was firstly proposed in biogenic pili from *G. sulfurreducens* (69). Measurements on individual pili showed high conductivities approximately  $50 \text{ mS cm}^{-1}$  at pH 7 (70), showing a temperature and pH dependent conductivity response (69, 70). It was suggested that aromatic amino acids in conductive pili play a key role for its metal-like conductivity (71). A later study showed that aromatic amino acids in conductive *G. sulfurreducens* pili were closely packed within 3-4 Å, which may permit overlapping  $\pi$ -orbitals of aromatic amino acids and charge delocalization, and thus metal-like conductivity (72).

On the other hand, electron hopping is a phenomenon where electrons are localized on a chain of redox active molecules, and are transferred to terminal electron acceptors via multistep bucket-brigade manner between adjacent redox centers (73). There has been a long history of developing electron hopping theory in electroactive redox polymers or biomolecules with localized redox sites (74, 75), since its initial introduction in 1979 (76). Earlier work showed that redox proteins such as Ru-modified azurin and cytochromes can have long-range electron hopping over 20 Å (77, 78). Such multistep hopping mechanism has also been observed between aromatic side chains of peptides (79, 80), and suggested to be responsible for conductive biofilm through filament associated redox proteins such as OmcS (21) or multiheme c-type cytochromes (81). Studies on the outer membrane multiheme cytochromes in *Shewanella* species showed that all haems in decaheme cytochrome MtrC were tightly packed at a separation less than 7 Å (82). A recent report showed that *G. sulfurreducens* conductive filaments were assembled by hexaheme cytochrome OmcS, with a tight packing distance at 3.5–6 Å over a micrometer length (83), corroborated with interatomic distances between adjacent porphyrins of the hexaheme cytochrome

at 4.1 Å or less (84). At such short distance, multistep electron hopping along the conductive filaments is possible. In addition, many studies suggest that the development of redox gradient as the redox potential drops with increasing distance from the anode surface drives electron hopping in electroactive biofilms (21, 85-87).

However, there is an ongoing debate over the exact mechanism underlying direct EET, e.g. (21, 88, 89) and (90-92). One of the key points debated is the molecular composition and structural packing of conductive filaments at atom resolution (Å). Metal-like conduction relies on the functioning of biogenic structures like pili as intrinsic metallic conductor. Conductive pili are often found to be as thin as 3 nm in diameter (93), comprised mainly by pilin protein monomers (72) with a N-terminal  $\alpha$ -helix combined with a short and flexible C-terminal region (94). This was recently challenged by a report suggesting OmcS filaments, instead of pili, were the primary conduits for long-range electron transport in *G. sulfurreducens* (83). This study pointed out that those conductive pili may in fact be OmcS filaments, coinciding with earlier work that showed that the *c*-type cytochrome OmcS was associated with conductive pili of *G. sulfurreducens* (95). While only non-filamentous PilA was found in the *G. sulfurreducens* (83), it was concluded that PilA was mainly involved producing OmcS filaments (96), which may explain correlation between PilA and biofilm conductivity (92). This was soon addressed by a Cryo-EM study of a 4 nm cytochrome-based *G. sulfurreducens* filament, showing that it indeed consisted of hexaheme cytochrome OmcS, but lacked evidence for the 3 nm diameter filaments which were presumably composed of PilA (84). Nonetheless, the aromatic amino acids of *G. sulfurreducens* PilA can still allow EET via multistep hopping mechanism (94), as long as the packing between adjacent redox active centers are less than 20 Å (77, 78).

## Aim and Outline of This Dissertation

In this dissertation, reactive transport modeling was used as a synthesizing tool for fundamental microbiological research (97). It provides a means to apply fundamental physics and chemistry to natural systems that couple microbially mediated processes. Our approach resolves spatial variabilities in cell metabolism at the sub-mm scale, including variability in rates of nitrogen incorporation in syntrophic consortia and electroactive biofilms. A primary goal of this dissertation is to assess the effect of different reaction mechanisms and electron transfer capabilities on the process of anaerobic methane oxidation in Chapters 2 and 3. Chapter 2 addresses the mechanism underlying electron transport within AOM consortia. The goal is to provide insight into microbial interactions and reactions using process-based modeling. Chapter 3 aims to provide knowledge that may unveil electron transport mechanism for large AOM consortia and the potential size constraints. Chapter 4 builds on the developments in Chapter 2 and Chapter 3, and aims to address the electron transport process in a *Geobacter* biofilm. Chapter 5 is a method development study for image processing in microbiology to automate the data processing used in Chapters 2 and 3.

## References

1. Lane N. Life Ascending: The Ten Great Inventions of Evolution. New York: W. W. Norton & Company; 2009.
2. Hosler JP, Ferguson-Miller S, Mills. DA. Energy transduction: proton transfer through the respiratory complexes. Annu Rev Biochem. 2006;**75**:165-87.
3. Lovley DR. Potential Role of Dissimilatory Iron Reduction in the Early Evolution of Microbial Respiration. In: Seckbach J, editor. Origins: Genesis, Evolution and Diversity of Life. Dordrecht: Springer; 2004. p. 299-313.

4. Lusk BG. Thermophiles; or, the Modern Prometheus: The Importance of Extreme Microorganisms for Understanding and Applying Extracellular Electron Transfer. *Frontiers in Microbiology*. 2019;**10**(818).
5. Shi L, Dong H, Requera G, Beyenal H, Lu A, Liu J, et al. Extracellular electron transfer mechanisms between microorganisms and minerals. *Nat Rev Microbiol*. 2016;**14**:651–62.
6. Gralnick JA, Newman DK. Extracellular respiration. *Mol Microbiol*. 2007;**65**:1–11.
7. Hernandez ME, Newman DK. Extracellular electron transfer. *Cell Mol Life Sci*. 2001;**58**:1562–71.
8. Lovley DR. Syntrophy goes electric: direct interspecies electron transfer. *Annu Rev Microbiol*. 2017;**71**:643-64.
9. Lovley DR. Happy together: microbial communities that hook up to swap electrons. *ISME J*. 2017;**11**(2):327-36.
10. Glasser NR, Saunders SH, Newman DK. The colorful world of extracellular electron shuttles. *Annu Rev Microbiol*. 2017;**71**:731–51.
11. Farag IF, Biddle JF, Zhao R, Martino AJ, House CH, León-Zayas RI. Metabolic potentials of archaeal lineages resolved from metagenomes of deep Costa Rica sediments. *ISME J*. 2020;**14**:1345–58.
12. Arbour TJ, Gilbert B, Banfield J. Diverse microorganisms in sediment and groundwater are implicated in extracellular redox processes based on genomic analysis of bioanode communities. *Front Microbiol*. 2020;**11**:1694.
13. Light SH, Su L, Rivera-Lugo R, Cornejo JA, Louie A, Iavarone AT, et al. A flavin-based extracellular electron transfer mechanism in diverse Gram-positive bacteria. *Nature*. 2018;**562**:140-4.

14. Rowe AR, Xu S, Gardel E, Bose A, Girguis P, Amend JP, et al. Methane-linked mechanisms of electron uptake from cathodes by *Methanosarcina barkeri*. *mBio*. 2019;**10**(2):e02448-18.
15. Morita M, Malvankar NS, Franks AE, Summers ZM, Giloteaux L, Rotaru AE, et al. Potential for direct interspecies electron transfer in methanogenic wastewater digester aggregates. *mBio*. 2011;**2**(4):e00159–11.
16. Kato S, Yumoto I, Kamagata Y. Isolation of acetogenic bacteria that induce biocorrosion by utilizing metallic iron as the sole electron donor. *Appl Environ Microbiol*. 2015;**81**:67–73.
17. McGlynn SE, Chadwick GL, Kempes CP, Orphan VJ. Single cell activity reveals direct electron transfer in methanotrophic consortia. *Nature*. 2015;**526**(7574):531-5.
18. Wegener G, Krukenberg V, Riedel D, Tegetmeyer HE, Boetius A. Intercellular wiring enables electron transfer between methanotrophic archaea and bacteria. *Nature*. 2015;**526**(7574):587-90.
19. He X, Chadwick G, Kempes C, Shi Y, McGlynn S, Orphan V, et al. Microbial interactions in the anaerobic oxidation of methane: Model simulations constrained by process rates and activity patterns. *Environ Microbiol*. 2019;**21**(2):631-47.
20. Strycharz SM, Malanoski AP, Snider RM, Yi H, Lovley DR, Tender LM. Application of cyclic voltammetry to investigate enhanced catalytic current generation by biofilm-modified anodes of *Geobacter sulfurreducens* strain DL1 vs. variant strain KN400. *Energy Environ Sci*. 2011;**4**:896-913.
21. Strycharz-Glaven SM, Snider RM, Guiseppi-Elie A, Tender LM. On the electrical conductivity of microbial nanowires and biofilms. *Energy Environ Sci*. 2011;**4**:4366–79.

22. Lebedev N, Strycharz-Glaven SM, Tender LM. Spatially Resolved Confocal Resonant Raman Microscopic Analysis of Anode-Grown *Geobacter sulfurreducens* Biofilms. *ChemPhysChem*. 2014;**15**:320– 7.
23. Bond DR, Strycharz-Glaven SM, Tender LM, Torres CI. On electron transport through *Geobacter* biofilms. *ChemSusChem*. 2012;**5**(6):1099-105.
24. Yan H, Chuang C, Zhugayevych A, Tretiak S, Dahlquist FW, Bazan GC. Inter-Aromatic Distances in *Geobacter Sulfurreducens* Pili Relevant to Biofilm Charge Transport. *Adv Mater*. 2015;**27**(11):1908-11.
25. Bonanni PS, Massazza D, Busalmen JP. Stepping stones in the electron transport from cells to electrodes in *Geobacter sulfurreducens* biofilms. *Phys Chem Chem Phys*. 2013;**15**(25):10300-6.
26. Orcutt B, Meile C. Constraints on mechanisms and rates of anaerobic oxidation of methane by microbial consortia: process-based modeling of ANME-2 archaea and sulfate reducing bacteria interactions. *Biogeosciences*. 2008;**5**:1587-99.
27. Hernandez ME, Newman DK. Extracellular electron transfer. *Cell Mol Life Sci*. 2001;**58**(11):1562-71.
28. Kracke F, Vassilev I, Krömer JO. Microbial electron transport and energy conservation—the foundation for optimizing bioelectrochemical systems. *Front Microbiol*. 2015;**6**:575.
29. Markoff J. Untersuchungen über die Gärungsprozesse bei der Verdauung der Wiederkäuer. *Biochemische Zeitschrift*. 1911;**34**:211-32.
30. Zuntz N, Heide RVD, KLEIN W. Zum Studium der Respiration und des Stoffwechsels der Wiederkäuer. *Landw Versuch Stat*. 1913;**79-80**:781.

31. Lugg JWH. Identification and measurement of the combustible gases that occur in the gaseous metabolic products of sheep. *J Agric Sci.* 1938;**28**(4):688-94.
32. Hungate RE. Hydrogen as an intermediate in the rumen fermentation. *Archiv für Mikrobiologie.* 1967;**59**:158–64.
33. Hungate RE. CHAPTER VI. Quantities of Carbohydrate Fermentation Products. *The Rumen and Its Microbes.* New York: Academic; 1966. p. 245-80.
34. Iannotti EL, Kafkewitz D, Wolin MJ, Bryant MP. Glucose fermentation products of *Ruminococcus albus* grown in continuous culture with *Vibrio succinogenes*: changes caused by interspecies transfer of H<sub>2</sub>. *J Bacteriol.* 1973;**114**:1231–40.
35. Hungate RE, Smith W, Bauchop T, Yu I, Rabinowitz JC. Formate as an intermediate in the bovine rumen fermentation. *J Bacteriol.* 1970;**102**(2):389-97.
36. Czerkawski JW, Breckenridge G. Fermentation of various glycolytic intermediates and other compounds by rumen micro-organisms, with particular reference to methane production. *British Journal of Nutrition.* 1972;**27**(1):131-46.
37. Neill AR, Grime DW, Dawson RMC. Conversion of choline methyl groups through trimethylamine into methane in the rumen. *Biochemical J.* 1978;**170**(3):529-35.
38. Bryant MP, Wolin EA, Wolin MJ, Wolfe RS. *Methanobacillus omelianskii*, a symbiotic association of two species of bacteria. *Arch Mikrobiol.* 1967;**59**(1):20-31.
39. Roxon JJ, Ryan AJ, Wright SE. Enzymatic reduction of tartrazine by *Proteus vulgaris* from rats. *Fd Cosmet Toxicol* 1967;**5**:645-56.
40. Gingell R, Walker R. Mechanisms of azo reduction by *Streptococcus faecalis* II. The role of soluble flavins. *Xenobiotica.* 1971;**1**(3):231-9.

41. Dubin P, Wright KL. Reduction of azo food dyes in cultures of *Proteus vulgaris*. *Xenobiotica*. 1975;**5**:563--71.
42. Lovley DR, Stolz JF, Jr GLN, Phillips EJP. Anaerobic production of magnetite by a dissimilatory iron-reducing microorganism. *Nature*. 1987;**330**:252–4.
43. Caccavo F, Lonergan DJ, Lovley DR, Davis M, Stolz JF, McInerney MJ. *Geobacter sulfurreducens* sp. nov., a hydrogen-and acetate-oxidizing dissimilatory metal-reducing microorganism. *Appl Environ Microbiol*. 1994;**60**(10):3752-9.
44. Myers CR, Neelson KH. Bacterial manganese reduction and growth with manganese oxide as the sole electron acceptor. *Science*. 1988;**240**:1319–21.
45. Lovley DR, Phillips EJ. Novel mode of microbial energy metabolism: organic carbon oxidation coupled to dissimilatory reuction of iron or manganese. *App Environ Microbiol*. 1988;**51**:683-9.
46. Arnold RG, DiChristina TJ, Hoffmann MR. Reductive dissolution of Fe(III) oxides by *Pseudomonas* sp. 200. *Biotechnol Bioeng*. 1988;**32**:1081-96.
47. Lovley DR. Dissimilatory Fe(III) and Mn(IV) reduction. *Microbiol Rev* 1991;**55**:259–87.
48. Lovley DR, Woodward JC. Mechanisms for chelator stimulation of microbial Fe(III)-oxide reduction. *Chem Geol*. 1996;**132**:19–24.
49. Lovley DR, Coates JD, Blunt-Harris EL, Phillips EJP, Woodward JC. Humic substances as electron acceptors for microbial respiration. *Nature*. 1996;**382**:445–8.
50. Lovley DR, Fraga JL, Blunt-Harris EL, Hayes LA, Phillips EJP, Coates JD. Humic substances as a mediator for microbially catalyzed metal reduction. *Acta Hydrochim Hydrobiol*. 1998;**26**:152–7.

51. Newman D, Kolter R. A role for excreted quinones in extracellular electron transfer. *Nature*. 2000;**405**:94–7.
52. Nevin KP, Lovley DR. Mechanisms for Fe(III) Oxide Reduction in Sedimentary Environments. *Geomicrobiol J*. 2002;**19**:141–59.
53. Brutinel ED, Gralnick JA. Shuttling happens: soluble flavin mediators of extracellular electron transfer in *Shewanella*. *Appl Environ Microbiol*. 2012;**93**:41–8.
54. Marsili E, Baron DB, Shikhare ID, Coursolle D, Gralnick JA, Bond DR. *Shewanella* secretes flavins that mediate extracellular electron transfer. *PNAS*. 2008;**105**(10):3968-73.
55. Mevers E, Su L, Pishchany G, Baruch M, Cornejo J, Hobert E, et al. An elusive electron shuttle from a facultative anaerobe. *eLife*. 2019;**8**:e48054.
56. Reguera G, McCarthy KD, Mehta T, Nicoll JS, Tuominen MT, Lovley DR. Extracellular electron transfer via microbial nanowires. *Nature nanotechnology*. 2005;**435**:1098–101.
57. Huang L, Liu X, Ye Y, Chen M, Zhou S. Evidence for the coexistence of direct and riboflavin-mediated interspecies electron transfer in *Geobacter* co-culture. *Environmental Microbiology*. 2020;**22**(1):243-54.
58. Renslow R, Babauta J, Kuprat A, Schenk J, Ivory C, Fredrickson J, et al. Modeling biofilms with dual extracellular electron transfer mechanisms. *Physical Chemistry Chemical Physics*. 2013;**15**(44):19262-83.
59. Jin Q, Bethke C. A new rate law describing microbial respiration. *Appl Environ Microbiol*. 2003;**69**:2340–8.
60. Jin Q, Bethke C. The thermodynamics and kinetics of microbial metabolism. *Am J Sci*. 2007;**307**:643–77.

61. Aghababaie M, Farhadian M, Jeihanipour A, Biria D. Effective factors on the performance of microbial fuel cells in wastewater treatment—a review. *Environmental Technology Reviews*. 2015;**4**(1):71-89.
62. Metzler DE. *Biochemistry: The Chemical Reactions of Living Things*. New York: Academic; 1977.
63. Harold FM. *The Vital Force: A Study of Bioenergetics*. New York: W.H. Freeman & Company; 1986. 47 p.
64. Karp G. *Cell and Molecular Biology*. 5th Ed ed: Wiley; 2008.
65. Meysman FJR, Risgaard-Petersen N, Malkin SY, Nielsen LP. The geochemical fingerprint of microbial long-distance electron transport in the seafloor. *Geochim Cosmochim Acta*. 2015;**152**:122–42.
66. IUPAC. *Compendium of Chemical Terminology (the "Gold Book")*. 2nd ed. Oxford: Blackwell Scientific Publications; 1997.
67. Milián-Medina B, Gierschner J.  $\pi$ -Conjugation. *WIREs Computational Molecular Science*. 2012;**2**(4):513-24.
68. Akamatu H, Inokuchi H, Matsunaga Y. Electrical Conductivity of the Perylene–Bromine Complex. *Nature*. 1954;**173**(4395):168–9.
69. Malvankar NS, Vargas M, Nevin KP, Franks AE, Leang C, Kim B-C, et al. Tunable metallic-like conductivity in microbial nanowire networks. *Nat Nanotechnol*. 2011;**6**:573–9.
70. Adhikari RY, Malvankar NS, Tuominen MT, Lovley DR. Conductivity of individual *Geobacter pili*. *RSC Adv*. 2016;**6**:8354–7.

71. Vargas M, Malvankar NS, Tremblay PL, Leang C, Smith JA, Patel P, et al. Aromatic amino acids required for pili conductivity and long-range extracellular electron transport in *Geobacter sulfurreducens*. *mBio*. 2013;**4**:e00105-13.
72. Malvankar NS, Vargas M, Nevin K, Tremblay PL, Evans-Lutterodt K, Nykypanchuk D, et al. Structural basis for metallic-like conductivity in microbial nanowires. *mBio*. 2015;**6**(2):e00084-15.
73. Blauch DN, Saveant JM. Dynamics of electron hopping in assemblies of redox centers. Percolation and diffusion. *Journal of the American Chemical Society*. 1992;**114**(9):3323-32.
74. Dalton EF, Surridge NA, Jernigan JC, Wilbourn KO, Facci JS, Murray RW. Charge transport in electroactive polymers consisting of fixed molecular redox sites. *Chem Phys*. 1990;**141**(1):143-57.
75. Blauch DN, Saveant JM. Dynamics of electron hopping in assemblies of redox centers. Percolation and diffusion. *J Am Chem Soc*. 1992;**114**(9):3323-32.
76. Kaufman FB, Engler EM. Solid-state spectroelectrochemistry of crosslinked donor bound polymer films. *J Am Chem Soc* 1979;**101**(3):547-9.
77. Cordes M, Köttgen A, Jasper C, Jacques O, Boudebous H, Giese B. Influence of Amino Acid Side Chains on Long-Distance Electron Transfer in Peptides: Electron Hopping via “Stepping Stones”. *Angewandte Chemie International Edition*. 2008;**47**(18):3461-3.
78. Winkler JR, Gray HB. Electron flow through metalloproteins. *Chemical Reviews*. 2014;**114**(7):3369-80.
79. Skourtis S, Balabin IA, Kawatsu T, Beratan DN. Protein dynamics and electron transfer: Electronic decoherence and non-Condon effects. *PNAS*. 2005;**102**:3552-7.

80. Schlag EW, Sheu SY, Yang DY, Selzle HL, Lin SH. Distal charge transport in peptides. *Angewandte Chemie*. 2007;**119**(18):3258-73.
81. Pirbadian S, El-Naggar MY. Multistep hopping and extracellular charge transfer in microbial redox chains. *Physical Chemistry Chemical Physics*. 2012;**14**(40):13802-8.
82. Edwards MJ, White GF, Norman M, Tome-Fernandez A, Ainsworth E, Shi L, et al. Redox linked flavin sites in extracellular decaheme proteins involved in microbe-mineral electron transfer. *Sci Rep*. 2015;**5**:11677.
83. Wang F, Gu Y, O'Brien JP, Sophia MY, Yalcin SE, Srikanth V, et al. Structure of microbial nanowires reveals stacked hemes that transport electrons over micrometers. *Cell*. 2019;**177**(2):361-9.
84. Filman DJ, Marino SF, Ward JE, Yang L, Mester Z, Bullitt E, et al. Cryo-EM reveals the structural basis of long-range electron transport in a cytochrome-based bacterial nanowire. *Communications Biology*. 2019;**2**(1):1-6.
85. Snider RM, Strycharz-Glaven SM, Tsoi SD, Erickson JS, Tender LM. Long-range electron transport in *Geobacter sulfurreducens* biofilms is redox gradient-driven. *PNAS*. 2012(109):15467–72.
86. Lin S, Usov PM, Morris AJ. The role of redox hopping in metal–organic framework electrocatalysis. *Chem Commun*. 2018;**54**:6965-74.
87. Babauta JT, Nguyen HD, Harrington TD, Renslow R, Beyenal H. pH, Redox Potential and Local Biofilm Potential Microenvironments Within *Geobacter sulfurreducens* Biofilms and Their Roles in Electron Transfer. *Biotechnol Bioeng*. 2012;**109**(10):2651–62.

88. Malvankar NS, Tuominen MT, Lovley DR. Comment on “On electrical conductivity of microbial nanowires and biofilms” by S. M. Strycharz-Glaven, R. M. Snider, A. Guiseppi-Elie and L. M. Tender, *Energy Environ. Sci.*, 2011, 4, 4366 *Energy Environ Sci.* 2012;**5**:6247-9.
89. Strycharz-Glaven SM, Tender LM. Reply to the ‘Comment on “On electrical conductivity of microbial nanowires and biofilms”’ by N. S. Malvankar, M. T. Tuominen and D. R. Lovley, *Energy Environ. Sci.*, 2012, 5, DOI: 10.1039/c2ee02613a. *Energy Environ Sci.* 2012;**5**:6250-5.
90. Yates MD, Strycharz-Glaven SM, Golden JP, Roy J, Tsoi S, Erickson JS, et al. Measuring conductivity of living *Geobacter sulfurreducens* biofilms. *Nat Nanotechnol.* 2016;**11**(11):910-3.
91. Malvankar NS, Rotello VM, Tuominen MT, Lovley DR. Reply to 'Measuring conductivity of living *Geobacter sulfurreducens* biofilms'. *Nat Nanotechnol.* 2016;**11**:913–4.
92. Malvankar NS, Vargas M, Nevin KP, Franks AE, Leang C, Kim B-C, et al. Tunable metallic-like conductivity in microbial nanowire networks. *Nat Nanotechnol.* 2011;**6**(9):573-9.
93. Malvankar NS, Yalcin SE, Tuominen MT, Lovley DR. Visualization of Charge Propagation Along Individual Pili Proteins Using Ambient Electrostatic Force Microscopy. *Nat Nanotechnol.* 2014;**9**:1012– 7.
94. Reardon PN, Mueller KT. Structure of the type IVa major pilin from the electrically conductive bacterial nanowires of *Geobacter sulfurreducens*. *J Biol Chem.* 2013;**288**(41):29260-6.
95. Leang C, Qian X, Mester T, Lovley DR. Alignment of the c-type cytochrome OmcS along pili of *Geobacter sulfurreducens*. *App Environ Microbiol.* 2010;**76**(12):4080-4.
96. Leang C, Malvankar NS, Franks AE, Nevin KP, Lovley DR. Engineering *Geobacter sulfurreducens* to produce a highly cohesive conductive matrix with enhanced capacity for current production. *Energy Environ Sci.* 2013;**6**:1901-8.

97. Meile C, Scheibe TD. Reactive transport modeling of microbial dynamics. *Elements*. 2019;**15**(2):111-6.

CHAPTER 2

MICROBIAL INTERACTIONS IN THE ANAEROBIC OXIDATION OF METHANE:  
MODEL SIMULATIONS CONSTRAINED BY PROCESS RATES AND ACTIVITY  
PATTERNS <sup>1</sup>

---

<sup>1</sup> He, X., Chadwick, G., Kempes, C., Shi, Y., McGlynn, S., Orphan, V. and Meile, C., 2019. Microbial interactions in the anaerobic oxidation of methane: model simulations constrained by process rates and activity patterns. *Environmental Microbiology*, 21(2), pp.631-647.

Reprinted here with permission of the publisher.

## Abstract

Proposed syntrophic interactions between the archaeal and bacterial cells mediating anaerobic oxidation of methane coupled with sulfate reduction include electron transfer through (a) the exchange of H<sub>2</sub> or small organic molecules between methane-oxidizing archaea and sulfate-reducing bacteria, (b) the delivery of disulfide from methane-oxidizing archaea to bacteria for disproportionation, and (c) direct interspecies electron transfer. Each of these mechanisms was implemented in a reactive transport model. The simulated activities across different arrangements of archaeal and bacterial cells and aggregate sizes were compared to empirical data for AOM rates and intra-aggregate spatial patterns of cell-specific anabolic activity determined by FISH-nanoSIMS. Simulation results showed that rates for chemical diffusion by mechanism (a) were limited by the build-up of metabolites, while mechanisms (b) and (c) yielded cell specific rates and archaeal activity distributions that were consistent with observations from single cell resolved FISH-nanoSIMS analyses. The novel integration of both intra-aggregate and environmental data provided powerful constraints on the model results, but the similarities in model outcomes for mechanisms (b) and (c) highlight the need for additional observational data (e.g. genomic or physiological) on electron transfer and metabolic functioning of these globally important methanotrophic consortia.

## Introduction

Anaerobic oxidation of methane (AOM) describes the conversion of methane to CO<sub>2</sub> in the absence of oxygen, and in marine sediments is primarily coupled to the reduction of sulfate, following the general reaction:



Hinrichs et al. (1999) first identified groups of uncultured archaea hypothesized to be involved in anaerobic oxidation of methane from deep-sea methane seeps using archaeal 16S rRNA diversity surveys and stable isotope analysis of archaeal lipids. Subsequently anaerobic methanotrophic archaea (ANME) were visualized in sediments and shown to form multi-celled aggregations with *deltaproteobacteria* bacteria, spanning from micron-scale aggregates to mats covering meter-scale reef-like structures (1-3). Since then, our understanding of the diversity of ANME archaea and bacteria involved in this process has expanded along with a growing list of terminal electron acceptors coupled to methane oxidation, including nitrate (4, 5); iron and manganese (6-8); and humic acid analogs (9).

AOM in marine sediments is estimated to consume about 382 Tg yr<sup>-1</sup> of methane, which is about three-quarters of the global net methane emission to the atmosphere (10). AOM thus acts as a significant sink for methane, a greenhouse gas with a warming potential 25 times that of CO<sub>2</sub> over 100 years (11). However, the details of the physiological mechanism underlying AOM are still not completely understood, and it is possible multiple mechanisms are used depending on the specific microorganisms and environments (e.g., (12-14)). For microbial consortia consisting of archaea and bacteria, classical syntrophic electron transfer through the exchange of solutes (mediated interspecies electron transfer, MIET) was proposed early on, where H<sub>2</sub>, formate, acetate, methanol and methylsulfides have been considered as intermediates that diffuse from methane-oxidizing archaea to sulfate-reducing bacteria (SRB-MIET; (15-20)). Alternatively, Milucka et al. (21) proposed the exchange of disulfide, produced by ANME archaea coupling methane oxidation to sulfate reduction directly, and consumed by associated sulfur disproportionating bacteria (HS<sub>2</sub><sup>-</sup>-MIET). More recently, direct interspecies electron transfer (DIET) has been hypothesized as a principal mechanism responsible for electron transfer in ANME-SRB consortia (22, 23). It has

been shown that methane-oxidation by ANME-2 archaea in deep-sea sediments can be catabolically and anabolically decoupled from sulfate-reduction and the activity of their deltaproteobacterial partners using soluble oxidants, including anthraquinone-2,6-disulfonate (AQDS), humic acids, and iron(III)-citrate (9), consistent with a syntrophic electron exchange between Archaea and Bacteria in the consortia (22, 23). Moreover, large S-layer associated multi-heme cytochromes were observed to be encoded by ANME-2 genomes, and appear to be related to electron transfer in ANME-2/SRB consortia as observed by transmission electron microscopy (TEM) (22, 24). TEM on thin sections of thermophilic AOM consortia further reported pili-like structures with diameters of 10 nm and apparent lengths of 100 nm to >1000 nm, which connect SRB HotSeep-1 and ANME-1 cells (23), suggestive of DIET.

In this study, we simulate the activity of AOM in microbial consortia for mediated interspecies electron transfer, in which the bacteria reduce sulfate, disproportionate disulfide, or participate in direct electron transfer (Fig. 1.1). Earlier efforts by McGlynn et al. (22) employed an idealized set of models to compare the physical and physiological processes and consequences of direct electron exchange to a diffusive intermediate for syntrophic aggregates. This generalized approach suggested that at measured AOM rates, chemical diffusivities can result in strong gradients of cellular activity in multi-celled syntrophic aggregates, which is inconsistent with single-cell activity measurements from stable-isotope incorporation studies using fluorescence *in situ* hybridization coupled with nanoscale secondary ion mass spectrometry (FISH-nanoSIMS; (22)). The importance of efficient exchange mechanisms between microbial partners can be illustrated by considering the spatial variation in substrate concentrations within an active microbial consortium. Consider an aggregate of several  $\mu\text{m}$  radius, in which sulfate-reducing bacteria surround an inner sphere of methane-oxidizing archaea. Assuming a constant, typical rate

of substrate consumption on the order of  $5 \text{ fmol cell}^{-1} \text{ d}^{-1}$ , and transport by chemical diffusion, substrate concentrations can vary substantially across the aggregate. In contrast, faster conductive transport yields almost uniform substrate levels, and presumably, microbial activity, across the aggregate (see Supporting Information Appendix A3). This simple calculation illustrates the fundamental difference between MIET and DIET mechanisms, but it lacks feedbacks of local environmental conditions (e.g. chemical concentrations, pH, etc.) on microbial activity.

Recent numerical modeling has shown the feasibility of direct electron transfer in single-cell pairs (25) and microbial biofilms (26, 27). However, modeling efforts have not yet been applied to characterize the direct extracellular electron transfer behavior between methane-oxidizing ANME archaea and its sulfate-reducing bacterial partner with feedbacks of local environmental conditions. Here, we build on the previous modeling efforts by (18, 22, 28), to evaluate the various hypotheses regarding the potential mechanisms of AOM within these uncultured archaeal-bacterial consortia. We compare the modeled methane oxidation rates and activity distribution patterns to observational data from methane seeps at Hydrate Ridge off the coast of Oregon, USA, and explore the effect of consortia size, the intra-aggregate spatial distribution of archaeal and bacterial cells, and pH variations. This allows for direct comparison of the different mechanisms. By assessing the sensitivity of model outputs towards poorly constrained model parameters (e.g. rate constants), in conjunction with comparison to data at both the macro and the micro scales, it is further possible to constrain model parameters for use in larger scale models.

### Modeling Procedure

The model domain included a single spherical microbial aggregate. Several different spatial distributions of archaea and bacteria within an aggregate were investigated (Fig. A1),

reflecting distribution patterns observed in nature (see e.g. Fig 1a in (22)). Cell volumes assigned to archaea and bacteria were based on observed cell numbers and sizes reported (1, 29, 30). Cell radii were set to 0.4  $\mu\text{m}$  for both archaea and bacteria, with a 1 archaea : 1 bacteria cell ratio.

### Governing equations

The governing equations simulating the reaction and transport processes are of the form:

$$\frac{\partial \phi C_i}{\partial t} = \phi \mathbf{R}_i + \nabla \cdot (\phi \mathbf{D}_i \nabla C_i), \quad \text{Eq. (2.1)}$$

where  $\phi$  is the porosity and  $C_i$  is the concentration of chemical species  $i$ .  $\mathbf{D}_i$  represents the in situ diffusion coefficient, adjusted for tortuosity and EPS as in Orcutt and Meile (2008), and  $\mathbf{R}_i$  is the net reaction rate.

The rate of a metabolic reaction  $X$  is expressed as (31, 32)

$$R^X = F_k^X F_T^X, \quad \text{Eq. (2.2)}$$

where  $F_k^X$  represents the reaction kinetics. It is implemented as the product of a cell-specific rate constant  $k$ , the cell density  $B$  (cells per volume), and the abundance of substrate  $S$  using a Monod expression with half-saturation constant  $K_m^S$ :

$$F_k^X = kB \frac{S}{K_m^S + S} \quad \text{Eq. (2.3)}$$

The thermodynamic factor ( $0 \leq F_T^X \leq 1$ ) reflects that there must be sufficient free energy available from the reactions to fuel ATP synthesis and cell maintenance, which is given by

$$F_T^X = \max \left( 0, 1 - \exp \left( -\frac{f_X}{\chi R_{gas} T} \right) \right), \quad \text{Eq. (2.4)}$$

where  $\chi$ , the number of ATP synthesized per reaction, is set to 1 (18),  $R_{gas}$  is the universal gas constant ( $8.314 \text{ J K}^{-1} \text{ mol}^{-1}$ ) and  $T$  is temperature (281.15 K).  $f_X$  represents the thermodynamic driving force, relating the free energy yield of that reaction to the energy required to synthesize ATP (31, 32), which is expressed as:

$$f_X = -\Delta G_X - \Delta G_{ATP}, \quad \text{Eq. (2.5)}$$

where  $\Delta G_{ATP}$  represents a minimum energy required for ATP synthesis. Tran and Uden (33) demonstrated ADP phosphorylation proceeded at energies as low as  $42 \text{ kJ mol}^{-1}$ . With a  $\text{H}^+/\text{ATP}$  ratio of 4 (Pänke and Rumberg 1997) and  $\Delta G_{\text{ADP} \rightarrow \text{ATP}} = +42 \text{ kJ mol}^{-1}$ , this results in  $\Delta G_{ATP}$  on the order of  $10 \text{ kJ mol}^{-1} \text{ H}^+$  ((35); note that this minimum energy requirement of 10 instead of 1  $\text{kJ mol}^{-1}$  used in Orcutt and Meile (2008) leads to maximum rates slightly lower than the one reported there).

The Gibbs free energy of the reaction is computed as:

$$\Delta G_X = \Delta G_X^0 + R_{gas} T \ln Q_X \quad \text{Eq. (2.6)}$$

with the reaction quotient  $Q = \prod a_i^{v_j}$ , where  $v$  are stoichiometric coefficients and  $a$  denote activities, computed as the product of concentrations and activity coefficients as given in Orcutt and Meile (2008).

Acid-base reactions of the DIC and borate system were accounted for using the kinetic formalism given in (36). To account for protonation/deprotonation on cell surfaces, surface site concentrations of  $1 \text{ } \mu\text{mol (mg dry cell)}^{-1}$  carboxy and  $1 \text{ } \mu\text{mol (mg dry cell)}^{-1}$  amino groups were considered (37), with an aggregate biomass of  $0.12 \text{ (mg dry cell) m}^{-3}$  (1). Kinetic constants were taken from the literature (38, 39), consistent with equilibrium constants given in (40, 41) and microscopic reversibility. See Supporting Information Appendix A5 for a detailed description.

Three different mechanisms for the interaction between archaea and bacteria were implemented (Fig. 2.1), as described below. In the absence of known intermediates, we considered acetate and  $\text{H}_2$  (not shown) as representative dissolved intermediates in MIET; for DIET, we assumed that electrons from the oxidation of methane are captured by an electron acceptor (D) from which they are transferred onto a redox-active molecule (reduced: MH; oxidized: M) located

on conductive pili, embedded in a matrix of extracellular polymeric substances (EPS), or transferred by dissolved electron carriers through diffusive transport processes. We did not differentiate between conductive pili or a conductive matrix in this study, but note that microbes have been shown to utilize pili-like structures (23, 42-44), extracellular biofilm matrix (45, 46), and multi-heme cytochromes (22) for extracellular electron transport.

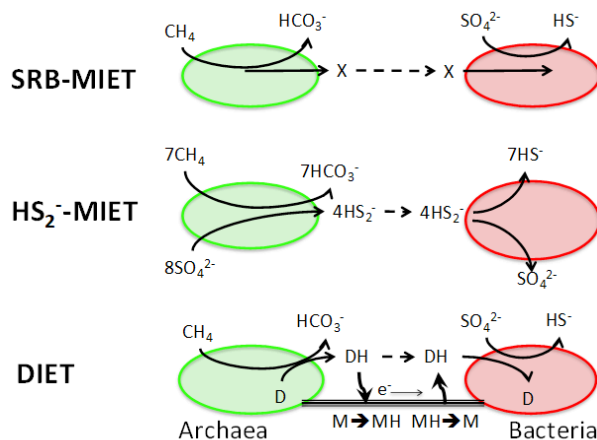


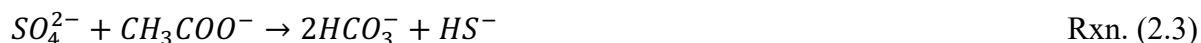
Fig. 2.1. Model representation with three distinct mechanisms (top: SRB-MIET, middle:  $\text{HS}_2^-$ -MIET pathway, bottom: DIET) for the electron transport within archaeal-bacterial consortia. D and DH represent a redox couple (e.g.,  $\text{H}^+/\text{H}_2$ ) which might operate in addition to DIET, M a localized redox molecule, X an intermediate species (acetate,  $\text{H}_2$ , etc.) Solid arrows denote reactions, dashed arrows diffusional transport.

### *Mediated interspecies electron transfer*

Methane is oxidized by the archaea, with the product, here acetate (Ac), serving as an electron donor for sulfate reducing bacteria (for reactions with  $\text{H}_2$  as intermediate see Orcutt and Meile 2008):



with  $\Delta G^\circ = 14.8 \text{ kJ (mol CH}_4\text{)}^{-1}$



with  $\Delta G^0 = -47.7 \text{ kJ (mol SO}_4\text{)}^{-1}$

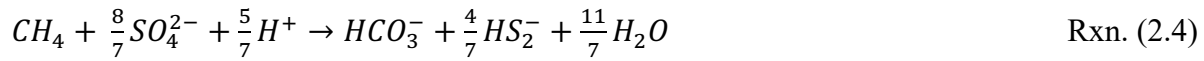
The kinetic factors are (see justification for multiple limiting substrate Monod kinetics in (47-50)):

$$F_k^{R2} = k_A B_A \frac{CH_4}{K_m^{CH_4} + CH_4} \quad \text{Eq. (2.7)}$$

$$F_k^{R3} = k_B B_B \frac{SO_4^{2-}}{K_m^{SO_4} + SO_4^{2-}} \frac{Ac}{K_m^{Ac} + Ac} \quad \text{Eq. (2.8)}$$

### *Disulfide pathway*

In the disulfide pathway, the archaea oxidize methane and reduce sulfate, with disulfide being disproportionated by the bacteria (21):



with  $\Delta G^0 = -62.6 \text{ kJ mol}^{-1} CH_4$



with  $\Delta G^0 = 52 \text{ kJ mol}^{-1} HS_2^-$

The kinetic factors are

$$F_k^{R4} = k_A B_A \frac{CH_4}{K_m^{CH_4} + CH_4} \frac{SO_4^{2-}}{K_m^{SO_4} + SO_4^{2-}} \quad \text{Eq. (2.9)}$$

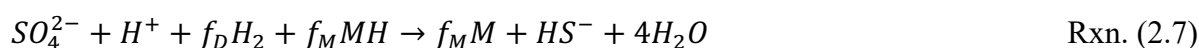
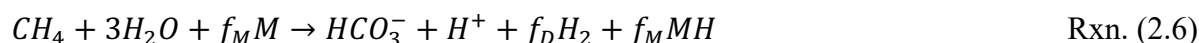
$$F_k^{R5} = k_B B_B HS_2^- \quad \text{Eq. (2.10)}$$

### *Direct interspecies electron transfer*

The archaea are considered responsible for methane oxidation and the bacteria for the reduction of sulfate. Direct electron transfer involves the loading of electrons from a primary electron acceptor (D) onto a redox-active molecule (e.g. cytochromes; reduced form: MH; oxidized form: M) located on conductive pili or matrix, the transfer from the archaea to the bacteria, and the offloading and use of electrons in sulfate reduction. The D molecule and its reduced form DH act as an 'electron pool' to temporally store electrons produced from methane oxidation.

Electrons are then moved from the archaea to the bacteria either via a DIET mechanism, or may be transferred onto solutes that are subject to diffusive exchange.

H<sub>2</sub> was modeled as the electron pool molecule (DH) in our models. This is highly idealized; it was chosen to minimize the level of model complexity in the light of our lack of knowledge on the actual mechanism, and because H<sub>2</sub>, with its fast turnover time, has been shown to be an important indicator for the energetics of methane production and consumption reactions (16). Thus,



where 8 electrons released in the oxidation of methane to CO<sub>2</sub> result in  $f_M \in [0,8]$  with  $f_D = (8 - f_M)/2$ , and the thermodynamic factor (Eq. 4) was calculated accordingly (see Supplementary Information Appendix A4). The default values for  $f_M$  and  $f_D$  in this study were 7.2 and 0.4, respectively. The values for  $f_M$  and  $f_D$  were varied in Fig. 5C for sensitivity analysis. The kinetic factors are

$$F_k^{R6} = k_A B_A \frac{CH_4}{K_m^{CH_4} + CH_4} M \quad \text{Eq. (2.11)}$$

$$F_k^{R7} = k_B B_B \frac{SO_4^{2-}}{K_m^{SO_4^{2-}} + SO_4^{2-}} MH \quad \text{Eq. (2.12)}$$

There is an ongoing debate over whether electrons transfer along the conductive pili/biofilms proceeds via electron superexchange (i.e. electron hopping; (26, 51)) or metallic-like conductivity (52, 53). Electron superexchange recently proposed by Strycharz-Glaven et al. (2011) is based on the abundance and prevalent role of multiple redox molecules located on conductive cell outer membranes, pili, or extracellular matrices (51). We modeled the direct electron transport via conjugated redox-active molecules building on recent evidence of the presence and expression of large multi-heme cytochrome genes in ANME-1 (54, 55) and ANME-2 (22, 55) genomes. It is described as (26):

$$J_{(x)} = k_f M H_{(x)} M_{(x+\delta)} - k_b M_{(x)} M H_{(x+\delta)} \quad \text{Eq. (2.13)}$$

where  $J$  is the electron flux in mol e<sup>-</sup> m<sup>-2</sup> s<sup>-1</sup>,  $x$  is the location along the filament,  $\delta$  is the distance between two redox molecules and  $k_f$  and  $k_b$  are forward and backward rate constants.

#### *Gradient-driven DIET*

In the case of concentration gradient-driven electron transport, the forward and backward electron transport rate constants are equal,  $k_f = k_b = k^0$ , and the flux can be simplified into a diffusion-like expression:

$$J_{G,(x)} = -D_{MH} \left( \frac{\partial MH}{\partial x} \right), \quad \text{Eq. (2.14)}$$

where  $D_{MH} = k^0 M_{tot} \delta$  is the effective diffusion coefficient (see Strycharz-Glaven et al. 2011 for a derivation), where  $M_{tot}$  is the total concentration (=M+MH). Thus, the governing equation for  $MH$  can be expressed as:

$$\phi \frac{\partial MH}{\partial t} = \nabla \cdot (\phi D_{MH} \nabla MH) + R_r \quad \text{Eq. (2.15)}$$

where  $D_{MH}$  is set to a constant value within the aggregate (see above) and 0 outside and  $R_r$  is the net production rate.

#### *Electric field-driven DIET*

In the presence of an electric field, forward and backward electron transport rate constants differ and the current conducted can be expressed as

$$J_{EF} = k^0 M \cdot MH \left( e^{\frac{nF(V/W)\delta}{2RgasT}} - e^{-\frac{nF(V/W)\delta}{2RgasT}} \right), \quad \text{Eq. (2.16)}$$

where  $V$  is the voltage between the archaea and bacteria,  $W$  is their distance,  $n$  is the number of electrons produced and  $F$  is the Faraday constant 96485.33 C mol<sup>-1</sup>. For a small  $\left(\frac{V}{W}\right) \delta$  value, the flux can be approximated as

$$J_{EF} = k^0 M \cdot MH \left( \frac{nF \left( \frac{V}{W} \right) \delta}{R_{gas} T} \right) = \alpha \frac{\partial \phi}{\partial x}, \quad \text{Eq. (2.17)}$$

where  $\alpha = k^0 M \cdot MH \left( \frac{nF \delta}{R_{gas} T} \right)$ , and  $\frac{\partial \phi}{\partial x} = \frac{V}{W}$  is the potential gradient or electric field  $E$ .

Thus, electron hopping on conductive pili or matrix driven by an electric field yields

$$\phi \frac{\partial MH}{\partial t} = \phi \nabla \cdot J_{EF} + \phi R_r \quad \text{Eq. (2.18)}$$

Assuming that the electric potential is set by the reaction central to cell metabolism,

$$\phi_A = \phi_A^o - \frac{R_{gas} T \ln Q_A}{nF} \quad \text{Eq. (2.19)}$$

$$\phi_B = \phi_B^o - \frac{R_{gas} T \ln Q_B}{nF} \quad \text{Eq. (2.20)}$$

where  $\phi_A^o$  and  $\phi_B^o$  are the standard potential for AOM and SR, respectively,  $n = 8$  for electrons transported per reaction (Reaction 1),  $Q_A$  and  $Q_B$  are the corresponding reaction quotients. Then, the electric field  $E$  is computed from the gradient in the electric potential  $\phi$  in Eqs. 2.19 & 2.20, which in turn then drives electron transport. Such electron hopping driving by an electric field can be expressed as

$$\phi \frac{\partial MH}{\partial t} = \phi R_r + \nabla \cdot (\phi \mathcal{D}_{MH} \nabla MH) + \phi \nabla \cdot J_{EF} \quad \text{Eq. (2.21)}$$

where  $R_r$  the net rate of production and consumption,  $MH$  is the extracellular concentration of reduced redox molecules.

### Model implementation

AOM consortia were represented as three-dimensional spheres with aggregate radii up to 25  $\mu\text{m}$ , comparable to observations (1, 22, 29, 56-59). The domain radius, which includes the surroundings of the consortia, was set to 2.5-times of the aggregate radius. In the model, the 3D spherical setting was represented by a circle, imposing rotational symmetry at the vertical axis. The observed distribution of archaea and bacteria in the aggregates varies from highly clustered to

interspersed (22). We thus modeled three distinct arrangements – ‘spherical layers’, in which archaea are surrounded by bacteria, ‘half-half’, consisting half spheres of bacteria and archaea, and two ‘enclosed hemispheres’ of archaea surrounded by bacteria (Fig. A1).

All reaction mechanisms contained  $\text{CH}_4$ ,  $\text{HCO}_3^-$ ,  $\text{CO}_2(\text{aq})$ ,  $\text{CO}_3^{2-}$ ,  $\text{SO}_4^{2-}$ ,  $\text{HS}^-$ ,  $\text{H}^+$  as state variables, with SRB-MIET and  $\text{HS}_2^-$ -MIET pathways both also including a dissolved intermediate, and DIET containing  $\text{H}_2$  and M and MH as described above. At the outer domain boundary, the state variables were set to either fixed concentrations reflecting the environmental conditions, or a no flux condition is imposed (Table 2.1; Supporting Information Appendix A6). Initial conditions were set to the environmental conditions, or for intermediates to a sufficiently low concentration to allow for methane oxidation to take place within the aggregates. We assume the same cell density and cell-specific volume in all models, with cell numbers varying with aggregate size. All simulations were run to steady state.

Cell-specific rate constants ( $k_A$  and  $k_B$ ) are unknown, and hence simulations were carried out in which they were varied across a wide range (see Table 2.1). Similarly, simulations for a range of initial ratios of electron donors and acceptors involved in DIET were carried out, varying the values of  $f_M, f_D$ . Additionally, simulations with  $M_{tot} = 0.01$  and  $1 \text{ mmol L}^{-1}$  and conductivity ( $\sigma$ ) ranging from  $10^{-4}$  to  $10^4 \text{ S m}^{-1}$ , encompassing the  $0.1\text{-}10 \text{ S m}^{-1}$  determined by (60, 61), were performed. The main model parameters are defined in Table A1 (Supplementary Information Appendix A5).

**Table 2.1.** Parameterization of reactions

Symbol	Value (unit)	Description
$K_m^{CH_4}, K_m^{SO_4}$	37 mM, 1mM	Half saturation constant for methane in AOM and SRB, respectively (18)
$r_{ANME}, r_{SRB}$	0.4 $\mu\text{m}$ , 0.4 $\mu\text{m}$	Radius of archaea, bacteria cell, respectively (1, 29-30)
$k_A, k_B$	$10^{-18}$ to $10^{-8}$	Archaea and bacteria rate constants: mol cell <sup>-1</sup> d <sup>-1</sup> for $k_A, k_B$ in SRB-MIET mol cell <sup>-1</sup> d <sup>-1</sup> for $k_A$ , m <sup>3</sup> cell <sup>-1</sup> d <sup>-1</sup> for $k_B$ in HS <sub>2</sub> -MIET m <sup>3</sup> cell <sup>-1</sup> d <sup>-1</sup> for $k_A, k_B$ in DIET, except for 1 <sup>st</sup> order reactions with respect to D, DH and M, MH, for which $k_B$ is in m <sup>6</sup> cell <sup>-1</sup> mol <sup>-1</sup> d <sup>-1</sup> , and for no dependency on M, MH, for which $k_A$ and $k_B$ are in mol cell <sup>-1</sup> d <sup>-1</sup> .
<b>DIET parameters</b>		
$[M_{tot}]$	$10^{-5}$ - $10^{-3}$ M	Concentration of redox molecules (see section <i>Electron transport</i> ). Baseline value: $10^{-5}$ M
$k^o$	$1 \cdot 10^4$ m <sup>4</sup> mol <sup>-1</sup> s <sup>-1</sup>	Rate constant of electron transport on conductive pili or matrix. Baseline value: $10^4$ m <sup>4</sup> mol <sup>-1</sup> s <sup>-1</sup>
$\delta$	0.7 nm	Redox molecules spacing width (53)
$\sigma$	$10^{-4}$ - $10^4$ S m <sup>-1</sup>	Conductivity of conductive pili or matrix (52). Baseline value: 0.1 S m <sup>-1</sup>

Parameters are set to baseline values if not noted otherwise. Temperature T is set to 281.15K; Aqueous diffusion coefficient:  $D_{CO_2} = 1.91 \times 10^{-9}$  m<sup>2</sup> s<sup>-1</sup>,  $D_{H_2} = 6.31 \times 10^{-8}$  m<sup>2</sup> s<sup>-1</sup> (71),  $D_{CO_3} = 1.19 \times 10^{-9}$  m<sup>2</sup> s<sup>-1</sup>,  $D_{H^+} = 6 \times 10^{-9}$  m<sup>2</sup> s<sup>-1</sup>,  $D_{OH} = 5.27 \times 10^{-9}$  m<sup>2</sup> s<sup>-1</sup> (72);  $D_{B(OH)_4} = 9.56 \times 10^{-10}$  m<sup>2</sup> s<sup>-1</sup> (73). Fixed concentration boundary conditions are imposed for all chemical species at the outer domain boundary except for HS<sub>2</sub> for which a no flux condition is imposed at the outer domain boundary, and for MH, R-COOH, R-NH<sub>2</sub>, for which no flux condition is imposed at the aggregate surface. Boundary conditions are set to:  $10^{-4}$  M HS,  $10^{-3}$  M HCO<sub>3</sub><sup>-</sup>, pH=8.2,  $10^{-2}$  M SO<sub>4</sub><sup>2-</sup>,  $10^{-3}$  M CH<sub>4</sub>,  $10^{-7}$  mM acetate

Models were implemented in COMSOL Multiphysics (COMSOL 5.3, COMSOL Inc., Burlington, MA, USA). Postprocessing was carried out in MATLAB 2016b (MathWorks, Natick, MA, USA).

### Statistical analysis

Increasing aggregate size can lead to differences in the distribution of activity within aggregates. In order to investigate whether the spatial variability differs between mechanisms, slopes (and variance) of (relative) activity vs. aggregate radius were calculated for individual aggregates with identical parameterization. For the observational data, slope and variance were computed for 41 archaeal aggregates paired with the specific *Desulfobacteraceae* lineage SEEP-SRB1a (AS) and 21 archaeal aggregates paired with non-SEEP-SRB1a *Deltaproteobacteria* (AD) first, and then combined to represent the variability of activity vs. size for the observational data (22). Finally, a Student's t-test was performed to assess if the slopes between the three model mechanisms and the observations differed significantly. Values of  $p < 0.05$  and  $p < 0.01$  were

considered significant and highly significant, respectively. The statistical analyses were performed using MATLAB 2016b (MathWorks, Natick, MA, USA).

### Results and Discussion

In this section we present our model simulations and compare them to observations. First, we examine the feasibility of different syntrophic reaction pathways (SRB-MIET, HS<sub>2</sub><sup>-</sup>-MIET, and DIET) by comparing modeled to measured AOM rates. Then, the possibility of these pathways is further assessed by comparing the spatial variation of archaeal and bacterial activity with FISH-nanoSIMS data of single-cell anabolic activity, across a range of aggregate radii and spatial arrangements of archaeal and bacterial cells in a consortium. Finally, we explore the variables that control the AOM rate and activity patterns in DIET pathway.

#### **Comparison of model simulations to measured sediment AOM rates**

We first estimated cell-specific AOM rates from data from Hydrate Ridge to compare model results to environmentally relevant dynamics. To that end, cell-specific rates were calculated from measured AOM rates per volume of sediment, combined with reported cell densities. We used Boetius et al. (2000) reported cell densities of  $9 \times 10^7$  consortia per gram dry sediment (gds) with each consortium containing  $\approx 100$  ANME-2 cells, corresponding to  $9 \times 10^9$  ANME cells gds<sup>-1</sup>. The consortia number and aggregate radius sampled during a subsequent cruise to the same area in August 2000 at the crest of the southern Hydrate Ridge (44°34' N, 125°09' W; 780 m water depth) yielded similar values (56, 57, 62, 63). Nauhaus et al. (2005) reported an AOM rate of  $2.5 \pm 0.3$   $\mu\text{mol gds}^{-1} \text{d}^{-1}$ , derived from measured sulfide accumulation and assuming a 1:1 ratio of methane oxidized to sulfate reduced, which results in a cell-specific rate of  $0.28 \pm 0.03$  fmol cell<sup>-1</sup> d<sup>-1</sup>, consistent with the estimate of Niemann et al. (64), who also estimated cell-specific rates of 0.13-0.21 fmol cell<sup>-1</sup> d<sup>-1</sup> for the sediment samples from the Hydrate Ridge (ANME-2) based

on studies by (1, 65). The  $0.34 \pm 0.15 \text{ } \mu\text{mol gds}^{-1} \text{ d}^{-1}$  rate of AOM reported by (66) from the RV Sonne cruise SO165-2 in 2002, translate into a cell-specific rate of  $3.8 \pm 1.7 \times 10^{-2} \text{ fmol cell}^{-1} \text{ d}^{-1}$ . Treude et al. (2003) reported  $1.27 \times 10^8$  aggregates  $\text{cm}^{-3}$  and a slurry density of  $0.2 \text{ gds cm}^{-3}$  from Hydrate Ridge, resulting in an aggregate density of  $6.35 \times 10^8 \text{ gds}^{-1}$ . Taking 100 ANME cells per aggregate with the reported AOM rate of  $0.58 \text{ } \mu\text{mol gds}^{-1} \text{ d}^{-1}$ , this gives a cell density of  $6.35 \times 10^{10}$  cells  $\text{gds}^{-1}$  and cell-specific AOM rate of  $0.01 \text{ fmol cell}^{-1} \text{ d}^{-1}$ . Finally, for a cell density of  $9 \times 10^9$  ANME cells  $\text{gds}^{-1}$ , the AOM rates reported in Nauhaus et al. (2002), Nauhaus et al. (2007) and Holler et al. (2009) correspond to 1.7, 25.6, and 33.3  $\text{fmol cell}^{-1} \text{ d}^{-1}$ , respectively.

These cell-specific AOM rates, on the order of  $10^{-2}$  to  $10^2 \text{ fmol cell}^{-1} \text{ d}^{-1}$ , were compared to those computed for the three different syntrophic reaction pathways considered. Because several parameters in the kinetic model formulations – most importantly the rate constants for archaeal and bacterial substrate utilization,  $k_A$  and  $k_B$ , respectively – are *a priori* poorly constrained, they were varied over a wide range to assess the sensitivity of the model (note also that unless specified otherwise, cell-specific rates reported here are consortia averages, to allow for a meaningful comparison across consortia of different sizes). Results from our model simulations suggest that all three modeled pathways can reach the cell-specific rates that approach, match, or even exceed the empirical AOM rate measurements (Fig. A2). But modeled AOM rates were considerably lower for SRB-MIET models (with an upper limit on the order of  $3 \times 10^{-2} \text{ fmol cell}^{-1} \text{ d}^{-1}$ ). At some point ( $k_A \geq 10^{-15} \text{ mol cell}^{-1} \text{ d}^{-1}$ ), AOM rates no longer increased with increasing maximum cell-specific rates ( $k_A, k_B$ ) for SRB-MIET models. This is caused by thermodynamic constraints that arise when diffusion is too slow to prevent local accumulation of reaction products, consistent with our previous findings (18). The maximum AOM rate for SRB-MIET of  $\sim 10^{-2} \text{ fmol cell}^{-1} \text{ d}^{-1}$  is achieved for the smallest aggregate considered ( $r = 1.5 \text{ } \mu\text{m}$ ), consistent with diffusion limiting the

removal of reaction products. Simulations of SRB-MIET with parameterizations that yield high methane oxidation rates result in unevenly distributed activity, with only cells close to the archaeal-bacterial border being active. For a given spatial arrangement of archaea and bacteria, smaller aggregates can sustain higher average cell-specific rates of AOM if the reaction mechanism relies on diffusional exchange of metabolites, due to the closer proximity of archaeal and bacterial cells and hence shorter distances between the location of production and consumption of chemical intermediate species. This high rate could also be achieved by distributing partner organisms such that every cell is in close contact with at least one cell of another type.

The thermodynamic constraints on archaeal cells were much more pronounced for the SRB-MIET than the disulfide pathway because the Gibbs free energy of reaction at standard state for the archaea is more negative for the latter mechanism (note the difference in  $\Delta G^0$  of reaction 2.2 ( $\Delta G^0 = 14.8 \text{ kJ (mol CH}_4\text{)}^{-1}$ ) and reaction 2.4 ( $\Delta G^0 = -62.6 \text{ kJ (mol CH}_4\text{)}^{-1}$ ). Additionally, the reaction quotient for the  $\text{HS}_2^-$ -MIET pathway varies with the power of 4/7 for the reduced product per methane oxidized, while it is linear for acetate or varies with the power of 4 for  $\text{H}_2$  in SRB-MIET, leading to less build-up of  $\text{HS}_2^-$  (see discussion in Supplementary Information Appendix A3). Our simulation results are consistent with the findings of Sørensen et al. (17), in which they suggested that intermediate species such as hydrogen, acetate, and methanol are excluded from the possible electron shuttles for AOM consortia due to thermodynamic and kinetic constraints. Thus, in the absence of mechanisms that enhance exchange beyond molecular diffusion in a three-dimensional arrangement of bacterial and archaeal cells, SRB-MIET does not seem to be able to support commonly observed rates of AOM.

## Comparison of simulations to intra-aggregate activity observations

Models that yield AOM rates between 0.01 and 100 fmol cell<sup>-1</sup> d<sup>-1</sup>, broadly consistent with field observations, were investigated further. We compared the outcome of these simulations with measurements from McGlynn et al. (2015), where anabolic activity was calculated for single cells, extracted from co-registered fluorescence *in situ* hybridization and nanoscale secondary ion mass spectrometry (FISH–nanoSIMS) combined with <sup>15</sup>N stable isotope probing. It was assumed that in the experiments of McGlynn et al. (2015) the spatial distribution of N assimilation is proportional to the metabolic rates, and that the <sup>15</sup>N incorporation reflects the activity associated with methane oxidation. For a growth yield  $Y_{CH_4}$  of 0.6 g cell dry weight per mol CH<sub>4</sub> oxidized (57), a specific growth rate of  $\mu_{cell} = 0.0068 \text{ d}^{-1}$  (22), and a biomass density  $\rho$  of  $4.8 \times 10^5 \text{ g cell dry weight m}^{-3}$  (22), the catabolic AOM rate ( $=\mu_{cell} * \rho / Y_{CH_4}$ ) is 1.5 fmol cell<sup>-1</sup> d<sup>-1</sup>. This falls well within the range of cell-specific environmental AOM rates, suggesting that the patterns of activity that have been observed by McGlynn et al. (2015) are comparable to those occurring under environmentally relevant conditions.

McGlynn et al. (2015) showed that the average cell-specific N uptake does not vary significantly with aggregate radius ( $n = 62$ ; slope = 0.02 and 0.006 for archaeal and bacterial cells, respectively; see Supporting Information Appendix A7 Fig. A4 A&B). Simulations for the SRB-MIET pathway yielded AOM rate distributions that differ from the observed <sup>15</sup>N assimilation patterns. Average cell-specific AOM rates for the SRB-MIET pathway significantly decrease when increasing the aggregate radius (Fig. 2.2). When the archaea and bacteria are spatially separated within a consortium, AOM by the SRB-MIET pathway becomes energetically less favorable as the aggregate radius increases and diffusion of intermediate species (e.g., H<sub>2</sub>, acetate) becomes limiting. As a consequence, the concentration of the product of methane oxidation (e.g.,

acetate or  $H_2$ ) builds up, ultimately making the reaction energetically less favorable. In contrast, the  $HS_2^-$ -MIET pathway mediated by a sulfate-reducing methanotrophic archaeon shows AOM rate distributions that are comparable with the observed  $^{15}N$  assimilation patterns. This difference between SRB-MIET and  $HS_2^-$ -MIET reflects that archaea are less thermodynamically challenged in the  $HS_2^-$ -MIET pathway. Similar to the model predictions for  $HS_2^-$ -MIET, AOM rate distribution patterns for the hypothesized DIET pathway are also consistent with the experimental nanoSIMS data from McGlynn et al. (2015). Even for very large AOM consortia with a radius of 25  $\mu m$ , the average cell-specific AOM rates in the model are within a few percent of the rates for a small aggregates with a radius of 1  $\mu m$ . Both of these models differ substantially from the SRB-MIET model, where cell-specific AOM rates in aggregates of 6  $\mu m$  radius are only  $\sim 10\%$  of those in 1.5  $\mu m$  sized aggregates (Fig. 2.2).

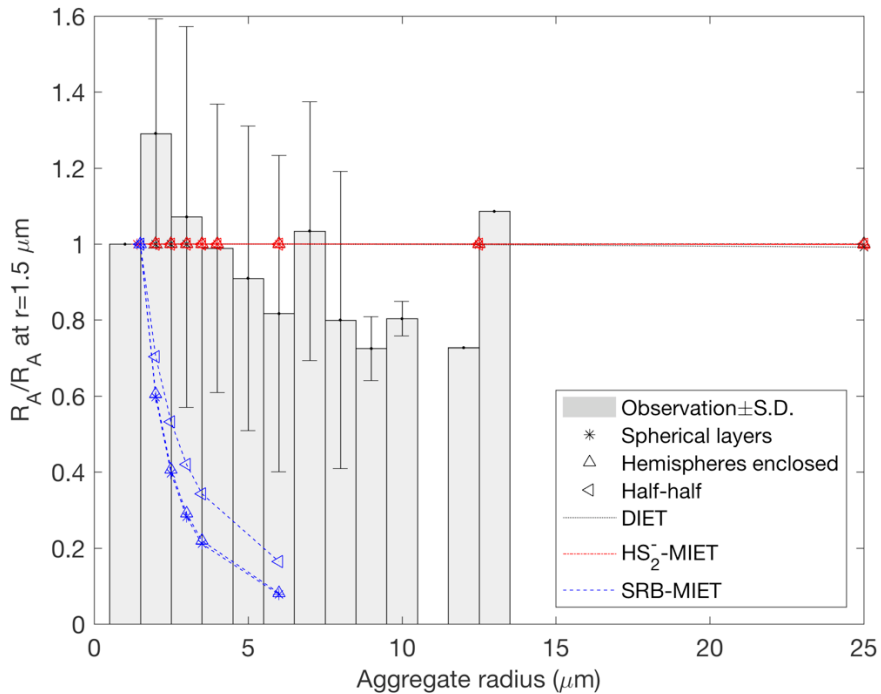


Fig. 2.2. Average cell-specific AOM rates, normalized to the value for the smallest aggregates vs. aggregate radius. The simulations shown were picked for rates that either lie within ( $HS_2^-$ -MIET

and DIET) or are close to (SRB-MIET) the observed range. Note that lines for HS<sub>2</sub><sup>-</sup>-MIET overlay those for DIET. Cell-specific parameterizations: DIET:  $k_A$  and  $k_B$   $10^{-13}$  m<sup>3</sup> cell<sup>-1</sup> d<sup>-1</sup>; HS<sub>2</sub><sup>-</sup>-MIET:  $k_A$   $10^{-14}$  mol cell<sup>-1</sup> d<sup>-1</sup> and  $k_B$   $10^{-14}$  m<sup>3</sup> cell<sup>-1</sup> d<sup>-1</sup>; SRB-MIET:  $k_A$  and  $k_B$   $10^{-15}$  mol cell<sup>-1</sup> d<sup>-1</sup>.

In nature, spatial arrangements of archaea and bacteria within an aggregate vary from highly-segregated to well-mixed (22, 29, 58). Empirical analyses of cell-specific anabolic activity within AOM consortia in McGlynn et al. (2015) revealed that the spatial arrangement of the archaea and bacteria does not influence the observed activity of the entire consortia and that cell-specific activity for individual archaea and bacteria is unrelated to the proximity to the nearest partner (see Fig 2b in McGlynn et al. 2015 and Fig. A5). These data contrast with the model simulations for the SRB-MIET pathway, where cell-specific rates varied with aggregate size and arrangement (Fig. 2.2).

The observational data showed that cell-specific anabolic activity (<sup>15</sup>N incorporation) is rather uniformly distributed within an aggregate, regardless of the AOM consortium radius or the segregation of archaea and bacteria (see Supporting Information Appendix A7 Figs. S4 C&D and S5 C&D). For SRB-MIET, intra-aggregate variability of cell-specific rates of both archaea and bacteria is more pronounced, and grows as aggregate radius or the segregation of archaea and bacteria increases (Fig. 2.3 A&D). Variability was lower at low AOM rates, and while the spatial variation in bacterial activity can approach the observed ones (in small aggregates at rates on the order of  $\sim 3 \times 10^{-2}$  fmol cell<sup>-1</sup> d<sup>-1</sup>), the modeled spatial variability in archaeal activities clearly exceeded the observed values, even for the smallest aggregates, independent of arrangement (Fig. 2.3 A). In contrast, DIET and HS<sub>2</sub><sup>-</sup>-MIET model simulations showed little to no trend of the intra-aggregate variation in archaeal cell-specific rates with aggregate size (Fig. 2.3 B&C), for all arrangements. The slight variation seen in the experimental data (see Supporting Information

Appendix A7 Figs. A4 C&D and A5 C&D) were not observed in DIET and HS<sub>2</sub><sup>-</sup>-MIET model simulations, which we tentatively attribute to the fact that model simulations only reflect variations in a limited set of substrates, but do not reflect other factors that may be biologically relevant to AOM consortia activity in situ including, e.g., trace nutrients (74). However, DIET and HS<sub>2</sub><sup>-</sup>-MIET model simulations showed some spatial intra-aggregate variation in bacterial cell-specific rates, which increases with aggregate size, separation between archaeal and bacterial cells, and an increase in  $k_B$  (Fig. 2.3 E&F).

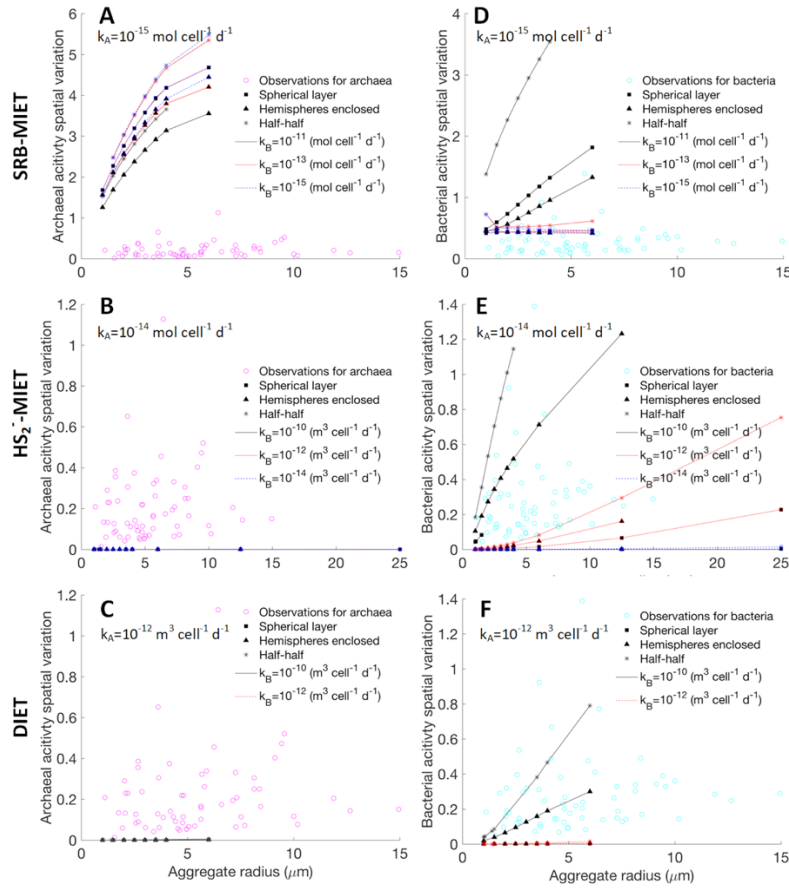


Fig. 2.3. Intra-aggregate variation of archaeal (A-C) and bacterial (D-F) activity. Spatial activity

variation is calculated as  $\left(\frac{\int (R-\bar{R})^2 dV}{V}\right)^{1/2} / \bar{R}$ , where  $R$  and  $V$  denote the rates and volumes of the

archaeal and bacterial regions, respectively, and  $\bar{R}$  is the volume averaged reaction rate. Cell

activities are for model simulations that yield rates close to the estimated environmental rates, using SRB-MIET (A,D):  $k_B$  in mol cell<sup>-1</sup> d<sup>-1</sup>; HS<sub>2</sub><sup>-</sup>-MIET (B,E):  $k_B$  in m<sup>3</sup> cell<sup>-1</sup> d<sup>-1</sup>; DIET (C,F):  $k_B$  in m<sup>3</sup> cell<sup>-1</sup> d<sup>-1</sup>. Statistical analysis shows that archaeal activity spatial variation of SRB-MIET ( $p < 0.01$ ) is significantly different than observations for archaeal activity spatial variation. Open circles are from observations and are the same for each archaeal and bacterial plot.

The modeled spatial variability in bacterial activity depends on the relative kinetics of bacterial and archaeal metabolism. In simulations with bacterial kinetics being fast compared to the archaea (e.g.,  $k_B = 10^{-10}$  m<sup>3</sup> cell<sup>-1</sup> d<sup>-1</sup>, compared to  $k_A = 10^{-14}$  mol cell<sup>-1</sup> d<sup>-1</sup>, which corresponds to  $k_B \sim 10^{-14}$  m<sup>3</sup> cell<sup>-1</sup> d<sup>-1</sup> for HS<sub>2</sub><sup>-</sup>-MIET; see Eqs. 2.9&2.10), all pathways showed an increase in the spatial variability of the bacterial cellular activity with increasing aggregate size (Fig. 2.3 D-F). At lower values of  $k_B$ , however, the cell-specific rates of the bacteria varied less for all modeled pathways, consistent with rather homogeneous activity distribution observed by McGlynn et al. (2015). For both MIET pathways (SRB-MIET and HS<sub>2</sub><sup>-</sup>-MIET), lower bacterial rate constants led to higher substrate levels in the surroundings of the aggregates (see e.g. Supporting Information Appendix A7 Fig. A6). We also observed a slight decrease of the spatial variability of the archaeal cellular activity at faster bacterial kinetics  $k_B$  (Fig. 2.3A), as a result of faster scavenging of methane oxidation products by bacterial cells. Such fast scavenging process by bacteria leads to a strong substrate gradient that is favorable for archaea, but unfavorable for bacteria.

The combined macro- and micro-scale observations provide constraints on the microbial kinetics, because the rate of AOM strongly depends on  $k_A$ , while the intra-aggregate activity patterns are dependent on the relative magnitude of  $k_B$ . This is reflected in the finding that for a fixed value of archaeal cell specific rate constant  $k_A$ , the rate of AOM remained relatively constant at the lower bacterial cell specific rate constants (Supporting Information Appendix A7 Fig. A7),

and then increased when  $k_B$  reached a certain value for models with SRB-MIET pathway. Faster  $k_B$  allowed depletion of electron exchange carriers produced by the archaea, preventing the build-up of products. This pattern held until a point was reached in which spatial gradient of exchanging chemical concentration becomes too large to sustain the bacterial reactions (not shown). For models simulating the DIET pathway, the rate of AOM slightly increased with an increase in  $k_B$  and then reached a maximum rate (Supporting Information Appendix A7 Fig. A7), reflecting that in our implementation, the rates of AOM and SR depend on M and MH (Eqns. 2.11 and 2.12). As the  $\text{HS}_2^-$  concentration reached in our simulations had a negligible impact on the energetics, the rate of AOM did not vary with  $k_B$  in the  $\text{HS}_2^-$ -MIET simulations.

### **Controls on the rate of AOM by direct interspecies electron transport**

At environmentally relevant rates of AOM, patterns in rates and intra-aggregate activity distributions across different aggregate sizes and archaeal-bacterial spatial arrangements are consistent with results from both DIET and  $\text{HS}_2^-$ -MIET simulations. However, recent genomic and microscopy evidence suggests DIET is taking place in these aggregates. For instance, metagenomic and transcriptomic analyses of ANME-1 dominated sample by Meyerdierks et al. (67) observed clustered genes annotated as secreted multi-heme c-type cytochromes that were expressed leading the authors to hypothesize that direct electron transfer may be a possible mode for the syntrophic association between ANME and their sulfate-reducing bacterial partner. More recently, McGlynn et al. (2015) and Wegener et al. (2015) provided further genomic, microscopy, and physiological evidence supporting the possibility of DIET as a syntrophic mechanism within various phylogenetic groups of methane-oxidizing ANME in partnership with sulfate-reducing bacteria. Below we explore factors that may control DIET, and assess the impact of process descriptions and parameters that are currently poorly constrained by observational data.

## Rate expressions and acid-base dynamics

The kinetic rate expressions used to describe syntrophic AOM reflect general controlling factors, but have not yet been established experimentally. To assess the effect of alternative rate laws, simulations in which the rate of AOM is independent of the concentration of the redox-active molecules fixed on conductive pili or matrix are compared to simulations that are dependent on M (oxidized) and MH (reduced; see Eqns. 2.11 and 2.12). Upon adjusting the values of  $k_A$  and  $k_B$ , our model simulations reveal the same increasing pattern in AOM rate ( $R_A$ ) with increasing  $k_A$  and  $k_B$  (Fig. 2.4). Such increasing rates of AOM with increasing  $k_A$  and  $k_B$  were found for SR rate expressions linearly depending on  $H_2$ , or independent of  $H_2$  (Eq. 2.12).

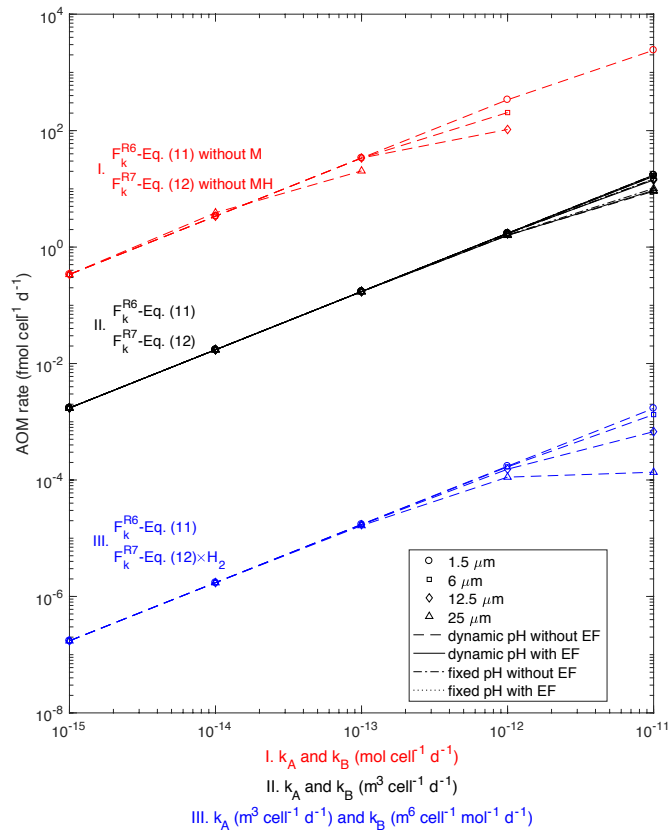


Fig. 2.4. Average cell-specific AOM rate with varying  $k_A$  and  $k_B$  for DIET. Simulations are for a spatial arrangement with a sphere of ANME surrounded by bacteria. Group II represents results

with different driving forces (with or without electric field, EF) for electron transport on conductive pili or matrix, and simulations with dynamically calculated pH or pH fixed at 8.2. Group I shows the outcomes for rate expressions in which both  $R_A$  and  $R_B$  are independent of the concentrations of M and MH, respectively. For group III,  $R_B$  depends linearly on  $H_2$  concentration, while for all other simulations it is independent of  $H_2$ .

We also tested the impact of intra-aggregate pH variation on AOM and model performance (see Supporting Information Appendix A5 for the calculation of pH). Simulations showed negligible difference between simulated pH and fixed pH models at small aggregate radii (1.5  $\mu\text{m}$  - 12.5  $\mu\text{m}$ ) for simulated AOM rates less than  $\sim 10 \text{ fmol cell}^{-1} \text{ d}^{-1}$ . However, at a larger aggregate radius (25  $\mu\text{m}$ ) and rates greater than  $10 \text{ fmol cell}^{-1} \text{ d}^{-1}$ , AOM rates with fixed pH simulations but otherwise identical parameterization were slightly higher than those of models with dynamic pH. For instance, with  $k_A$  and  $k_B$  at  $10^{-11} \text{ m}^3 \text{ cell}^{-1} \text{ d}^{-1}$ , modeled AOM rates with fixed pH exceeded the ones with pH simulated by approx. 10% for aggregates with  $r = 25 \mu\text{m}$ . Thus, our simulations suggest that intra-aggregate pH variations are unlikely the main control on AOM rates. The modeled pH remained similar to the imposed seawater value of 8.2, indicating that protons produced in the oxidation of methane (Reaction 2.6) are efficiently buffered at environmentally relevant rates. However, in direct extracellular electron transfer, the transfer of electron can be much faster than proton diffusion, which can lead to pH gradients (27, 68). Our modeled DIET simulations showed the establishment of such pH gradients, however these gradients only occurred at rates exceeding values reported from methane seep environments ( $> 10^3 \text{ fmol cell}^{-1} \text{ d}^{-1}$ ) at large aggregate size (25  $\mu\text{m}$ ). Our additional simulations with artificially accelerated proton diffusion allowed for higher rates, indicating the potential role of pH variations to limit AOM at high rates and large aggregate size. We note that in addition to the modeled thermodynamic impact here, a

decrease in pH at higher AOM rates may also impede proton transport across outer cell membranes, impacting extracellular electron transport as documented by Okamoto et al. (69) for *Shewanella oneidensis* MR-1.

### *Electron transport*

The nature and description of electron transport between archaea and bacterial partners is a critical issue in AOM aggregates. Described in detail in section *Direct interspecies electron transfer*, we here explore the impact of several key factors that determine the electron transport rate and cell-specific activities.

#### *Concentration of redox molecules in cell-to-cell electron transport*

The transport coefficient for redox-active molecules (reduced: MH; oxidized: M) located on conductive pili or matrix was estimated to be on the order of  $10^{-7} \text{ m}^2 \text{ s}^{-1}$  (see Eq. 2.14 below, with  $M_{tot} = 0.01 \text{ mmol L}^{-1}$ ;  $k^0 = 10^4 \text{ m}^4 \text{ mol}^{-1} \text{ s}^{-1}$ ,  $\delta = 0.7 \text{ nm}$ ), comparable to a value reported for a conductive filament network (charge diffusion coefficient of  $3.5 \times 10^{-7} \text{ m}^2 \text{ s}^{-1}$ ; (54)). This exceeds chemical diffusion by several orders of magnitude. Here, the concentration of redox molecules was varied across a range of 0.01-1  $\text{mmol L}^{-1}$  to explore its impact on electron transport in our models. With the increase of  $M_{tot}$ , AOM rates increased linearly, as shown in Fig. 2.5 A. This is qualitatively consistent with the findings reported by Storck et al. (25), who showed that a 10-fold decrease of the amount of conductive pili or matrix ( $N_{nw}$ ) from 100 to 10 per cell pair lead to 60% decrease of electron transport rate. The amount of conductive pili or matrix ( $N_{nw}$ ) is directly related to the total redox molecule concentration ( $M_{tot}$ ). However, simulations in which the reaction kinetics were independent of M and MH showed little impact of an increase in  $M_{tot}$  (and hence transport coefficient) on AOM, indicating that in our model, AOM is limited by the reaction, rather than electron transport processes. For instance, in model simulations with kinetic rate expressions

independent of  $M$  and  $MH$ , the AOM rate remained constant when  $M_{tot}$  increases from 0.01 to 1 mmol L<sup>-1</sup> ( $k_A$  and  $k_B$  at 10<sup>-15</sup> mol cell<sup>-1</sup> d<sup>-1</sup>, aggregate radius  $r = 25 \mu\text{m}$ ).

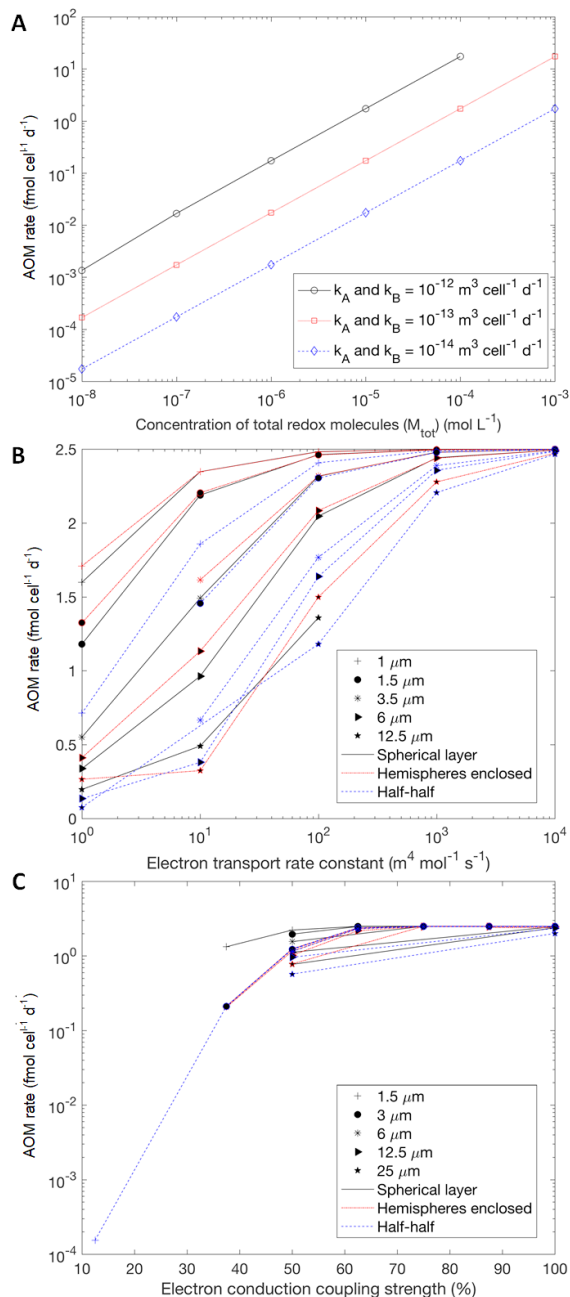


Fig. 2.5. Simulations of AOM by DIET (A) with varying redox molecule concentration ( $M_{tot}$ ),  $k_A$  and  $k_B$ , an aggregate radius of 1.5  $\mu\text{m}$ , a spatial arrangement with a sphere of ANME surrounded by bacteria. (B) AOM rates vary with electron transport rate constant  $k^0$ . (C) Plot of AOM rates

with varying coupling strength (defined as  $f_M/8 \times 100$ , Reaction 6) between electron production and conduction.  $k_A$  and  $k_B$  are fixed at  $10^{-12} \text{ m}^3 \text{ cell}^{-1} \text{ d}^{-1}$  for (B) and (C). Baseline values apply to all other parameters.

#### *Electrical field as an additional driving force*

Electron transport can be driven by a concentration gradient in electron carriers (M and MH) or an electric field (26). Considering the electrical field as a driving force for electron transport in addition to the gradient in oxidized cytochromes did not significantly impact on AOM rates (Fig. 2.4). Furthermore, there was no significant difference between simulations with electric field as sole driving force and simulations with redox gradient as driving force (not shown). This finding that electron transport between archaea and bacteria is not limiting is also supported by results showing that increasing electron transfer rate constant ( $k^0$ ) had little impact on AOM rate for  $k^0 > 10^2 \text{ m}^4 \text{ mol}^{-1} \text{ s}^{-1}$ , corresponding to a transport coefficient of  $>10^{-9} \text{ m}^2 \text{ s}^{-1}$ . However, the simulated AOM rate significantly decreased at  $k^0 \leq 10^2 \text{ m}^4 \text{ mol}^{-1} \text{ s}^{-1}$  (Fig. 2.5 B). Noticeably, the variation of intra-aggregate archaeal and bacterial activity also began to significantly increase and differ from observations at  $k^0 < 10^2 \text{ m}^4 \text{ mol}^{-1} \text{ s}^{-1}$  (Supporting Information Appendix A7 Fig. A8). Storck et al. (2016) reported that doubling the electron transfer rate constant leads to a doubling of electron transfer rate, also implying a doubling of the oxidation rate. Our model simulations suggest that the finding from Storck et al. (2016) remains true at small  $k^0$  ( $\leq 10^2 \text{ m}^4 \text{ mol}^{-1} \text{ s}^{-1}$ ). Overall, the electron transfer rate constant is a critical factor controlling electron transfer by impacting the effective diffusion coefficient ( $D_{MH}$ ) of redox-active molecule (M and MH).

#### *Voltage loss*

Voltage losses can negatively affect transport efficiency in DIET, and ohmic losses ( $\eta_{res}$ ) and activation losses ( $\eta_{act}$ ) have been suggested to be dominant factors (25). Ohmic losses ( $\eta_{res}$ )

and activation losses ( $\eta_{act}$ ) were calculated using the Ohm's law and Butler–Volmer equation, respectively. Here we investigated the importance of these two voltage loss terms and compare them to the voltage available from the AOM reaction (Eq. 2.19).

Ohmic loss ( $\eta_{res}$ ) is a result of electronic resistance and has been explored in some recent studies (44,52-53). It can be calculated as (25)

$$\eta_{res} = \rho_{nw} \cdot L_{nw} \cdot I / (N_{nw} \cdot N_{ANME} \cdot A_{nw}), \quad \text{Eq. (2.22)}$$

where  $\rho_{nw}$  is the electrical resistivity of a pilus,  $L_{nw}$  is the length of a single pilus,  $A_{nw}$  is the cross-sectional area of a single pilus,  $N_{nw}$  is the number of conductive pili per cell,  $I$  is the current generated as a result of methane oxidation and can be estimated as  $I = R_{AOM} \cdot N_{ANME} \cdot n \cdot F$ , where  $R_{AOM}$  is the methane oxidation rate,  $N_{ANME}$  is the number of archaeal cells and  $n$  the electrons transferred per reaction. We take conductive pili as an example to illustrate the factors that control voltage losses in DIET. With an electrical resistivity of a pilus ( $\rho_{nw}$ ) of  $1 \Omega \cdot \text{m}$  (25), a cross-sectional area of a single pilus ( $A_{nw}$ ) of  $1.26 \times 10^{-17} \text{ m}^2$  (25), length of a single pilus  $L_{nw}$  on the order of the aggregate size ( $10^{-6} \text{ m}$ ), a current  $I$  of  $7 \times 10^{-13} \text{ A}$  (at  $R_{AOM} = 10 \text{ fmol cell}^{-1} \text{ d}^{-1}$ ) and 10 conductive pili ( $N_{nw}$ ) per cell,  $\eta_{res}$  is  $7 \times 10^{-5} \text{ V}$ . This is substantially smaller than the AOM potential obtained from our model simulations, which is on the order of  $10^{-2} \text{ V}$ , and suggests that ohmic loss is not a determining factor in our current model.

Activation loss ( $\eta_{act}$ ) is another factor that may influence DIET electron transport, accounting for the voltage losses when an electron is transferred from the cell to the conductive pili or vice versa, due to the activation energy needed for a redox reaction. According to Storck et al. (2016) and Strycharz-Glaven et al. (2011), the redox activation losses can be approximated as

$$\eta_{act} = \frac{I \cdot R_{gas} \cdot T \cdot L_{nw}}{N_{nw} N_{ANME} \delta n^2 F^2 A_{act} k^0 \left(\frac{M_{tot}}{2}\right)^2} \text{ when } \delta \cdot \eta_{act} / W < 0.05, \quad \text{Eq. (2.23)}$$

where  $I$  is the current generated as a result of methane oxidation and is the same as described in the equation for ohmic loss ( $\eta_{res}$ ),  $L_{nw}$  is the length of a single pilus,  $R_{gas}$  is the universal gas constant ( $8.314 \text{ J K}^{-1} \text{ mol}^{-1}$ ),  $T$  is the temperature in K,  $N_{nw}$  is the number of conductive pili per cell,  $N_{ANME}$  is the number of archaeal cells,  $\delta$  is the redox molecules spacing width,  $n$  the electrons transferred per reaction,  $F$  is the Faraday constant  $96485.33 \text{ C mol}^{-1}$ ,  $A_{act}$  is the redox activation area per cell (equivalent to 10% of cell surface area),  $k^0$  is the electron transport rate constant, and  $M_{tot}$  is the total concentration (=M+MH) (25). With the same parameters and the current  $I$  estimated above, the maximum  $\eta_{act}$  can be estimated to be  $1 \times 10^{-7} \text{ V}$  at  $M_{tot} = 0.01 \text{ mmol L}^{-1}$  and  $k^0 = 10^4 \text{ m}^4 \text{ mol}^{-1} \text{ s}^{-1}$ , which is negligible. In contrast, a value of  $k^0 = 1 \text{ m}^4 \text{ mol}^{-1} \text{ s}^{-1}$ , a decrease by a factor of  $10^4$  from the default  $k^0$  discussed above would result in an activation loss at an order of  $1 \times 10^{-3} \text{ V}$ , suggesting activation loss becomes the dominating factor for voltage loss. This is consistent with the findings reported by Storck et al. (2016).

#### *Coupling strength between electron production and conduction*

To test how electron transport via the diffusion of dissolved electron carriers ( $DH = \text{H}_2$  in our model) and conduction of pili or matrix may impact AOM, the fraction of electrons transported via conductive pili or matrix was varied. This was implemented as factors  $f_M$  and  $f_D$  in reactions 2.6 & 2.7, where higher values of  $f_M$  imply lower production of the reduced electron pool molecules  $DH$ . Simulations suggested that higher loading percentage onto conductive pili or matrix leads to higher AOM rate in general (Fig. 2.5 C). AOM rates drastically declined at electron conduction coupling strengths (% , defined as  $f_M/8 \times 100$ , Reaction 2.6) below 50%. At coupling strength of less than 50%, AOM rates differed between simulations with different spatial arrangements. It is also noted that the variation of archaeal activity significantly ( $p < 0.05$ ) increases at lower coupling strengths (<40%, see Supporting Information Appendix A7 Fig. A9A). The declining AOM rates

and increasing intra-aggregate activity variation are due to the increasing thermodynamic constraints resulting from the build-up of  $H_2$ , which increases the reaction quotient,  $Q_{R6} = \prod a_i^{v_j} = \frac{a_{HCO_3} a_H a_{H_2}^{f_D} a_{MH}^{f_M}}{a_{CH_4} a_M^{f_M}}$ , and subsequently increases  $\Delta G$  and decreases  $F_T$  to the point where  $F_T$  for reaction R6 (Eq. 2.4) becomes 0. Our simulations indicated that under baseline parameterization electron transport of at least 50% by conduction gives AOM rates and intra-aggregate activity spatial variation pattern consistent with observations.

A decrease in AOM rates was observed when incubating ANME-1 consortia with  $H_2$  and methane (23), when considering  $H_2$  as the potential dissolved electron carriers (D and DH). This might be due to electron transport being limited by diffusion of DH (here  $H_2$ ), possibly in combination with syntrophic decoupling. Once electrons are loaded onto conductive pili or matrix over a certain percentage ( $\geq 50\%$ ), electron transfer does not limit AOM. At a slow effective diffusion of redox molecules with small electron transfer rate constant, AOM rates would have a higher dependency on the activation loss and resistance loss on conductive pili or matrix.

### **Metabolic coupling in syntrophic communities**

The results of our 3D modeling simulations suggest good agreement between measurements (aggregate AOM rates and spatial activity patterns) and the DIET models. The comparison with cell-specific data from McGlynn et al. (2015) help constrain parameters such as  $k_A$ ,  $k_B$ ,  $M_{tot}$ ,  $k^0$  and  $f_M$ . Thus, the models developed here serve as predictive tools for assessing potential syntrophic relationships and major parameters that may influence sulfate-coupled AOM *in situ*. For example, if future measurements of AOM consortia yielded lower cell-specific AOM rates ( $<10^{-3}$  fmol cell<sup>-1</sup> d<sup>-1</sup>) then the diffusion controlled SRB-MIET could be a possible mechanism for small aggregates ( $\leq 6\mu\text{m}$ ). Yet it should be noted that the models presented here are not exhaustive for the range of metabolic possibilities. For example, we have not considered the

potential for metabolic switching behavior (70). Our modeling efforts could also be adapted and applied to AOM consortia using other terminal electron acceptors, including nitrate (4, 5) and metal oxides (6, 9). Ultimately the broad-scale mechanisms modeled here will need to be connected to more detailed perspectives of the entire physiology and metabolism of the cell, as for example informed by genome-enabled metabolic models. It is important to also stress that activation and ohmic losses are largely dependent on electron transport distance and abundance of conductive pili or matrix (here expressed by  $L_{nw}$  and  $N_{nw}$ ). These are likely to vary spatially within an aggregate (23, 43), and thus require further observational studies that constrain these and other characteristics that impact electron conduction.

Finally, it is noteworthy that not only do the small-scale observations help differentiate between mechanisms, but the combination of environmental rate estimates with intra-aggregate activity distribution helps constrain rate constants. Specifically, we find that  $k_A$  is well constrained by cell specific AOM rates and is on the order of  $>10^{-15} \text{ m}^3 \text{ cell}^{-1} \text{ d}^{-1}$  for DIET and  $>10^{-17} \text{ mol cell}^{-1} \text{ d}^{-1}$  for MIET pathways;  $k_B$  is no more than 100-fold larger than  $k_A$  to be consistent with the observed intra-aggregate activity patterns (Fig. 2.3 D-F). The product of  $M_{tot}$  and  $k^0$  determines the effective diffusion coefficient  $D_{MH}$ , which has to exceed  $10^{-9} \text{ m}^2 \text{ s}^{-1}$  to be consistent with observations (compare, e.g., the simulated variation in activity in Fig. A8, where  $k^0$  has to exceed  $10^2 \text{ m}^4 \text{ mol}^{-1} \text{ s}^{-1}$  at  $M_{tot} = 0.01 \text{ mmol L}^{-1}$ ,  $\delta = 0.7 \text{ nm}$  with the observed variability shown in Figs. A4 C&D and A5 C&D; and the variation of AOM rates with aggregate size and cell arrangement shown in Fig. 2.2 and the corresponding  $^{15}\text{N}$  assimilation in Figs. A4 A and A5 A).  $f_M$  determines the fraction of electron transport via conduction (see reactions 2.6&2.7) and is constrained to give electron conduction coupling strengths greater than 50% in order to be consistent with observed patterns in AOM rates with regard to aggregate size and arrangement, as well as intra-aggregate

activity. This connection between micro- and macro-scale observations can help us better understand the response of those microbial organisms to a small-scale environmental disturbance and ultimately how such changes would lead to large-scale variation.

### Conclusion

We presented reactive transport models describing electron transfer within sulfate reduction-coupled AOM consortia of archaeal and bacterial cells. Microbial activities were simulated for diverse arrangements of archaeal and bacterial cells and consortium sizes. We excluded SRB-MIET as a viable pathway of electron transport in these consortia because the simulated microbial activities are unevenly distributed within each consortium and are limited by the build-up of metabolites. These predictions are inconsistent with experimental observations. Instead our models support DIET as a viable mechanism for extracellular electron transfer within sulfate-coupled AOM consortia. Our proposed DIET model yielded cell specific rates and archaeal activity distributions that were consistent with empirical observations, with little impact of the spatial distribution of bacterial and archaeal cells and consortium sizes. These modeling efforts can be used to guide further empirical and theoretical explorations into the identity and kinetics of extracellular redox-active components within AOM consortia with important environmental roles.

### Acknowledgements

This work was supported by the Genomic Sciences Program in the DOE Office of Science, Biological and Environmental Research DE-SC0016469. The authors declare no conflict of interest.

## References

1. Boetius A, Ravensschlag K, Schubert CJ, Rickert D, Widdel F, Gieseke A, et al. A marine microbial consortium apparently mediating anaerobic oxidation of methane. *Nature*. 2000;**407**:623–6.
2. Orphan VJ, House CH, Hinrichs KU, McKeegan KD, DeLong EF. Methane-consuming archaea revealed by directly coupled isotopic and phylogenetic analysis. *Science*. 2001;**293**:484–7.
3. Michaelis W, Seifert R, Nauhaus K, Treude T, Thiel V, Blumenberg M, et al. Microbial reefs in the Black Sea fueled by anaerobic oxidation of methane. *Science* 2002;**297**(5583):1013-5.
4. Raghoebarsing AA, Pol A, Van de Pas-Schoonen KT, Smolders AJ, Ettwig KF, Rijpstra WIC, et al. A microbial consortium couples anaerobic methane oxidation to denitrification. *Nature*. 2006;**440**(7086):918-21.
5. Haroon MF, Hu S, Shi Y, Imelfort M, Keller J, Hugenholtz P, et al. Anaerobic oxidation of methane coupled to nitrate reduction in a novel archaeal lineage. *Nature*. 2013;**500**:567–70.
6. Beal EJ, House CH, Orphan VJ. Manganese- and iron-dependent marine methane oxidation. *Science*. 2009;**325**:184–7.
7. Ettwig KF, Zhu B, Speth D, Keltjens JT, Jetten MSM, Kartal B. Archaea catalyze iron-dependent anaerobic oxidation of methane. *Proc Natl Acad Sci USA*. 2016;**113**(45):12792–6.
8. Bar-Or I, Elvert M, Eckert W, Kushmaro A, Vigderovich H, Zhu Q, et al. Iron-coupled anaerobic oxidation of methane performed by a mixed bacterial-archaeal community based on poorly reactive minerals. *Environ Sci Technol*. 2017;**51**:12293-301.
9. Scheller S, Yu H, Chadwick GL, McGlynn SE, Orphan VJ. Artificial electron acceptors decouple archaeal methane oxidation from sulfate reduction. *Science*. 2016;**351**(6274):703-7.

10. Reeburgh WS. Oceanic methane biogeochemistry. *Chemical Rev.* 2007;**107**(2):486-513.
11. Forster P, Ramaswamy V, Artaxo P, Berntsen T, Betts R, Fahey DW, et al. Chapter 2: Changes in Atmospheric Constituents and in Radiative Forcing. In: Solomon S, Qin D, Manning M, Chen Z, Marquis M, Averyt KB, et al., editors. *Contribution of Working Group I to the Fourth Assessment Report of the Intergovernmental Panel on Climate Change*. Cambridge, United Kingdom and New York, NY, USA: Cambridge University Press; 2007. p. 130-234.
12. Alperin M, Hoehler T. The Ongoing Mystery of Sea-Floor Methane. *Science*. 2010;**329**(5989):288-9.
13. McGlynn SE. Energy metabolism during anaerobic methane oxidation in ANME archaea. *Microbes Environ.* 2017;**32**(1): 5-13.
14. Timmers PH, Welte CU, Koehorst JJ, Plugge CM, Jetten MS, Stams AJ. Reverse Methanogenesis and respiration in methanotrophic archaea. *Archaea*. 2017;**2017**:1654237.
15. Reeburgh WS. Methane consumption in Cariaco Trench waters and sediments. *Earth Planet Sc Lett.* 1976;**28**:337-44.
16. Hoehler TM, Alperin MJ, Albert DB, Martens CS. Field and laboratory studies of methane oxidation in an anoxic marine sediment: Evidence for a methanogen-sulfate reducer consortium. *Global Biogeochemical Cycles*. 1994;**8**:451-63.
17. Sørensen KB, Finster K, Ramsing NB. Thermodynamic and kinetic requirements in anaerobic methane oxidizing consortia exclude hydrogen, acetate, and methanol as possible electron shuttles. *Microbial Ecology*. 2001;**42**:1-10.
18. Orcutt B, Meile C. Constraints on mechanisms and rates of anaerobic oxidation of methane by microbial consortia: process-based modeling of ANME-2 archaea and sulfate reducing bacteria interactions. *Biogeosciences*. 2008;**5**:1587-99.

19. Valentine DL, Reeburgh WS. New perspectives on anaerobic methane oxidation. *Environ Microbiol.* 2000;**2**:477-84.
20. Moran JJ, Beal EJ, Vrentas JM, Orphan VJ, Freeman KH, House CH. Methyl sulfides as intermediates in the anaerobic oxidation of methane. *Environ Microbiol.* 2008;**10**:162-73.
21. Milucka J, Ferdelman TG, Polerecky L, Franzke D, Wegener G, Schmid M, et al. Zero-valent sulphur is a key intermediate in marine methane oxidation. *Nature.* 2012;**491**(7425):541-6.
22. McGlynn SE, Chadwick GL, Kempes CP, Orphan VJ. Single cell activity reveals direct electron transfer in methanotrophic consortia. *Nature.* 2015;**526**(7574):531-5.
23. Wegener G, Krukenberg V, Riedel D, Tegetmeyer HE, Boetius A. Intercellular wiring enables electron transfer between methanotrophic archaea and bacteria. *Nature.* 2015;**526**(7574):587-90.
24. Krukenberg V, Riedel D, Gruber-Vodicka HR, Buttigieg PL, Tegetmeyer HE, Boetius A, et al. Gene expression and ultrastructure of meso- and thermophilic methanotrophic consortia. *Environ Microbiol.* 2018;**20**:1651-66.
25. Storck T, Virdis B, Batstone DJ. Modelling extracellular limitations for mediated versus direct interspecies electron transfer. *ISME J.* 2016;**10**(3):621-31.
26. Strycharz-Glaven SM, Snider RM, Guiseppi-Elie A, Tender LM. On the electrical conductivity of microbial nanowires and biofilms. *Energy Environ Sci.* 2011;**4**:4366–79.
27. Korth B, Rosa LF, Harnisch F, Picioreanu C. A framework for modeling electroactive microbial biofilms performing direct electron transfer. *Bioelectrochemistry.* 2015;**106**:194-206.
28. Alperin MJ, Hoehler TM. Anaerobic methane oxidation by archaea/sulfate-reducing bacteria aggregates: 2. Isotopic constraints. *Am J Sci.* 2009;**309**(10):869-957.

29. Knittel K, Lösekann T, Boetius A, Kort R, Amann R. Diversity and distribution of methanotrophic archaea at cold seeps. *Appl Environ Microbiol.* 2005;**71**(1):467-79.
30. Aoki M, Ehara M, Saito Y, Yoshioka H, Miyazaki M, Saito Y, et al. A Long-Term Cultivation of an Anaerobic Methane-Oxidizing Microbial Community from Deep-Sea Methane-Seep Sediment Using a Continuous-Flow Bioreactor. *PLoS one.* 2014;**9**(8):e105356.
31. Jin Q, Bethke C. A new rate law describing microbial respiration. *Appl Environ Microbiol.* 2003;**69**:2340–8.
32. Jin Q, Bethke C. The thermodynamics and kinetics of microbial metabolism. *Am J Sci.* 2007;**307**:643–77.
33. Tran QH, Uden G. Changes in the proton potential and the cellular energetics of *Escherichia coli* during growth by aerobic and anaerobic respiration or by fermentation. *Eur J Biochem* 1998;**251**:538–43.
34. Pänke O, Rumberg B. Energy and entropy balance of ATP synthesis. *BBA-Bioenergetics* 1997;**1322**(2):183-94.
35. Hoehler TM, Alperin MJ, Albert DB, Martens CS. Apparent minimum free energy requirements for methanogenic Archaea and sulfate-reducing bacteria in an anoxic marine sediment. *FEMS Microbiol Ecology.* 2001;**38**:33-41.
36. Zeebe RE, Wolf-Gladrow D. Chapter 2. Kinetics. In: Halpern D, editor. *CO<sub>2</sub> in Seawater: Equilibrium, Kinetics, Isotopes.* 3rd ed. San Diego, USA: Elsevier Science; 2005.
37. Konhauser K. Chapter 3. Cell surface reactivity and metal sorption. In: Konhauser K, editor. *Introduction to geomicrobiology:* Blckwell Publishing; 2006.

38. Kaplan H, Stevenson KJ, Hartley BS. Competitive labelling, a method for determining the reactivity of individual groups in proteins. The amino groups of porcine elastase. *Biochem J.* 1971;**124**(1): 289-99.
39. Wallerstein J, Weininger U, Khan MAI, Linse S, Akke M. Site-specific protonation kinetics of acidic side chains in proteins determined by pH-dependent carboxyl <sup>13</sup>C NMR relaxation. *J Am Chem Soc.* 2015;**137**(8):3093–101.
40. Phoenix VR, Martinez RE, Konhauser KO, Ferris FG. Characterization and implications of the cell surface reactivity of *Calothrix* sp. strain KC97. *Applied and Environmental Microbiology.* 2002;**68**(10):4827-34.
41. Burgess I, Seivewright B, Lennox RB. Electric field driven protonation/deprotonation of self-assembled monolayers of acid-terminated thiols. *Langmuir.* 2006;**22**(9):4420–8.
42. Reguera G, McCarthy KD, Mehta T, Nicoll JS, Tuominen MT, Lovley DR. Extracellular electron transfer via microbial nanowires. *Nature.* 2005;**435**:1098–101.
43. Reguera G, Nevin KP, Nicoll JS, Covalla SF, Woodard TL, Lovley DR. Biofilm and nanowire production leads to increased current in *Geobacter sulfurreducens* fuel cells. *Appl Environ Microbiol.* 2006;**72**:7345–8.
44. El-Naggar MY, Wanger G, Leung KM, Yuzvinsky TD, Southam G, Yang J, et al. Electrical transport along bacterial nanowires from *Shewanella oneidensis* MR-1. *PNAS.* 2010;**107**:18127-31.
45. Ordóñez MV, Schrott GD, Massazza DA, Busalmen JP. The relay network of *Geobacter* biofilms. *Energy Environ Sci.* 2016;**9**:2677–81.

46. Virdis B, Millo D, Donose BC, Lu Y, Batstone DJ, Krömer JO. Analysis of electron transfer dynamics in mixed community electroactive microbial biofilms. *RSC Adv.* 2016;**6**:3650–60.
47. Beyenal H, Chen SN, Lewandowski Z. The double substrate growth kinetics of *Pseudomonas aeruginosa*. *Enzyme Microb Technol.* 2003:92-8.
48. Zinn M, Witholt B, Egli T. Dual nutrient limited growth: models, experimental observations, and applications. *J Biotechnol.* 2004;**113**:263-79.
49. Cherif M, Loreau M. Towards a more biologically realistic use of Droop's equations to model growth under multiple nutrient limitation. *Oikos.* 2010;**119**:897-907.
50. Gonzo EE, Wuertz S, Rajal VB. The continuum heterogeneous biofilm model with multiple limiting substrate Monod kinetics. *Biotechnol Bioeng.* 2014;**111**:2252-64.
51. Strycharz-Glaven SM, Tender LM. Reply to the ‘Comment on “On electrical conductivity of microbial nanowires and biofilms”’ by N. S. Malvankar, M. T. Tuominen and D. R. Lovley, *Energy Environ. Sci.*, 2012, 5, DOI: 10.1039/c2ee02613a. *Energy Environ Sci.* 2012;**5**:6250-5.
52. Malvankar NS, Vargas M, Nevin KP, Franks AE, Leang C, Kim B-C, et al. Tunable metallic-like conductivity in microbial nanowire networks. *Nat Nanotechnol.* 2011;**6**(9):573-9.
53. Malvankar NS, Mark TT, Lovley DR. Comment on “On electrical conductivity of microbial nanowires and biofilms” by S. M. Strycharz-Glaven, R. M. Snider, A. Guiseppi-Elie and L. M. Tender, *Energy Environ. Sci.*, 2011, 4, 4366. *Energy Environ Sci.* 2012;**5**:6247.
54. Meysman FJR, Risgaard-Petersen N, Malkin SY, Nielsen LP. The geochemical fingerprint of microbial long-distance electron transport in the seafloor. *Geochim Cosmochim Acta* 2015;**152**:122–42.

55. Kletzin A, Heimerl T, Flechsler J, van Niftrik L, Rachel R, Klingl A. Cytochromes c in Archaea: distribution, maturation, cell architecture, and the special case of *Ignicoccus hospitalis*. *Front Microbiol.* 2015;**6**:439.
56. Nauhaus K, Boetius A, Krüger M, Widdel F. In vitro demonstration of anaerobic oxidation of methane coupled to sulphate reduction in sediment from a marine gas hydrate area. *Environ Microbiol.* 2002;**4**:296–305.
57. Nauhaus K, Albrecht M, Elvert M, Boetius A, Widdel F. In vitro cell growth of marine archaeal-bacterial consortia during anaerobic oxidation of methane with sulfate. *Environ Microbiol.* 2007;**9**(1):187-96.
58. Orphan VJ, Turk KA, Green AM, House CH. Patterns of <sup>15</sup>N assimilation and growth of methanotrophic ANME-2 archaea and sulfate-reducing bacteria within structured syntrophic consortia revealed by FISH-SIMS. *Environ Microbiol.* 2009;**11**:1777–91.
59. Dekas AE, Chadwick GL, Bowles MW, Joye SB, Orphan VJ. Spatial distribution of nitrogen fixation in methane seep sediment and the role of the ANME archaea. *Environ Microbiol.* 2013;**16**(10):3012–29.
60. Malvankar NS, Vargas M, Nevin KP, Franks AE, Leang C, Kim BC, et al. Tunable metallic-like conductivity in microbial nanowire networks. *Nat Nanotechnol.* 2011;**6**:573-9.
61. Eaktasang N, Kang CS, Lim H, Kwean OS, Cho S, Kim Y, et al. Production of electrically-conductive nanoscale filaments by sulfate-reducing bacteria in the microbial fuel cell. *Bioresour Technol.* 2016;**210**:61-7.
62. Nauhaus K, Treude T, Boetius A, Krüger M. Environmental regulation of the anaerobic oxidation of methane: a comparison of ANME-I and ANME-II communities. *Environ Microbiol.* 2005;**7**(1):98-106.

63. Holler T, Wegener G, Knittel K, Boetius A, Brunner B, Kuypers MM, et al. Substantial  $^{13}\text{C}/^{12}\text{C}$  and D/H fractionation during anaerobic oxidation of methane by marine consortia enriched *in vitro*. *Environ Microbiol Rep*. 2009(5):370-6.
64. Niemann H, Elvert M, Hovland M, Orcutt B, Judd A, Suck I, et al. Methane emission and consumption at a North Sea gas seep (Tommeliten area). *Biogeosciences* 2005;2:335–51.
65. Treude T, Boetius, A. K, K., Wallmann K, Jørgensen BB. Anaerobic oxidation of methane above gas hydrates at Hydrate Ridge, NE Pacific Ocean. *Mar Ecol Prog Ser*. 2003;264:1-14.
66. Wegener G, Boetius A. An experimental study on short-term changes in the anaerobic oxidation of methane in response to varying methane and sulfate fluxes. *Biogeosciences*. 2009;6(5):867-76.
67. Meyerdierks A, Kube M, Kostadinov I, Teeling H, Glöckner FO, Reinhardt R, et al. Metagenome and mRNA expression analyses of anaerobic methanotrophic archaea of the ANME-1 group. *Environ Microbiol*. 2010;12:422–39.
68. Franks AE, Nevin KP, Jia H, Izallalen M, Woodard TL, Lovley DR. Novel strategy for three-dimensional real-time imaging of microbial fuel cell communities: monitoring the inhibitory effects of proton accumulation within the anode biofilm. *Energy Environ Sci*. 2009;2:113-9.
69. Okamoto A, Tokunou Y, Kalathil S, Hashimoto K. Proton transport in the outer-membrane flavocytochrome complex limits the rate of extracellular electron transport. *Angew Chem Int Ed Engl*. 2017;56:9082–6.
70. Steunou AS, Bhaya D, Bateson MM, Melendrez MC, Ward DM, Brecht E, et al. In situ analysis of nitrogen fixation and metabolic switching in unicellular thermophilic cyanobacteria inhabiting hot spring microbial mats. *PNAS*. 2006;103:2398-403.

71. Schulz HD. Quantification of early diagenesis: dissolved constituents in marine pore water. In: Schulz HD, Zabel M, editors. *Marine Geochemistry*: Springer Berlin Heidelberg; 2000. p. 85-128.
72. Gupta N, Gattrell M, MacDougall B. Calculation for the cathode surface concentrations in the electrochemical reduction of CO<sub>2</sub> in KHCO<sub>3</sub> solutions. *J Appl Electrochem*. 2006;**36**(2):161-72.
73. Zhou Y, Fang C, Fang Y, Zhu F. Volumetric and transport properties of aqueous NaB(OH)<sub>4</sub> solutions. *Chin J Chem Eng*. 2013;**21**(9):1048-56.
74. Glass, J and Orphan, VJ. Trace metal requirements for microbial enzymes involved in the production and consumption of methane and nitrous oxide. *Front Microbiol* 2012;**3**: 61.

## CHAPTER 3

# CONTROLS ON INTERSPECIES ELECTRON TRANSPORT AND SIZE LIMITATION OF ANAEROBICALLY METHANE OXIDIZING MICROBIAL CONSORTIA <sup>2</sup>

---

<sup>2</sup> He, X., Chadwick, G., Kempes, C., Orphan, V. and Meile, C. (2020) Controls and size limitations of anaerobic methane oxidizing consortia metabolism. To be Submitted to mBio.

## Abstract

About 382 Tg yr<sup>-1</sup> of methane rising through the seafloor is oxidized anaerobically (1), preventing it from reaching the atmosphere where it acts as a strong greenhouse gas. Microbial consortia composed of anaerobic methanotrophic archaea and sulfate-reducing bacteria couple the oxidation of methane to the reduction of sulfate under anaerobic conditions via a syntrophic process. Recent experimental studies and modeling efforts show that direct interspecies electron transfer (DIET) is involved in this syntrophy. Here we explore the physiological controls on this critical process through modeling combined with FISH-nanoSIMS isotopic analysis of large, segregated AOM consortia that reveal a decline in metabolic activity away from the archaea-bacteria interface. Our simulations of metabolic interactions between the bacteria and archaea yield results consistent with our empirical FISH-nanoSIMS data of anabolic activity profiles and show that ohmic resistance and activation loss are the two main factors causing the declining metabolic activity, where activation loss dominated at distance < ~8 μm. The simulations indicated that sulfate-reducing bacterial cells remain metabolically active at distance up to ~30 μm from the archaea-bacteria interface, suggesting a maximum spatial distance between syntrophic partners organized in layered consortia where the partners are well separated. Notably, our model simulations predict that a hybrid metabolism that combines DIET with a small contribution of diffusive exchange of electron donors offers energetic advantages for syntrophic consortia.

## Introduction

Anaerobic oxidation of methane (AOM) coupled to sulfate reduction (SR) is a globally important process commonly catalyzed by a consortium of anaerobic methanotrophic archaea (ANME) and sulfate-reducing bacteria (SRB) (2-5). AOM in marine sediments reduce emissions of the potent greenhouse gas methane (1) to the overlying water and the atmosphere. Due to the

role of methane in atmospheric radiative forcing (6), it is important to understand the processes and mechanisms involved in AOM. Recent studies suggest that direct extracellular electron transfer, observed in *Geobacter* biofilms (7, 8) and coculture aggregates (9, 10), also takes place in AOM consortia (11-13). Such direct interspecies electron transfer (DIET) between bacteria and archaea is an effective transport mechanism over long spatial distances (14). It overcomes limitations inherent in the diffusive exchange of dissolved electron carrying molecules (mediated interspecies electron transfer, MIET) that lead to the build-up of reaction products making the reaction energetically unfavorable, and the subsequent shut-down of metabolic activity (13, 15).

DIET is proposed to occur through a variety of complementary mechanisms including direct contact between cells and its electron acceptors using outer surface c-type cytochromes (16), through electrically conductive pili (17) or within a matrix of conductive extracellular polymeric substances (18, 19). Genomic and transcriptomic data of enrichments with different types of AOM consortia (ANME-1a/HotSeep-1, ANME-1a/Seep-SRB2 and ANME-2c/Seep-SRB2) revealed that genes encoding for flagella or type IV pili, and/or surface bound or extracellular c-type cytochromes were highly expressed (20). Notably, ANME-2 genomes encode large multiheme cytochromes containing S-layer domains (11) thought to be analogous to the gram negative porin-cytochrome conduits used for extracellular electron transfer (21). Observations using transmission electron microscopy (TEM) showed staining consistent with heme-rich areas and pili/wire-like structures in the intracellular space in AOM consortia (11, 12, 20). These features suggest that DIET may be the principal mechanism to sulfate-dependent AOM. While this hypothesis awaits direct experimental confirmation and is hampered by a lack of any pure cultures of microorganisms carrying out this metabolism, modeling efforts indicated that DIET can support cell specific AOM

rates and archaeal activity distributions that were consistent with observations from single cell resolved FISH-nanoSIMS analyses (13).

Recently, the limitation of direct electron transfer to support metabolic activity of cells at large distances from their electron acceptor was demonstrated quantitatively in biofilms of *Geobacter sulfurreducens* (22). These results suggest that even in a model system known for its propensity for extracellular electron transfer, the extent to which conductive biomolecules can support optimal cell growth away from the source of electron donors is limited. The distances over which this metabolic limitation was observed in *G. sulfurreducens* were not previously observed in the McGlynn et al. (2015) study due to the limited size of AOM consortia analyzed, as well as the physical mixing of ANME and SRB cells to varying degrees which decrease the distance between the syntrophic partners (14). To better understand the mechanism of metabolic coupling between syntrophic partners in AOM consortia in light of these previous results, we measured and analyzed the metabolic activity of individual cells in exceptionally large and segregated AOM aggregates (radius ~20  $\mu\text{m}$ ) using FISH-nanoSIMS. Measurements of  $^{15}\text{NH}_4^+$  incorporation as a proxy for cellular anabolic activity were then used to validate a reactive transport model across AOM aggregates of differing size. The results of these simulations were consistent with our empirical observations, forming a basis to explore the types of syntrophic mechanisms used in AOM and the factors that may ultimately limit aggregate size. We also investigate the potential for environmentally-sourced electron donors used by the SRB in the partial decoupling of archaeal methanotrophy and bacterial sulfate-reduction.

## Materials and Methods

### **Experimental data**

#### *Sample collection*

Methane seep sediments covered with white bacterial mats were collected from Jaco Scar off of Costa Rica at 1811m water depth, (Lat. 9.1163, Long. -84.8372). Samples were collected by push core (PC6) during dive number AD4912 on May 27, 2017 by DSV Alvin launched from R/V Atlantis on research cruise AT37-13. The sediment core was processed shipboard into depth horizons that were placed in separate Whirl-Pak bags, and stored under anoxic conditions in a large mylar bag filled with Ar. These sediments were stored at 4°C until they were returned to lab, mixed with N<sub>2</sub> sparged 0.2µm filtered seawater from above the sampling site, and incubated in 1L pyrex bottles with a secured butyl rubber stopper and provided with a 100% methane headspace (30 psi).

#### *Stable isotope probing incubation and sampling*

Stable isotope incubation experiments were conducted using slurried sediment from PC6 corresponding to the 3-6cm depth horizon. Sediment was mixed 1:3 with N<sub>2</sub> sparged, 0.2µm filtered seawater from above the sampling site (28mM sulfate), and amended with 1mM NH<sub>4</sub>Cl with 99% <sup>15</sup>N abundance supplied from Cambridge Isotope Laboratories, Inc and incubated at 4°C. Headspace composition was 100% methane at 30psi. After 7 days, subsamples were collected for analysis, by first shaking the incubation bottle to resuspend the sediment slurry and then collecting an aliquot using an N<sub>2</sub> flushed needle and syringe. 1mL of sediment was chemically fixed by mixing with 1mL of 4% paraformaldehyde in 3×PBS and incubated for one hour at room temperature. Sediment containing AOM aggregates were washed three times with 3×PBS and finally resuspended in 50:50 PBS:EtOH and stored at -20°C.

### *Resin imbedding and FISH staining*

50 $\mu$ L of fixed sediment in 50:50 PBS:EtOH was mixed with 750 $\mu$ L PBS in a 2mL microcentrifuge tube and sonicated on ice with microtip sonication probe (Branson), 3x for ten seconds at setting 3. Aggregates were separated from sediment particles by underlaying the sonicated liquid with 1mL of Percoll and spinning at max speed for 30 minutes in a tabletop microcentrifuge at 4°C. The top aqueous layer containing concentrated aggregates were removed and pelleted by spinning at 10,000g at room temp for one minute. The pellet was gently removed and immobilized in molten 3% noble agar in PBS. Once solidified agar was trimmed to a small cube around the pellet and imbedded in glycol methacrylate (Technovit 8100) resin following the manufacturer's protocol. Semi-thin section (1-2 $\mu$ m thick) were cut using a microtome and deposited on water droplets on polylysine coated slides with Teflon-lined wells (Tekdon, Inc). FISH hybridization on thin sections was conducted as described previously (14). ANME-2b specific probe ANME-2b-729 with a dual 3'/5' Cy3 label and a universal bacterial probe EUB338mix (EUB338, -II, and -III) labeled with FITC were used at 35% FA concentration (supplied by Integrated DNA Technologies). Sections were counterstained with DAPI (5  $\mu$ g/mL) in CitiFluor mounting media and fluorescently imaged with a fluorescent microscope (Elyra 7, Zeiss) at 100x magnification (Plan-APOCHROMAT 100x objective).

### *Nanoscale secondary ion mass spectrometry (nanoSIMS)*

Sections were rinsed with DI water to remove DAPI and mounting media then glass slides were scored with a diamond scribe, broken and filed to fit into the nanoSIMS sample holder. Sections and slide fragments were sputter coated with 40nm of gold (Cressington). Areas containing aggregates of interest were pre-sputtered using a primary cesium ion beam at 90pA (D1=1) until  $^{14}\text{N}^{12}\text{C}^-$  ion counts stabilized (~5 minutes). NanoSIMS images were acquired in

10 $\mu$ m x 10 $\mu$ m rasters with 128x128 pixels with 0.3pA (D1 = 3, ES = 3) Cs<sup>+</sup> ion beam with 12ms/pixel dwell time. Between 20 to 30 10  $\mu$ m x 10 $\mu$ m acquisitions were tiled across the aggregate with approximately 2 $\mu$ m overlap, and the data was manually stitched together post analysis to create final data products. In addition to the new FISH-nanoSIMS data generated for this study, we also incorporated select nanoSIMS data as a point of comparison from published studies with similar experimental designs(14, 23). Regions of interest (ROIs) consisting of individual archaeal and bacterial cells within a consortium were identified and segmented by hand using the nanoSIMS <sup>14</sup>N<sup>12</sup>C<sup>-</sup> ion images. Phylogenetic identities for each cell were assigned based on comparison to the corresponding FISH image. Distances between cells were calculated based on the centroid of each segmented cell in MATLAB.

#### *Cell-specific activity calculation*

Growth rates were calculated from nanoSIMS data by (24)

$$\mu = \frac{-\ln\left(1 - \frac{F_{final} - F_{nat}}{F_{label} - F_{nat}}\right)}{T_{incub}} \quad \text{Eq. (3.1)}$$

where  $\mu$  is the growth rate (encompassing both cell maintenance and generation of new cells),  $T_{incub}$  is the length of the incubation (7 days),  $F_{label}$  is the labeling strength of the nitrogen

source provided,  $\frac{{}^{15}\text{NH}_4^+}{{}^{14}\text{NH}_4^+ + {}^{15}\text{NH}_4^+}$ ,  $F_{final}$  is the nanoSIMS measurement, and  $F_{nat} = 0.0036$  is the

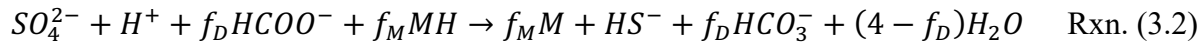
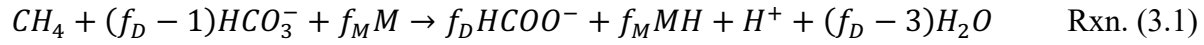
natural <sup>15</sup>N abundance. The cell-specific metabolic rates (in mol CH<sub>4</sub> cell<sup>-1</sup> d<sup>-1</sup>) were calculated as

$$R_{obs} = \mu \cdot \rho \cdot B_{cell} / Y_{CH_4} \quad \text{Eq. (3.2)}$$

where  $\rho$  is the g cell dry weight per m<sup>3</sup>,  $B_{cell}$  is the cell density in m<sup>3</sup> per cell,  $Y_{CH_4}$  is the growth yield in g cell dry weight per mol CH<sub>4</sub> oxidized.

#### **Modeling approach**

Electron transfer between archaea and bacteria was implemented as a mixed DIET-MIET mechanism where electrons from the oxidation of methane are captured by either redox-active molecules ( $M$ ) that conductively connect archaeal and bacterial partners, or by formate ( $\text{HCOO}^-$ ), which can exchange between the syntrophic partners by diffusion. Although we chose formate as the intermediate between ANME and SRB in this study, other small molecules could also be considered as the putative intermediates for AOM (13, 15). This highly simplified description minimizes model complexity, reflecting the limited knowledge on the actual mechanism. These metabolic pathways are captured by



where  $f_M$  and  $f_D$  represent the fraction of electron conduction via MIET and DIET, respectively ( $f_M \in [0,8]$  and  $f_D = (8-f_M)/2 \in [0,4]$ , with  $f_M = 8$  and  $f_D = 0$  in the absence of MIET).

#### Rate expression

Cellular metabolic rate and response can be captured by

$$R^X = F_k^X F_T^X \quad (25, 26) \quad \text{Eq. (3.3)}$$

where  $F_k^X$  represents the reaction kinetics of reaction  $X$  and is the product of a cell-specific rate constant  $k$ , the cell density  $B_{cell}$ , and the dependence on substrate availability (13):

$$F_k^{R1} = k_A B_A \frac{\text{CH}_4}{K_m^{\text{CH}_4} + \text{CH}_4} M \quad \text{Eq. (3.4)}$$

$$F_k^{R2} = k_B B_B \frac{\text{SO}_4}{K_m^{\text{SO}_4} + \text{SO}_4} \text{MH} \quad \text{Eq. (3.5)}$$

The thermodynamic factor ( $0 \leq F_T^X \leq 1$ ) reflects that there must be sufficient free energy available from the reactions to fuel ATP synthesis and cell maintenance and is given by (13)

$$F_T^X = \max \left( 0, 1 - \exp \left( -nF \frac{\eta_{net}^X - \eta_{ATP}}{\chi R_{gas} T} \right) \right) \quad \text{Eq. (3.6)}$$

where  $n$  is the number of electrons per reaction,  $\chi$ , the number of ATP synthesized per reaction, is set to 1 (15),  $R_{gas}$  is the universal gas constant ( $8.314 \text{ J K}^{-1} \text{ mol}^{-1}$ ) and  $T$  is temperature ( $277.15 \text{ K}$ ),  $\eta_{ATP}$  represents the potential related to the energy required to synthesize ATP by  $\eta_{ATP} = -\Delta G_{ATP}/nF$  where  $F$  is the Faraday constant and  $\Delta G_{ATP} = -10 \text{ kJ mol}^{-1}$  (25, 26). The net available potential is given by

$$\eta_{net}^X = \eta_{rxn,X} - \eta_{act} - \eta_{om} \quad \text{Eq. (3.7)}$$

where  $\eta_{rxn,X}$  is calculated from the Gibbs free energy  $\Delta G_X$  of reaction for archaea ( $X=R(1)$ ) and bacteria ( $X=R(2)$ ),  $\eta_{act}$  and  $\eta_{om}$  are the voltage losses associated with activation and ohmic resistance, respectively.

Activation loss describes the energetic loss occurring during the electron transfer between cell and conductive pili/matrix. The voltage drops associated with the electron conduction between  $M$  and  $MH$  can be described by the Butler-Volmer equation assuming a one-step, single-electron transfer process (27). The activation loss  $\eta_{act}$  is related to the current density:

$$\frac{I}{N_{nw}} = FA_{act}k_{act}M_{tot} \left( \exp\left(\frac{(1-\beta)F}{R_{gas}T}\eta_{act}\right) - \exp\left(\frac{-\beta F}{R_{gas}T}\eta_{act}\right) \right) \quad \text{Eq. (3.8)}$$

where  $I$  is the current produced by methane oxidation ( $I = f_M R_I N_{ANME} F$ , where  $R_I$  is the methane oxidation rate in  $\text{fmol cell}^{-1} \text{ d}^{-1}$ ,  $N_{ANME}$  is the number of archaeal cells and  $F$  is the Faraday constant),  $A_{act}$  is the redox active surface area in  $\text{m}^2$  per cell (27),  $k_{act}$  is the activation loss associated constant in  $\text{m s}^{-1}$ ,  $\beta$  is the charge transfer coefficient,  $M_{tot}$  is the concentration of electron carrying molecules ( $M_{tot} = [M] + [MH]$ ).  $N_{nw}$  is the total conductive connections within an AOM consortium and can be described as  $N_{nw} = M_{tot} V_{agg} k_{nw}$ , where  $V_{agg}$  is the volume of consortium, and  $k_{nw}$  is the constant associated with conductive network. Conductive network density can be described as  $N_{nw,cell} = N_{nw}/N_{ANME}$ .

The ohmic loss results from electronic resistance to the flow of electrons through the conductive pili/matrix. The corresponding voltage drop is proportional to current density and is given by (27):

$$\eta_{om} = \frac{R_{nw}I}{N_{nw}} = \frac{d}{\sigma A_{nw}} \frac{f_M R_1 N_{ANMEF}}{M_{tot} V_{agg} k_{nw}} \quad \text{Eq. (3.9)}$$

Here,  $R_{nw}$  is the electrical resistance ( $\Omega$ ) which can be further described as  $d/(\sigma A_{nw})$ , where  $\sigma$  is the electrical conductivity of pilus ( $S\ m^{-1}$ ),  $d$  is the distance from archaeal-bacterial interface,  $A_{nw}$  is the cross-section area of a single pilus.

Several of the above parameters are poorly constrained, including the characteristics and concentration of redox active molecules ( $M_{tot}$ ), the conductive network density ( $N_{nw,cell}$ ), its conductivity ( $\sigma$ ) and the various constants ( $k_A$ ,  $k_B$ ,  $k_D$  and  $k_{act}$ ). Other physiological parameters, such as  $A_{act}$ , are highly tunable by the cell (27). Thus, it should be noted that the same modeled activity levels and patterns can be achieved for different combinations of these parameters. For instance, decreasing  $N_{nw,cell}$  10-fold can be counterbalanced by increasing conductivity  $\sigma$  and cell redox active factor  $k_{act} \times A_{act}$  by a factor of 10, as is evident from the expressions for activation loss (Eq. 3.10) and ohmic resistance (Eq. 3.11). To deal with these compensating effects we identified the key combined parameters of the system and varied those in our simulations. The above equations are sensitive to changes in the combined independent parameters the maximum metabolic activities  $k_A B_A$ , and  $k_B B_B$ , the maximum cell-specific current  $F A_{act} k_{act} M_{tot}$ , the resistance  $d/(\sigma A_{nw})$ , the effective concentrations  $\frac{CH_4}{K_m^{CH_4}}$ , and  $\frac{SO_4}{K_m^{SO_4}}$  where  $CH_4$  and  $SO_4^{2-}$  should be interpreted as the background environmental concentrations, and the activation parameters  $\frac{\beta \eta_{act}}{R_{gas} T}$  and  $n \frac{\eta_{net}^X - \eta_{ATP}}{\chi R_{gas} T}$ .

### Implementation

A spherical AOM aggregate was implemented at the center of a domain that represents the surrounding environment with a radius of  $2.5\times$  that of the aggregate ( $r_{agg}$ ). The spatial distribution of archaea and bacteria in the aggregate (Fig. 3.1A) was set to reflect the distribution patterns observed in the nanoSIMS analysis (Fig. 3.1B). A specific cell ratio of 1:1 was set to archaea and bacteria, with same radii of  $0.4\ \mu\text{m}$  for both archaeal and bacterial cells (3, 28, 29). It is acknowledged that different AOM aggregates may have different cell radii and biovolumes (30), which would impact the estimates of cell-specific rates as which the model results are reported below.

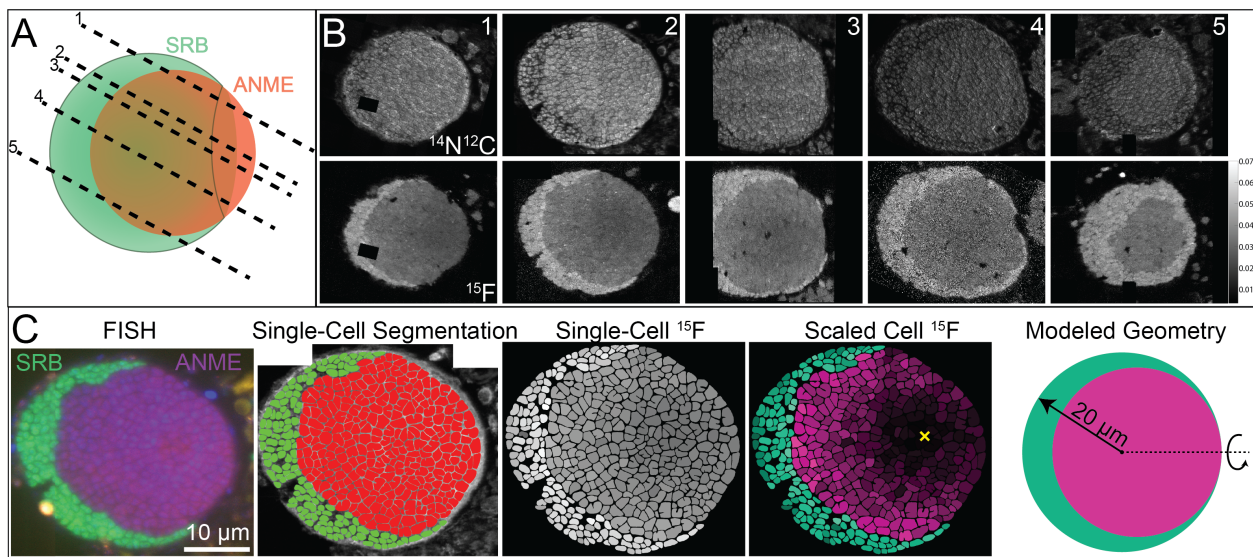


Fig. 3.1. Overview of AOM consortia structure, nanoSIMS data acquisition, analysis, and model geometry. A) Cartoon of AOM consortia structure based on FISH-nanoSIMS observations of five parallel sections corresponding to dashed lines. B) Five parallel sections highlighted in A analyzed by nanoSIMS. Top row: raw  $^{14}\text{N}^{12}\text{C}^-$  secondary ion counts illustrating the position of cells. Bottom row: fractional abundance of  $^{15}\text{N}$  calculated as  $^{15}\text{N}^{12}\text{C}^- / (^{15}\text{N}^{12}\text{C}^- + ^{14}\text{N}^{12}\text{C}^-)$ , all scaled to same intensity. Note SRB assimilate significantly more  $^{15}\text{N}$  on average than their ANME counterparts as has been previously shown (11). C) Illustration of nanoSIMS data extraction and

modelled geometry. From left to right: FISH image indicating phylogenetic identity of cells (green general bacterial probe [Eub338mix], red ANME-2b specific probe [ANME-2b-729], blue DNA stain [DAPI]); segmentation image showing SRB and ANME cells manually segmented based on observation of FISH and nanoSIMS data; individual segmented cells shaded by their total  $^{15}\text{N}$  fractional abundance; SRB and ANME cells scaled by minimum and maximum values within the population; illustration of modelled aggregate geometry, dashed line represents axis of rotation. Yellow X marks approximate minimum of ANME cell activity. Note: additional sections were visually inspected to help verify aggregate structure, only those analyzed by nanoSIMS analysis are shown.

The concentration fields of  $\text{CH}_4$ ,  $\text{HCO}_3^-$ ,  $\text{CO}_2(\text{aq})$ ,  $\text{CO}_3^{2-}$ ,  $\text{SO}_4^{2-}$ ,  $\text{HS}^-$ ,  $\text{H}^+$ ,  $\text{OH}^-$ ,  $\text{HCOO}^-$ ,  $\text{HCOOH}$  and  $\text{B}(\text{OH})_4^-$  were simulated subject to diffusive transport and reaction, with aqueous diffusion coefficients listed in Table 3.1. The concentrations at the outer domain boundary were set to fixed concentrations reflecting environmental conditions (Table 3.1), which were also used as initial conditions. The distribution of  $MH$  depends on metabolic rate and electron hopping on conductive pili or matrix. This can be expressed as (31, 32)

$$\frac{\partial MH}{\partial t} = \phi f_M R^X + \nabla \cdot (\mathcal{D}_M \nabla [MH]) + \nabla \cdot J_{EF} \quad \text{Eq. (3.10)}$$

where  $D_M = k_D M_{tot} \delta$  is an effective diffusion coefficient (31, 32) that depends on electron conduction constant ( $k_D$ ), the distance between two redox-active molecules ( $\delta$ ) and the concentration of electron carrying molecules, and  $\nabla \cdot J_{EF}$  reflects the electron transfer rate driven by a local electric field adapted from (31, 32). This flux is given by  $J_{EF} = k_{EF} [M][MH] (e^{\frac{\beta FE \delta}{R_{gas} T}} - e^{-\frac{(1-\beta) FE \delta}{R_{gas} T}})$ , where  $k_{EF}$  is the electric field associated rate constant and  $E$  is the electric field strength (31, 32).

Acid-base reactions govern the speciation of cell surface-associated immobile carboxy (R-COOH) and amino groups (R-NH<sub>2</sub>). We considered the dissolved inorganic carbon (DIC) and borate system (33) to quantitatively calculate the carbonate system and dynamically simulate acid-base reactions, using the kinetic implementation described in (33, 34), with a total boron (T<sub>B</sub>) concentration of 0.427 mM and total DIC (T<sub>DIC</sub>) of 2.36 mM. Archaeal and bacterial cell density and cell size were held constant in all models, with cell numbers varying with AOM consortia radii. The model was implemented in COMSOL Multiphysics 5.4 (COMSOL Inc., Burlington, MA, USA) and simulations were run to steady state.

Baseline simulations presented below use the parameterization shown in Table 3.1. It was constrained by literature values where available, and chosen to yield rates and rate distributions consistent with the observations.

Table 3.1. Summary of parameters used in model implementation

Symbol	Value	Units	Description	Baseline value	Reference and note
<b><i>Kinetics and thermodynamics</i></b>					
$k_A$	10 <sup>-13</sup> -10 <sup>-17</sup>	m <sup>3</sup> cell <sup>-1</sup> d <sup>-1</sup>	Archaea rate constants	4×10 <sup>-16</sup>	Estimated
$k_B$	10 <sup>-13</sup> -10 <sup>-17</sup>	m <sup>3</sup> cell <sup>-1</sup> d <sup>-1</sup>	Bacteria rate constants	4×10 <sup>-16</sup>	
$K_m^{CH_4}$	1-20	mM	Half saturation constant for methane	7	(35)
$K_m^{SO_4}$	1-10	mM	Half saturation constant for sulfate	5	(36)
$f_D$	0-4	-	Fraction of electron conduction via MIET	0.4	Estimated
$f_M$	0-8	-	Fraction of electron conduction via DIET	7.4	Estimated
$\chi$	1	-	Number of ATP synthesized per reaction	1	(15)
$\eta_{ATP}$	0.013	V	Potential related to the energy required to synthesize ATP	0.013	Calculated
$\Delta G_{ATP}$	-10	kJ mol <sup>-1</sup>	Energy required to synthesize ATP	-10	(25, 26)
$R_{gas}$	8.314	J K <sup>-1</sup> mol <sup>-1</sup>	Gas constant	8.314	
$F$	96485.3	C mol <sup>-1</sup>	Faraday constant	96485.3	
$T$	277.15	K	Incubation temperature	277.15	Measured
$n$	8	-	Electrons transferred per reaction	8	Calculated
$k_H^o$	0.0014	mol kg <sup>-1</sup> bar <sup>-1</sup>	Henry's law constant for methane solubility in water at 298.15 K	0.0014	(37)
$d(\ln(k_H))/d(1/T)$	1600	K	Henry's law temperature dependence constant for methane	1600	
$k_H(T)$	0.0021	mol kg <sup>-1</sup> bar <sup>-1</sup>	Henry's law constant for methane solubility in water at T = 277.15 K	0.0021	Calculated

$\rho_{SW}$	$1.03 \times 10^3$	$\text{kg m}^{-3}$	Density of seawater	$1.03 \times 10^3$	(38)
<b>Geometry</b>					
$r_A$	0.4	$\mu\text{m}$	Radius of archaea cell	0.4	(3, 28, 29)
$r_B$	0.4	$\mu\text{m}$	Radius of bacteria cell	0.4	
$r_{agg}$	5-200	$\mu\text{m}$	Radius of AOM aggregate	20	Imposed
$r_{env}$	12.5-500	$\mu\text{m}$	Radius of environment surrounding aggregate	50	Imposed
$N_{ANME}$	varied	cells	Number of archaeal cells	$2.68 \times 10^6$	Calculated
$V_{agg}$	varied	$\text{m}^3$	Volume of aggregate	$3.35 \times 10^{-14}$	Calculated
<b>Cell-specific activity</b>					
$\mu$	varied	$\text{d}^{-1}$	Cell growth rate		Calculated from
$\rho$	$4.8 \times 10^5$	$\text{g cell dry weight per m}^3$	Biomass density of cells	$4.8 \times 10^5$	(11)
$B_{cell}$	$2.68 \times 10^{-19}$	$\text{m}^3$ per cell	Cell density	$2.68 \times 10^{-19}$	Calculated
$Y_{CH_4}$	0.2-0.72	$\text{g cell dry weight per mol CH}_4$ oxidized	Growth yield for archaeal cells	0.65	(39)
$Y_{SO_4}$	0.1-1	$\text{g cell dry weight per mol SO}_4^{2-}$ reduced	Growth yield for bacterial cells	0.55	Imposed
$T_{incub}$	7	d	Length of the incubation	7	Measured
$F_{label}$	1	-	Labeling strength of $^{15}\text{N}$	1	Measured
$F_{nat}$	0.0036	-	Natural abundance of $^{15}\text{N}$	0.0036	(24)
$F_{final}$	varied	-	Single-cell nanoSIMS measurement	-	Measured
<b>Electron conduction</b>					
$M_{tot}$	0.01-100	mM	Concentration of redox molecules	10	Estimated
$k_D$	$10^{-5}$ - $10^5$	$\text{m}^4 \text{mol s}^{-1}$	Rate constant of electron transport on conductive pili or matrix	$10^5$	Estimated
$k_{EF}$	$10^{-9}$ - $10^5$	$\text{m}^4 \text{mol s}^{-1}$	Electric field rate constant	$10^{-5}$	Estimated
$k_{act}$	$2.5 \times 10^{-10}$ - $10^{-7}$	$\text{m s}^{-1}$	Activation loss rate constant	$2 \times 10^{-9}$	Estimated
$k_{nw}$	$10^{17}$ - $10^{20}$	$\text{mol}^{-1}$	Constant associated with conductive network	$1.2 \times 10^{19}$	Estimated
$\delta$	0.7	nm	Redox molecules spacing width	0.7	(40)
$\sigma$	$10^{-4}$ - $10^{-1}$	$\text{S m}^{-1}$	Conductivity of conductive pili or matrix	$10^{-2}$	(10, 17, 41-47)
$\beta$	0.5	-	Charge transfer coefficient	0.5	(27)
$N_{nw}$	$10^5$ - $10^8$	-	Total conductive connections in an aggregate	$4 \times 10^6$	Estimated
$N_{nw,cell}$	1-1000	-	Number of connections per cell	64	Estimated
$d_{nw}$	4	nm	Diameter of a single pilus	4	(17)
$A_{nw}$	$1.26 \times 10^{-17}$	$\text{m}^2$	Cross-section area of a single pilus	$1.26 \times 10^{-17}$	Calculated
$A_{act}$	$10^{-14}$ - $10^{-12}$	$\text{m}^2$	Redox active surface area per cell, 10% of the cell surface area	$2 \times 10^{-13}$	Calculated (27)

Aqueous diffusion coefficient:  $D_{\text{CO}_2} = 1.91 \times 10^{-9} \text{ m}^2 \text{ s}^{-1}$ ,  $D_{\text{CO}_3} = 1.19 \times 10^{-9} \text{ m}^2 \text{ s}^{-1}$ ,  $D_{\text{H}^+} = 6 \times 10^{-9} \text{ m}^2 \text{ s}^{-1}$ ,  $D_{\text{OH}^-} = 5.27 \times 10^{-9} \text{ m}^2 \text{ s}^{-1}$ ,  $D_{\text{B(OH)}_4} = 9.56 \times 10^{-10} \text{ m}^2 \text{ s}^{-1}$ ,  $D_{\text{HCOO}^-} = 4.9 \times 10^{-10} \text{ m}^2 \text{ s}^{-1}$ ,  $D_{\text{HCOOH}} = 1.516 \times 10^{-9} \text{ m}^2 \text{ s}^{-1}$ ,  $D_{\text{HS}^-} = 1.19 \times 10^{-9} \text{ m}^2 \text{ s}^{-1}$ ,  $D_{\text{CH}_4} = 9.95 \times 10^{-9} \text{ m}^2 \text{ s}^{-1}$ ,  $D_{\text{SO}_4} = 6.37 \times 10^{-10} \text{ m}^2 \text{ s}^{-1}$ . Fixed concentration boundary conditions are imposed for all chemical species at the outer domain boundary except for MH, for which no flux condition is imposed at the aggregate surface. Boundary conditions are set to: 0.1 mM  $\text{HS}^-$ , 2.3 mM  $\text{HCO}_3^-$ , pH = 8.2, 28 mM  $\text{SO}_4^{2-}$ , 4.5 mM  $\text{CH}_4$ , 10  $\mu\text{M}$   $\text{HCOO}^-$ . Henry's law constant for methane solubility in water  $k_{\text{H}}(T)$  is determined to be  $0.0021 (\text{mol kg}^{-1} \text{ bar}^{-1})$  using  $k_{\text{H}}(T) = k_{\text{H}}^{\circ} \exp(d(\ln(k_{\text{H}}))/d(1/T) ((1/T) - 1/(298.15 \text{ K})))$ , where  $k_{\text{H}}^{\circ}$  is Henry's law constant for solubility in water at

298.15 K ( $\text{mol kg}^{-1} \text{ bar}^{-1}$ ) and  $d(\ln(k_H))/d(1/T)$  is the temperature dependence constant (K) (37). The concentration of  $\text{CH}_4$  in incubation medium then can be derived using  $[\text{CH}_4] = p_{\text{CH}_4} k_H(T) \rho_{\text{SW}}$ , where  $p_{\text{CH}_4}$  is the  $\text{CH}_4$  pressure (bar),  $\rho_{\text{SW}}$  is the density of incubation medium.

## Statistical analysis

Data are represented as mean  $\pm$  standard error. The statistical difference between the observed and simulated cell-specific activity patterns was assessed by one-way analysis of covariance (ANCOVA) of the slopes of the regression of cell-specific activity vs. distance from archaea-bacteria interface. Values of  $p < 0.05$  were considered statistically significant, whereas values of  $p > 0.05$  indicated no statistical significance for the slopes of the regression lines. The statistical analyses were performed using MATLAB 2018 (MathWorks, Natick, MA, USA).

## Results and Discussion

### *Large, segregated aggregates display significant spatial variation in cellular activity*

Previous experimental work measuring the activity of individual cells in syntrophic ANME-SRB aggregates demonstrated a lack of significant correlation between cellular activity and distance to syntrophic partner over short distances ( $\sim$  a few cell diameters; (11)). These observations were sufficient to rule out molecular diffusion as the major mechanism of electron transfer between the two partners, but were limited in their spatial extent due to relatively small aggregate size, as well as the complex three-dimensional structure of many AOM consortia that made it difficult to confidently assign distances to nearest partner that may lie above and below the plane when analyzing single two-dimensional sections. We have occasionally observed exceptionally large AOM consortia in nanoSIMS analyses where significant variations in activity appear to be related to distance from their nearest partner (for example Fig. B1). While these previous observations suggested that cellular activity might be correlated with distance to nearest syntrophic partner over large distances, it was not possible to determine a precise magnitude of the activity gradients without additional information about the three-dimensional aggregate structure.

To overcome these challenges, we cut and analyzed parallel sections through a large well segregated ANME-2/SRB consortia after  $^{15}\text{NH}_4^+$  stable isotope probing allowing us to roughly reconstruct the spatial distribution of both partners across the entire consortia (Fig. 3.1A-B). Two features of this  $>50\ \mu\text{m}$  AOM consortia made it ideal to study. First, the spatial organization of the syntrophic partnership is simple and well defined, with no incursions of bacteria into the ANME-dominated interior of the aggregate. Second, the bacteria form a crescent around the archaeal core, instead of a complete shell. Had the bacteria formed a complete shell there would be perfect correlation between ANME distance to nearest syntrophic partner, and distance to the surface of the aggregate, making these two potential controls on cellular activity difficult to disentangle. With a crescent geometry however, some ANME can be found at the surface of the consortia closest to the surrounding environment and at great distance from the nearest SRB, allowing us to distinguish between the effect of syntrophic distance and distance to environment which supplies the growth substrates  $\text{CH}_4$ ,  $\text{SO}_4^{2-}$  and the tracer  $^{15}\text{NH}_4^+$ . Since the minimum of ANME activity was observed to be near the aggregate surface, far from the SRB, we can conclude that distance to partner is more significant than substrate limitation due to distance from the aggregate surface (Fig. 3.1C).

#### *A unifying model across aggregate size*

Observations of  $^{15}\text{N}$  incorporation in single cells from a section cut approximately normal to the ANME-SRB interface revealed a decrease in the anabolic activity of both ANME and SRB with increasing distance to their nearest syntrophic partners (Fig. 3.2A). This effect was highly significant and explained large portions of the variability of cellular activity in the two populations, with a slope of  $-0.0238 \pm 0.0009\ \text{fmol cell}^{-1}\ \text{d}^{-1}\ \mu\text{m}^{-1}$  ( $R^2 = 0.69$ ) and  $-0.0594 \pm 0.0083\ \text{fmol cell}^{-1}\ \text{d}^{-1}\ \mu\text{m}^{-1}$  ( $R^2 = 0.27$ ) for archaea and bacteria, respectively (Fig. 3.2A). Our base model in which 92.5%

of the electrons produced in the oxidation of  $\text{CH}_4$  are transferred to the bacteria via DIET and 7.5% of the electrons are transferred via MIET provides the best fit the activities observed in aggregates across a wide range of aggregate sizes (Fig. 3.2). Cell-specific activities decrease slightly with increasing distance from the nearest syntrophic partner in a simulated 20  $\mu\text{m}$  radius aggregate, with slopes of  $-0.0267 \pm 0.0004 \text{ fmol cell}^{-1} \text{ d}^{-1} \mu\text{m}^{-1}$  ( $R^2 = 0.9954$ ) and  $-0.0653 \pm 0.0017 \text{ fmol cell}^{-1} \text{ d}^{-1} \mu\text{m}^{-1}$  ( $R^2 = 0.9936$ ), for archaea and bacteria activity, respectively (Fig. 3.2A). ANCOVA revealed that the slopes and intercepts of the regressions of model results and of observational data do not differ significantly, with  $p = 0.30$  and  $0.71$  for archaea and bacteria, respectively. Simulations for a small aggregate with the identical model parameterization retained good agreement between observed and modeled metabolic activity pattern (Fig. 3.2B), with  $p = 0.96$  for both archaea and bacteria comparing to observations.

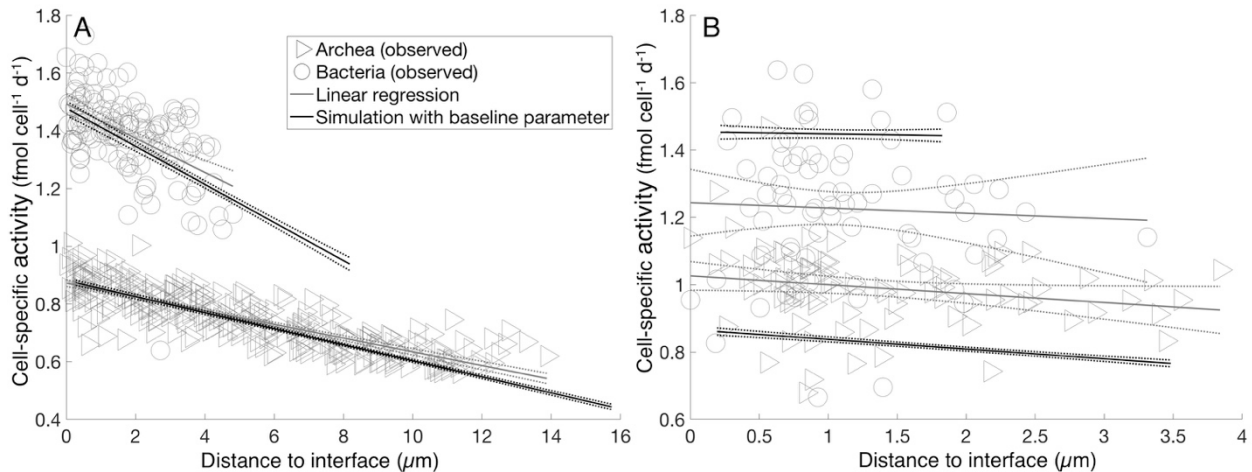


Fig. 3.2. Measured and modeled cell-specific activity in aggregates with a radius of 20  $\mu\text{m}$  (A, this study) and 5  $\mu\text{m}$  (B, (11)), plotted against their distance from the closest syntrophic partner ('interface'). Data were fitted using linear regression with 95% confidence interval. Note that the cell specific rate constants were not re-tuned to match the activities in the small aggregate.

*How far apart can ANME and SRB cells be and remain active in AOM consortia?*

The metabolic activity of syntrophic AOM aggregates can be limited by the availability of electron donors and acceptors, as reflected in the overall reactions (Rxn 3.1&3.2). Here we investigate the internal and external constraints that potentially limit the metabolic activity within the context of the observed aggregate arrangement. All archaeal and bacterial cells remained active over a wide range of aggregate sizes in our model simulations (Fig. 3), however the simulated activity of individual cells did decrease with increasing distance from their syntrophic partners. This effect is observed in model simulations for both archaea (Fig. 3A) and bacteria (Fig. 3B) and is slightly steeper for the latter. The shape and magnitude of the activity decrease curve was nearly identical between aggregates of different sizes, highly consistent with what we observed with anode-respiring *G. sulfurreducens* biofilms of different thicknesses under high and low anode potentials (22). We included in our model simulations segregated aggregates with radii up to 100  $\mu\text{m}$  (same spatial arrangement as shown in Fig. 1C). Cellular activities in strongly segregated large aggregates experienced a >70% drop in activity as separation distances increase to 15  $\mu\text{m}$  and 30  $\mu\text{m}$  for bacteria and archaea, respectively (Fig. 3).

Simulations including molecular diffusion (MIET) of potential syntrophic intermediates such as formate in addition to DIET revealed that metabolic activity could become severely limited with large separation distances between partners (aggregate size  $r_{agg} = 60 \mu\text{m}$ , see Fig. A9), even though formate-based MIET only accounted for 7.5% of the electron transfer from archaea to bacteria. It is noted that even at this size extreme, the mass transport of substrates and metabolites including  $\text{CH}_4$ ,  $\text{SO}_4^{2-}$ ,  $\text{HS}^-$ ,  $\text{H}^+$ ,  $\text{HCO}_3^-$  was not limiting due to the relatively high concentrations of methane and sulfate at the boundary, varying by a factor less than 1% except for  $\text{HS}^-$ , which varies from 0.1 across the aggregate (data not shown). These results suggest that this distance dependent decrease in cellular activity may be a critical factor determining the size of mono-species clusters

within AOM consortia. Larger aggregates thus would be expected to have a more interspersed distribution of archaeal and bacterial partners in order to maintain high levels of single cell activity, or once a segregated aggregate size limit is reached, larger consortia then separate into two or transform into a larger clustered morphology as bacteria grow into the archaeal core (39).

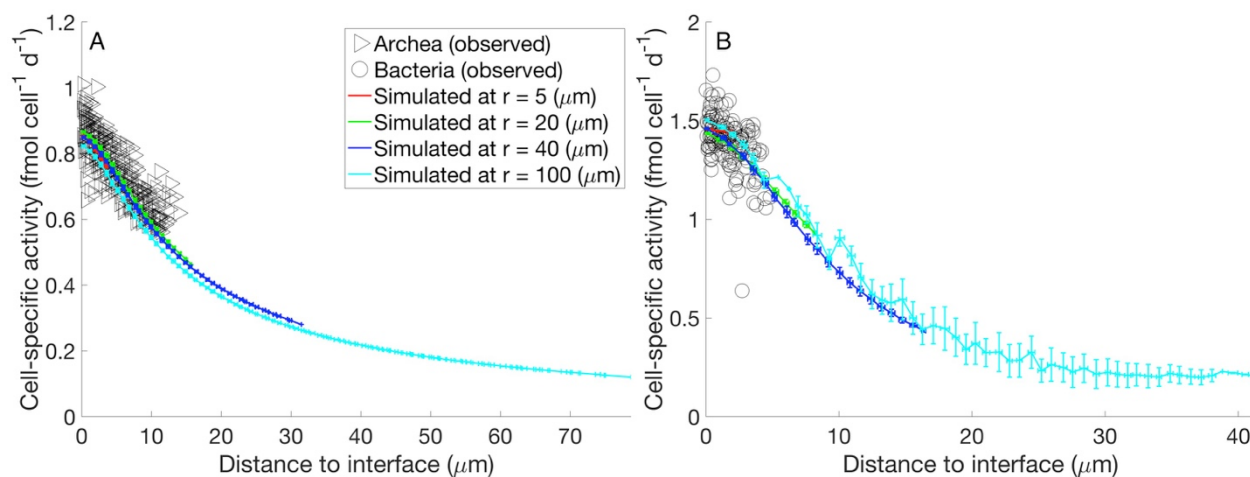


Fig. 3.3 Cell-specific activity vs. distance from syntrophic partner for archaea (A) and bacteria (B). For a wide range of aggregate sizes ( $r_{agg} = 5, 20, 40$  and  $100 \mu\text{m}$ ), the simulated activity distribution is similar and depends on the distance from the interface between archaea and bacteria. At a distance of approx.  $30 \mu\text{m}$ , the activity of the bacteria approaches 0 (B).

#### *What controls the spatial distribution of activity?*

The spatial variation of the cell metabolic activity was found to depend on the usable electric potential ( $\eta_{net}$ ), that is set by the available energy from the reaction (at approximately  $0.0357 \text{ V}$  for archaea and bacteria), minus the effect of losses. The activation loss was the main limiting factor for loss at distances approximately  $\leq 8 \mu\text{m}$  to the partner interface, while ohmic losses were important at larger distances (Fig. 3.4). This pattern was observed for both archaeal and bacterial cells. Activation loss was maximal at the archaea-bacteria interface, with a value of  $0.013 \text{ V}$  and decreased away from the archaea-bacteria interface. In contrast, ohmic resistance loss increased from 0 to  $\sim 0.02 \text{ V}$  as the distance from archaea-bacteria interface increased, leading to a

maximum total potential loss at a value of  $\sim 0.023$  V for archaea and bacteria. As the net available potential ( $\eta_{net}$ ) approaches the minimum potential required for ATP synthesis ( $\sim 0.013$  V; (25, 26)), metabolic rates decrease due to energetic limitations, as indicated by the thermodynamic factor  $F_T$  approaching 0 (Fig. 3.4).

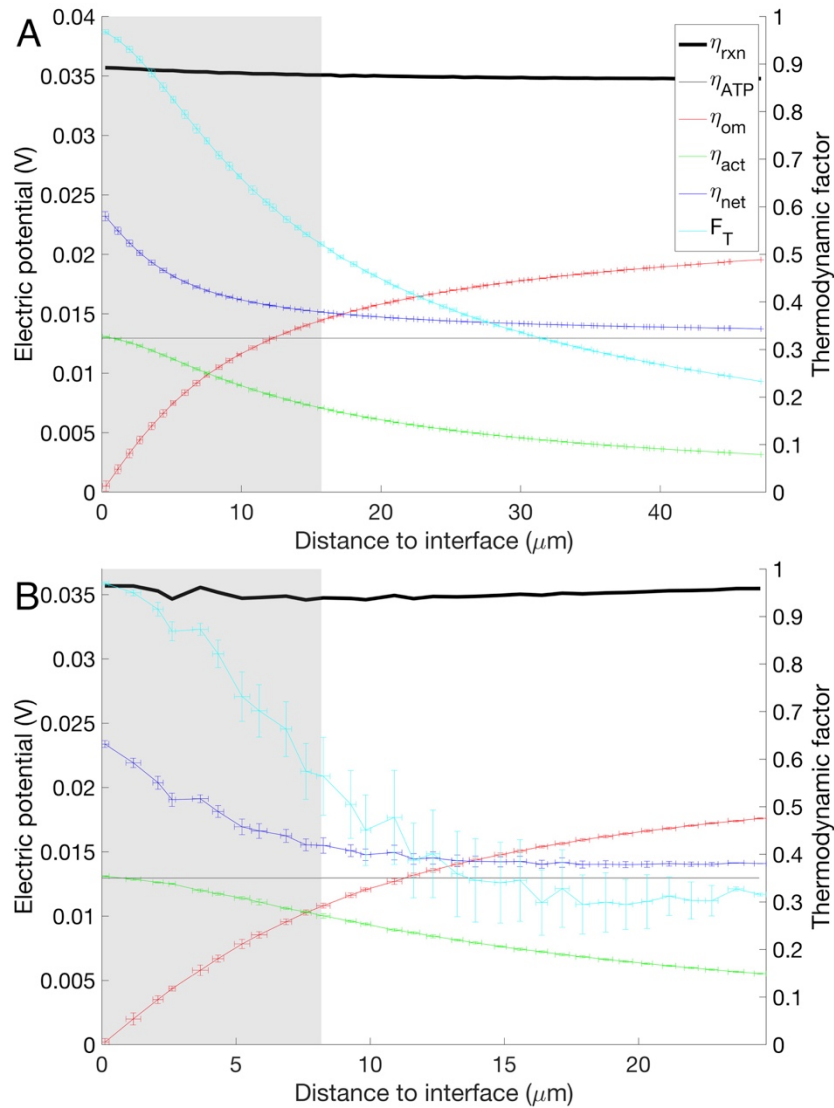


Fig. 3.4. Factors controlling cell activity as a function of the distance from the archaea-bacteria interface at aggregate radius of  $60 \mu\text{m}$  for archaea (A) and bacteria (B). The left axis reflects electric potential for activation loss ( $\eta_{act}$ ), ohmic resistance loss ( $\eta_{om}$ ), net available potential ( $\eta_{net}$ ), potential from reaction ( $\eta_{rxn}$ ), and minimum potential required for ATP synthesis ( $\eta_{ATP}$ ).

The right axis reflects thermodynamic factor  $F_T$ . The shaded areas highlight the range of distances encountered in the observed aggregate with a 20  $\mu\text{m}$  radius (Fig. 1).

Voltage losses depend on a number of factors, including the concentration of redox active molecules ( $M_{tot}$ ), conductive network density ( $N_{nw,cell}$ ), their conductivity ( $\sigma$ ), cell redox active factor ( $k_{act} \times A_{act}$ ) and cell rate constants ( $k_A, k_B$ ). Activation loss was strongly impacted by  $k_A, k_B, N_{nw,cell}$  and  $k_{act} \times A_{act}$ , less so by  $M_{tot}$  and  $\sigma$  (Fig. 3.5A). Increasing  $k_{act}, N_{nw,cell}, k_{act} \times A_{act}$  by a factor two or  $k_A, k_B$  by 1.5-fold reduced the activation loss by  $6.4 \pm 0.9$  mV,  $6.3 \pm 1.3$  mV,  $6.4 \pm 0.9$  mV and  $3.9 \pm 1.6$  mV, respectively, while increasing  $M_{tot}$  or  $\sigma$  by a factor of two led to an increase of activation loss by  $1.0 \pm 1.1$  mV and  $0.4 \pm 0.7$  mV, respectively.  $k_A, k_B$  and  $N_{nw,cell}$  showed similar effects on activation and ohmic resistance losses, but changes in  $k_{act} \times A_{act}, M_{tot}$  and  $\sigma$  had opposite impacts, with an increase by a factor two of  $k_{act} \times A_{act}, M_{tot}$  and  $\sigma$  leading to change in ohmic resistance losses by  $0.5 \pm 0.7$  mV,  $2.4 \pm 1.9$  mV and  $-1.6 \pm 1.1$  mV, respectively (Fig. 3.5B). In total,  $k_A, k_B, k_{act} \times A_{act}$  and  $N_{nw,cell}$  exhibited substantial impact on net available potential, whereas  $M_{tot}$  and  $\sigma$  showed moderate effects, in part due to the counteracting effect on  $\eta_{act}$  and  $\eta_{om}$  for  $M_{tot}$  and  $\sigma$  (Fig. 3.5A&B). It should be noted that these results are insensitive to changes in  $k_D$  and  $k_{EF}$  (Figs. S14&S15). In agreement with results reported previously (13), we observed no significant difference between simulations with electric field as the sole driving force and simulations with redox gradient as the driving force. Note that changes in these parameters not only affect the overall energetics for the AOM consortium, but they can also affect how cell activity varies with distance from a syntrophic partner, where changes in  $M_{tot}, \sigma$  and  $k_{act} \times A_{act}$  alter the shape of the activity-separation distance pattern, while  $k_A, k_B$  and  $N_{nw,cell}$  mostly affect the slope of the linear relationship, but not the shape (Fig. B16).

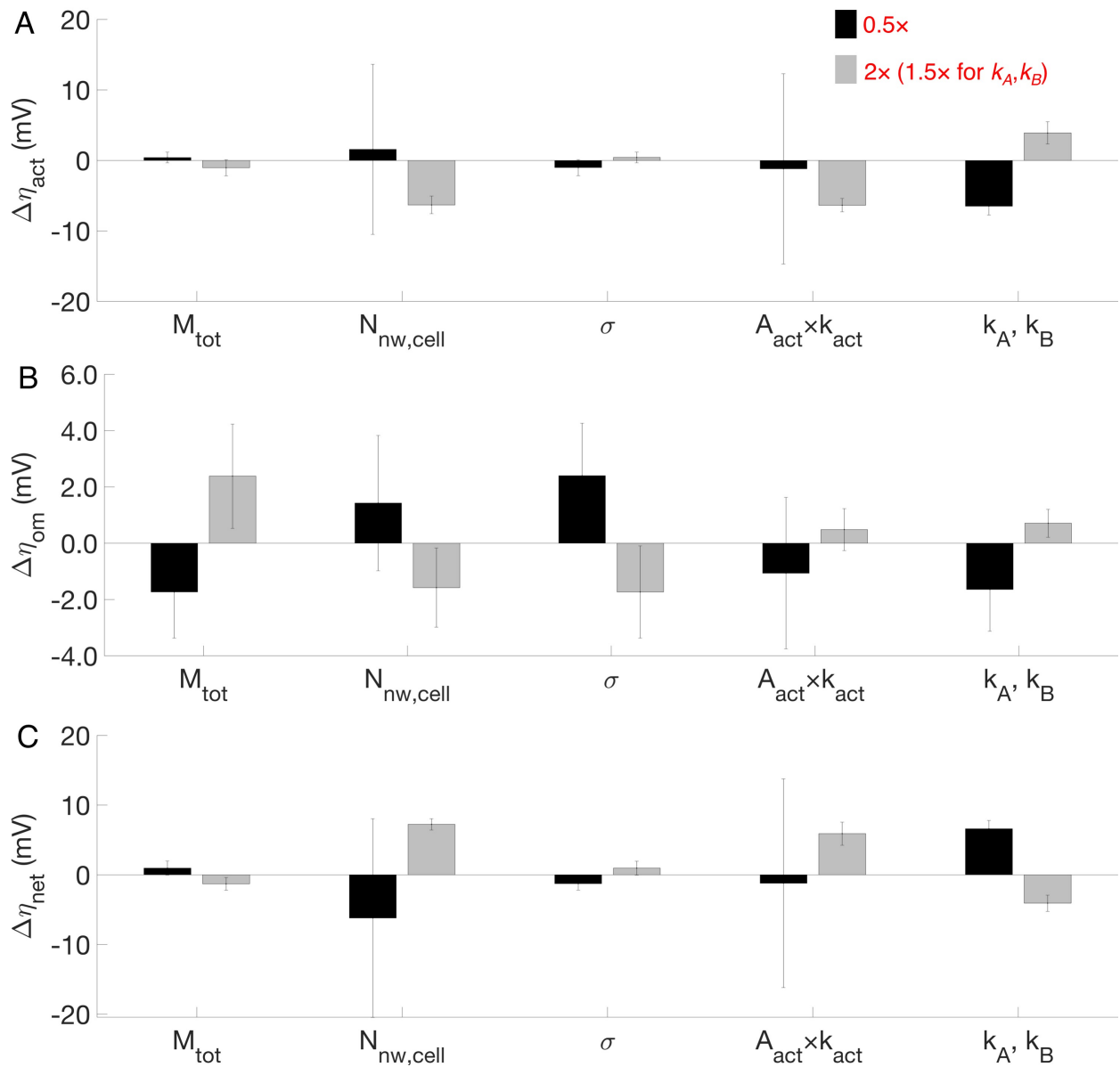


Fig. 3.5. Changes of activation loss  $\Delta\eta_{act}$  (A), ohmic resistance loss  $\Delta\eta_{om}$  (B) and net available potential  $\Delta\eta_{net}$  (C) due to a change in total redox active molecules ( $M_{tot}$ ), number of conductive connections ( $N_{nw,cell}$ ), conductivity ( $\sigma$ ), cell redox active factor ( $k_{act} \times A_{act}$ ), cell rate constants ( $k_A, k_B$ ). Error bars reflect that the impact is not exactly constant with distance for archaea-bacteria interface (see appendix Fig. B11-13).

Because several poorly characterized model parameters impact the resulting magnitude of activity and spatial patterns of electric losses (Figs. 3.5, B11-B13), our work emphasizes important

targets for future study and observation, such as an assessment of the number of pili/wire-like structures recently observed to be involved in EET for some archaeal/ bacterial syntrophic consortia (12, 20). The accurate quantification of these connections is challenging, as not all such structures are necessarily conductive, and most observations are two-dimensional sections through a three-dimensional matrix of extracellular material. However, the extent to which archaeal and bacterial cell are connected is important, because variations in the extent of conductive connections can substantially alter the metabolic activity pattern by influencing both activation loss  $\eta_{act}$  (Fig. 3.5A) and ohmic resistance loss  $\eta_{om}$  (Fig. 3.5B), and hence the net available potential  $\eta_{net}$  (Fig. 3.5C). Halving  $N_{nw,cell}$  significantly limited the metabolic activity due to the reduced availability of  $\eta_{net}$  (Fig. 3.5C), in agreement with Storck *et al.* (2016), who reported that decreasing conductive network density ( $N_{nw,cell}$ ) by a factor of 10 led to a 60% decrease of electron transport rate. Doubling  $N_{nw,cell}$  resulted in a homogenous distribution of metabolic activity, similar to the finding in the study by Storck *et al.* (2016), in which electron transport rate increased slightly for a 10-fold increase in  $N_{nw,cell}$ , suggesting a plateau was reached. Furthermore, while no data on AOM consortia conductivity  $\sigma$  have been published yet, such measurements have been made in *Geobacter* biofilms (17, 41-44), *Geobacter* pilin nanofilaments (17, 45), *Desulfovibrio desulfuricans* nanofilaments (46), methanogenic aggregates from anaerobic wastewater reactor (10), granule from anaerobic bioreactors (47), among others. The conductivity  $\sigma$  has a significant impact, with a reduction by a factor of 10 to  $10^{-3}$  S m<sup>-1</sup> drastically reducing the metabolic activity (Fig. B16C). By increasing conductivity to  $10^{-1}$  S m<sup>-1</sup>, metabolic activity reached a homogenous spatial distribution, owing to the increased  $\eta_{net}$  at higher conductivity (Fig. 3.5C).

### *Type and strength of syntrophic coupling between archaea and bacteria*

A hybrid DIET-MIET mechanism as implemented in our baseline simulation can lead to a higher energy yield than electron transfer by DIET alone. The conditions for sulfate-reducing bacterial cells were slightly more energetically favorable with a 92.5% DIET / 7.5% MIET hybrid metabolism (Fig. 3.6 and Fig. B2), with  $\Delta G_{R(2)}$  of  $-26.1 \text{ kJ mol}^{-1}$  for 100% DIET vs.  $-27.3 \text{ kJ mol}^{-1}$  for a model with mixed DIET and MIET (specific parameters included:  $CH_4 = 4.5 \text{ mM}$ ,  $SO_4^{2-} = 28 \text{ mM}$ ,  $HCO_3^- = 2.3 \text{ mM}$ ,  $HS^- = 0.1 \text{ mM}$ ,  $HCOO^- = 1 \text{ }\mu\text{M}$ ,  $MH = M = 5 \text{ mM}$ ,  $pH = 8.2$ , and  $T = 277.15\text{K}$ ). As a consequence of this difference in reaction energetics, bacterial activity in the 100% DIET simulation decreases more rapidly with separation distance (Fig. B2) than our baseline 92.5/7.5 hybrid model.

Simulations with chemical conditions that vary spatially at rates matching those observed in the  $^{15}\text{N}$  FISH-nanoSIMS experiments show that at  $< 90\%$  DIET, methane oxidation shut down due to the buildup of formate, leading to a net energy gain ( $\Delta G_{R(1)} - \Delta G_{loss}$ ) less than the minimum requirement for ATP production ( $\Delta G_{ATP}$ ). At 100% electron conduction by DIET, archaea were generally active and not limited by the accumulation of reaction products, but the bacteria become susceptible to limitation from voltage losses. Consistent with the simplified thermodynamic calculations (Fig. 3.6), the model simulations showed a narrow window with approximately 90-100% DIET that enabled energetically favorable conditions for both bacterial and archaeal cells (Fig. 3.6). Importantly, a hybrid mechanism can affect the balance of energy gains between the syntrophic partners, which results in improved energetic conditions for the partner most energetically constrained, thereby benefitting *both* archaea and bacteria (Fig. 3.6).

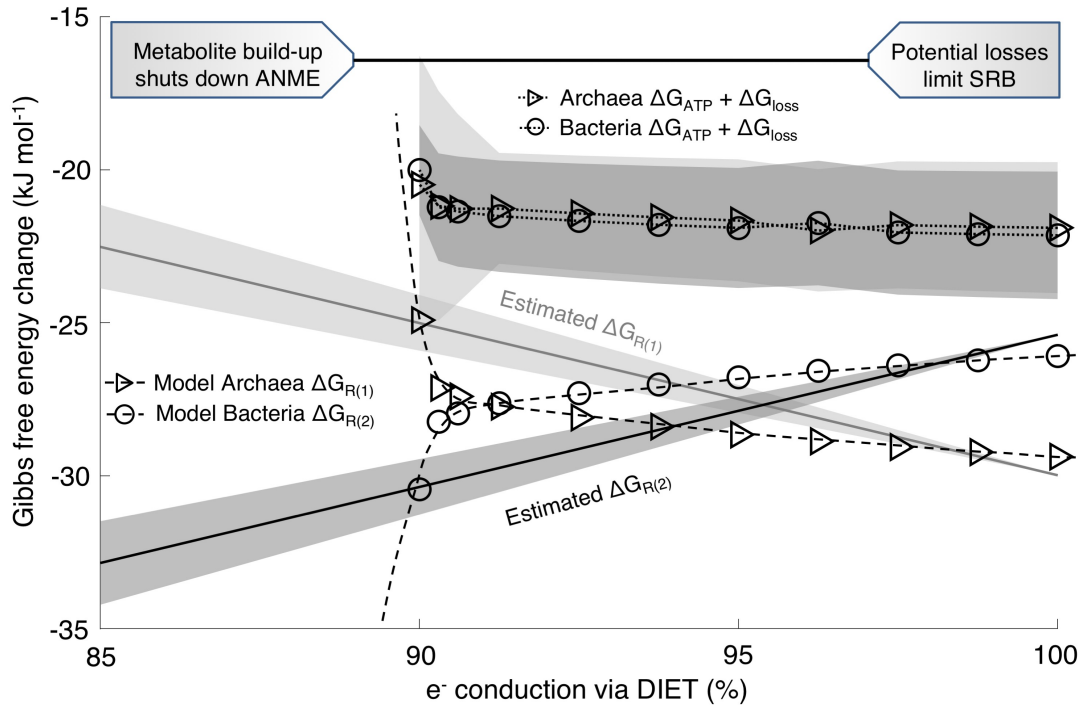


Fig. 3.6. The Gibbs free energy change ( $\Delta G$ ) against the change of electron conduction via DIET, while circles and triangles represent bacteria and archaea respectively. Simulations were run at aggregate radius of 20  $\mu\text{m}$  with baseline parameters. The estimated  $\Delta G_{R(1)}$  and  $\Delta G_{R(2)}$  were calculated with  $\text{CH}_4 = 4.5 \text{ mM}$ ,  $\text{SO}_4^{2-} = 28 \text{ mM}$ ,  $\text{HCO}_3^- = 2.3 \text{ mM}$ ,  $\text{HS}^- = 0.1 \text{ mM}$ ,  $\text{MH} = \text{M} = 5 \text{ mM}$ ,  $\text{pH} = 8.2$ , and  $T = 277.15\text{K}$ , with  $\text{HCOO}^-$  varying between 0.1-100  $\mu\text{M}$  to reflect different intra-aggregate and/or environmental conditions. The light and dark grey shaded areas represent the resulting 95% confidence interval for the Archaea and Bacteria, respectively.

#### *Potential for decoupling of archaea and bacteria metabolisms*

We considered metabolic decoupling between the ANME and SRB partners, where the bacteria may use electron donors derived from the external environment rather than be provided the syntrophic partner. We explored the impact of externally-sourced formate on bacterial metabolism by loosening the coupling between archaeal and bacterial metabolism (see Appendix A2). Formate concentrations in marine sediments range from below detection limit (0.37  $\mu\text{M}$ ) to 10.38  $\mu\text{M}$  in

Baltic Sea sediments (48), 2-18  $\mu\text{M}$  in northern Gulf of Mexico sediments (49), up to 59.5  $\mu\text{M}$  in Hydrate Ridge sediments (50), 12.1  $\mu\text{M}$  in Aarhus Bay sediments (51), and 36-158  $\mu\text{mol/kg}$  in the fluid from Lost City hydrothermal field (52). Thus, simulations were carried out for 1-100  $\mu\text{M}$  formate in the environment. Increasing formate from 1  $\mu\text{M}$  to 15  $\mu\text{M}$  led to a significant increase of bacterial activity at the aggregate surface, while showing nearly no impact on archaeal cells (Fig. B8A). At a lower  $\text{HCOO}^-$  concentration (1  $\mu\text{M}$ ), bacterial cells exhibited a slight shortage of  $\text{HCOO}^-$  supply away from the archaea-bacteria interface (Fig. B8B). At high formate ( $> 15 \mu\text{M}$ ), carrying out archaeal  $\text{CH}_4$  oxidation could become thermodynamically unfavorable due to the accumulation of  $\text{HCOO}^-$  (not shown). Noticeably, the Gibbs free energy change for sulfate reduction ( $\Delta G_{\text{R}(2)}$ ) significantly decreased from  $\sim -27.5 \text{ kJ mol}^{-1}$  to  $-30.05 \text{ kJ mol}^{-1}$  when changing formate from 1  $\mu\text{M}$  to 15  $\mu\text{M}$  (Fig. B8C), leading to a significant increase of bacterial thermodynamic constraint  $F_T$  from 0.35 to 0.7 at the aggregate surface, while no significant changes were observed for archaea (Fig. B8D). Notably, the increased formate from 1  $\mu\text{M}$  to 15  $\mu\text{M}$  did not significantly impact the total flux of  $\text{HCOO}^-$ , though an increase of  $\text{HCOO}^-$  concentration within consortium was observed (Fig. B8B).

### Conclusions

We report on the metabolic activity distribution of individual cells in a large AOM consortium using FISH-nanoSIMS. A decline in cell activity with the increasing distance from archaea-bacteria interface was observed in a section through the center of the aggregate, cut approximately normal to the ANME-SRB interface. These results provide the first quantitative assessment of the growth penalty that exists over large separation distances between these syntrophic partners, an effect which is not apparent in small or well-mixed aggregates as we have reported earlier (11, 13). A reactive transport model accounting for thermodynamic limitations on

cell metabolism, as well as activation and ohmic resistance losses in the exchange of electrons between syntrophic microorganisms successfully reproduced these observations. Ohmic resistance is shown to limit activity for electron transport over at further distance ( $> 8 \mu\text{m}$  in our model), with the abundance of redox active molecules ( $M_{tot}$ ), conductive network density ( $N_{nw,cell}$ ), cell redox active factor ( $k_{act} \times A_{act}$ ), their conductivity ( $\sigma$ ) and associated cell rate constants ( $k_A, k_B$ ) having a strong impact on magnitude and distribution of metabolic activity within microbial aggregates. Within the context of a strongly segregated AOM aggregate, cell activity decreases with distance to the syntrophic partner even with electron transfer via DIET over sufficiently long distances. This decrease in activity is expected to constrain the maximal size of mono-species clusters within AOM consortia. It has been long speculated that close cooperation and rearrangement between microbial clusters might be necessary to form a large syntrophic aggregate with efficient metabolite transfer between partners (53). While the general trend remains true, DIET allows for much bigger clusters than can be supported with MIET alone. Our model also revealed advantages of a hybrid DIET-MIET mechanism, allowing for balanced microbial energetics for both syntrophic partners, but opening up the potential for decoupling of the sulfate-reducing bacterial partner from the methanotrophic archaea by utilizing electron donors from environment. This decoupling has been observed in thermophilic AOM consortia where it has been shown that the ANME-1 sulfate-reducing bacterial partner ‘HotSeep-1’ can utilize  $\text{H}_2$  and grow independently of ANME. The addition of  $\text{H}_2$  to incubations can be used to decouple and specifically culture HotSeep-1, even though MIET using  $\text{H}_2$  is not thought to be an important form of syntrophic electron transfer (12), as detectible hydrogenases are lacking in ANME (54) and SRB (55) genomes recovered from cold seeps, and experimental data demonstrated that excess hydrogen addition does not inhibit AOM activity in sediment incubations and enrichment cultures

(56-58). However, while we have modeled the MIET intermediate as formate in this study, other small redox active molecules, for example flavins, may act as electron shuttles. Future work will help understand these mechanistic questions by a careful comparison of ANME and SRB genomic potential and expression with their cellular activity patterns.

#### Acknowledgements

This work was supported by the U.S. Department of Energy, Office of Science, Office of Biological and Environmental Research, Genomic Science Program under Award Number DE-SC0016469 and DE-SC0020373 (to CM and VJO). The authors declare no conflict of interest.

#### References

1. Reeburgh WS. Oceanic methane biogeochemistry. *Chemical Rev.* 2007;**107**(2):486-513.
2. Hinrichs KU, Hayes JM, Sylva SP, Brewer PG, DeLong EF. Methane-consuming Archaeobacteria in marine sediments. *Nature.* 1999;**398**(6730):802–5.
3. Boetius A, Ravensschlag K, Schubert CJ, Rickert D, Widdel F, Gieseke A, et al. A marine microbial consortium apparently mediating anaerobic oxidation of methane. *Nature.* 2000;**407**:623–6.
4. Orphan VJ, House CH, Hinrichs KU, McKeegan KD, DeLong EF. Methane-consuming archaea revealed by directly coupled isotopic and phylogenetic analysis. *Science.* 2001;**293**:484–7.
5. Joye SB, Boetius A, Orcutt BN, Montoya JP, Schulz HN, Erickson MJ, et al. The anaerobic oxidation of methane and sulfate reduction in sediments from Gulf of Mexico cold seeps. *Chem Geol.* 2004;**205**(3):219-38.
6. Myhre G, Shindell D, Bréon F-M, Collins W, Fuglestvedt J, Huang J, et al. Anthropogenic and Natural Radiative Forcing. In: Stocker TF, Qin D, Plattner G-K, Tignor M, Allen SK,

Boschung J, et al., editors. *Climate Change 2013: The Physical Science Basis Contribution of Working Group I to the Fifth Assessment Report of the Intergovernmental Panel on Climate Change*. New York, NY, USA: Cambridge University Press; 2013.

7. Reguera G, McCarthy KD, Mehta T, Nicoll JS, Tuominen MT, Lovley DR. Extracellular electron transfer via microbial nanowires. *Nature*. 2005;**435**:1098–101.

8. Stams AJ, De Bok FAM, Van Eekert MHA, Dolfing J, Schraa G. Exocellular electron transfer in anaerobic microbial communities. *Environ Microbiol*. 2006;**8**(3):371-82.

9. Summers ZM, Fogarty HE, Leang C, Franks AE, Malvankar NS, Lovley DR. Direct exchange of electrons within aggregates of an evolved syntrophic coculture of anaerobic bacteria. *Science*. 2010;**330**(6009):1413-5.

10. Morita M, Malvankar NS, Franks AE, Summers ZM, Giloteaux L, Rotaru AE, et al. Potential for direct interspecies electron transfer in methanogenic wastewater digester aggregates. *mBio*. 2011;**2**:e00159-11.

11. McGlynn SE, Chadwick GL, Kempes CP, Orphan VJ. Single cell activity reveals direct electron transfer in methanotrophic consortia. *Nature*. 2015;**526**(7574):531-5.

12. Wegener G, Krukenberg V, Riedel D, Tegetmeyer HE, Boetius A. Intercellular wiring enables electron transfer between methanotrophic archaea and bacteria. *Nature*. 2015;**526**(7574):587-90.

13. He X, Chadwick G, Kempes C, Shi Y, McGlynn S, Orphan V, et al. Microbial interactions in the anaerobic oxidation of methane: model simulations constrained by process rates and activity patterns. *Environ Microbiol*. 2019;**21**(2):631-47.

14. McGlynn SE. Energy metabolism during anaerobic methane oxidation in ANME archaea. *Microbes Environ*. 2017;**32**(1): 5-13.

15. Orcutt B, Meile C. Constraints on mechanisms and rates of anaerobic oxidation of methane by microbial consortia: process-based modeling of ANME-2 archaea and sulfate reducing bacteria interactions. *Biogeosciences*. 2008;**5**:1587-99.
16. Rotaru A-E, Shrestha PM, Liu F, Markovaite B, Chen S, Nevin KP, et al. Direct interspecies electron transfer between *Geobacter metallireducens* and *Methanosarcina barkeri*. *Appl Environ Microbiol*. 2014;**80**:4599-605.
17. Malvankar NS, Vargas M, Nevin KP, Franks AE, Leang C, Kim BC, et al. Tunable metallic-like conductivity in microbial nanowire networks. *Nat Nanotechnol*. 2011;**6**:573-9.
18. Virdis B, Millo D, Donose BC, Lu Y, Batstone DJ, Krömer JO. Analysis of electron transfer dynamics in mixed community electroactive microbial biofilms. *RSC Adv*. 2016;**6**:3650–60.
19. Ordóñez MV, Schrott GD, Massazza DA, Busalmen JP. The relay network of *Geobacter* biofilms. *Energy Environ Sci*. 2016;**9**:2677–81.
20. Krukenberg V, Riedel D, Gruber-Vodicka HR, Buttigieg PL, Tegetmeyer HE, Boetius A, et al. Gene expression and ultrastructure of meso- and thermophilic methanotrophic consortia. *Environ Microbiol*. 2018;**20**:1651-66.
21. Richardson DJ, Butt JN, Fredrickson JK, Zachara JM, Shi L, Edwards MJ, et al. The ‘porin-cytochrome’ model for microbe-to-mineral electron transfer. *Mol Microbiol*. 2012;**85**(2):201-12.
22. Chadwick GL, Otero FJ, Gralnick JA, Bond DR, Orphan VJ. NanoSIMS imaging reveals metabolic stratification within current-producing biofilms. *PNAS*. 2019;**116**(41):20716-24.
23. Scheller S, Yu H, Chadwick GL, McGlynn SE, Orphan VJ. Artificial electron acceptors decouple archaeal methane oxidation from sulfate reduction. *Science*. 2016;**351**(6274):703-7.

24. Trembath-Reichert E, Morono Y, Ijiri A, Hoshino T, Dawson KS, Inagaki F, et al. Methyl-compound use and slow growth characterize microbial life in 2-km-deep seafloor coal and shale beds. *PNAS*. 2017;**114**(44):E9206-E15.
25. Jin Q, Bethke C. A new rate law describing microbial respiration. *Appl Environ Microbiol*. 2003;**69**:2340–8.
26. Jin Q, Bethke C. The thermodynamics and kinetics of microbial metabolism. *Am J Sci*. 2007;**307**:643–77.
27. Storck T, Virdis B, Batstone DJ. Modelling extracellular limitations for mediated versus direct interspecies electron transfer. *ISME J*. 2016;**10**(3):621-31.
28. Knittel K, Lösekann T, Boetius A, Kort R, Amann R. Diversity and distribution of methanotrophic archaea at cold seeps. *Appl Environ Microbiol*. 2005;**71**(1):467-79.
29. Aoki M, Ehara M, Saito Y, Yoshioka H, Miyazaki M, Saito Y, et al. A Long-Term Cultivation of an Anaerobic Methane-Oxidizing Microbial Community from Deep-Sea Methane-Seep Sediment Using a Continuous-Flow Bioreactor. *PloS one*. 2014;**9**(8):e105356.
30. Levar CE, Hoffman CL, Dunshee AJ, Toner BM, Bond DR. Redox potential as a master variable controlling pathways of metal reduction by *Geobacter sulfurreducens*. *ISME J*. 2017;**11**(3):741-52.
31. Strycharz-Glaven SM, Snider RM, Guiseppi-Elie A, Tender LM. On the electrical conductivity of microbial nanowires and biofilms. *Energy Environ Sci*. 2011;**4**:4366–79.
32. Dalton EF, Surridge NA, Jernigan JC, Wilbourn KO, Facci JS, Murray RW. Charge transport in electroactive polymers consisting of fixed molecular redox sites. *Chem Phys*. 1990;**141**(1):143-57.

33. Zeebe RE, Wolf-Gladrow D. Chapter 2. Kinetics. In: Halpern D, editor. CO<sub>2</sub> in Seawater: Equilibrium, Kinetics, Isotopes. 3rd ed. San Diego, USA: Elsevier Science; 2005.
34. DOE. Handbook of methods for the analysis of the various parameters of the carbon dioxide system in sea water. Version 2 ed. Dickson AG, Goyet C, editors 1994.
35. Bowles MW, Samarkin VA, Hunter KS, Finke N, Teske AP, Girguis PR, et al. Remarkable capacity for anaerobic oxidation of methane at high methane concentration. *Geophys Res Lett*. 2019;**46**(21):12192-201.
36. Roychoudhury AN. Sulfate respiration in extreme environments: a kinetic study. *Geomicrobiol J*. 2004;**21**(1):33-43.
37. Sander R. Compilation of Henry's law constants (version 4.0) for water as solvent. *Atmos Chem Phys*. 2015;**15**:4399–981.
38. Chester R, Jickells T. Chapter 7. Descriptive Oceanography: water column parameters. *Marine Geochemistry*. 3rd ed: Wiley-Blackwell; 2012. p. 125-53.
39. Nauhaus K, Albrecht M, Elvert M, Boetius A, Widdel F. In vitro cell growth of marine archaeal-bacterial consortia during anaerobic oxidation of methane with sulfate. *Environ Microbiol*. 2007;**9**(1):187-96.
40. Polizzi NF, Skourtis SS, Beratan DN. Physical constraints on charge transport through bacterial nanowires. *Faraday Discuss*. 2012;**155**:43-61.
41. Malvankar NS, Lau J, Nevin KP, Franks AE, Tuominen MT, Lovley DR. Electrical conductivity in a mixed-species biofilm. *Appl Environ Microbiol*. 2012;**78**(16):5967-71.
42. Dhar BR, Ren H, Chae J, Lee HS. Recoverability of electrical conductivity of a *Geobacter*-enriched biofilm. *J Power Sources*. 2018;**402**:198-202.

43. Li C, Lesnik KL, Fan Y, Liu H. Redox conductivity of current-producing mixed species biofilms. *PloS one*. 2016;**11**(5):e0155247.
44. Phan H, Yates MD, Kirchhofer ND, Bazan GC, Tender LM, Nguyen T-Q. Biofilm as a redox conductor: a systematic study of the moisture and temperature dependence of its electrical properties. *Phys Chem Chem Phys*. 2016;**18**(27):17815-21.
45. Tan Y, Adhikari RY, Malvankar NS, Ward JE, Nevin KP, Woodard TL, et al. The low conductivity of *Geobacter uraniireducens* pili suggests a diversity of extracellular electron transfer mechanisms in the genus *Geobacter*. *Front Microbiol*. 2016;**7**:980.
46. Eaktasang N, Kang CS, Lim H, Kwean OS, Cho S, Kim Y, et al. Production of electrically-conductive nanoscale filaments by sulfate-reducing bacteria in the microbial fuel cell. *Bioresour Technol*. 2016;**210**:61-7.
47. Shrestha PM, Malvankar NS, Werner JJ, Franks AE, Elena-Rotaru A, Shrestha M, et al. Correlation between microbial community and granule conductivity in anaerobic bioreactors for brewery wastewater treatment. *Bioresour Technol*. 2014;**174**:306-10.
48. Zinke LA, Glombitza C, Bird JT, Røy H, Jørgensen BB, Lloyd KG, et al. Microbial organic matter degradation potential in Baltic Sea sediments is influenced by depositional conditions and in situ geochemistry. *Appl Environ Microbiol*. 2019;**65**(4):e02164-18.
49. Zhuang G-C, Montgomery A, Joye SB. Heterotrophic metabolism of C1 and C2 low molecular weight compounds in northern Gulf of Mexico sediments: Controlling factors and implications for organic carbon degradation. *Geochim Cosmochim Acta*. 2019;**247**:243-60.
50. Valentine DL, Kastner M, Wardlaw GD, Wang X, Purdy A, Bartlett DH. Biogeochemical investigations of marine methane seeps, Hydrate Ridge, Oregon. *J Geophys Res-Biogeophys*. 2005;**110**:G02005.

51. Webster G, Sass H, Cragg BA, Gorra R, Knab NJ, Green CJ, et al. Enrichment and cultivation of prokaryotes associated with the sulphate–methane transition zone of diffusion-controlled sediments of Aarhus Bay, Denmark, under heterotrophic conditions. *FEMS Microbiol Ecol.* 2011;**77**(2):248-63.
52. Lang SQ, Butterfield DA, Schulte M, Kelley DS, Lilley MD. Elevated concentrations of formate, acetate and dissolved organic carbon found at the Lost City hydrothermal field. *Geochim Cosmochim Acta.* 2010;**74**(3):941-52.
53. Schink B, Thauer RK, editors. Energetics of syntrophic methane formation and the influence of aggregation. *Granular Anaerobic Sludge: Microbiology and Technology Proceedings of the GASMAT-workshop; 1987; Lunteren, Netherlands: Puduc Wageningen.*
54. Wang FP, Zhang Y, Chen Y, He Y, Qi J, Hinrichs KU, et al. Methanotrophic archaea possessing diverging methane-oxidizing and electron-transporting pathways. *ISME J.* 2014;**8**(5):1069-78.
55. Skennerton CT, Chourey K, Iyer R, Hettich RL, Tyson GW, Orphan VJ. Methane-fueled syntrophy through extracellular electron transfer: uncovering the genomic traits conserved within diverse bacterial partners of anaerobic methanotrophic archaea. *MBio.* 2017;**8**(4):e00530-17.
56. Nauhaus K, Treude T, Boetius A, Krüger M. Environmental regulation of the anaerobic oxidation of methane: a comparison of ANME-I and ANME-II communities. *Environ Microbiol.* 2005;**7**(1):98-106.
57. Meulepas RJ, Jagersma CG, Khadem AF, Stams AJ, Lens PN. Effect of methanogenic substrates on anaerobic oxidation of methane and sulfate reduction by an anaerobic methanotrophic enrichment. *Appl Environ Microbiol.* 2010;**87**(4):1499-506.

58. Wegener G, Krukenberg V, Ruff SE, Kellermann MY, Knittel K. Metabolic capabilities of microorganisms involved in and associated with the anaerobic oxidation of methane. *Front Microbiol.* 2016;7:46.

## CHAPTER 4

# SPATIALLY RESOLVED ELECTRON TRANSPORT THROUGH ANODE-RESPIRING *GEOBACTER* BIOFILMS: CONTROLS AND CONSTRAINTS <sup>3</sup>

---

<sup>3</sup> He, X., Chadwick, G., Jiménez Otero, F., Orphan, V. and Meile, C. (2020) Spatially Resolved Electron Transport through Anode-Respiring *Geobacter* Biofilms: Controls and Constraints. To be Submitted to ChemSusChem.

## Abstract

Microbial fuel cells (MFCs) harness the electricity produced in the microbial oxidation of organic molecules, with applications in renewable energy production, environmental remediation or for powering remote sensors. MFCs with anode-respiring *Geobacter sulfurreducens* have been shown to produce high current densities; however electron transport in *G. sulfurreducens* biofilms is not fully understood. Here, we utilize a spatially resolved numerical model describing this electron transfer to constrain mechanisms and controls on metabolic activity. Our model reproduces the metabolic activity profile obtained using stable isotope probing with nanoSIMS under high (+0.24V) and low (-0.1V) anode potentials. The simulations indicate that the distribution of the electric potential and pH both control cellular metabolism: Activation loss and ohmic resistance loss are responsible for the observed general declining trend of metabolic activity with distance from the anode, while low pH (approximately 6.15) is implicated in the lower microbial activity near the anode surface that was observed at high anode potential. Model simulations reproducing the experimentally determined activity patterns also support the presence of both high and low-potential modes of activity in *G. sulfurreducens* biofilms, with a shift from a redox-active molecule with a mid-potential of -0.07 V to one with a mid-potential of -0.15 V at an electric potential of -0.15 V. In addition to reproducing the observed activity distribution patterns, the model further reproduces independent data on currents maintained after disconnecting the electrode, supported by electrons temporarily stored in reduced redox-active molecules. Our model thus provides valuable insights into the fundamental mechanisms of electron transfer at micro-scale in conductive biofilms. It can be used to inform MFCs designs that maximize current

production by minimizing the impact of inhibitory factors, such as low pH near the electrode and substantially decreased electric potential at the farther distance away from electrode in *G. sulfurreducens* biofilms.

### Introduction

Extracellular electron transfer (EET) can be carried out through the transport of chemical substances (mediated electron transfer) or by electron flow (direct electron transfer, DET) via physical contact using outer surface c-type cytochromes,(1) electrically conductive pili(2) or a matrix of extracellular polymeric substances.(3-5) DET is potentially much more efficient than MET, and effective over long distances(6). As such, microorganisms capable of DET have attracted attention in the fields of microbial physiology, microbial ecology, and biotechnology over the last decade(7-9). Particularly, understanding the EET mechanisms in current generating biofilms on electrodes in microbial fuel cells (MFCs) and the factors controlling their metabolic rates is important for the optimization of practical applications and a better understanding of natural and/or industrial systems.(10)

*Geobacter sulfurreducens*, one of the best studied model organisms carrying out DET, has been demonstrated to grow in thick biofilms that produce high current densities in MFCs in which the anode serves as the sole terminal electron acceptor(11, 12). Anode potential regulates metabolism, electrochemical respiration and anabolic activity in *G. sulfurreducens* biofilms.(13-18) However, despite many novel experimental findings in the past decade, a major challenge still exists to understand the fundamental EET mechanisms in *G. sulfurreducens* biofilms.(19-22) Recent studies of anode-respiring *G. sulfurreducens* biofilms have revealed that redox-active molecules such as outer membrane and/or

extracellular multi-heme c-type cytochromes(7, 23-26) and Fe-containing proteins(27), rather than chemical intermediates,(28-31) play important roles in the electron transfer from *G. sulfurreducens* to the electrode. Several studies suggest conductive filaments (pili) may play a key role in the long-range EET of *G. sulfurreducens*(32-37), while other studies show conductive pili may not be necessary.(38, 39)

Understanding how *G. sulfurreducens* produces such high current densities, and what ultimately is responsible for limiting this process motivates the development of a reactive transport model. Such models account for the fundamental physics and chemistry in natural systems and can quantitatively integrate microbiological insights into an environmental context(40). For example, Marcus et al. (2007)(41) and Torres et al. (2008)(42) showed that EET in *G. sulfurreducens* biofilms can be limited by biofilm conductivity, electron donor flux and local potential. Our own earlier efforts have successfully developed reactive transport modeling framework accounting for sulfate-coupled anaerobic oxidation of methane mediated by syntrophic associations between anaerobic methanotrophic archaea and sulfate-reducing bacteria across a range of aggregate geometries and sizes. These models were validated with empirical data from methane-oxidizing aggregates using fluorescence in situ hybridization (FISH) coupled with nanoscale secondary ion mass spectrometry (nanoSIMS) to measure cell-specific spatial patterns in  $^{15}\text{NH}_4^+$  incorporation (a proxy for anabolic activity) in archaea and sulfate-reducing bacteria (43, 44). Here, we adopt a similar approach to study the spatially resolved electrochemical activity and metabolic activity in *G. sulfurreducens* biofilms. Earlier studies suggest that both pH(45-47) and electric potential dependencies(13-18, 48) shape cell activity within biofilms, yet no robust cell activity data was available. Recent

data collected using stable isotope probing coupled to nanoSIMS revealed distinct metabolic activity stratifications in anode-respiring *G. sulfurreducens* biofilms under two different anode redox potentials(49). These unique experimental results provide significant constraints on reaction transport models of EET, enabling us to identify the controls on current production with relevance to the functioning of MFCs.

## Materials and Methods

### **Experimental data**

The experimental data used in this study are described in Chadwick et al. (2019). In brief, the anabolic activity of *G. sulfurreducens* biofilms was measured by <sup>15</sup>N fractional abundance using nanoSIMS.(49) *G. sulfurreducens* biofilms were incubated with <sup>15</sup>NH<sub>4</sub><sup>+</sup> as the nitrogen in an anaerobic chamber with graphite electrodes (3 cm<sup>2</sup>) serving as the electron acceptor. The electrode was poised at anode electric potentials of -0.1 V or +0.24 V vs. standard hydrogen electrode. Acetate (20 mM) was provided as the electron donor. After incubation for 6h (the duration of one doubling time), the intact *G. sulfurreducens* biofilms on the electrode were chemically fixed, embedded in resin, and thin sectioned. Spatial patterns of anabolic activity (cellular <sup>15</sup>N incorporation) in the electrode-attached biofilm were then measured on a CAMECA nanoSIMS 50L instrument. Using cellular <sup>15</sup>N enrichment data, the growth rate ( $\mu$  in d<sup>-1</sup>) of *G. sulfurreducens* was calculated as

$$\mu = \frac{-\ln \left( 1 - \frac{F_{final} - F_{nat}}{F_{label} - F_{nat}} \right)}{T_{incub}} \quad \text{Eq. (4.1)}$$

where  $T_{incub}$  is the length of the incubation (d),  $F_{label}$  is the labeling strength of the nitrogen source provided (<sup>15</sup>NH<sub>4</sub>/(<sup>14</sup>NH<sub>4</sub>+<sup>15</sup>NH<sub>4</sub>) = 0.06),  $F_{final}$  is the <sup>15</sup>N fractional abundance measured in the biofilm using nanoSIMS, and  $F_{nat} = 0.0036$  is the natural <sup>15</sup>N fractional abundance. The observed N assimilation is related to modeled metabolic rates through the

growth yield ( $Y_{Ac}$  in grams dry weight per mol Ac oxidized), and cell-specific metabolic rates ( $R_{obs}$  in fmol-Ac cell<sup>-1</sup> d<sup>-1</sup>) were calculated as

$$R_{obs} = \mu \cdot \rho / Y_{Ac} \quad \text{Eq. (4.2)}$$

where  $\rho$  is biomass density (Table 1). Following King et al. (2009),(50)  $Y_{Ac}$  was calculated as a function of acetate uptake ( $U_{Ac}$ , see Eq 4)

$$Y_{Ac} = \max\left(0, a \frac{U_{Ac}-c}{b+U}\right) \quad \text{Eq. (4.3)}$$

where the constants a, b and c are set to 5 grams dry weight (gdw) mol-Ac<sup>-1</sup>, 2 mM-Ac gdw<sup>-1</sup> h<sup>-1</sup>, and 1 mM-Ac gdw<sup>-1</sup> h<sup>-1</sup>, respectively (Fig. C1B). For the experimental conditions, this resulted in a growth yield  $Y_{Ac}$  of 4.32 gdw mol-Ac<sup>-1</sup>, consistent with values reported in earlier experimental studies (ranging from 1 to 11 gdw mol-Ac<sup>-1</sup>).(51, 52)

## Model Description

The model describes acetate oxidation, with the produced electrons being transported to the anode via electron conduction. The rate of acetate oxidation is set to depend on both the acetate concentration, the availability of the extracellular electron acceptor, pH and the redox potential in the biofilm.

### *Metabolic Reactions*

We model the EET in *G. sulfurreducens* biofilms with by representing three central processes: acetate uptake and oxidation with electron transfer to reduced redox-active molecules  $Cyt_{red}(Fe^{2+})$ , electron transport in conductive biofilm, and finally electron off-loading onto the anode.

### *Acetate uptake*

The uptake of acetate ( $U_{Ac}$  in mM-Ac gdw<sup>-1</sup> h<sup>-1</sup>) can be described as a function of acetate availability(50) using

$$U_{Ac} = v_{max} \frac{[Ac]}{K_{m,Ac} + [Ac]} \quad \text{Eq. (4.4)}$$

where  $v_{max}$  and  $K_{m,Ac}$  are set to 20 mM-Ac  $\text{gdw}^{-1} \text{h}^{-1}$  and 10  $\mu\text{M}$ , respectively, reflecting the relationships established in King et al. 2009 (Fig. C1A).

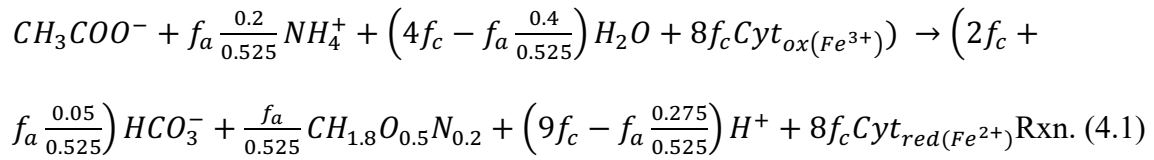
#### *Electron transfer to $Cyt_{red}$ by acetate oxidation*

Eight electrons are produced per mol Ac oxidized, in which a fraction ( $f_c$ ) goes to catabolic reactions that produce  $\text{CO}_2$ , and the remainder is used in anabolic reactions ( $f_a$ , with  $f_a + f_c = 1$ ) that produce biomass, which is represented by  $\text{CH}_{1.8}\text{O}_{0.5}\text{N}_{0.2}$ . (20) With that, the fraction of carbon that goes to biomass synthesis ( $f_a$ ) from acetate oxidation is

$$f_a = \frac{Y_{Ac}}{24.6 [g \text{ mol}^{-1}] \times 2} \quad \text{Eq. (4.5)}$$

where the factor of 2 represents 2 mol carbon goes to biomass ( $\text{CH}_{1.8}\text{O}_{0.5}\text{N}_{0.2}$ ) per mol acetate oxidized.

The electron transfer from acetate oxidation to reduced redox-active molecules  $Cyt_{red(Fe^{2+})}$  and  $\text{CO}_2$  is given as



For convenience, we refer to  $Cyt_{ox(Fe^{3+})}$  and  $Cyt_{red(Fe^{2+})}$  as  $Cyt_{ox}$  and  $Cyt_{red}$ , respectively. We estimate the metabolic rate  $R_{geo}$  as a function of the availability of acetate and oxidized redox molecule  $Cyt_{ox}$ , as well as external constraints including an electric potential dependency ( $F_\theta$ ) and a pH dependency ( $F_{pH}$ ):

$$R_{geo} = k_{cell} B_{geo} \frac{[Ac]}{K_{m,Ac} + [Ac]} [Cyt_{ox}] \cdot F_\theta \cdot F_{pH} \quad \text{Eq. (4.6)}$$

where  $k_{cell}$  is the cell-specific rate constant,  $B_{geo}$  is the cell density,  $K_{m,Ac}$  is the half-saturation constant for acetate. The electric potential dependency ( $F_{\theta}$ ) is formulated as a function of the electric potential in the biofilm,  $\phi_{net}$  (see Eq 10),(41, 42, 53) leading to(42)

$$F_{\theta} = \frac{1}{e^{\frac{-F(\phi_{net} - \phi_{Ox/Red}^{0'})}{RT}} + 1} \quad \text{Eq. (4.7)}$$

where  $\phi_{Ox/Red}^{0'}$  is the mid-potential of the redox-active center. The pH dependency ( $F_{pH}$ ) is expressed as

$$F_{pH} = \frac{g}{g + e^{-g(pH - C_{pH})}} \quad \text{Eq. (4.8)}$$

where  $g = 20$  and  $C_{pH}$  is varied in the simulation with a default value of 6.15. Eq (8) represents the pH impact on cell metabolism of *G. sulfurreducens*, which grow optimally at near-neutral pH(49). Torres et al. (2009) showed that anode-respiring bacteria could be completely inhibited at pH values less than 6,(45) agreeing with the 99% decrease of metabolic rate at pH 5.9 reflected in Eq (8). This observation is further corroborated by findings of Franks et al. (2009) that indicate severe inhibition of *G. sulfurreducens* growth and 50% drop in current production by changing bulk pH from 6.9 to 6.15, and is consistent with the observed decrease in growth of *G. sulfurreducens* from  $0.21 \pm 0.1 \text{ h}^{-1}$  to nearly zero ( $0.04 \pm 0.02 \text{ h}^{-1}$ ) on the soluble electron acceptor fumarate when the pH decreased from 7 to 6.(46)

#### *Electron conduction in G. sulfurreducens biofilms*

Early studies indicated metallic-like conductive EET in *G. sulfurreducens*(12, 23, 34, 54, 55), where electrons are delocalized along a chain of molecules and are free to move throughout the material.(56) In contrast, electron hopping allows the electron transport between localized sites on a network of redox-active molecules (e.g. hemes) via tunneling

or overcoming potential barriers, (19, 25, 57-60) similar to electron conduction in other known organic molecules.(56, 61) This mechanism, which is explored here, is supported by experimental findings that reveal small spatial distances (a few Å) between those subunits(38) and the presence of heme redox gradient(25). The electron hopping process in the presence of redox gradients (here the concentration gradient of  $Cyt_{red}$ ) is commonly modeled as analogous to a random walk (second term on the right-hand side of Eq (9)), and the observed exponential dependence of the current on the electric potential gradient(62, 63) is represented by last term in Eq (4.9). Thus, electron conduction via electron hopping driven by redox gradient and electric field(62, 64) results in:

$$\frac{\partial[Cyt_{red}]}{\partial t} = 8f_c R_{geo} + \nabla \cdot (\mathcal{D}_{cyt} \nabla[Cyt_{red}]) + \nabla \cdot (k_{EF}[Cyt_{ox}][Cyt_{red}] \left( \exp\left(\frac{\beta F \delta E}{R_{gas} T}\right) - \exp\left(-\frac{(1-\beta)F \delta E}{R_{gas} T}\right) \right)) \quad \text{Eq. (4.9)}$$

where the first term on the right-hand side represents the loading of electrons onto  $Cyt_{ox}$  at the location of acetate oxidation.  $D_{cyt} = k_D Cyt_{tot} \delta$  is an effective diffusion coefficient,  $k_D$  is the electron transfer rate constant,  $Cyt_{tot}$  is the total concentration ( $= [Cyt_{ox}] + [Cyt_{red}]$ ),  $\delta$  is the spatial distance between adjacent redox-active molecules,  $E$  is the local electric field, and  $\beta$  is the charge transfer coefficient (see Table 4.1). The electric potential in the biofilm ( $\phi_{net}$ ) is described by

$$\phi_{net} = \phi_{anode} - \phi_{om} - \phi_{act} \quad \text{Eq. (4.10)}$$

where  $\phi_{anode}$  is the poised anode potential,  $\phi_{om}$  and  $\phi_{act}$  are the ohmic and activation voltage losses, respectively.  $\phi_{om}$  is expressed as (65)

$$\phi_{om} = \frac{R_{nw} I}{N_{nw}} = \frac{d}{\sigma A_{nw}} \frac{8f_c R_{geo} N_{geo} F}{Cyt_{tot} V_{bio} k_{nw}} \quad \text{Eq. (4.11)}$$

where  $I$  is the current produced by acetate oxidation ( $I = 8fcR_{geo}N_{geo}F$ ),  $N_{geo}$  is the number of *G. sulfurreducens* cells,  $R_{nw}$  is the electrical resistance ( $\Omega$ ) which can be further described as  $d/(\sigma A_{nw})$ ,  $\sigma$  is the biofilm conductivity,  $d$  is the distance from the anode surface,  $A_{nw}$  is the cross-section area of a single connecting filament,  $N_{nw}$  is the total conductive connections and can be described as  $N_{nw} = Cyt_{tot}V_{bio}k_{nw}$ , where  $V_{bio}$  is the volume of biofilm dependent on biofilm thickness ( $L_{bio}$ ) and electrode surface area ( $A_{anode}$ ), and  $k_{nw}$  is the converting factor associated with conductive biofilm.  $\phi_{act}$  is described using Butler-Volmer equation by(65)

$$I = N_{nw}FA_{act}k_{act}[Cyt_{tot}](\exp\left(\frac{(1-\beta)F}{R_{gas}T}\phi_{act}\right) - \exp\left(\frac{-\beta F}{R_{gas}T}\phi_{act}\right)) \quad \text{Eq. (4.12)}$$

where  $A_{act}$  is the redox molecule surface area per cell in  $m^2$  and  $k_{act}$  is the redox molecule electron transport rate constant ( $m\ s^{-1}$ ). Note that the modeled ohmic loss and activation loss depend on the value of  $N_{nw}\sigma$  and  $N_{nw}A_{act}k_{act}$ , respectively, where  $N_{nw}$  is the product of cell-specific connection numbers ( $N_{nw,cell}$ ) and the cell density ( $N_{geo}$ ).

At the anode, electrons are transferred from  $Cyt_{red}$  to the electrode:



The flux of electrons to the anode can be described using the Butler–Volmer equation

$$J_c = k_{anode}([Cyt_{red}]\exp\left(\frac{\beta F}{R_{gas}T}(\phi_{anode} - \phi_{Ox/Red}^{0'})\right) - [Cyt_{ox}]\exp\left(\frac{-(1-\beta)F}{R_{gas}T}(\phi_{anode} - \phi_{Ox/Red}^{0'})\right)) \quad \text{Eq. (4.13)}$$

where  $k_{anode}$  is electron off-loading constant that varies with the imposed electrode potential. The difference in  $k_{anode}$  at high (+0.24V) and low potential (-0.1V) reflects the observation that when biofilms grown at low potential were switched to high potential for the short duration of the isotope labeling experiment, the activity pattern appeared to retain

that of a low potential biofilm, suggesting that some features of the biofilm matrix or cell metabolic systems were different between the two conditions (Fig 5F in reference (49)). Notably, the value of  $k_{anode}$  did not affect the shape of the metabolic profile in the low potential simulations, but was necessary to match the maximum observed in the cell activity in the experimental data.

#### *Shift of redox pair mid-potential as a function of external potential*

Experimental studies have shown that redox-active molecule mid-potential in *G. sulfurreducens* biofilms can be regulated by the anode electric potential,(13-18) with at least two different types of redox-active molecule pairs with mid-potentials near -0.07 V and -0.15 V, respectively(14, 15). It has been noted that the low mid-potential redox centers (-0.15 V) are required for cells to function under low electrode potential, while the redox centers poised at -0.07 V only operate at high electrode potential.(17, 18) In our model, this is represented by a switch function that shifts the mid-potential from -0.07 V to -0.15 V at a critical potential  $\phi_c$ . In order to mimic the response of the change of external potential we implement the redox pair mid-potential as a continuous function (see Fig. C2):

$$\phi_{Ox/Red}^{0'} = \frac{x}{e^{y(\phi_{net}-\phi_c)+1}} + z \quad \text{Eq. (4.14)}$$

where constants x, y, and z are set to 0.08 V, -90 [1/V], and -0.15 V, respectively.  $\phi_c$  is the critical shifting potential for mid-potential of redox-active center with a default value of -0.15 V.

#### **Model implementation**

Reflecting the observations of Chadwick et al. (2019), which showed that the variation in  $^{15}\text{N}$  uptake is predominantly in the direction perpendicular to the electrode surface, a one-dimensional dynamic model was implemented in COMSOL Multiphysics

5.4 (COMSOL Inc., Burlington, MA, USA). Batch simulations exploring the parameter space were executed using MATLAB 2018 (MathWorks, Natick, MA, USA), and simulations were run to steady state. Matching the observational data, the thickness of the biofilm was set to 20  $\mu\text{m}$  and 15  $\mu\text{m}$  for simulations under high (+0.24 V) and low (-0.1 V) anode potentials, respectively, with a 1.8 mm bulk-liquid environment beyond the biofilm surface. The concentration fields of acetate,  $\text{HCO}_3^-$ ,  $\text{CO}_2(\text{aq})$ ,  $\text{CO}_3^{2-}$ ,  $\text{H}^+$ , and  $\text{OH}^-$  were simulated subject to diffusive transport and reaction, with aqueous diffusion coefficients listed in Table 4.1. Acid-base reactions govern the dynamic carbonate system and the speciation of cell surface-associated immobile carboxy (R-COOH), phosphate (R- $\text{PO}_4\text{H}_2$ ) and amino groups (R-NH<sub>2</sub>) are simulated using the kinetic implementation described previously (66). The concentrations at the outer domain boundary were set to fixed concentrations reflecting environmental conditions (Table 4.1), which were also used as initial conditions. No flux conditions were imposed at the anode surface, where  $C_{ytred}$  was converted to  $C_{ytox}$  at a rate set by  $J_c$ , representing the off-loading of electrons to electrode.

Table 4.1. Model parameter and description

Symbol	Units	Value (baseline value)	Description	Reference
<b>Constants</b>				
F	C mol <sup>-1</sup>	96485	Faraday constant	
R <sub>gas</sub>	J K <sup>-1</sup> mol <sup>-1</sup>	8.314	Gas constant	
<b>Geometry</b>				
$L_{bio}$	$\mu\text{m}$	15	Growth at low anode potential	(49)
		20	Growth at high anode potential	
$A_{anode}$	cm <sup>2</sup>	3	Anode surface area	
$V_{bio}$	m <sup>3</sup>	$4.5 \times 10^{-9}$	Volume of biofilm at low anode potential	Calculated
		$6 \times 10^{-9}$	Volume of biofilm at high anode potential	
<b>Cell growth and Kinetics</b>				
$f_a$	-	0.08	Fraction of Ac oxidation goes toward anabolism	Estimated
$f_c$	-	0.92	Fraction of Ac oxidation goes toward catabolism	1- $f_a$
T	K	303.15	Temperature	(49)
$k_{cell}$	mol cell <sup>-1</sup> d <sup>-1</sup>	$10^{-14}$ - $10^{-16}$ ( $6 \times 10^{15}$ )	Cell-specific acetate consumption rate constant	Estimated
$N_{geo}$	-	$9.2 \times 10^9$	Number of cells at low anode potential	Calculated

		$1.2 \times 10^{10}$	Number of cells at high anode potential	
$B_{geo}$	cell $m^{-3}$	$2.04 \times 10^{18}$	Cell density	Calculated
$\mu$	$d^{-1}$	varied	Cell growth rate	Calculated
$T_{incub}$	h	6.2	Incubation time	(49)
$F_{label}$	-	0.06	Labeling strength of the $^{15}N$ source	(49)
$F_{final}$	-	varied	Labeling strength at the end of the incubations (nanoSIMS measurement)	(49)
$F_{nat}$	-	0.0036	Natural $^{15}N$ abundance	
$R_{obs}$	famol-Ac cell $^{-1} d^{-1}$	varied	Observed cell-specific metabolic rate	Calculated
$R_{geo}$	famol-Ac cell $^{-1} d^{-1}$	varied	Modeled cell-specific metabolic rate	Simulated
$\rho$	gdw cell $^{-1}$	$9.5 \times 10^{-14}$	Biomass density	Estimated from(67)
$Y_{Ac}$	gdw mol-Ac $^{-1}$	4.32	Growth yield	Calculated
$U_{Ac}$	mM-Ac gdw $^{-1} h^{-1}$		Uptake of acetate	Estimated from (50)
$v_{max}$	mM-Ac gdw $^{-1} h^{-1}$	20	Maximum uptake rate of acetate	
$K_{m,Ac}$	$\mu M$	10	Half-saturation concentration of acetate	
$[R-COOH]_T$	$\mu mol mg^{-1}$	0.25	Total concentration of cell surface carboxy groups	(68-71)
$[R-NH_2]_T$	$\mu mol mg^{-1}$	0.25	Total concentration of cell surface amino groups	
$[R-PO_4H_2]_T$	$\mu mol mg^{-1}$	0.25	Total concentration of cell surface phosphate groups	
<b>Electron conduction</b>				
$C_{ytred}$	mM	varied	Reduced redox-active molecules	Calculated
$C_{ytox}$	mM	varied	Oxidized redox-active molecules	Calculated
$C_{ytot}$	mM	1-100 (10)	Total redox-active molecules ( $C_{ytot} = C_{ytox} + C_{ytred}$ )	Estimated
$D_{eyt}$	$m^2 s^{-1}$	$10^{-5}-10^{-10}$ ( $7 \times 10^{-7}$ )	Effective diffusion coefficient	Calculated
$k_D$	$m^4 mol s^{-1}$	$10^{-5}-10^5$ (100)	Electron transfer rate constant	Estimated
$\delta$	nm	0.7	Spatial distance between adjacent redox-active molecules	(72)
$\sigma$	S $m^{-1}$	$10^{-4}-10^{-2}$ ( $1.5 \times 10^{-3}$ )	Biofilm conductivity	(12, 73-75)
$d$	$\mu m$	varied	Distance from anode surface	Estimated
$A_{nw}$	$m^2$	$1.26 \times 10^{-17}$	Cross-section area of a single pilus	Calculated
$d_{nw}$	nm	4	Diameter of a single pilus	(2)
$A_{act}$	$m^2$	$10^{-14}-10^{-13}$	Redox active surface area	(65)
$\beta$	-	0.5	Charge transfer coefficient	(65)
$k_{EF}$	$m^4 mol s^{-1}$	$10^{-5}-10^5$ (10)	Electric field rate constant	Estimated
$k_{act}$	$m s^{-1}$	$10^{-11}-10^{-8}$ ( $1 \times 10^{-9}$ )	Activation loss rate constant	Estimated
$k_{nw}$	$mol^{-1}$	$10^{17}-10^{20}$ ( $1 \times 10^{19}$ )	Constant associated with conductive biofilm	Estimated
$k_{anode}$	$m s^{-1}$	$10^{-5}-10^{-10}$	Electron off-loading constant at electrode	Estimated
$F_{\theta}$	-	varied	Electric potential dependency	Calculated
$F_{pH}$	-	varied	pH dependency	Calculated
$\phi_{anode}$	V	-0.1 +0.24	Poised low anode potential Poised high anode potential	(49)
$\phi_{ox/red}^{0'}$	V	-0.07, -0.15	Redox-active center mid-potential	(14, 15)
$\phi_{act}$	V	varied	Activation voltage loss	Calculated

$\phi_{om}$	V	varied	Ohmic voltage loss	Calculated
$\phi_{net}$	V	varied	External electric potential	Calculated
$J_c$	$\text{mol m}^{-2} \text{s}^{-1}$	varied	Flux of electrons to the anode	Calculated
$I$	A	varied	Current in biofilms	Calculated
$N_{nw,cell}$	-	1-200 (49)	Number of connections per cell	Estimated
$N_{nw}$	-	$10^{10}$ - $10^{12}$ ( $6 \times 10^{11}$ )	Total number of connections	Estimated
$C_{pH}$	-	6-6.4 (6.15)	Critical pH value at which metabolism is moderately inhibited	Estimated
$\phi_c$	V	-0.15-0.1 (-0.15)	Critical potential at which redox molecule mid-potential is shifted	Estimated

Aqueous diffusion coefficient:  $D_{CO_2} = 1.91 \times 10^{-9} \text{ m}^2 \text{ s}^{-1}$ ,  $D_{CO_3} = 1.19 \times 10^{-9} \text{ m}^2 \text{ s}^{-1}$ ,  $D_{H^+} = 6 \times 10^{-9} \text{ m}^2 \text{ s}^{-1}$ ,  $D_{OH^-} = 5.27 \times 10^{-9} \text{ m}^2 \text{ s}^{-1}$ ,  $D_{acetate} = 6.4 \times 10^{-10} \text{ m}^2 \text{ s}^{-1}$ ,  $D_{NH_4} = 4 \times 10^{-9} \text{ m}^2 \text{ s}^{-1}$ , diffusion coefficients are modified for tortuosity (76) and for the presence of organic molecules (77). Fixed concentration boundary conditions were imposed for all chemical species at the outer domain boundary except for  $CO_2$ ,  $CO_3^{2-}$ ,  $Cyt_{red}$ ,  $R-COOH$ ,  $R-NH_2$ ,  $R-PO_4H_2$ . No flux conditions were imposed at the bulk-biofilm interface and anode surface for  $CO_2$ ,  $CO_3^{2-}$ ,  $Cyt_{red}$ . Fixed concentration boundary conditions were imposed for all chemical species at anode surface except for  $Cyt_{red}$ , in which a flux  $J_c$  (Eq. 13) was imposed to represent the electron discharge onto electrode. Boundary conditions are set to: 20 mM acetate, 23.8 mM  $HCO_3^-$ , pH = 6.8.

## Results and Discussion

### **Spatial resolution on metabolic activity**

Our simulations reproduced the distinct metabolic profiles in *G. sulfurreducens* biofilms under two different anode electric potentials (Fig. 4.1). The model shows that *G. sulfurreducens* were most active close to the electrode surface for both high and low anode electric potentials, with maximum cell-specific activity approximately at 30 fmol cell<sup>-1</sup> day<sup>-1</sup> near the electrode, comparable to the value reported in literature with similar conditions(78). At high anode electric potential (+0.24 V), two metabolic activity peaks were observed at a distance ~2  $\mu\text{m}$  and ~12  $\mu\text{m}$  away from the anode surface, respectively. Metabolic activity was slightly inhibited at the anode surface, whereas no such effect was observed for simulations under low anode potential (-0.1V). In agreement with experimental data, model simulations with low anode potential yield metabolic activity in

*G. sulfurreducens* biofilms approaching zero at a distance  $>10\ \mu\text{m}$  from the electrode, with no secondary peak in activity.

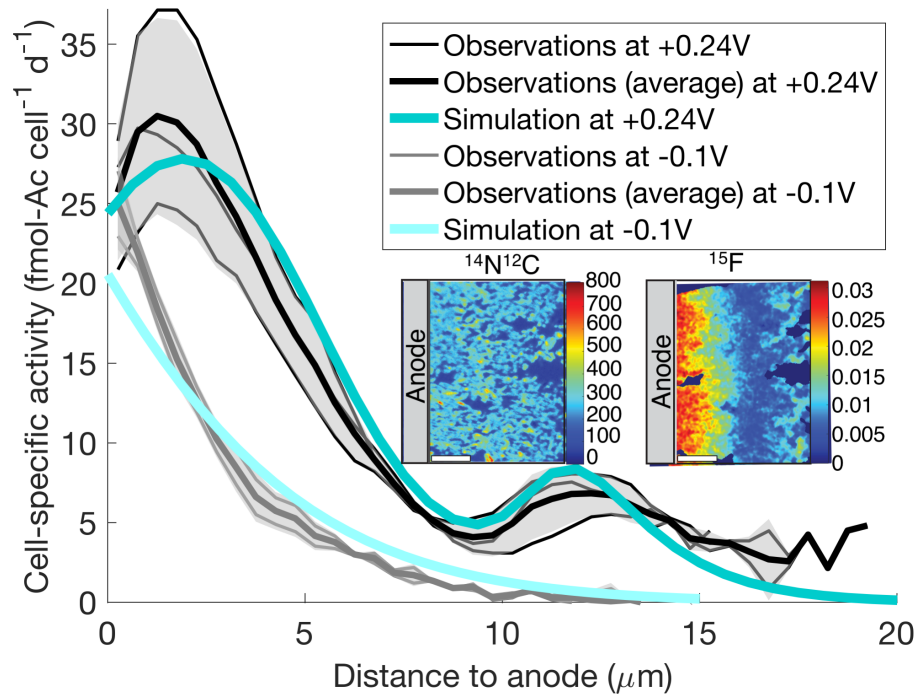


Fig. 4.1. Model validation with <sup>15</sup>N observations using nanoSIMS at high (+0.24V) and low (-0.1V) anode potentials. Average <sup>15</sup>N incorporation values for three biological replicates for the high potential condition and two biological replicates for low potential conditions. Experimental data is binned in half-micron increments from the electrode surface and recast into metabolic rates using Eq.(2). Modeling results (blue lines) are binned in a similar way for direct comparison. Inset: a characteristic nanoSIMS image from a biofilm grown at +0.24V oriented with anode on the left side, bulk media on the right. The <sup>14</sup>N<sup>12</sup>C image shows the extent of the biofilm, while <sup>15</sup>F fractional abundance of <sup>15</sup>N ( $^{15}\text{F} = \frac{^{15}\text{N}^{12}\text{C}}{^{14}\text{N}^{12}\text{C} + ^{15}\text{N}^{12}\text{C}}$ ) reveals both a major peak of isotope incorporation at the biofilm-anode interface and a secondary peak in activity near the biofilm surface. The horizontal white scale bar corresponds to 5 μm.

## Potential losses are the dominant factor shaping the distribution of metabolic activity

In the model, two controlling factors - the electric potential dependency ( $F\theta$ ) and the pH dependency ( $F_{pH}$ ) - contribute to the observed metabolic activity profiles (Fig. C5). Reduced microbial activity with increasing distance from the anode surface is the dominant trend in both experimental data and modeling results (Fig. 4.1), and this pattern is driven by the decreasing electric potential ( $\phi_{\text{net}}$ ) (Fig. 4.2A&B). Two factors, activation loss ( $\phi_{\text{act}}$ ) and ohmic resistance loss ( $\phi_{\text{om}}$ ), contribute in different ways to this potential loss, preventing *G. sulfurreducens* from experiencing the poised anode potential ( $\phi_{\text{anode}}$ ) throughout the biofilm. Activation losses occur in order to overcome the activation energy barrier of a redox reaction(19, 79), such as the transfer of electrons on the conductive biofilms ( $\text{Cyt}_{\text{red}} \rightleftharpoons \text{Cyt}_{\text{ox}} + e^-$ ), and from the biofilm onto the electrode (Rxn 4.2). The ohmic loss results from the electronic resistance on biofilms and at the electrode surface. The combined effect of these losses is that at the anode surface, *G. sulfurreducens* cells experienced an electric potential  $\sim 0$  V and  $\sim -0.17$  V for simulations with the anode poised at +0.24V and -0.1V, respectively. Activation loss dominated in the first 6  $\mu\text{m}$  away from the electrode surface, while ohmic resistance was the main loss term at a farther distance at high anode potential (Fig. 4.2). Together these losses reduce the electric potential experienced by cells in a linear fashion with distance from the anode. This causes the decrease in metabolic activity away from the electrode surface as quantified by the potential constraint ( $F\theta$ ) (Fig. 4.2). Compared to this potential constraint, the pH dependency plays a relatively minor role in this overall activity pattern (Fig. C3), but can

become important under certain incubation conditions and at high anode potentials, as described below.

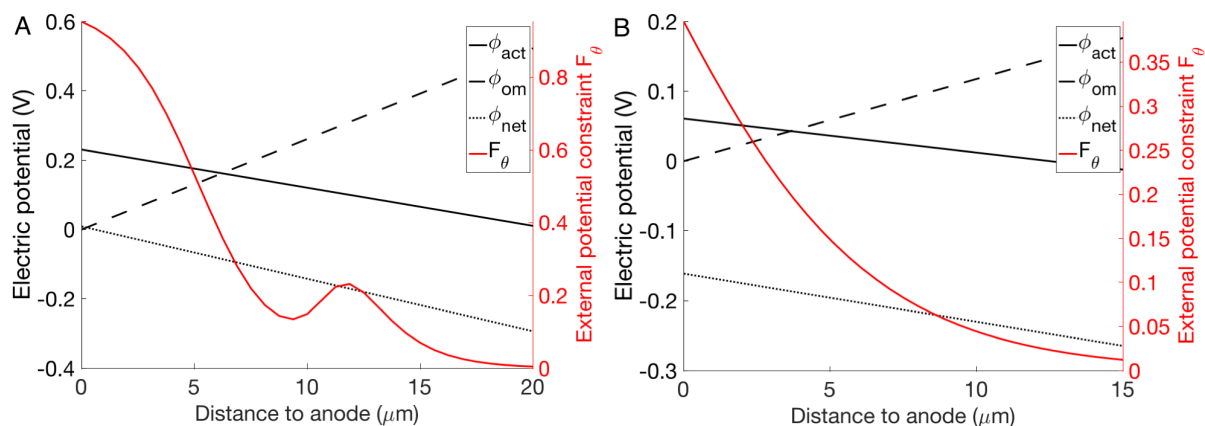


Fig. 4.2. The modeled effects of activation ( $\phi_{\text{act}}$ ) and ohmic resistance ( $\phi_{\text{om}}$ ) losses on net effective electric potential ( $\phi_{\text{net}}$ ) through the biofilm, and the resulting potential constraints on metabolic activity ( $F_\theta$ ) in red. A and B represent model results for high (+0.24V) and low (-0.1V) anode potentials, respectively.

### A secondary metabolic peak arises from redox centers with different midpoint potentials

A secondary metabolic peak at a distance  $> 10 \mu\text{m}$  from the electrode surface was consistently observed for *G. sulfurreducens* biofilms under high anode potential (49). Our model reproduced this feature of the metabolic activity profile (Fig. 4.1), and the pattern arises from the potential constraint  $F_\theta$  (Fig. 4.2A). This second peak observed in the model is caused by switch in the redox center mid-potential  $\phi_{\text{Ox/Red}}^{0'}$  from -0.07 V to -0.15 V, which occurs at a distance of  $\sim 10 \mu\text{m}$  from the electrode where the effective electrical potential ( $\phi_{\text{net}}$ ) crosses the critical potential ( $\phi_c$ ). No secondary peak occurs in biofilms simulated at low anode potential (Fig. 4.2B), because  $\phi_{\text{net}}$  at the anode surface is already below  $\phi_c$ , and therefore the entire biofilm is utilizing the lower potential redox center.

To further explore the effect the shifting mechanism had on the metabolic activity profiles, we varied the critical switching potential  $\phi_c$  from -0.15 V to +0.05 V (Fig. C2). As expected, increasing the critical potential  $\phi_c$  from -0.15V shifted the second activity peak towards the anode surface because  $\phi_{\text{net}}$  crosses the critical threshold more rapidly as  $\phi_c$  increases (Fig. C3). Eventually only one activity peak remained at critical potentials of -0.05V and above. This is because under these conditions, when  $\phi_{\text{net}} < \phi_c$  even at the anode surface the effective potential and the pH inhibition. Furthermore, the critical potential can increase the pH dependency, which exerts its effect primarily at the anode surface (Fig. C4, and discussed below).

### **pH effects on metabolic activity near the anode surface**

A feature of the metabolic activity pattern not explained by potential losses and redox center switching is the slight decrease in activity observed at the anode surface in *G. sulfurreducens* biofilms grown at +0.24V (Fig. 4.1). Simulations show that *G. sulfurreducens* grown at high anode potentials experienced a stronger pH gradient than those at low potential, with pH values at the anode of ~6.15 and ~6.45 at high and low anode potential, respectively (Fig. C3). The decrease of the simulated metabolic activity near the anode surface at high anode potential is attributed to this difference in pH, and is reflected in the model by the decrease in  $F_{pH}$  as pH approaches and falls below the threshold  $C_{pH}$  (Fig. C3A & B).

To better understand the role of pH in shaping biofilm activity we numerically examined the effect of varying experimental conditions and biological model parameters. Examination of the pH threshold shows that  $C_{pH}$  values below 6.15 eliminate the decrease in metabolic activity at the anode surface (see Fig. C6). Conversely, increasing  $C_{pH}$  causes

a more intense drop in  $F_{pH}$  that begins further out in the biofilm, leading to more severe growth inhibition at the anode surface and shifting the first metabolic activity peak farther away from the anode (Fig. C6). We can exclude the possibility that the low metabolic activity was caused by the limited diffusion of substrate to the biofilm, as demonstrated by the high simulated acetate concentrations throughout the biofilm (Fig. C7) and the previously acquired experimental data from thick *G. sulfurreducens* biofilms.(49)

pH inhibition depends on both the pH buffering capacity and the level of metabolic activity. A reduced pH buffering capacity, modeled here by lowering the solution  $\text{HCO}_3^-$  concentration, can significantly limit the removal of  $\text{H}^+$  and subsequently inhibit the metabolic activity on the inner biofilm layer, while a high buffering capacity can diminish the pH inhibition at anode surface (Fig. 4.3 and Fig. C8). These results agree with a recent study showing that lowering phosphate buffer from 100 mM to 12.5 mM resulted in a > 80% decrease of the current production in an anode-respiring bacteria community, owing to the reduced  $\text{H}^+$  transport capacity.(45) As a consequence, anode-respiring *G. sulfurreducens* biofilms may have an active outer-layer and an inactive inner layer if a low pH region develops within the inner layer due to poor buffering capacity of the media.

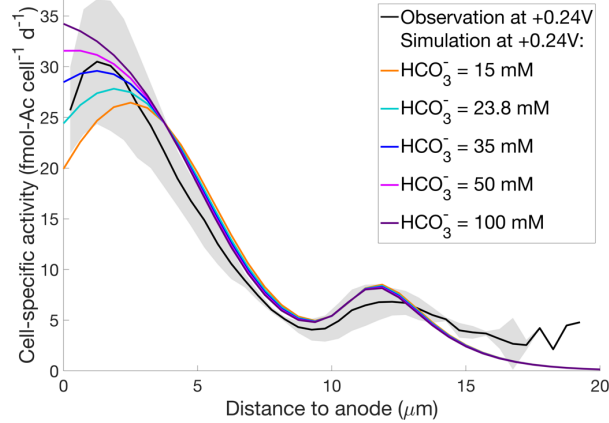


Fig. 4.3. The impact of bicarbonate buffering capacity on activity patterns at high anode potential for the early activity peak near electrode. The shaded area represents 95% confidence interval for the observations.

### Electron conduction and storage within the *G. sulfurreducens* biofilms

Cell-specific electron transfer rate ( $e^- \text{ cell}^{-1} \text{ s}^{-1}$ ) and current ( $\text{fA cell}^{-1}$ ) were estimated using the modeled activity data shown in Fig. 4.1. Model simulation results show maximum cell specific currents of approximately  $200\text{-}250 \text{ fA cell}^{-1}$  ( $1.25 \times 10^6\text{-}1.5 \times 10^6 e^- \text{ cell}^{-1} \text{ s}^{-1}$ ) and  $130 \text{ fA cell}^{-1}$  ( $0.8 \times 10^6 e^- \text{ cell}^{-1} \text{ s}^{-1}$ ) near the electrode at high and low anode potential, respectively (Fig. C9A). The cell-specific current in our model is on the same order of magnitude as earlier reports on *G. sulfurreducens* DL-1 ( $\sim 100 \text{ fA cell}^{-1}$ )(31), *Shewanella oneidensis* MR-1 ( $75\text{-}200 \text{ fA cell}^{-1}$ )(80), and *S. loihica* PV-4 ( $100\text{-}400 \text{ fA cell}^{-1}$ )(81). Furthermore, the simulated current densities ( $3.8 \text{ A m}^{-2}$  and  $1.3 \text{ A m}^{-2}$  at high and low anode potential, respectively) compare favorably to those observed in the experiments modeled here ( $3\text{-}4 \text{ A m}^{-2}$ ) (49) and fall within the range of several reported microbial fuel cells using *G. sulfurreducens*(12, 82).

Many studies suggest that the development of redox gradients as a result of the drop in redox potential with distance from the anode surface is essential for electron hopping in

electroactive biofilms.(19, 48, 83, 84) Our model simulations show redox potentials comparable to observations(84) (see Fig. C9C). The redox gradient was the dominant driving force for electron transport in the system with low anode potential (Fig. C9C), with a linear increase of  $Cyt_{ox}$  concentrations from about 10% of the  $Cyt_{tot}$  at the anode surface to approximately 70% at the outer edge of the biofilm at low anode potential (Fig. C9D). This redox gradient leads to the reduction of redox-active centers coupled to acetate oxidation (Rxn 4.1) by *G. sulfurreducens* cells and the oxidation of redox-active centers at anode surface (Eq 4.13). Additionally, the electric field (i.e. the voltage gradient) can also act as driving force for electron hopping, both when the electro-inactive counterions are immobilized(62, 63, 85) and mobile(86-88). Our model, however, suggests that electric field can be, but not necessarily is, an important additional driving force for electron transport towards the electrode (Fig. C10A). Without the electric field as additional driving force, the cell specific activity pattern remains unaffected at effective diffusion coefficient  $D_{cyt} > 10^{-10} \text{ m}^2 \text{ s}^{-1}$  (Fig. C10A&C), comparable to diffusion coefficients in dilute aqueous solution. At slower diffusion, the cell specific activity was significantly impacted due to the limited transport of  $Cyt_{red}$  (Fig. C10B).

Our simulations reveal that cytochrome-associated electrons in  $Cyt_{red}$  are concentrated at the bulk-biofilm interface and decrease linearly towards the anode surface. Similar observations on the distribution of  $Cyt_{red}$  in *G. sulfurreducens* biofilms have been reported earlier.(19, 25, 26, 35, 48, 89) This distribution determines the redox potential in the biofilms,

$$\Phi_{Ox/Red} = \Phi_{Ox/Red}^{0'} + \frac{R_{gas}T}{F} \ln \left( \frac{[Cyt_{ox}]}{[Cyt_{red}]} \right) \quad \text{Eq. (15)}$$

which reflects the tendency of redox-active centers to accept or release electrons. The increasing  $Cyt_{red}$  concentration towards the bulk-biofilm interface inevitably leads to a decreasing  $\phi_{Ox/Red}$  farther away from the anode surface (Fig. C9D). Indeed, an earlier study directly observed that redox potential decreases significantly with increasing distance from the anode surface. Direct measurement of redox-active center-dependent redox potential may be difficult, as cytochromes are typically inaccessible to equilibrium electrodes in the biofilm matrix.(84) However, the overall oxidation status of redox-active centers can be estimated by electrochemical impedance and adsorption spectroscopy.(13, 24, 90) Those redox titration studies showed that *G. sulfurreducens* biofilms or cytochromes were predominantly reduced at lower potentials,(13, 24, 90) agreeing with our simulation result overall (Fig. C9E). However, those studies suggest that cytochrome would be substantially oxidized above +0.1V. The difference between the experimental observations and our simulations are likely attributed to the experimental procedure in which the cytochrome sample was purified(91, 92) or that *G. sulfurreducens* cells were starved and no acetate was provided prior and during the electrochemical titration(13, 24). Noticeably, electron stored in reduced  $Cyt_{red}$  can be recovered as current when the electric potential is sufficient to transport electrons toward electrode.(25, 93) Assuming each  $Cyt_{red}$  holds one electron, under our modeled conditions the stored electrons in  $Cyt_{red}$  at steady state are estimated to be  $\sim 1.84\text{-}1.99 \times 10^{-18}$  mol  $e^-$  cell $^{-1}$  and  $0.8\text{-}3.4 \times 10^{-18}$  mol  $e^-$  cell $^{-1}$  at high and low anode potential setting respectively, with more stored electrons in  $Cyt_{red}$  at the biofilm surface. Assuming minimum maintenance requirement at  $1.9 \times 10^{-2}$  mol  $e^-$  gdw $^{-1}$  h $^{-1}$  (51) and biomass density  $\rho$  at  $9.5 \times 10^{-14}$  gdw cell $^{-1}$  (Table 4.1), then the stored electrons in  $Cyt_{red}$  at steady state would be sufficient to support such a basic rate for approximately 7 min and

11 min at high and low anode potential setting, respectively, even when electrode is disconnected. This is similar to reported value (8 min) from Esteve-Núñez et al. (2008)(94).

### Sensitivity analysis

Nine model parameters that are poorly constrained were considered in a sensitivity analysis. This included the cell-specific rate constant ( $k_{cell}$ ), the activation constant ( $k_{act}$ ), the electron transport rate constant ( $k_D$ ), the electric field driven rate constant ( $k_{EF}$ ), the electrode discharge constant ( $k_{anode}$ ), the abundance of redox-active molecules ( $Cyt_{tot}$ ), the density of conductive network connections ( $N_{nw,cell}$ ), biofilm conductivity ( $\sigma$ ), and the redox-active cell surface area ( $A_{act}$ ). Our results show that  $k_{cell}$  influenced the magnitude and location of both first and second metabolic peak, while  $k_{act}$  primarily influenced the location of first and second metabolic peak,  $k_{anode}$  mainly affected the magnitude of both first and second metabolic peak,  $k_D$  and  $k_{EF}$  showed negligible impact (Fig. 4.4A-E). Although the relative magnitude of impact on potential losses and pH was limited (Fig. C11), a reduction in  $k_{cell}$  and  $k_{anode}$  led to lower metabolic rates and diminished the first metabolic peak (Fig. 4.4A&E) as a result of slightly increased pH (Fig. C11D). Noticeably, the model results became less sensitive to  $k_{anode}$  at high values. For instance, increasing  $k_{anode}$  from  $2.8 \times 10^{-8} \text{ m s}^{-1}$  to  $1.12 \times 10^{-7} \text{ m s}^{-1}$  had little impact on the metabolic pattern (Fig. 4.4E).

In contrast, electrochemical properties of the *G. sulfurreducens* biofilm had a significantly greater impact on the metabolic activity (Fig. 4.4F-H). Simulations show that  $Cyt_{tot}$  significantly influenced the magnitude and location of both first and second metabolic peak, while  $N_{nw,cell}$ ,  $\sigma$ , and  $A_{act}$  primarily influenced the location of first and second metabolic peak. Increasing  $Cyt_{tot}$ ,  $N_{nw,cell}$ ,  $\sigma$  and  $A_{act}$  increased the metabolic activity

(Fig. 4.4F-H), but also decreased the activity near the electrode by substantially lowering pH (Fig. C11D). Our model simulations showed that increasing biofilm conductivity four-fold to  $0.06 \text{ S m}^{-1}$  diminished the ohmic resistance loss (Fig. C11A) in the *G. sulfurreducens* biofilms, while activation loss (Fig. C11B) substantially increased and pH was significantly lowered (Fig. C12D) near the electrode, thus making the electric potential more positive (Fig. C11C). This is in line with an earlier study showing that biofilms with a relatively high conductivity ( $\geq 0.05 \text{ S m}^{-1}$  (42) or  $\sim 0.1 \text{ S m}^{-1}$  (95)) had negligible potential losses, with only proton transport being a limiting factor (42).

Close examination of the anodic current density suggests that increasing those model parameters, except the electron conduction rate constant ( $k_D$ ) and electric field transport constant ( $k_{EF}$ ), lead to an increase of current density at the anode (Fig. 4.4). Earlier studies found that current density of *G. sulfurreducens* was correlated with biomass density (cells per unit anode surface area) on the anode (78). Under conditions where growth efficiency remains relatively constant (see Figs. S1&S4), higher cell-specific activity implies higher biomass density assuming constant biofilm thickness. Noticeably, electrochemical properties of the *G. sulfurreducens* biofilms such as the abundance of redox-active molecules ( $Cyt_{tot}$ ), the density of conductive network connections ( $N_{nw,cell}$ ), biofilm conductivity ( $\sigma$ ) showed relatively higher impact on the anodic current density than the rest of parameters shown in Fig. 4.4. A significant increase of current density by a factor of 43%, 29% and 25% was observed by increasing  $Cyt_{tot}$ ,  $N_{nw,cell}$  and  $\sigma$  four-fold (Fig. 4.4). Our simulation results suggest anodic current density can be increased even though the cell metabolism at the anode surface is limited by the accumulation of protons (Fig. 4.4 and Fig. C12).

Analyzing model parameter sensitivities also allowed us to assess the controversy over the stratification of cell activity in *G. sulfurreducens* biofilms, with reports of peak activities near(35, 82, 96-98) and away from the anode surface(99, 100). Anode-respiring *G. sulfurreducens* biofilms may show a stratified biofilm structure with a live outer-layer and dead inner layer if a low pH region develops within the inner layer. As indicated by the metabolic activity profiles in Fig. 4.4, the location of the peak cell-specific activity depends on the distinct electrochemical properties of the biofilm, which in turn affects current densities (Fig. 4.4). It is possible that these electrochemical properties and metabolic activity can be regulated and optimized under different environment conditions.(101-105) As a consequence, different incubation conditions can lead to biofilms that have different abilities to control potential losses and H<sup>+</sup> transport yielding observations that differ in active cell layer stratification in *G. sulfurreducens* biofilms. (99, 100) (35, 82, 96-98).

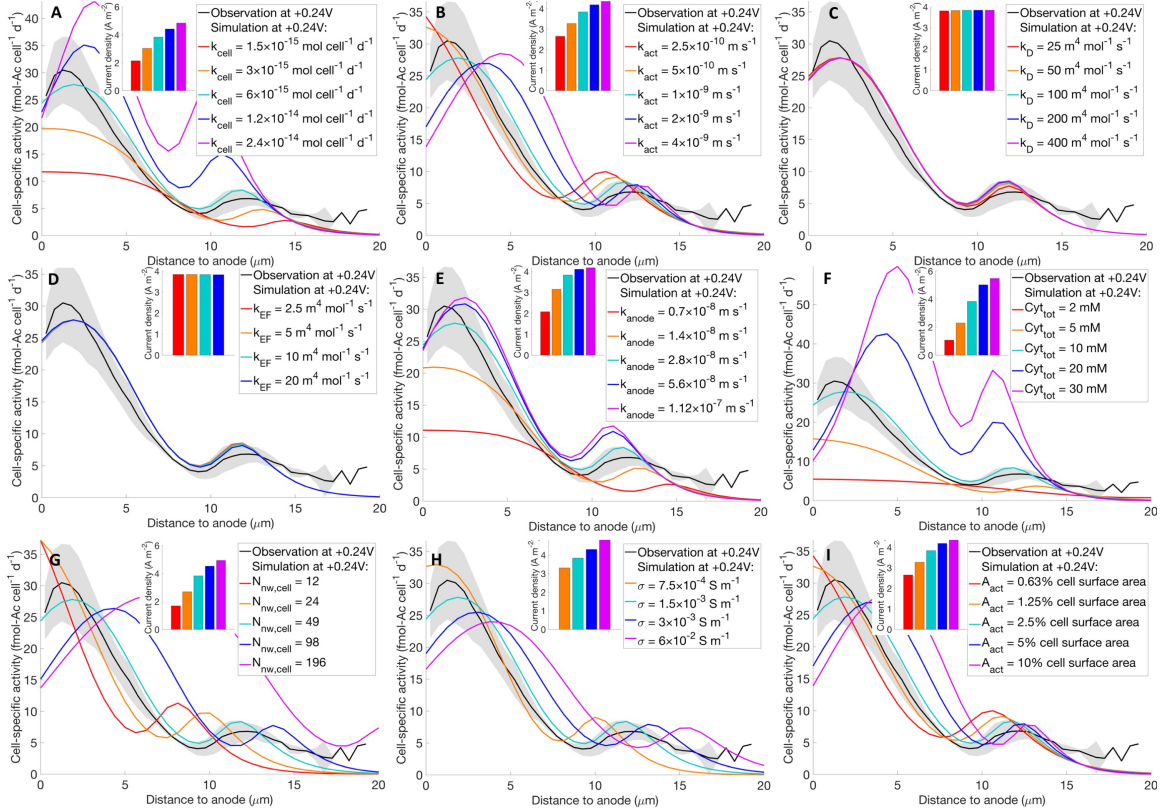


Fig. 4.4. Sensitivity analysis of model parameters and their impact on cell specific activity and current density (inset): (A) cell-specific rate constant; (B) activation constant; (C) electron transport rate constant; (D) electric field driven rate constant; (E) electrode discharge constant; (F) the abundance of redox-active molecules; (G) the density of conductive network connections; (H) conductive biofilm conductivity; (I) redox-active cell surface area. Shaded area represents 95% confidence interval for observations.

### Implications

This model synthesizes existing knowledge and establishes a quantitative framework of the extracellular electron transfer in anode-respiring *G. sulfurreducens* biofilms that can further guide experimental studies on kinetic and electrochemical properties of *G. sulfurreducens* biofilms under different growth conditions. We have identified experimentally tunable parameters such as media buffering capacity that can lead

to markedly different metabolic activity patterns, which can serve as valuable future experimental tests of the validity of our modeling framework. Additionally, biofilms grown with mutant strains of *G. sulfurreducens* lacking the low potential redox-active system CbcL could test our prediction that the second activity peak is due to a switch in redox centers(106), providing a connection between genetically encoded metabolic proteins and cellular activity in biofilms. This approach of combining spatially resolved metabolic modeling with high resolution quantitative activity imaging provides much greater ability to constrain models, as compared to those only considering bulk processes such as the concentration of chemical species in the media and total current density. Finally, our model provides a foundation for optimizing MFCs design for higher current densities. High buffering capacity is needed to maintain a healthy pH condition particularly near the electrode, but efforts to reduce potential losses by increasing conductivity, the abundance of redox-active centers and conductive network density through genetic engineering will likely have the greatest positive impact on overall metabolic activity and current production.

#### Acknowledgements

This work was supported by the U.S. Department of Energy, Office of Science, Office of Biological and Environmental Research, Genomic Science Program under Award Number DE-SC0016469 and DE-SC0020373 (to CM and VJO). We thank D. Bond for assisting with the initial *G. sulfurreducens* bioreactor experiments used in this study.

## References

1. Rotaru A-E, Shrestha PM, Liu F, Markovaite B, Chen S, Nevin KP, et al. Direct interspecies electron transfer between *Geobacter metallireducens* and *Methanosarcina barkeri*. *Appl Environ Microbiol.* 2014;**80**:4599-605.
2. Malvankar NS, Vargas M, Nevin KP, Franks AE, Leang C, Kim BC, et al. Tunable metallic-like conductivity in microbial nanowire networks. *Nat Nanotechnol.* 2011;**6**:573-9.
3. Viridis B, Millo D, Donose BC, Lu Y, Batstone DJ, Krömer JO. Analysis of electron transfer dynamics in mixed community electroactive microbial biofilms. *RSC Adv.* 2016;**6**:3650–60.
4. Ordóñez MV, Schrott GD, Massazza DA, Busalmen JP. The relay network of *Geobacter* biofilms. *Energy Environ Sci.* 2016;**9**:2677–81.
5. Saunders SH, Tse ECM, Yates MD, Otero FJ, Trammell SA, Stemp EDA, et al. Extracellular DNA promotes efficient extracellular electron transfer by pyocyanin in *Pseudomonas aeruginosa* biofilms. *bioRxiv.* 2019;doi:<https://doi.org/10.1101/2019.12.12.872085>.
6. He X, Chadwick G, Kempes C, Shi Y, McGlynn S, Orphan V, et al. Microbial interactions in the anaerobic oxidation of methane: model simulations constrained by process rates and activity patterns. *Environ Microbiol.* 2019;**21**(2):631-47.
7. Summers ZM, Fogarty HE, Leang C, Franks AE, Malvankar NS, Lovley DR. Direct exchange of electrons within aggregates of an evolved syntrophic coculture of anaerobic bacteria. *Science.* 2010;**330**:1413–5.

8. Manzella MP, Reguera G, Kashefi K. Extracellular electron transfer to Fe (III) oxides by the hyperthermophilic archaeon *Geoglobus ahangari* via a direct contact mechanism. *Appl Environ Microbiol.* 2013;**79**(15):4694-700.
9. Kracke F, Vassilev I, Krömer JO. Microbial electron transport and energy conservation—the foundation for optimizing bioelectrochemical systems. *Front Microbiol.* 2015;**6**:575.
10. Cologgi DL, Lampa-Pastirk S, Speers AM, Kelly SD, Reguera G. Extracellular reduction of uranium via *Geobacter* conductive pili as a protective cellular mechanism. *PNAS.* 2011;**108**(37):15248–52.
11. Bond DR, Lovley DR. Electricity Production by *Geobacter sulfurreducens* Attached to Electrodes. *Appl Environ Microbiol.* 2003;**69**(3):1548–55.
12. Malvankar NS, Tuominen MT, Lovley DR. Biofilm conductivity is a decisive variable for high-current-density *Geobacter sulfurreducens* microbial fuel cells. *Energy Environ Sci.* 2012;**5**(2):5790-7.
13. Li DB, Li J, Liu DF, Ma X, Cheng L, Li WW, et al. Potential regulates metabolism and extracellular respiration of electroactive *Geobacter* biofilm. *Biotechnol Bioeng.* 2019;**116**(5):961-71.
14. Yoho RA, Papat SC, Torres CI. Dynamic Potential-Dependent Electron Transport Pathway Shifts in Anode Biofilms of *Geobacter sulfurreducens*. *ChemSusChem.* 2014;**7**(12):3413-9.
15. Rimboud M, Quemener ED-L, Erable B, Bouchez T, Bergel A. Multi-system Nernst–Michaelis–Menten model applied to bioanodes formed from sewage sludge. *Bioresour Technol.* 2015;**195**:192-69.

16. Yoho RA, Popat SC, Rago L, Guisasola A, Torres CI. Anode biofilms of *Geoalkalibacter ferrihydriticus* exhibit electrochemical signatures of multiple electron transport pathways. *Langmuir*. 2015;**31**(45):12552-9.
17. Levar CE, Chan CH, Mehta-kolte MG, Bond DR. An inner membrane cytochrome required only for reduction of high redox potential extracellular electron acceptors. *MBio*. 2014;**5**(6):1-9.
18. Zacharoff L, Chan CH, Bond DR. Reduction of low potential electron acceptors requires the CbcL inner membrane cytochrome of *Geobacter sulfurreducens*. *Bioelectrochemistry*. 2016;**107**:7-13.
19. Strycharz-Glaven SM, Snider RM, Guiseppi-Elie A, Tender LM. On the electrical conductivity of microbial nanowires and biofilms. *Energy Environ Sci*. 2011;**4**:4366–79.
20. Korth B, Rosa LF, Harnisch F, Picioreanu C. A framework for modeling electroactive microbial biofilms performing direct electron transfer. *Bioelectrochemistry*. 2015;**106**:194-206.
21. Bonanni PS, Bradley DF, Schrott GD, Busalmen JP. Limitations for current production in *Geobacter sulfurreducens* biofilms. *ChemSusChem*. 2013;**6**(4):711-20.
22. Rousseau R, Delia M-L, Bergel A. A theoretical model of transient cyclic voltammetry for electroactive biofilms. *Energy Environ Sci*. 2014;**7**:1079-94.
23. Malvankar NS, Mester T, Tuominen MT, Lovley DR. Supercapacitors Based on c-Type Cytochromes Using Conductive Nanostructured Networks of Living Bacteria. *ChemPhysChem*. 2012;**13**:463–8.

24. Liu Y, Kim H, Franklin RR, Bond DR. Linking Spectral and Electrochemical Analysis to Monitor C-Type Cytochrome Redox Status in Living *Geobacter sulfurreducens* Biofilms. *ChemPhysChem*. 2011;**12**:2235– 41.
25. Lebedev N, Strycharz-Glaven SM, Tender LM. Spatially Resolved Confocal Resonant Raman Microscopic Analysis of Anode-Grown *Geobacter sulfurreducens* Biofilms. *ChemPhysChem*. 2014;**15**:320– 7.
26. Liu Y, Bond DR. Long-distance electron transfer by *G. sulfurreducens* biofilms results in accumulation of reduced c-type cytochromes. *ChemSusChem*. 2012;**5**:1047–53.
27. Lebedev N, Stroud RM, Yates MD, Tender LM. Spatially Resolved Chemical Analysis of *Geobacter sulfurreducens* Cell Surface. *ACS nano*. 2019;**13**(4):4834-42.
28. Lovley DR, Nevin KP. A shift in the current: new applications and concepts for microbe-electrode electron exchange. *Curr Opin Chem Biol*. 2011;**22**(3):441-8.
29. Schröder U. Anodic electron transfer mechanisms in microbial fuel cells and their energy efficiency. *Phys Chem Chem Phys*. 2007;**9**(21):2619-29.
30. Busalmen JP, Esteve-Núñez A, Berná A, Feliu JM. C-type cytochromes wire electricity-producing bacteria to electrodes. *Angew Chem*. 2008;**47**(26):4874-7.
31. Jiang X, Hu J, Petersen ER, Fitzgerald LA, Jackan CS, Lieber AM, et al. Probing single-to multi-cell level charge transport in *Geobacter sulfurreducens* DL-1. *Nat Commun*. 2013;**4**(1):1-6.
32. Reguera G, McCarthy KD, Mehta T, Nicoll JS, Tuominen MT, Lovley DR. Extracellular electron transfer via microbial nanowires. *Nature*. 2005;**435**(7045):1098.

33. Lampa-Pastirk S, Veazey JP, Walsh KA, Feliciano GT, Steidl RJ, Tessmer SH, et al. Thermally Activated Charge Transport in Microbial Protein Nanowires. *Sci Rep.* 2016;**6**:23517.
34. Malvankar NS, Yalcin SE, Tuominen MT, Lovley DR. Visualization of Charge Propagation Along Individual Pili Proteins Using Ambient Electrostatic Force Microscopy. *Nat Nanotechnol.* 2014;**9**:1012– 7.
35. Steidl RJ, Lampa-Pastirk S, Reguera G. Mechanistic stratification in electroactive biofilms of *Geobacter sulfurreducens* mediated by pilus nanowires. *Nat Commun.* 2016;**7**:12217.
36. Vargas M, Malvankar NS, Tremblay PL, Leang C, Smith JA, Patel P, et al. Aromatic amino acids required for pili conductivity and long-range extracellular electron transport in *Geobacter sulfurreducens*. *MBio.* 2013;**4**(2):e00105-13.
37. Liu X, Tremblay PL, Malvankar NS, Nevin KP, Lovley DR, Vargas M. *Geobacter sulfurreducens* strain expressing *Pseudomonas aeruginosa* type IV pili localizes OmcS on pili but is deficient in Fe (III) oxide reduction and current production. *Appl Environ Microbiol.* 2014;**80**(3):1219-24.
38. Wang F, Gu Y, O'Brien JP, Sophia MY, Yalcin SE, Srikanth V, et al. Structure of microbial nanowires reveals stacked hemes that transport electrons over micrometers. *Cell.* 2019;**177**(2):361-9.
39. Liu X, Zhuo S, Rensing C, Zhou S. Syntrophic growth with direct interspecies electron transfer between pili-free *Geobacter* species. *The ISME J.* 2018;**12**(9):2142.
40. Meile C, Scheibe TD. Reactive transport modeling of microbial dynamics. *Elements.* 2019;**15**(2):111-6.

41. Marcus AK, Torres CI, Rittmann BE. Conduction-based modeling of the biofilm anode of a microbial fuel cell. *Biotechnol Bioeng.* 2007;**98**(6):1171-82.
42. Torres CI, Marcus AK, Parameswaran P, Rittmann BE. Kinetic Experiments for Evaluating the Nernst-Monod Model for Anode-Respiring Bacteria (ARB) in a Biofilm Anode. *Environ Sci Technol.* 2008;**42**(17):6593-7.
43. He X, Chadwick G, Kempes C, Shi Y, McGlynn S, Orphan V, et al. Microbial interactions in the anaerobic oxidation of methane: Model simulations constrained by process rates and activity patterns. *Environ Microbiol.* 2019;**21**(2):631-47.
44. He X, Chadwick GL, Kempes C, Orphan VJ, Meile C. Controls on interspecies electron transport and size limitation of anaerobically methane oxidizing microbial consortia. 2020;Under review.
45. Torres C, Kato Marcus A, Rittmann B. Proton transport inside the biofilm limits electrical current generation by anode-respiring bacteria. *Biotechnol Bioeng.* 2008;**100**(5):872-81.
46. Franks AE, Nevin KP, Jia HF, Izallalen M, Woodard TL, Lovley DR. Novel strategy for three-dimensional real-time imaging of microbial fuel cell communities: Monitoring the inhibitory effects of proton accumulation within the anode biofilm. *Energy Environ Sci.* 2009;**2**(1):113–9.
47. Logan BE. Exoelectrogenic bacteria that power microbial fuel cells. *Nat Rev Microbiol.* 2009;**7**(5):375-81.
48. Snider RM, Strycharz-Glaven SM, Tsoi SD, Erickson JS, Tender LM. Long-range electron transport in *Geobacter sulfurreducens* biofilms is redox gradient-driven. *PNAS.* 2012(109):15467–72.

49. Chadwick GL, Otero FJ, Gralnick JA, Bond DR, Orphan VJ. NanoSIMS imaging reveals metabolic stratification within current-producing biofilms. PNAS. 2019;**116**(41):20716-24.
50. King EL, Tuncay K, Ortoleva P, Meile C. In silico *Geobacter sulfurreducens* metabolism and its representation in reactive transport models. Appl Environ Microbiol. 2009;**75**(1):83-92.
51. Esteve-Núñez A, Rothermich M, Sharma M, Lovley D. Growth of *Geobacter sulfurreducens* under nutrient-limiting conditions in continuous culture. Environ Microbiol. 2005;**7**(5):641-8.
52. Tang YJ, Chakraborty R, Martín HG, Chu J, Hazen TC, Keasling JD. Flux Analysis of Central Metabolic Pathways in *Geobacter metallireducens* during Reduction of Soluble Fe(III)-Nitrilotriacetic Acid. Appl Environ Microbiol. 2007;**73**:3859–64.
53. LaRowe DE, Dale AW, Amend JP, Van Cappellen P. Thermodynamic limitations on microbially catalyzed reaction rates. Geochim Cosmochim Acta. 2012;**90**:96-109.
54. Malvankar NS, Vargas M, Nevin KP, Franks AE, Leang C, Kim B-C, et al. Tunable metallic-like conductivity in microbial nanowire networks. Nat Nanotechnol. 2011;**6**(9):573-9.
55. Malvankar NS, Tuominen MT, Lovley DR. Lack of cytochrome involvement in long-range electron transport through conductive biofilms and nanowires of *Geobacter sulfurreducens*. Energy Environ Sci. 2012;**5**:8651-9.
56. Edwards PP, Gray HB, Lodge MTJ, Williams RJP. Electron transfer and electronic conduction through an intervening medium. Angew Chem. 2008;**47**:6758–65.

57. Strycharz SM, Malanoski AP, Snider RM, Yi H, Lovley DR, Tender LM. Application of cyclic voltammetry to investigate enhanced catalytic current generation by biofilm-modified anodes of *Geobacter sulfurreducens* strain DL1 vs. variant strain KN400. *Energy Environ Sci.* 2011;**4**:896-913.
58. Bond DR, Strycharz-Glaven SM, Tender LM, Torres CI. On electron transport through *Geobacter* biofilms. *ChemSusChem.* 2012;**5**(6):1099-105.
59. Yan H, Chuang C, Zhugayevych A, Tretiak S, Dahlquist FW, Bazan GC. Inter-Aromatic Distances in *Geobacter Sulfurreducens* Pili Relevant to Biofilm Charge Transport. *Adv Mater.* 2015;**27**(11):1908-11.
60. Bonanni PS, Massazza D, Busalmen JP. Stepping stones in the electron transport from cells to electrodes in *Geobacter sulfurreducens* biofilms. *Phys Chem Chem Phys.* 2013;**15**(25):10300-6.
61. Waleed Shinwari M, Jamal Deen M, Starikov EB, Cuniberti G. Electrical conductance in biological molecules. *Adv Funct Mater.* 2010;**20**:1865–83.
62. Dalton EF, Surridge NA, Jernigan JC, Wilbourn KO, Facci JS, Murray RW. Charge transport in electroactive polymers consisting of fixed molecular redox sites. *Chem Phys.* 1990;**141**(1):143-57.
63. Jernigan JC, Surridge NA, Zvanut ME, Silver M, Murray RW. Electrical-field-driven electron self-exchange in a mixed-valent osmium(II/III) bipyridine polymer: solid-state reactions of low exothermicity. *J Phys Chem.* 1989;**93**(11):4620-7.
64. Saito J, Murugan M, Deng X, Guionet A, Miran W, Okamoto A. Electrochemical Techniques and Applications to Characterize Single- and Multicellular Electric Microbial

Functions. In: Krishnaraj RN, Sani RK, editors. Bioelectrochemical Interface Engineering. Hoboken, NJ: John Wiley & Sons, Inc.; 2020. p. 37-54.

65. Storck T, Virdis B, Batstone DJ. Modelling extracellular limitations for mediated versus direct interspecies electron transfer. ISME J. 2016;**10**(3):621-31.

66. Zeebe RE, Wolf-Gladrow D. Chapter 2. Kinetics. In: Halpern D, editor. CO<sub>2</sub> in Seawater: Equilibrium, Kinetics, Isotopes. 3rd ed. San Diego, USA: Elsevier Science; 2005.

67. Yi H, Nevin KP, Kim BC, Franks AE, Klimes A, Tender LM, et al. Selection of a variant of *Geobacter sulfurreducens* with enhanced capacity for current production in microbial fuel cells. Biosens Bioelectron. 2009;**24**(12):3498-503.

68. Jiang W, Saxena A, Song B, Ward BB, Beveridge TJ, Myneni SC. Elucidation of functional groups on gram-positive and gram-negative bacterial surfaces using infrared spectroscopy. Langmuir. 2004;**20**(26):11433-42.

69. Chang E, Brewer AW, Park DM, Jiao Y, Lammers LN. Surface complexation model of rare earth element adsorption onto bacterial surfaces with lanthanide binding tags. Appl Geochem. 2020;**112**:104478.

70. Van der Wal A. Chapter 3. Determination of the total charge in the cell walls of Gram-positive bacteria. Electrochemical characterization of the bacterial cell surface: Wageningen Agricultural University, University, Wageningen, The Netherlands.; 1996.

71. Konhauser K. Chapter 3. Cell surface reactivity and metal sorption. In: Konhauser K, editor. Introduction to geomicrobiology: Blackwell Publishing; 2006.

72. Polizzi NF, Skourtis SS, Beratan DN. Physical constraints on charge transport through bacterial nanowires. Faraday Discuss. 2012;**155**:43-61.

73. Dhar BR, Ryu H, Ren H, Domingo JWS, Chae J, Lee HS. High Biofilm Conductivity Maintained Despite Anode Potential Changes in a *Geobacter*-Enriched Biofilm. *ChemSusChem*. 2016;**9**(24):3485-91.
74. Yates MD, Golden JP, Roy J, Strycharz-Glaven SM, Tsoi S, Erickson JS, et al. Thermally activated long range electron transport in living biofilms. *Phys Chem Chem Phys*. 2015;**17**(48):32564-70.
75. Adhikari RY, Malvankar NS, Tuominen MT, Lovley DR. Conductivity of individual *Geobacter pili*. *RSC Advances*. 2016;**6**(10):8354-7.
76. Boudreau BP. *Diagenetic models and their implementation*: Springer-Verlag; 1997.
77. Stewart PS. Diffusion in biofilms. *J Bacteriol*. 2003;**185**(5):1485–91.
78. Ishii SI, Watanabe K, Yabuki S, Logan BE, Sekiguchi Y. Comparison of electrode reduction activities of *Geobacter sulfurreducens* and an enriched consortium in an air-cathode microbial fuel cell. *Appl Environ Microbiol*. 2008;**74**(23):7348-55.
79. Larsson S. Conductivity in Cuprates Arises from Two Different Sources: One-Electron Exchange and Disproportionation. *J Supercond Nov Magn*. 2017;**30**(2):275-85.
80. McLean JS, Wanger G, Gorby YA, Wainstein M, McQuaid J, Ishii SI, et al. Quantification of electron transfer rates to a solid phase electron acceptor through the stages of biofilm formation from single cells to multicellular communities. *Environ Sci Technol*. 2010;**44**(7):2721-7.
81. Liu H, Newton GJ, Nakamura R, Hashimoto K, Nakanishi S. Electrochemical characterization of a single electricity-producing bacterial cell of *Shewanella* by using optical tweezers. *Angew Chem Int Ed*. 2010;**49**(37):6596-9.

82. Nevin KP, Richter H, Covalla SF, Johnson JP, Woodard TL, Orloff AL, et al. Power output and columbic efficiencies from biofilms of *Geobacter sulfurreducens* comparable to mixed community microbial fuel cells. *Environ Microbiol.* 2008;**10**(10):2505-14.
83. Lin S, Usov PM, Morris AJ. The role of redox hopping in metal–organic framework electrocatalysis. *Chem Commun.* 2018;**54**:6965-74.
84. Babauta JT, Nguyen HD, Harrington TD, Renslow R, Beyenal H. pH, Redox Potential and Local Biofilm Potential Microenvironments Within *Geobacter sulfurreducens* Biofilms and Their Roles in Electron Transfer. *Biotechnol Bioeng.* 2012;**109**(10):2651–62.
85. Jernigan JC, Murray RW. Consequences of restricted ion mobility in electron transport through films of a polymeric osmium-polypyridine complex. *J Phys Chem.* 1987;**91**(8):2030-2.
86. Savéant JM. Electron hopping between fixed sites: “Diffusion” and “migration” in counter-ion conservative redox membranes at steady state. *J Electroanal Chem.* 1988;**242**(1-2):1-21.
87. Savéant JM. Electron hopping between fixed sites: Equivalent diffusion and migration laws. *J Electroanal Chem.* 1986;**201**(1):211-3.
88. Buck RP. Diffusion-migration impedances for finite, one-dimensional transport in thin-layer and membrane cells: Part II. Mixed conduction cases: Os(III)/Os(II)ClO<sub>4</sub> polymer membranes including steady-state I–V responses. *J Electroanal Chem.* 1987;**219**(1-2):23-48.

89. Robuschi L, Tomba JP, Schrott GD, Bonanni PS, Desimone PM, Busalmen JP. Spectroscopic slicing to reveal internal redox gradients in electricity-producing biofilms. *Angew Chem Int Ed*. 2013;**52**(3):925-8.
90. Jain A, Gazzola G, Panzera A, Zanoni M, Marsili E. Visible spectroelectrochemical characterization of *Geobacter sulfurreducens* biofilms on optically transparent indium tin oxide electrode. *Electrochim Acta*. 2011;**56**(28):10776–85.
91. Inoue K, Qian X, Morgado L, Kim B-C, Mester T, Izallalen M, et al. Purification and Characterization of OmcZ, an Outer-Surface, Octaheme c-Type Cytochrome Essential for Optimal Current Production by *Geobacter sulfurreducens*. *Appl Environ Microbiol*. 2010;**76**(12):3999-4007.
92. Qian X, Mester T, Morgado L, Arakawa T, Sharma ML, Inoue K, et al. Biochemical characterization of purified OmcS, a c-type cytochrome required for insoluble Fe (III) reduction in *Geobacter sulfurreducens*. *Biochim Biophys Acta*. 2011;**1807**(4):404-12.
93. Bonanni PS, Schrott GD, Robuschi L, Busalmen JP. Charge accumulation and electron transfer kinetics in *Geobacter sulfurreducens* biofilms. *Energy Environ Sci*. 2012;**5**(3):6188-95.
94. Esteve-Núñez A, Sosnik J, Visconti P, Lovley DR. Fluorescent properties of c-type cytochromes reveal their potential role as an extracytoplasmic electron sink in *Geobacter sulfurreducens*. *Environ Microbiol*. 2008;**10**(2):497-505.
95. Torres CI, Marcus AK, Lee HS, Parameswaran P, Krajmalnik-Brown R, Rittmann BE. A kinetic perspective on extracellular electron transfer by anode-respiring bacteria. *FEMS Microbiol Rev*. 2010;**34**(1):3-17.

96. Schrott GD, Ordoñez MV, Robuschi L, Busalmen JP. Physiological stratification in electricity-producing biofilms of *Geobacter sulfurreducens*. *ChemSusChem*. 2014;**7**:598–603.
97. Reguera G, Nevin KP, Nicoll JS, Covalla SF, Woodard TL, Lovley DR. Biofilm and nanowire production leads to increased current in *Geobacter sulfurreducens* fuel cells. *Appl Environ Microbiol*. 2006;**72**:7345-8.
98. Franks AE, Glaven RH, Lovley DR. Real-time spatial gene expression analysis within current-producing biofilms. *ChemPhysChem*. 2012;**5**:1092–8.
99. Sun D, Chen J, Huang H, Liu W, Ye Y, Cheng S. The effect of biofilm thickness on electrochemical activity of *Geobacter sulfurreducens*. *Int J Hydrogen Energy*. 2016;**41**(37):16523-8.
100. Sun D, Cheng S, Zhang F, Logan BE. Current density reversibly alters metabolic spatial structure of exoelectrogenic anode biofilms. *J Power Sources*. 2017;**356**:566–71.
101. Richter LV, Sandler SJ, Weis RM. Two isoforms of *Geobacter sulfurreducens* PilA have distinct roles in pilus biogenesis, cytochrome localization, extracellular electron transfer, and biofilm formation. *J Bacteriol*. 2012;**194**(10):2551-63.
102. Ueki T, Lovley DR. Genome-wide gene regulation of biosynthesis and energy generation by a novel transcriptional repressor in *Geobacter* species. *Nucleic Acids Res*. 2010;**38**(3):810–21.
103. Nevin KP, Kim B-C, Glaven RH, Johnson JP, Woodard TL, Methé BA, et al. Anode biofilm transcriptomics reveals outer surface components essential for high density current production in *Geobacter sulfurreducens* fuel cells. *PLoS ONE*. 2008;**4**(5):e5628.

104. Holmes DE, Chaudhuri SK, Nevin KP, Mehta T, Methé BA, Liu A, et al. Microarray and genetic analysis of electron transfer to electrodes in *Geobacter sulfurreducens*. Environ Microbiol. 2006;**8**(10):1805-15.
105. Ding YHR, Hixson KK, Giometti CS, Stanley A, Esteve-Núñez A, Khare T, et al. The proteome of dissimilatory metal-reducing microorganism *Geobacter sulfurreducens* under various growth conditions. Biochim Biophys Acta. 2006;**1764**(7):1198-206.
106. Levar CE, Hoffman CL, Dunshee AJ, Toner BM, Bond DR. Redox potential as a master variable controlling pathways of metal reduction by *Geobacter sulfurreducens*. ISME J. 2017;**11**(3):741-52.

CHAPTER 5  
REGISTERING FISH IMAGES TO NANOSIMS IMAGES USING  
CONVOLUTIONAL NEURAL NETWORK MODELS <sup>4</sup>

---

<sup>4</sup> He, X., Meile, C. and Bhandarkar, S. (2020) Registering FISH images to nanoSIMS images using CNN. To be Submitted to Imaging Science Journal.

## Abstract

The use of nanoscale secondary ion mass spectrometry (nanoSIMS) and fluorescence in situ hybridization (FISH) microscopy provides a high-resolution, multimodal representation of the identity and cell activity of the targeted microbial communities in microbiological researches. Registering FISH images and nanoSIMS images is of great interest to many microbiologists. However, it is a challenging task to register or overlay FISH images and nanoSIMS images considering the morphological distortion and substantial amount of background noise in both images. In this study we apply convolutional neural network (CNN) models to extract features at different layers or scales. All images were preprocessed using image segmentation and binarization to remove background noise. The extracted features were filtered by applying match thresholding in order to obtain the most significant feature point sets. Next, we used shape context to minimize the transformation cost for feature matching. Lastly, we employed the thin-plate spline (TPS) model to register FISH images and nanoSIMS images. Among the six tested CNN models, VGG (VGG16 and VGG19), GoogLeNet and ShuffleNet produced the best registration results even for highly deformed FISH images. ResNet (ResNet18 and ResNet101) performed relatively well on a more sophisticated image with multiple components. Notably, image preprocessing with segmentation and binarization significantly improved the registration results. Our study demonstrated that CNNs coupled with image preprocessing can be useful in the registration or alignment of multimodal images with significant background noise and morphology distortion. This paper is one of the first to use and evaluate deep-learned CNN features for this specific multimodal image registration problem.

## Introduction

Nanoscale secondary ion mass spectrometry (nanoSIMS) is a powerful tool for revealing element distribution at nanometer-scale resolution, and is used in many fields (1). Combining nanoSIMS imaging technique with fluorescence in situ hybridization (FISH) microscopy allows us to study microbial activities at a sub-cellular level (2). In our experimental scenario, nanoSIMS and FISH images of anaerobic methane-oxidizing archaea and sulfate-reducing bacteria aggregates were acquired from deep-sea sediments (12), where FISH images identify the different organisms using different colored probes, whereas nanoSIMS images provide isotope maps of the same aggregate. By combining these two image modalities, we can identify cellular activities and correlate them with the identity and location of cells within an aggregate.

However, there exists unequal magnification and distortion between the nanoSIMS and FISH images since they have different modalities. The thickness of the sample required for nanoSIMS analysis, and the penetration characteristics of the X-ray beam, result in the distortion of the nanoSIMS images (3). There are several registration algorithms that utilize geometrical information to align the input images (4). Noticeably, feature-based registration methods rely on point or shape correspondences between two images. The features can either be derived automatically from the underlying image characteristics, such as corners or contours of anatomical structures, or from markers with known positions. Once the corresponding points have been automatically or manually selected, their locations in the two images can be used to reconstruct a spatial transformation (5). This transformation is then applied to one of the two images so that the differences, e.g. in

scaling, rotation, translation or distortion, between the two images, are minimized (6). In contrast, intensity-based methods treat the images or image volumes as whole entities. Instead of specific features, only pixel intensity values are considered in order to determine the transformation of interest. Suitably defined similarity measures are crucial for a meaningful intensity-based comparison of two images.

Currently, there are several software packages available to process nanoSIMS data, including WinImage software (<http://www.winimage.com>), L'Image software (<http://limagesoftware.net>), the OpenMIMS plugin for ImageJ (<http://nano.bwh.harvard.edu/MIMSsoftware>), and Look @ NanoSIMS (<http://nanosims.geo.uu.nl/nanosims-wiki/doku.php/nanosims:lans>) (7). Notably, Look@NanoSIMS offers a way to align FISH images with nanoSIMS images manually. However, the process is time-consuming and tedious especially when dealing with a large number of images.

Here, we propose an automated program that registers FISH images and nanoSIMS images using convolutional neural network (CNN) models. Six CNN models include ShuffleNet (8), GoogLeNet (9), ResNet-18 and ResNet-101 (10), VGG16 and VGG19 (11) are selected to test and evaluate the registration performance. The FISH and nanoSIMS images that were provided were acquired using methods previously published by McGlynn et al. (12). The convolutional feature map is extracted at various resolutions and used for feature point selection. Shape context is then applied to identify matched features and the thin-plate spline (TPS) model is employed to register the FISH images to nanoSIMS images using the obtained transformation matrix.

## Review of Related Work

Deep learning has been increasingly recognized as a powerful toolbox for multimodal image registration, primarily in the fields of medical imaging (e.g. CT and MR images) (13-16) and remote sensing (17-19). The convolutional neural network (CNN) is one of the most widely used deep neural network (DNN) with well-defined convolutional layers, max pooling layers and softmax layer, in addition to a number of other specifically designed layers. The CNN has been exploited for feature extraction in image classification (20-23), image segmentation (24-27) and image registration (28-31) tasks. Over the past decade, many variants of the CNN have been developed for multimodal image registration. Recently, Uzunova et al. (32) proposed a statistical appearance model obtained from the FlowNet, a CNN variant that models the optical flow estimation problem as a supervised learning task (33), that can be applied to multimodal medical image registration. Hermessi et al. (13) developed a fully convolutional Siamese architecture for feature extraction and cross-correlation-based similarity metric learning. The high-frequency subbands extracted from the decomposed input images via the shearlet transform were then used for multimodal image registration by computing a weighted normalized cross-correlation between feature maps extracted using a CNN. Ferrante et al. (34) employed unsupervised CNN-based registration models for multimodal image registration of different human organs. They showed that CNN models trained in a different domain can be transferred to perform unsupervised CNN-based registration in a given domain. Training a CNN from scratch for each multimodal image registration problem is time-consuming and computationally intensive. By employing a CNN architecture that is pretrained on a rich image database of several million images, one can easily transfer the pre-learned weights

to solve a specific image registration problem without further training (see selected examples in Table 5.1). In this work, we expand upon these earlier works (35)-(44), and apply six well-known CNN architectures, i.e., ShuffleNet (8), GoogLeNet (9), ResNet-18 and ResNet-101 (10), VGG16 and VGG19 (11) with pretrained model weights on the ImageNet data set to extract features and register multimodal microbiological images.

Table 5.1. Selected examples using pretrained CNN architecture for image registration

CNN architecture	Target image	Pretrained Dataset	Reference
Alexnet, VGG-16, VGG-19, GoogLeNet, Inception-v3, ResNet-50, ResNet-101	Medical image	ImageNet	(35)
2-channel CNN	Medical image	benchmark dataset consists images of Yosemite, Notre Dame, and Liberty	(36)
FlowNet	Medical image	Flying Chair dataset	(37)
NeurReg	Medical image	Hippocampus dataset	(38)
AlexNet	Daily life images	ImageNet	(39)
VGG19	Remote sensing	ImageNet	(40)
VGG19	Medical image	ImageNet	(41)
VGG16	Medical image	ImageNet	(42)
VGG16	Remote sensing	ImageNet	(43)
VGG16	Remote sensing	ImageNet	(44)

## Methods

### Workflow

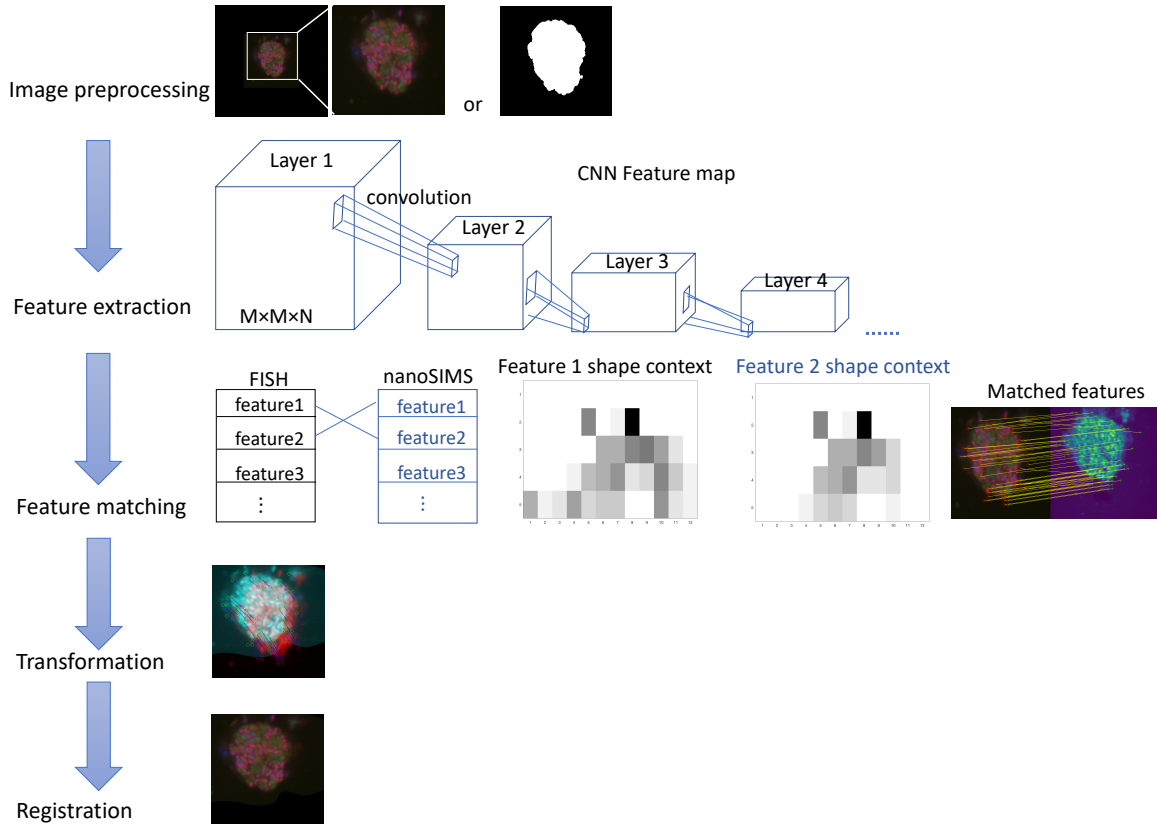


Fig. 5.1. Workflow of registering FISH images to nanoSIMS images.  $M \times M \times N$  represents feature map height  $\times$  feature map width  $\times$  feature map channels in CNN layers. Representative shape contexts for two closely related points are shown in the feature matching process. Note that darker color in shape context indicates larger value.

### Preprocessing

FISH images are intensity measurements represented in their respective coordinate systems in (R,G,B) channels (Fig. 5.2A), whereas nanoSIMS images are stored as ion counts at each location (Fig. 5.2F). Multiple thresholding methods, including automatic

thresholding, iterative thresholding, adaptive thresholding, global thresholding using Otsu's method and dual thresholding with region growing were evaluated; global threshold using Otsu's method (45) was chosen for final thresholding based on tested performance (Fig. 5.2B&G). A global threshold was first generated using Otsu's method to minimize the intra-class variance (weighted sum of variances of black and white pixels in a binary image), and was modified manually based on trial and error to preserve aggregate morphology. Region-based segmentation (e.g. watershed segmentation) and edge-based segmentation were used for image segmentation. Aggregate(s) from the FISH image were then chosen and cropped to best match the nanoSIMS image (Fig. 5.2C-E and H-J). The multi-scale Laplacian of Gaussian (LoG) operator was implemented to detect the edges in the images by finding zero-crossings in the second derivative of the image intensity function (46). The LoG operator highlights regions of rapid intensity change by measuring the second spatial derivative of an image  $I(x,y)$  for a given standard deviation  $\sigma$ :

$$\nabla^2[I(x,y) * G(x,y)] = \nabla^2G(x,y) * I(x,y)$$

where the LoG kernel can be written as

$$\nabla^2G(x,y) = LoG(x,y) = -\frac{1}{\pi\sigma^4} \left(1 - \frac{x^2 + y^2}{2\sigma^2}\right) e^{-\frac{x^2+y^2}{2\sigma^2}}$$

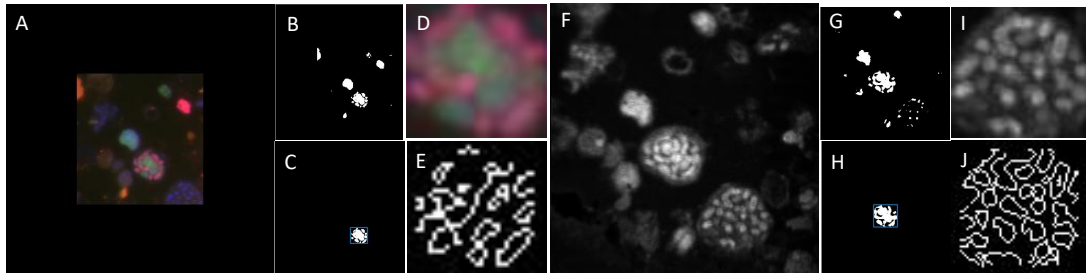


Fig. 5.2 Preprocessing FISH (A-E) and nanoSIMS (F-J) images. (A, F) Raw images. (B, G) Adaptive thresholding. (C, H) ROI selection. (D, I) Selected aggregate. (E, J) Multi-scale LoG edge detection (Initial  $\sigma = 2$ , final  $\sigma = 0.5$ , step size = 0.1).

## **Non-rigid registration using CNN**

The convolutional neural network (CNN) has recently emerged as a promising framework for image classification and registration. Among many CNN architectures, ShuffleNet (8), GoogLeNet (9), ResNet-18 and ResNet-101 (10), VGG16 and VGG19 (11) are well known for their high accuracy and speed in image classification, with pretrained weights derived from the several million training images in the ImageNet database (<http://www.image-net.org>). Although images of neither microorganisms nor microbial aggregates are available in the ImageNet database, deep CNN architectures that are pre-trained on ImageNet are excellent at general image feature extraction. To the best of our knowledge, this is the first documented application of deep CNN models to extract features from and subsequently register multimodal microbial images. Input images are either raw RGB images or preprocessed binary FISH and nanoSIMS images. All input images are rescaled to a size of 224 x 224 pixels and fed through the convolutional layers. Feature points are extracted from the FISH and nanoSIMS images at multiple CNN layers, and further used to register the FISH images and nanoSIMS images using TPS interpolation.

### *VGG16 and VGG19*

VGG16 is the runner-up of the ImageNet Large Scale Visual Recognition Challenge (ILSVRC) 2014 (11). VGG16 has 5 convolutional layers and 3 fully connected layers, whereas VGG19 has one extra convolutional layer in layers 3-5, as shown in Fig. 5.3 and Fig. 5.4, consisting of 138 and 144 million parameters respectively. Feature points are extracted from the FISH and nanoSIMS images at layers pool3, pool4 and pool5.

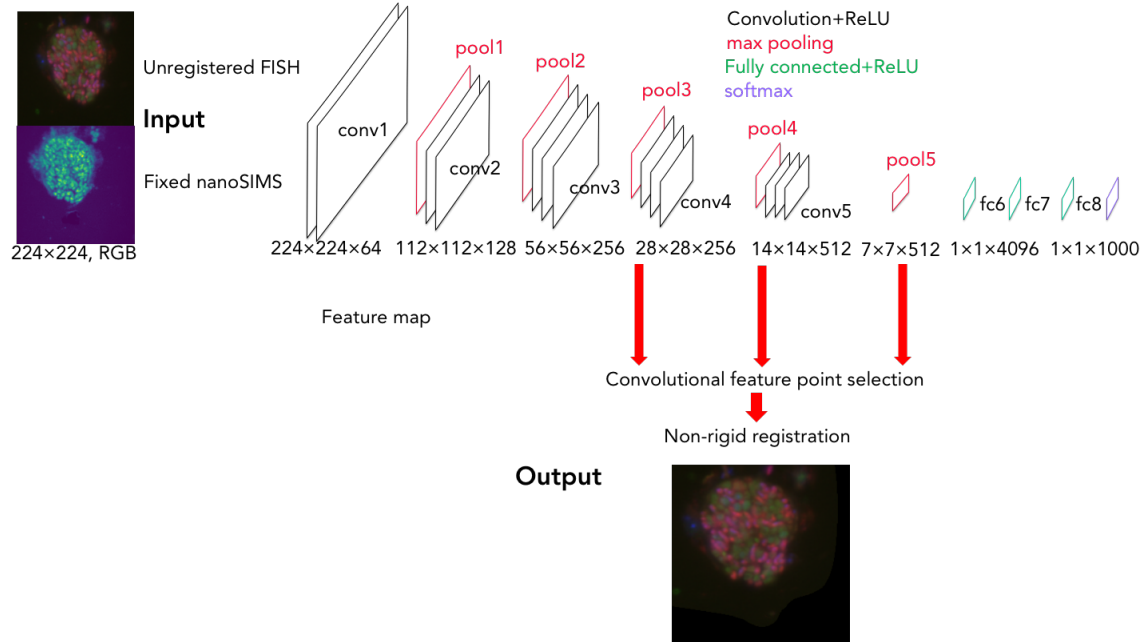


Fig. 5.3. Schematic representation of the non-rigid image registration using the VGG16 CNN. Parallelograms denote convolutional layers. ReLU is an activation function defined as  $f(x) = \max(0, x)$ .

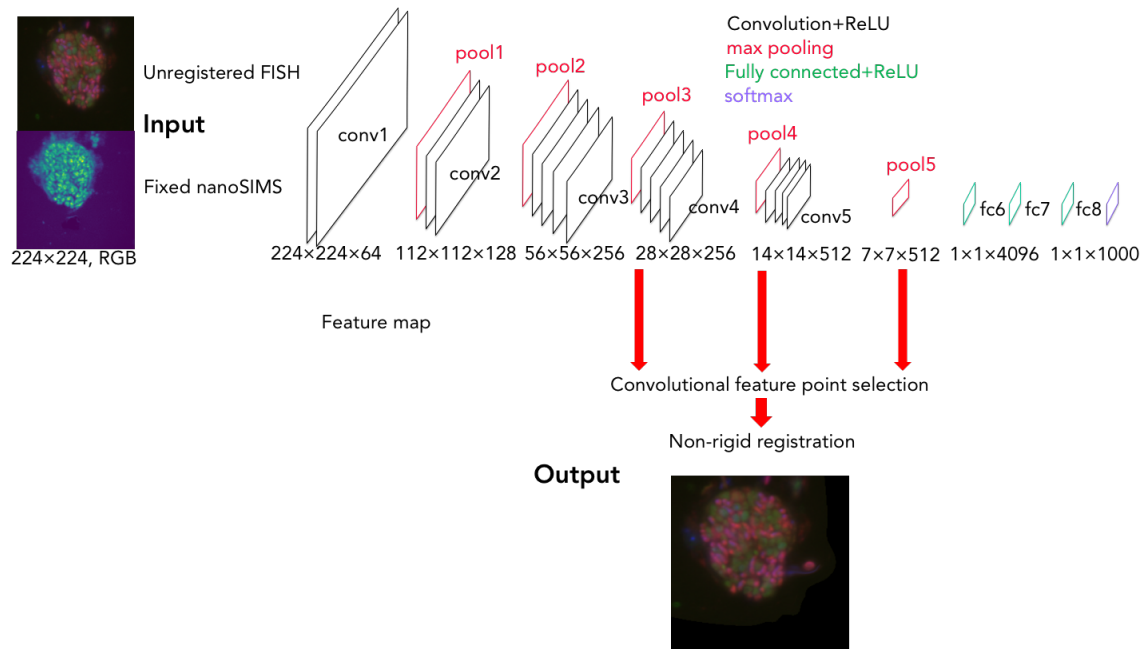


Fig. 5.4. Schematic representation of the non-rigid image registration using the VGG19 CNN. Parallelograms denote convolutional layers.

## GoogLeNet

The GoogLeNet proposed by He et al. (10) is the winner of ILSVRC 2014 and its main structure is shown in Fig. 5.5. The GoogLeNet CNN is inspired by LeNet with the inclusion of an inception module. The inception module comprises of a  $1 \times 1$  convolutional layer,  $3 \times 3$  convolutional layer,  $5 \times 5$  convolutional layer, and  $3 \times 3$  max pooling layer stacked together at the output to extract the image features. The goal is to convolve the image with operators of different sizes starting with the smallest  $1 \times 1$  convolutional layer and ending with the largest  $5 \times 5$  convolutional layer, permitting the network to go deeper but with much fewer parameters via implementation of a  $1 \times 1$  convolutional layer (4 million parameters vs. 138 million parameters in the VGG16 network). Feature points are extracted from the FISH and nanoSIMS images at layers pool2, pool3 and pool4.

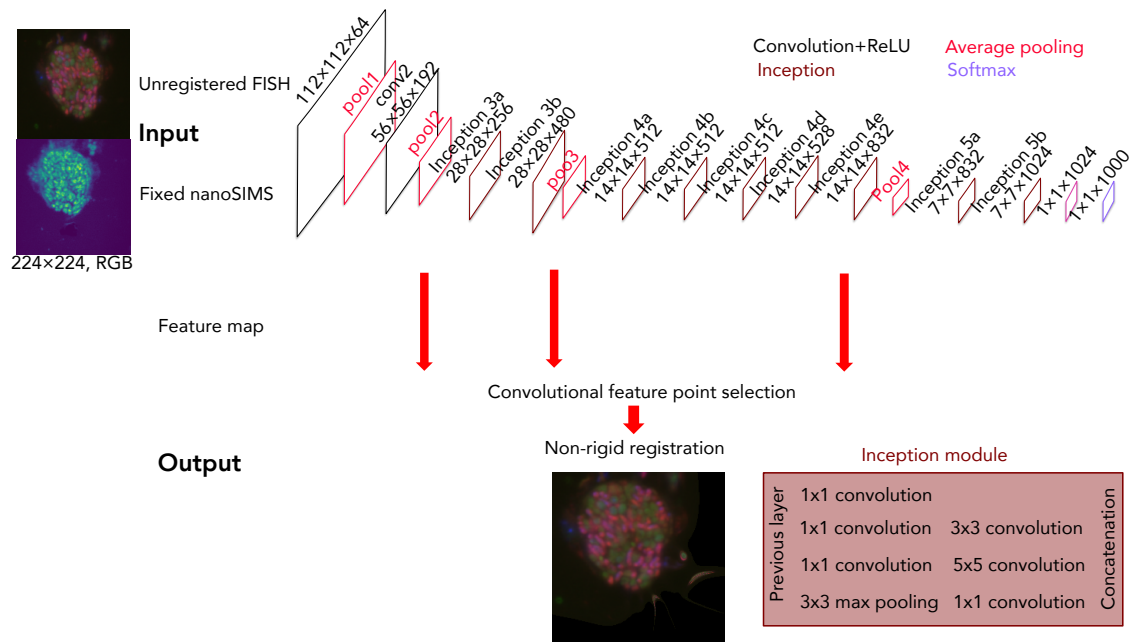


Fig. 5.5. Schematic representation of the non-rigid image registration using CNN with GoogLeNet. The details of inception modules are omitted in this schematic drawing. Parallelograms denote convolutional layers.

### ShuffleNet

ShuffleNet is specifically designed for mobile devices, utilizing elementwise group convolution and channel shuffle to require significantly less computational power while maintaining high accuracy (8). Feature points are extracted from FISH and nanoSIMS images at each ReLU layer after depth concatenation or elementwise addition, as shown in Fig. 5.6.

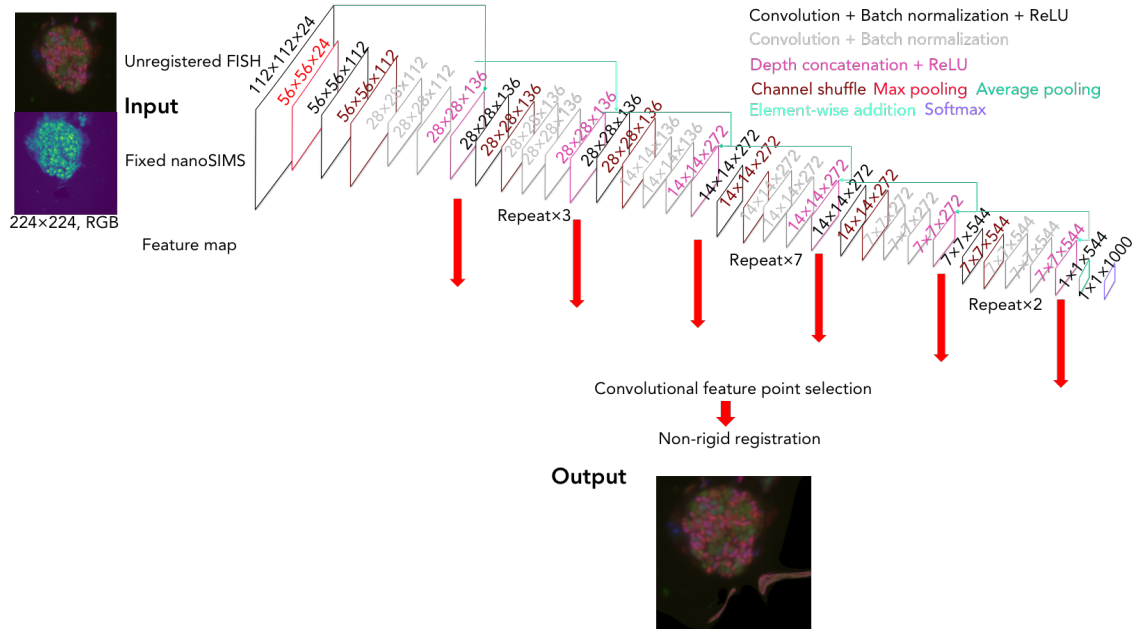


Fig. 5.6. Schematic representation of the non-rigid image registration using CNN with ShuffleNet. Parallelograms denote convolutional layers.

### ResNet18 and ResNet101

Residual neural networks (ResNet) utilizes skip connections (double- or triple-layer skips) to jump over some layers. ResNet18 is 18 layers deep and ResNet101 is 101 layers deep (10), as shown in Fig. 5.7 and Fig. 5.8, respectively. Skipping over some layers can help avoid vanishing gradients, by using activations from a previous layer. Feature points are extracted from FISH and nanoSIMS images at each ReLU layer after elementwise addition.

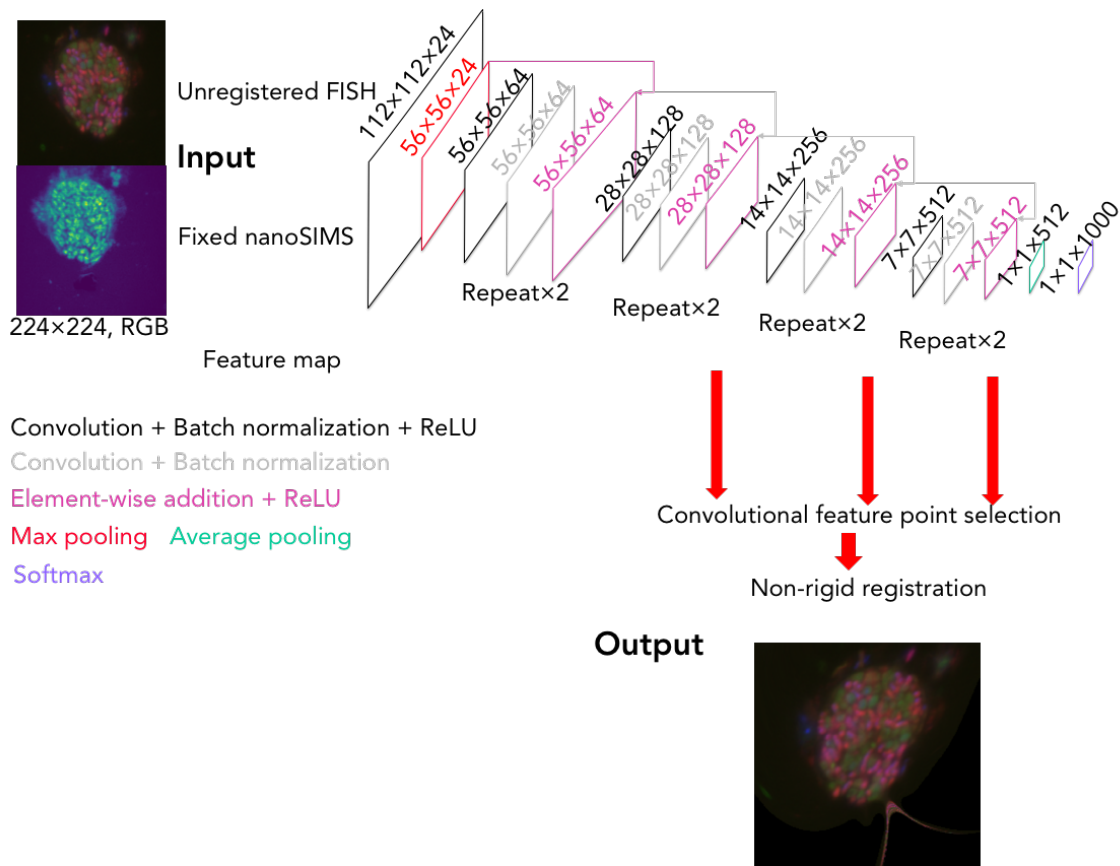


Fig. 5.7. Schematic representation of the non-rigid image registration using CNN with ResNet18. Parallelograms denote convolutional layers. ReLU is an activation function defined as  $f(x) = \max(0, x)$ .

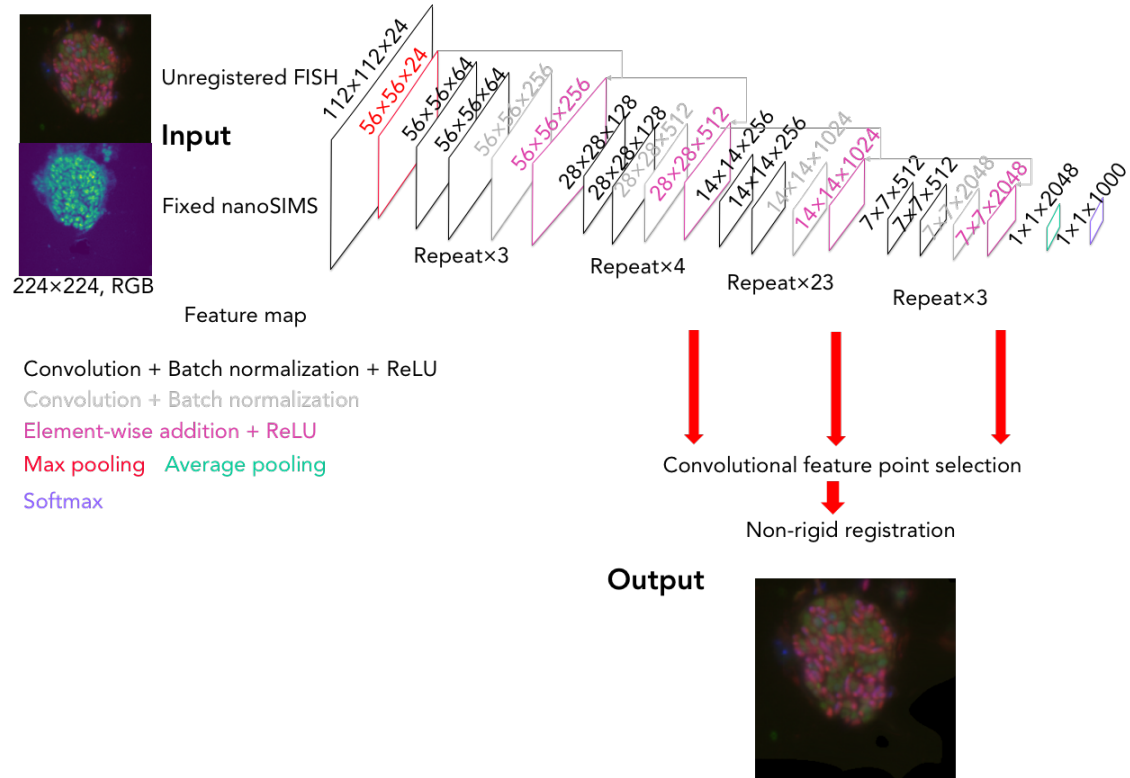


Fig. 5.8. Schematic representation of the non-rigid image registration using CNN with ResNet101. Parallelograms denote convolutional layers.

### Feature points extraction and matching

After feeding both FISH and nanoSIMS images using raw images or the preprocessed images into each CNN model following the workflow in Fig. 5.1, we collect features from the final layer of each individual module in the CNN architecture starting with layer size of 28x28 and ending with layer size of 7x7, as indicated in Figs. 5.3 - 5.8. The selection of convolutional layers aims to include both high- and low-level features and was based on heuristics. After obtaining each feature layer, we normalized the feature maps by applying the transformation  $z = (x - \mu)/\sigma$ , where  $x$  are the feature points in each feature map,  $\mu$  and  $\sigma$  are the mean and standard deviation of feature points  $x$ . Exhaustive search

was used to implement the point matching procedure as shown in Fig. 5.9. Next, we computed the feature distance map by calculating the symmetric matrix of pairwise feature distance values and concatenated the processed feature distance maps into a single feature distance map. We then compare the concatenated feature distance map from each FISH and nanoSIMS image by selecting the smallest value from each row. Next, we use the match threshold for selecting the top 20% matched points.

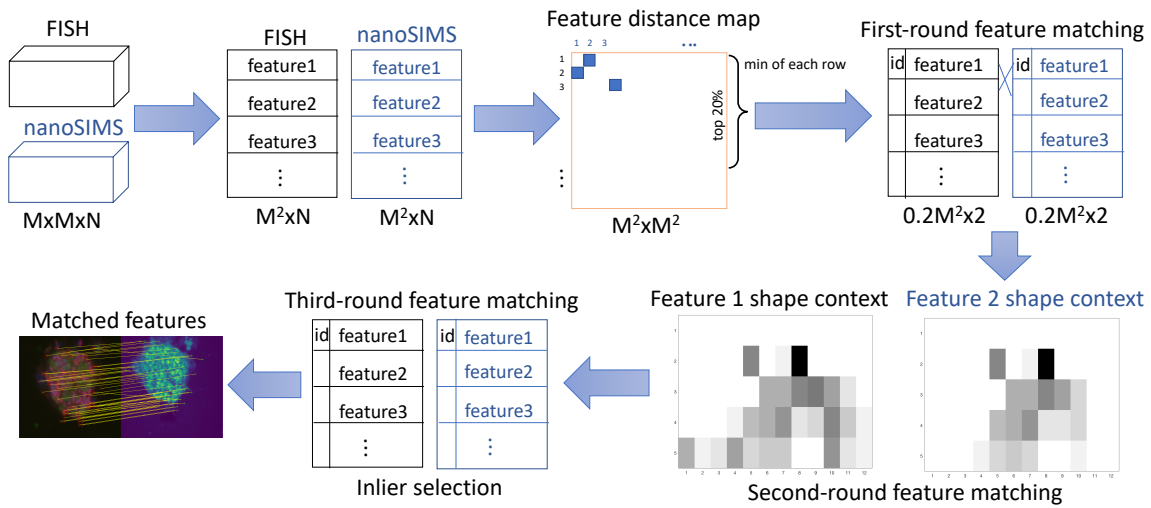


Fig. 5.9. Workflow of feature matching and inlier selection after extracting features from CNN models.  $M \times M \times N$  represents feature map height  $\times$  feature map width  $\times$  feature map channels in CNN layers.

### Shape context

After selecting preliminary matching features, shape context is used to find the matching that minimizes the transformation cost by directly measuring shape similarity and recovering the neighborhood structure of a point (47). Given  $n$  feature points on a shape contour, the shape context at point  $p_i$  is defined as a histogram  $h_i$  of the relative coordinates of the remaining  $n-1$  points

$$h_i(k) = \#\{q \neq p_i: (q - p_i) \in \text{bin}(k)\}$$

where the bins uniformly divide the log-polar space. To obtain a shape context descriptor, we first calculate the distance between points in the matched feature map as previously described and normalize by the mean. Next we compute log-distance for normalized distances and create a distance histogram. We also compute and normalize the angles between the selected points. We then can have the shape context descriptor by directly counting points in each radius and angle region as previously assigned.

After obtaining shape context descriptor for the matched feature points of FISH and nanoSIMS images, we calculate the cost matrix (C) between those two shape context descriptors using Pearson's chi-squared test (12):

$$C_{i,j} = 1/2 \sum_{k=1}^K \frac{(h_i(k) - h_j(k))^2}{h_i(k) + h_j(k)}$$

where  $h_i$  and  $h_j$  are the obtained shape context descriptor (normalized k-bin histograms as previously described) for the matched feature points  $p_i$  on FISH and  $q_j$  nanoSIMS images.

### *Bipartite graph matching*

Now consider minimizing the total cost of matching by

$$H(\pi) = \sum_i C(p_i, q_{\pi(i)})$$

where  $\pi$  is a permutation. This is a problem of weighted bipartite matching that can be done in  $O(N^3)$  time using the Hungarian method (48). In this paper, a more efficient algorithm called Jonker-Volgenant algorithm (49) was used to solve the linear sum assignment problem to find point-to-point matching in  $H(\pi)$ .

Finally, we calculated the Euclidian distance of each matched feature pair and only keep the ones that falls between 25% and 75% quantile of the distance population for inlier selection. The values of matching threshold were chosen based on trial and error.

### *Transformation and Registration*

Transformation is a process to map source space  $S(u,v)$  and destination space  $D(x,y)$  (5). Typically, image warping is performed by applying a set of reference points  $[P(u_1,v_1), P(u_2,v_2), \dots, P(u_n,v_n)]$  and  $[P'(x_1,y_1), P'(x_2,y_2), \dots, P'(x_n,y_n)]$  in both  $S(u,v)$  and  $D(x,y)$ , respectively (6). Then, a set of geometric transformations (5) or parametric transformations (50) can be calculated that minimize the cost to warp  $S(u,v)$  onto  $D(x,y)$ . Given a finite set of point correspondences between two shapes, image transformation and registration  $T: \mathbb{R}^2 \rightarrow \mathbb{R}^2$  can be realized by applying TPS model (51). TPS registration as non-rigid registration aligns images with deformations applied globally. The underlying transformation is considered to be the radial-basis function where the foreground pixels of the moving image deform under the influence of the control points  $p_i$ , where  $i = 1, \dots, n$ . TPS transformation may be written as a radial basis function

$$f(x, y) = a_1 + a_2x + a_3y + \sum_{i=1}^n w_i \varphi(\|(x, y) - p_i\|)$$

where,  $i = 1, \dots, n$  and  $\varphi(r)$  is the radial-basis kernel as  $\varphi(r) = r^2 \log r$ , where  $r$  is the Euclidean distance (denoted by  $\|\bullet\|$ ) between two control points.  $w_i$  are the non-linear TPS mapping coefficients for the control points,  $a_1, a_2, a_3$  are linear coefficients which define a flat plane that best matches all control points, and those coefficients can be defined by

$$L^{-1}Y = (W|a_1a_2a_3)^T$$

where  $W = w_i, i = 1, \dots, n$ , is a vector of all  $w_i$ ,  $L$  is composed of the matrices  $K, P, P^T$  and filled with zeros on its bottom-right corner as

$$L = \begin{bmatrix} K & P \\ P^T & O \end{bmatrix}$$

where  $O$  is a  $3 \times 3$  matrix of zeros, and  $K$  is matrix of  $\varphi(r)$

$$K = \begin{bmatrix} 0 & \varphi(r_{1,2}) & \dots & \varphi(r_{1,n}) \\ \varphi(r_{2,1}) & 0 & \dots & \varphi(r_{2,n}) \\ \vdots & \vdots & \ddots & \vdots \\ \varphi(r_{n,1}) & \varphi(r_{n,2}) & \dots & 0 \end{bmatrix}$$

With the 0 in the diagonal reflecting that the distance between control points in the corresponding images ( $r_{i,i}$ ) is 0.

Given a set of control points, we define  $P$  are the positions of all points  $p_i$  as

$$P = \begin{bmatrix} 1 & x_1 & y_1 \\ 1 & x_2 & y_2 \\ \vdots & \vdots & \vdots \\ 1 & x_n & y_n \end{bmatrix}$$

where  $n$  is the number of points.

$Y$  is a matrix include a vector  $V$  with any  $n$ -vector form  $(v_1, v_2, \dots, v_n)$  and padded with zeros

$$Y = (V | 0 \ 0 \ 0)^T = \begin{bmatrix} v_1 \\ v_2 \\ \dots \\ v_n \\ 0 \\ 0 \\ 0 \end{bmatrix}$$

The unknown coefficients matrix  $(W | a_1 \ a_2 \ a_3)$  can be solved through finding the inverse  $L^{-1}$  using lower-upper (LU) factorization (52).

### Similarity registration

Alternatively, similarity registration was used as a comparison to our proposed non-rigid registration using CNN. Similarity registration allows scaling images by applying a combination of translation (a, b), rotation ( $\theta$ ), and scaling (S):

$$\begin{bmatrix} x_2 \\ y_2 \\ 1 \end{bmatrix} = \begin{bmatrix} S\cos\theta - S\sin\theta a \\ S\sin\theta & S\cos\theta & b \\ 0 & 0 & 1 \end{bmatrix} \begin{bmatrix} x_1 \\ y_1 \\ 1 \end{bmatrix}$$

### Quantitative image registration assessment

Registered images were directly compared to images that were registered manually. Three different error metrics were employed to assess the registration accuracy at the pixel and structural level: root mean squared error (RMSE), structural similarity index (SSIM), and average absolute intensity difference (AAID). RMSE is one of the most popular evaluation methods for quantifying the image registration difference (53), simply calculating the square root of the mean square error of pixels between two images

$$RMSE = \sqrt{\frac{\sum_{i=1}^N (\hat{y}_i - y_i)^2}{N}}$$

SSIM is a popular method to evaluate the perceived similarity in structural information between two images (54), by computing a weighted combination of the luminance index, the contrast index and the structural index as

$$SSIM = [l(\hat{y}, y)]^\alpha [c(\hat{y}, y)]^\beta [s(\hat{y}, y)]^\gamma$$

where luminance index  $l(\hat{y}, y) = \frac{2\mu_{\hat{y}}\mu_y + c_1}{\mu_{\hat{y}}^2 + \mu_y^2 + c_1}$ , contrast index  $c(\hat{y}, y) = \frac{2\sigma_{\hat{y}}\sigma_y + c_2}{\sigma_{\hat{y}}^2 + \sigma_y^2 + c_2}$ , and structural index  $s(\hat{y}, y) = \frac{\sigma_{\hat{y}y} + c_3}{\sigma_{\hat{y}}\sigma_y + c_3}$ , and  $\mu_{\hat{y}}$ ,  $\mu_y$ ,  $\sigma_{\hat{y}}$ ,  $\sigma_y$ , and  $\sigma_{\hat{y}y}$  are the local means, standard deviations, and cross-covariance for images  $\hat{y}$ ,  $y$ . Weights  $\alpha$ ,  $\beta$  and  $\gamma$  are set to 1.

AAID evaluates the intensity difference between two images by calculating (55)

$$AAID = \frac{1}{MNQ} \sum_{i=1}^M \sum_{j=1}^N \sum_{k=1}^Q |\hat{y}_{i,j,k} - y_{i,j,k}|$$

where M, N, and Q represent the dimension of images.

RMSE and AAID is smaller when the registration result is better, whereas SSIM is higher for a better aligned image.

### Results and Discussion

We applied six different CNN models to extract the image features and used these features to align FISH images to nanoSIMS images. As shown in Fig. 5.2, identifying the regions of interest (ROIs) is critical to align the FISH and nanoSIMS images by filtering out background noise. To test the impact of preprocessing images on the feature recognition and final registration, we used optimal thresholding to convert the raw RGB images to binary images. Results indicate that preprocessing with binary thresholding significantly improved the accuracy of image registration (upper two panels in Figs. 5.10, 5.15 and 5.20) by extracting most important features (Figs. 5.11, 5.16 and 5.21) identifying the feature points more accurately (Figs. 5.12-5.13, 5.17-5.18, and 5.22-5.23). The background noise in raw RGB images negatively influenced the feature extraction. Converting images to binary mode removes most of the background noise meanwhile keeping the main components. It is paramount to identify the suitable thresholding value so that the components left behind in the FISH and nanoSIMS images are the same. It is a rare outcome of thresholding procedure that the remaining components in the FISH and nanoSIMS are the same especially for an image with multiple objects. The residual components in the FISH and nanoSIMS images did not match well even after exhaustive

trial and error iterations. This caused misalignment in some CNN models due to the less accurate feature extraction and less successful feature matching.

Overall, our results show that TPS-based registration is better than registration based on similarity metrics (Figs. 5.14, 5.19 and 5.24). Our results indicate that VGG (VGG16 and VGG19), GoogLeNet, ShuffleNet, and ResNet101 registered images with a relatively high accuracy at both pixel and structure level (Figs. 5.10, 5.15 and 5.20). We examined the performance of those CNN networks on three different types of images: a deformed and misplaced image (Figs. 5.10-5.14), a significantly deformed image (Figs. 5.15-5.19), and a deformed image with multiple components (Figs. 5.20-5.24). Learned features from each convolutional layers were visualized by using a multi-resolution image pyramid and Laplacian Pyramid Gradient Normalization (56). In general, features identified by ResNet and ShuffleNet were more complex than VGG and GoogLeNet models (Figs. 5.11, 5.16 and 5.20). The complexity of featured learned by the CNN models can be critical for registering images with different level of composition complexity. For instance, for images with a single component as shown in Fig. 5.10 and Fig. 5.15, VGG and GoogLeNet models showed a better registration result, though it is not accurately reflected in Fig. 5.14 due to the presence of artifacts introduced during the transformation and registration procedures. These artifacts did not affect the alignment of targeting aggregate, but negatively affected the calculation of image registration accuracy. Nevertheless, our proposed models were able to identify features with a relatively high accuracy of feature matching (Figs. 5.13, 5.18, 5.23).

### **Case study 1: Moderately deformed FISH image**

We first examine the registration for a modestly deformed FISH image. Although the aggregate in the image is relatively simple, binarization of nanoSIMS images could not remove some background noise in close proximity of the target aggregate (red rectangles in Fig. 5.10). As a result, some artifacts may be introduced during the image registration (Fig. 5.10), and thus negatively affect the quantification of image registration accuracy (Fig. 5.14). It is clear that registration using RGB images as input produced unsatisfactory registration results (Fig. 5.10). Among the six CNN models, VGG, GoogLeNet, and ShuffleNet registered the target aggregate at a higher accuracy than ResNet models (Fig. 5.14). It is likely that the learned features from ResNet were too deep and sophisticated for an image in this study (Fig. 5.11), which is also reflected in the feature matching shown in Figs. 5.12 and 5.13.

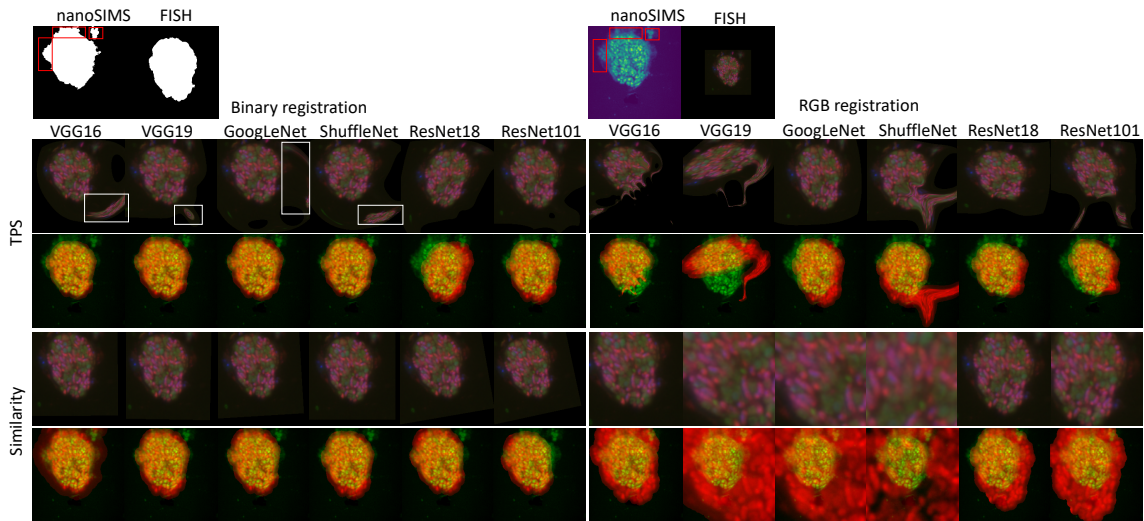


Fig. 5.10. Image registration results for a moderately deformed FISH image and nanoSIMS image using binary (left) and RGB (right) as input with TPS- (upper two panels) and similarity-based (lower two panels) registration. Red rectangles indicate background noise that was carried over into the binarized image, whereas white rectangles indicate artifacts

produced along with image registration as a result of background noise in the nanoSIMS image.

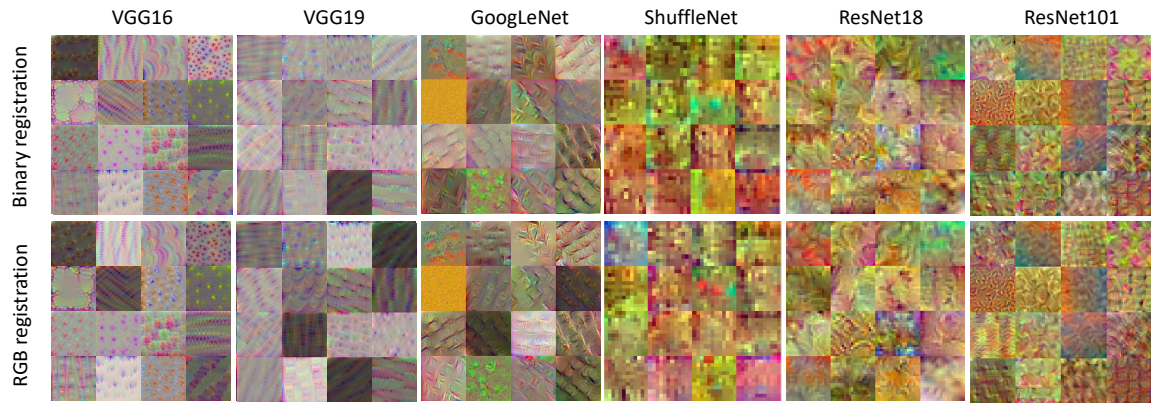


Fig. 5.11. Feature extraction results during registration of a moderately deformed FISH image and nanoSIMS image using binary- (upper panel) and RGB-based registration (lower panel).

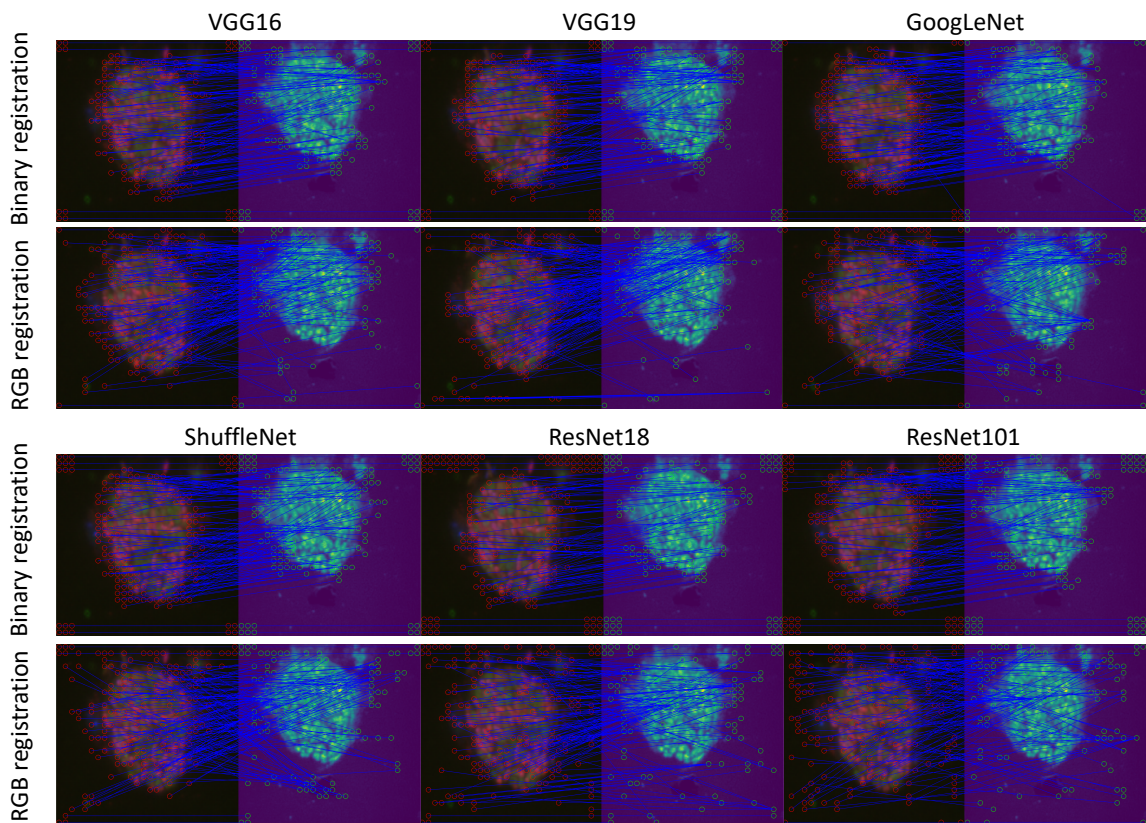


Fig. 5.12. Feature mapping before final thresholding during registration of a moderately deformed FISH image and nanoSIMS image using binary- (upper two panels) and RGB-based registration (lower two panels).

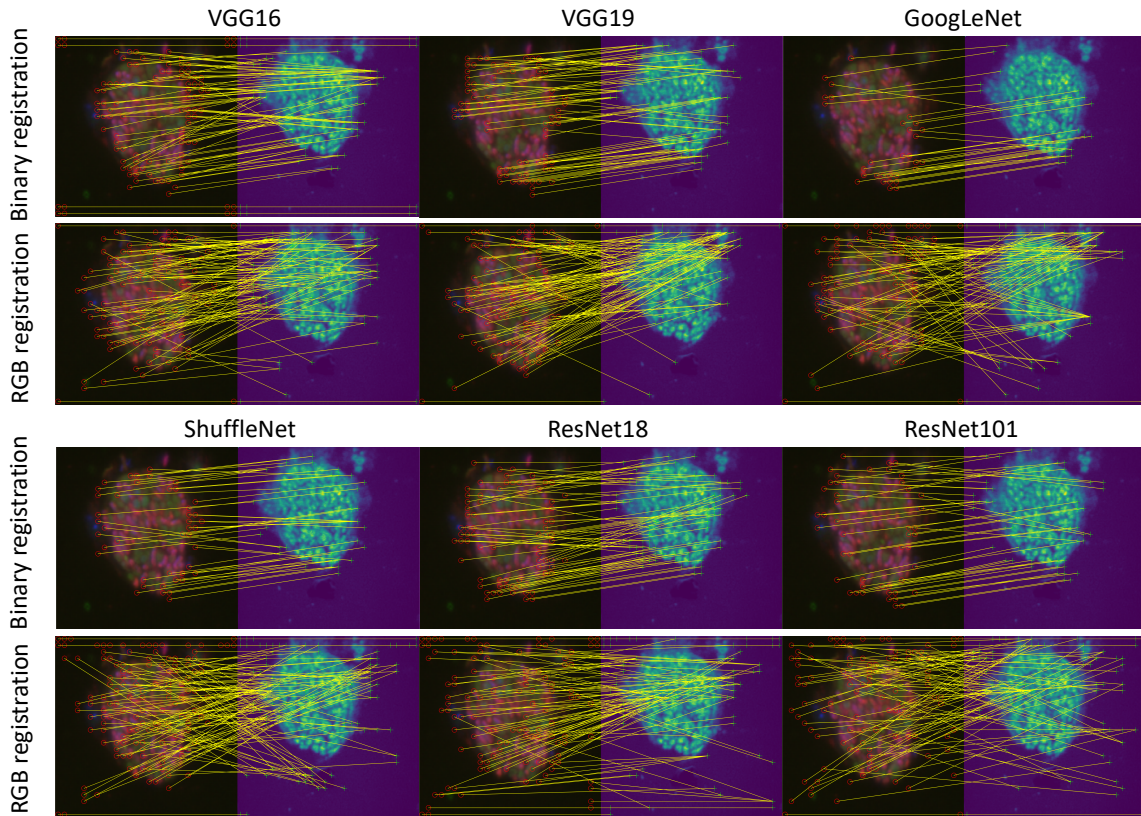


Fig. 5.13. Feature mapping after final thresholding during registration of a moderately deformed FISH image and nanoSIMS image using binary- (upper two panels) and RGB-based registration (lower two panels).

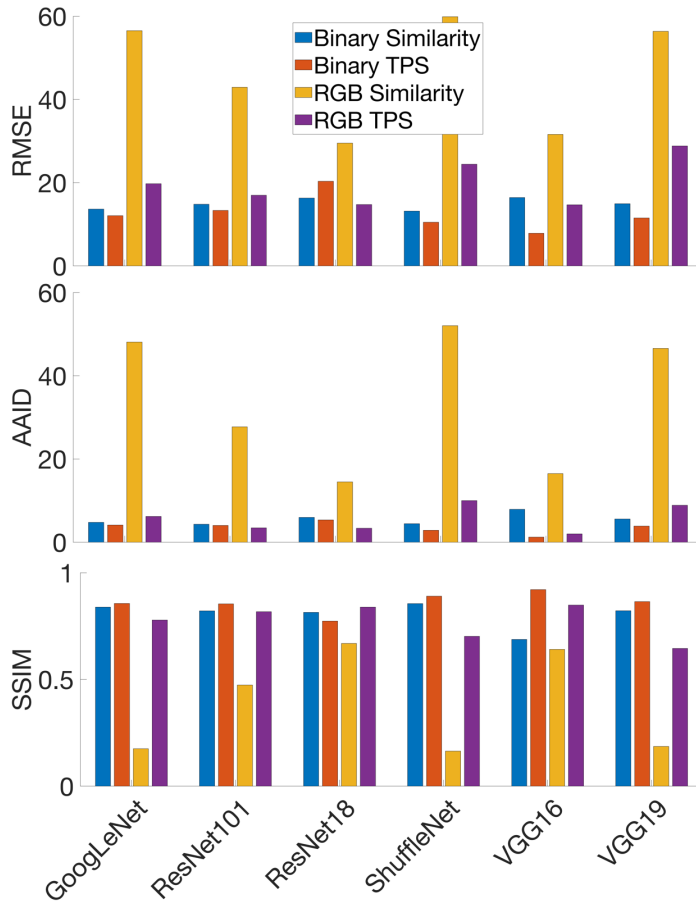


Fig. 5.14. Image registration accuracy for a moderately deformed FISH image: RMSE (upper panel), AAID (middle panel), and SSIM (lower panel). RMSE and AAID are smaller when the registration result is better, whereas SSIM is higher for a better aligned image.

### Case study 2: Significantly deformed FISH image

Next we examine the registration results for a significantly deformed FISH image. It is noted that the morphology of binary FISH and nanoSIMS images had significant difference based on human visual perception (Fig. 5.15). Our registration results show that all six CNN models performed relatively well with TPS-based registration (Figs. 5.15 and 5.19). The pixel differences in RMSE and AAID were very small (Fig. 5.19). The SSIM

index was also close to 1 for all six models (Fig. 5.19). However, registration results of the ResNet models were still worse than those of other models, likely due to the depth of the features the ResNet learned for a less sophisticated target aggregate in the image (Fig. 5.16), in a manner similar to case study 1 (Fig. 5.11).

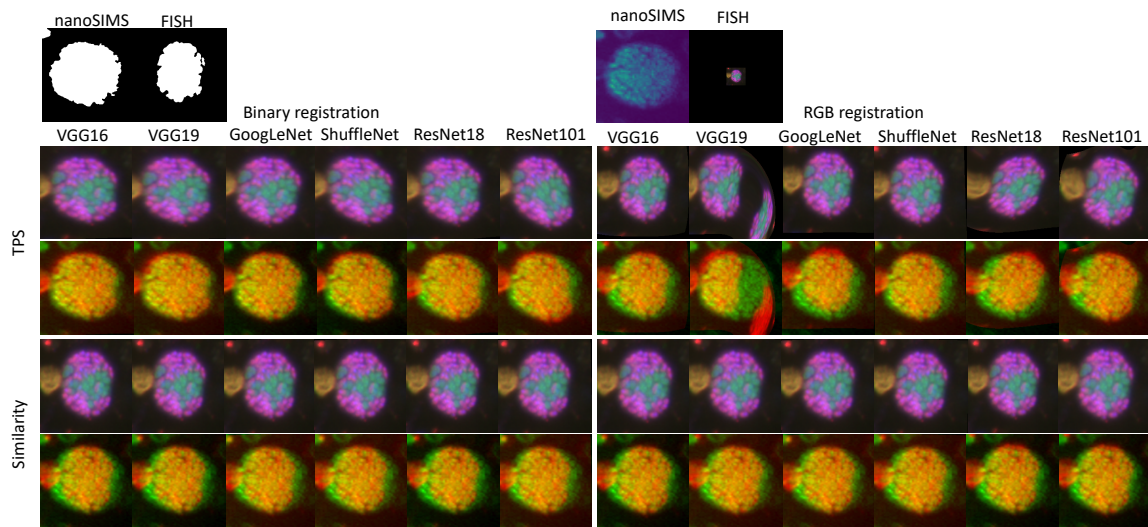


Fig. 5.15. Image registration for a significantly deformed FISH image onto nanoSIMS image using binary (left) and RGB (right) as input with TPS (upper two panels) and similarity (lower two panels) registration.

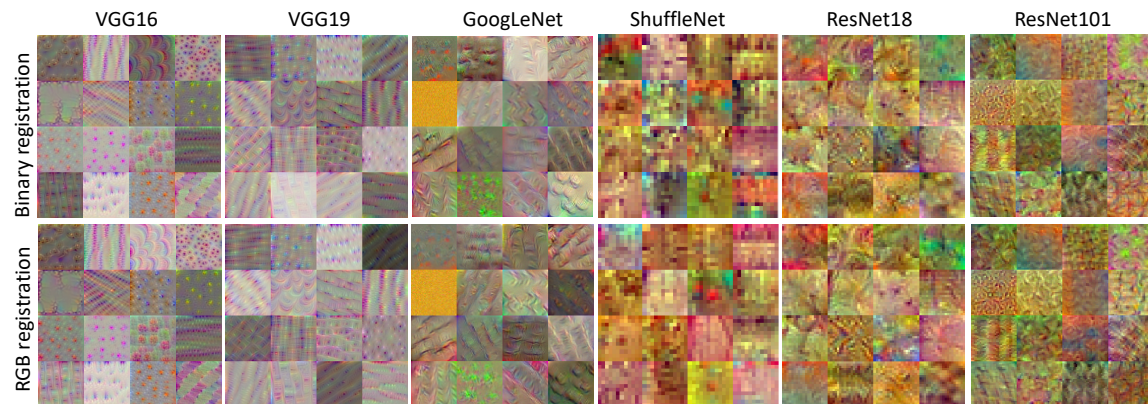


Fig. 5.16. Feature extraction results for a significantly deformed FISH image and nanoSIMS image using binary- (upper panel) and RGB-based registration (lower panel).

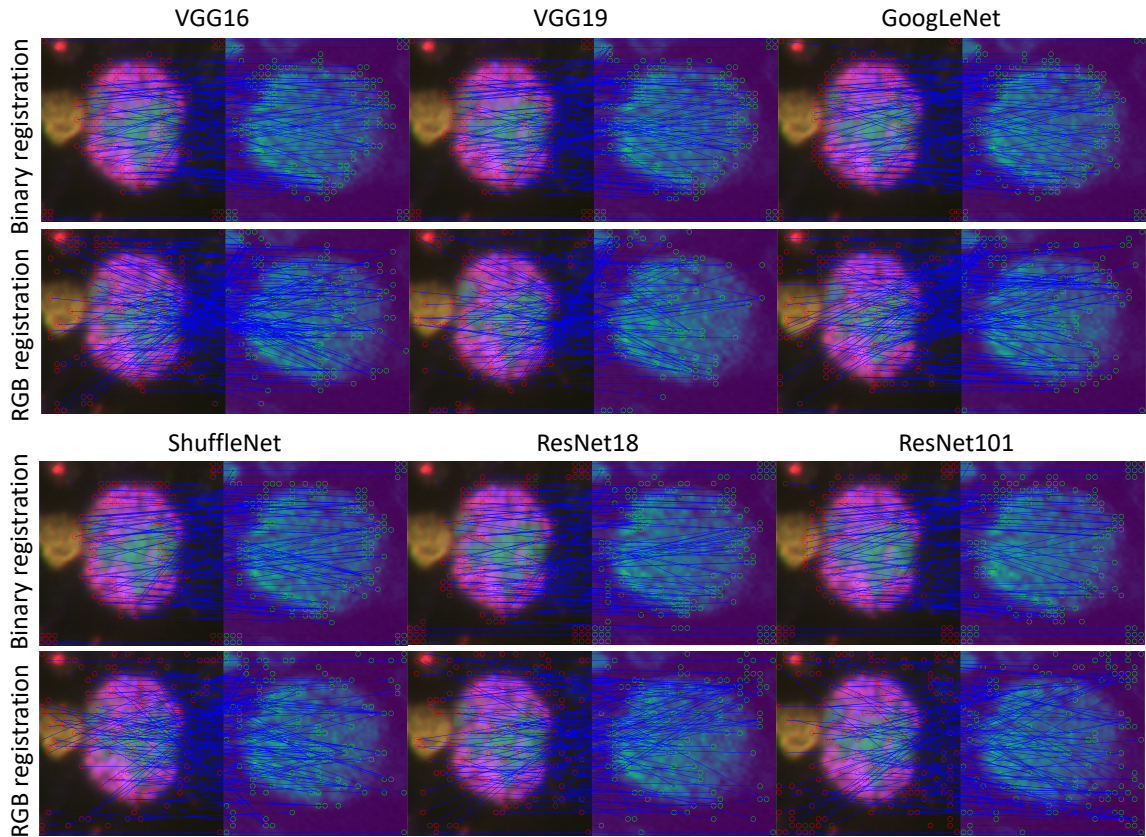


Fig. 5.17. Feature mapping before final thresholding for a significantly deformed FISH image and nanoSIMS image using binary- (upper two panels) and RGB-based registration (lower two panels).

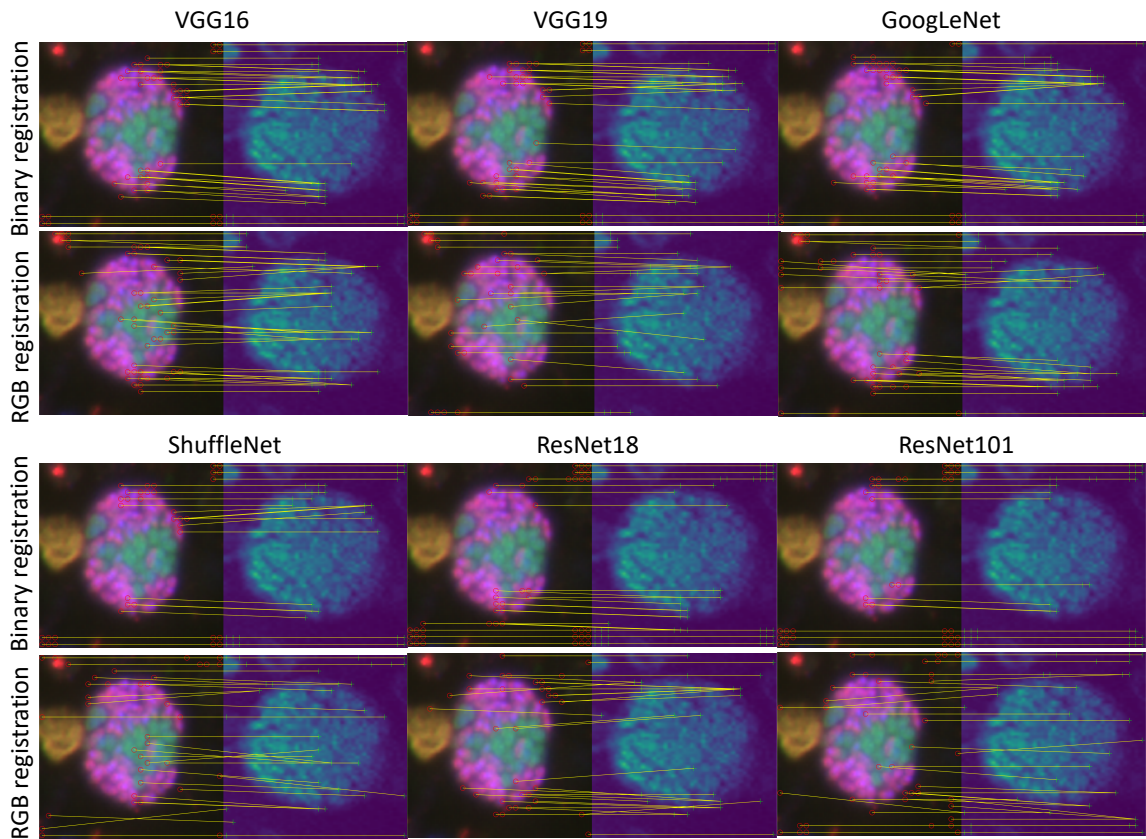


Fig. 5.18. Feature mapping after final thresholding during registration of a significantly deformed FISH image and nanoSIMS image using binary- (upper two panels) and RGB-based registration (lower two panels).

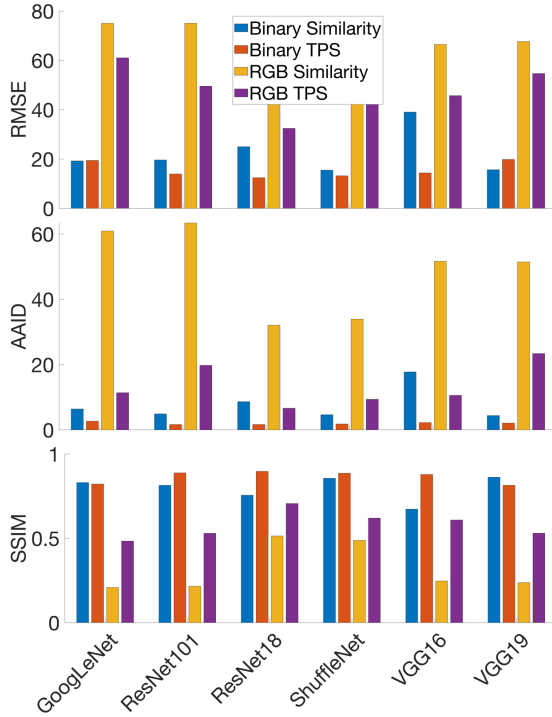


Fig. 5.19. Image registration accuracy for a significantly deformed FISH image: RMSE (upper panel), AAID (middle panel), and SSIM (lower panel). RMSE and AAID is smaller when the registration result is better, whereas SSIM is higher for a better aligned image.

### Case study 3: Deformed FISH image with multiple components

Finally, we examine the registration results for a more complicated scenario comprising of a deformed FISH image with multiple components. A dominant aggregate exists in the image and was chosen as the ROI (Fig. 5.20). All six of our examined models still performed well in this study (Fig. 5.20), showing small pixel difference and high structural similarity (Fig. 5.24). ResNet performed noticeably better than in less complicated cases. As we hypothesized earlier in case study 1 and 2, this may be largely owing to the fact that ResNet was good at recognizing deep and sophisticated features (Fig. 5.21). Nonetheless, higher-level features extracted by other CNN models (VGG,

GoogLeNet and ShuffleNet) were also able to register FISH images reliably in this study. The differences between the CNN models chosen for this study in identifying matched features were minor (Figs. 5.22 and 5.23), and so were the final registration results (Figs. 5.20 and 5.24) when using binary images as input. It is noted that feature matching quality for the target aggregate is what matters for the final registration. The presence of mismatches between small components (Fig. 5.23) due to the binarization preprocessing (Fig. 5.20) did not impact the registration of target aggregate. Although a dominant object exists in the image examined here, it is noted that there is no need to first remove other smaller components in the two images before proceeding to register or align the corresponding components in this study. This is largely due to the features extracted using the CNN models were mostly found to be from the dominant object in the image (Figs. 5.22 and 5.23).

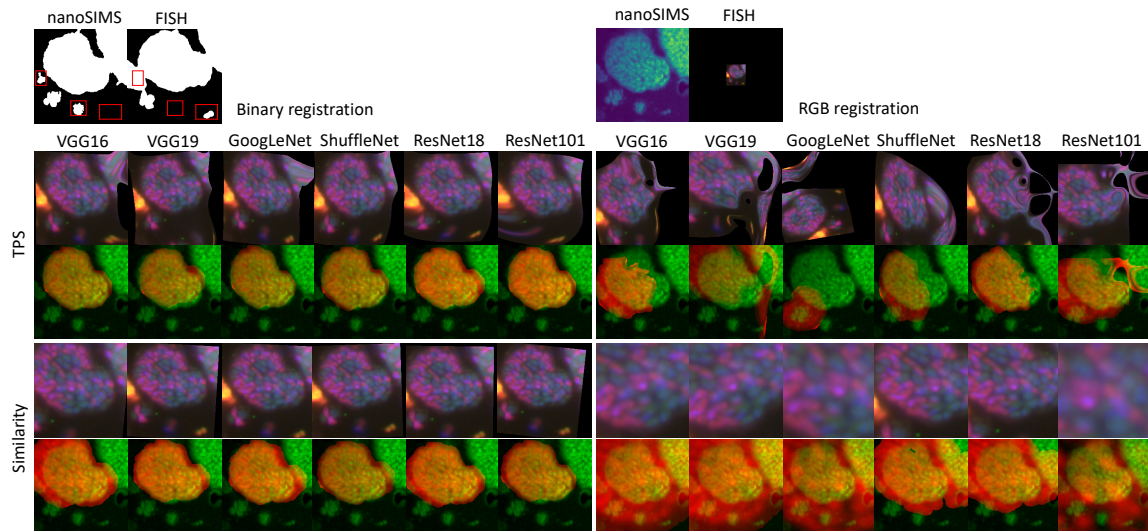


Fig. 5.20. Feature extraction results for registration of a deformed FISH image with multiple components and a nanoSIMS image using binary- (upper panel) and RGB-based registration (lower panel).

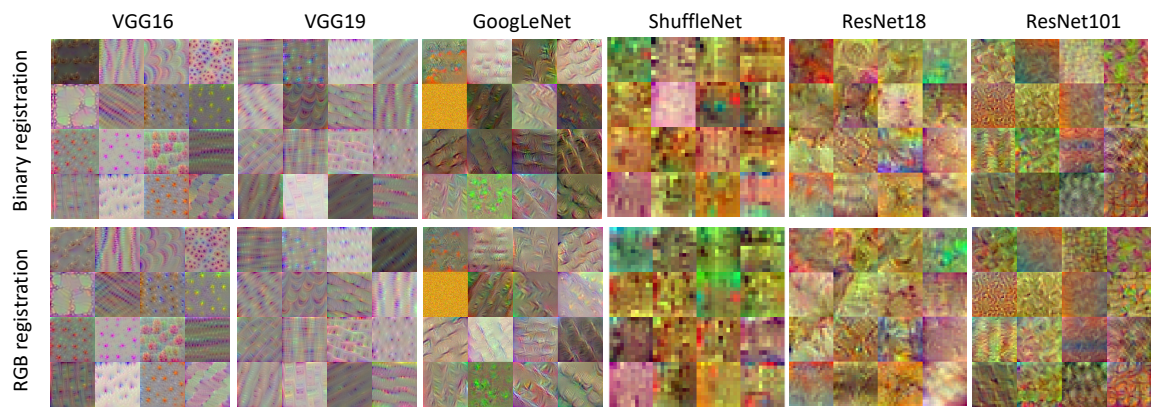


Fig. 5.21. Feature extraction results for registration of a deformed FISH image with multiple components and a nanoSIMS image using binary- (upper panel) and RGB-based registration (lower panel).

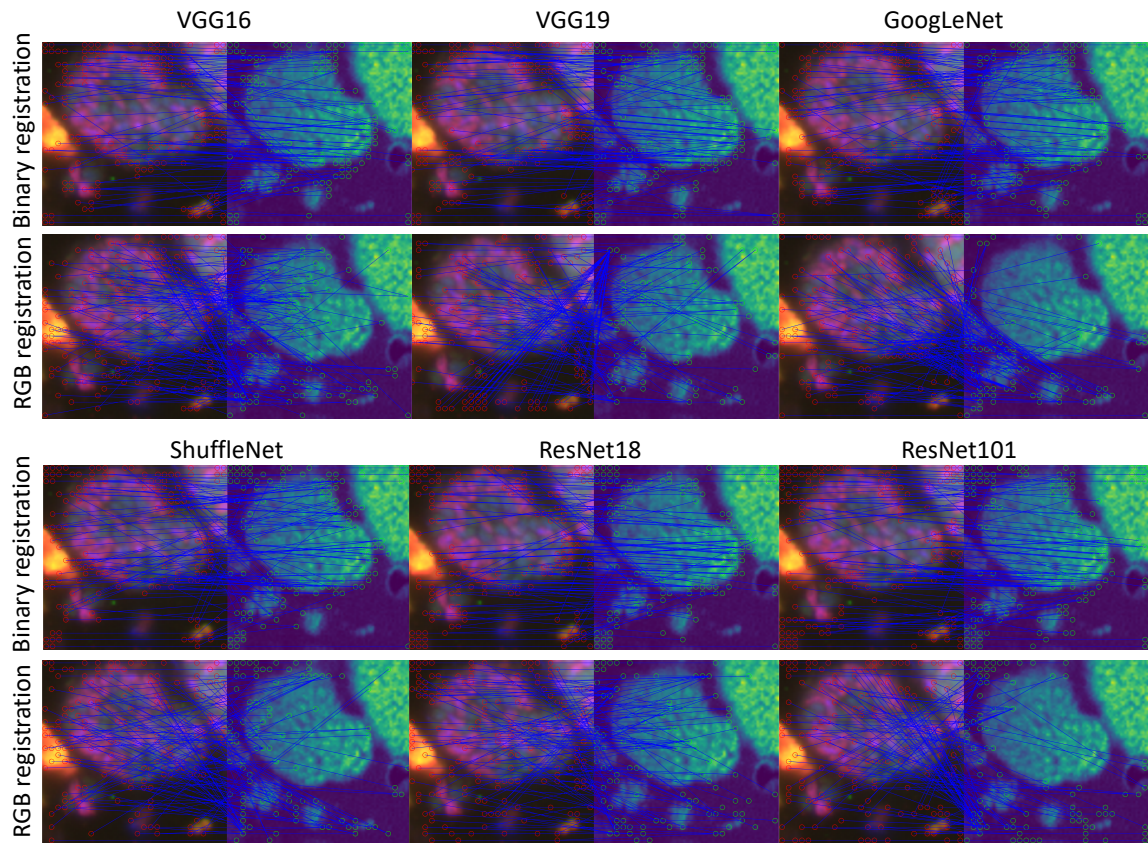


Fig. 5.22. Feature mapping before final thresholding for a deformed FISH image with multiple components onto nanoSIMS image using binary (upper two panels) and RGB registration (lower two panels).

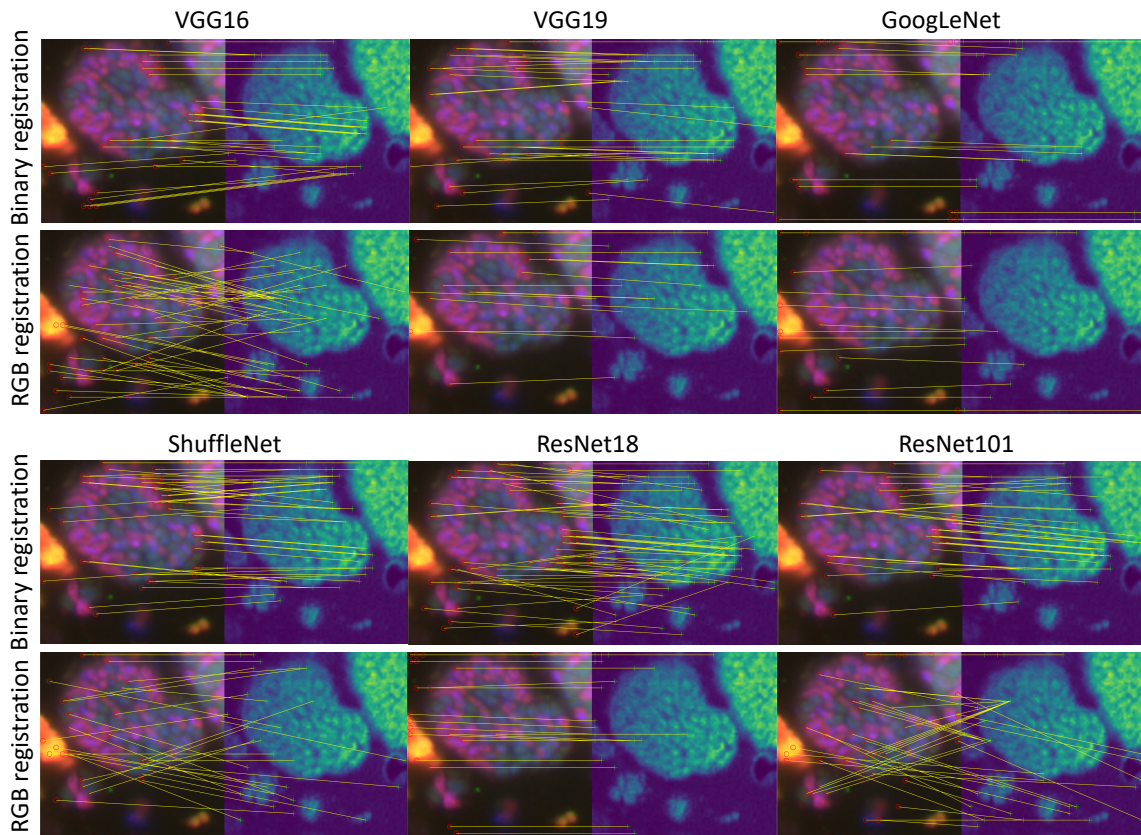


Fig. 5.23. Feature mapping after final thresholding for registration of a deformed FISH image with multiple components and nanoSIMS image using binary- (upper two panels) and RGB-based registration (lower two panels).

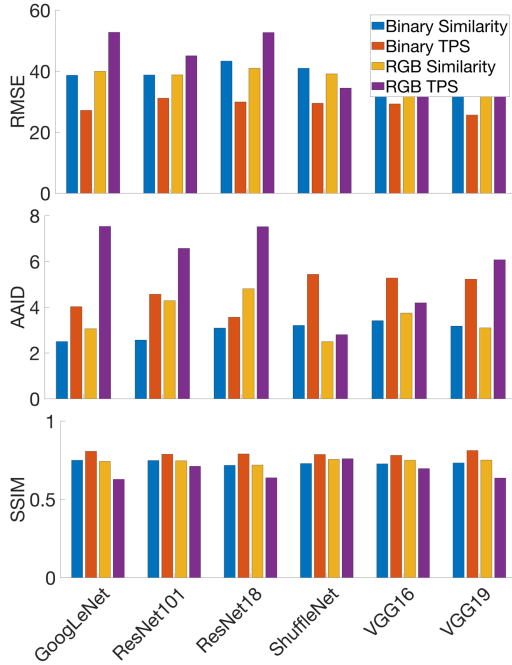


Fig. 5.24. Image registration accuracy for a deformed FISH image with multiple components and nanoSIMS image: RMSE (upper panel), AAID (middle panel), and SSIM (lower panel). RMSE and AAID is smaller when the registration result is better, whereas SSIM is higher for a better aligned image.

### Conclusion

We tested six CNN models using TPS-based non-rigid registration for different FISH and nanoSIMS images. VGG (VGG16 and VGG19), GoogLeNet and ShuffleNet performed best for distorted FISH images with a single aggregate in case studies 1 and 2, whereas ResNet (ResNet18 and ResNet101) did well in a more complicated scenario in case study 3. VGG, GoogLeNet and ShuffleNet models were able to accurately extract the most significant convolutional features and therefore perform accurate feature point matching, whereas the ResNet models extracted more complicated features at a deeper layer. We demonstrated that image preprocessing with segmentation and binarization are

critical for final image registration. It is also noted that images with significant background noise that cannot be easily removed via simple thresholding and binarization procedures still pose a significant challenge. Our future work will focus on preserving the single aggregate morphology and reducing background noise in images with multiple aggregates. Additionally, it will also be of general interest in microbiology to improve the image resolution by using more sophisticated image processing algorithms in the future.

#### Acknowledgment

This work was supported by the U.S. Department of Energy, Office of Science, Office of Biological and Environmental Research, Genomic Science Program under Award Number DE-SC0016469 and DE-SC0020373 to CM.

#### References

1. Boxer SG, Kraft ML, Weber PK. Advances in imaging secondary ion mass spectrometry for biological samples. *Annual Review of Biophysics*. 2009;**38**:53-74.
2. Dekas AE, Connon SA, Chadwick GL, Trembath-Reichert E, Orphan VJ. Activity and interactions of methane seep microorganisms assessed by parallel transcription and FISH-NanoSIMS analyses. *The ISME Journal*. 2015;**10**:678–92.
3. Moore KL, Schröder M, Lombi E, Zhao F-J, McGrath SP, Hawkesford MJ, et al. NanoSIMS analysis of arsenic and selenium in cereal grain. *New Phytologist*. 2010;**185**(2):434-45.
4. Brown LG. A survey of image registration techniques. *ACM Computing Surveys*. 1992;**24**(4):325-76.

5. Heckbert PS. Fundamentals of texture mapping and image warping. Berkeley, CA: University of California, Berkeley; 1989.
6. Arad N, Reinfeld D. Image warping using few anchor points and radial functions. *Computer Graphics Forum*. 14: Blackwell Science Ltd; 1995. p. 35-46.
7. Polerecky L, Adam B, Milucka J, Musat N, Vagner T, Kuypers MM. Look@NanoSIMS—a tool for the analysis of nanoSIMS data in environmental microbiology. *Environmental microbiology*. 2012;**14**(4):1009-23.
8. Zhang X, Zhou X, Lin M, Sun J, editors. ShuffleNet: An Extremely Efficient Convolutional Neural Network for Mobile Devices. *Proceedings of the IEEE conference on computer vision and pattern recognition*; 2018.
9. Szegedy C, Liu W, Jia Y, Sermanet P, Reed S, Anguelov D, et al., editors. Going deeper with convolutions. *Proceedings of the IEEE conference on computer vision and pattern recognition*; 2015.
10. He K, Zhang X, Ren S, Sun J, editors. Deep residual learning for image recognition. *Proceedings of the IEEE conference on computer vision and pattern recognition*; 2016.
11. Simonyan K, Zisserman A. Very deep convolutional networks for large-scale image recognition. *3rd International Conference on Learning Representations*; San Diego, CA, USA2015.
12. McGlynn SE, Chadwick GL, Kempes CP, Orphan VJ. Single cell activity reveals direct electron transfer in methanotrophic consortia. *Nature*. 2015;**526**(7574):531-5.
13. Hermessi H, Mourali O, Zagrouba E. Convolutional neural network-based multimodal image fusion via similarity learning in the shearlet domain. *Neural Computing and Applications*. 2018;**30**(7):2029-45.

14. Hu Y, Modat M, Gibson E, Li W, Ghavami N, Bonmati E, et al. Weakly-supervised convolutional neural networks for multimodal image registration. *Medical Image Analysis*. 2018;**49**:1-13.
15. Ma K, Wang J, Singh V, Tamersoy B, Chang Y-J, Wimmer A, et al., editors. Multimodal image registration with deep context reinforcement learning. *Medical Image Computing and Computer Assisted Intervention – MICCAI 2017 International Conference on Medical Image Computing and Computer-Assisted Intervention*; 2017; Cham: Springer.
16. Haskins G, Kruger U, Yan P. Deep learning in medical image registration: a survey. *Machine Vision and Applications*. 2020;**31**(1):8.
17. Zhong J, Yang B, Huang G, Zhong F, Chen Z. Remote sensing image fusion with convolutional neural network. *Sens Imaging*. 2016;**17**(1):10.
18. Zampieri A, Charpiat G, Girard N, Tarabalka Y, editors. Multimodal image alignment through a multiscale chain of neural networks with application to remote sensing. *Proceedings of the European Conference on Computer Vision (ECCV)*; 2018.
19. Zhang H, Ni W, Yan W, Xiang D, Wu J, Yang X, et al. Registration of multimodal remote sensing image based on deep fully convolutional neural network. *IEEE Journal of Selected Topics in Applied Earth Observations and Remote Sensing*. 2019;**12**(8):3028-42.
20. Wang J, Yang Y, Mao J, Huang Z, Huang C, Xu W, editors. Cnn-rnn: A unified framework for multi-label image classification. *Proceedings of the IEEE conference on computer vision and pattern recognition*; 2016.
21. Zhang M, Li W, Du Q. Diverse region-based CNN for hyperspectral image classification. *IEEE Transactions on Image Processing*. 2018;**27**(6):2623-34.

22. Han D, Liu Q, Fan W. A new image classification method using CNN transfer learning and web data augmentation. *Expert Systems with Applications*. 2018;**95**:43-56.
23. Li Q, Cai W, Wang X, Zhou Y, Feng DD, Chen M, editors. Medical image classification with convolutional neural network. *13th International Conference on Control Automation Robotics & Vision (ICARCV)*; 2014.
24. Liu F, Lin G, Shen C. CRF learning with CNN features for image segmentation. *Pattern Recognition*. 2015;**48**(10):2983-92.
25. Kayalibay B, Jensen G, van der Smagt P. CNN-based segmentation of medical imaging data. *arXiv preprint arXiv:170103056*. 2017.
26. Milletari F, Navab N, Ahmadi SA, editors. V-net: Fully convolutional neural networks for volumetric medical image segmentation. *Fourth international conference on 3D vision (3DV)*; 2016.
27. Bao S, Chung AC. Multi-scale structured CNN with label consistency for brain MR image segmentation. *Computer Methods in Biomechanics and Biomedical Engineering: Imaging & Visualization*. 2018;**6**(1):113-7.
28. Cao X, Yang J, Zhang J, Nie D, Kim M, Wang Q, et al., editors. Deformable image registration based on similarity-steered CNN regression. *International Conference on Medical Image Computing and Computer-Assisted Intervention*; 2017; Cham: Springer.
29. Miao S, Wang ZJ, Liao R. A CNN regression approach for real-time 2D/3D registration. *IEEE transactions on medical imaging*. 2016;**35**(5):1352-63.
30. Sokooti H, De Vos B, Berendsen F, Lelieveldt BP, Išgum I, Staring M, editors. Nonrigid image registration using multi-scale 3D convolutional neural networks.

International Conference on Medical Image Computing and Computer-Assisted Intervention 2017: Springer.

31. Jiang P, Shackleford JA, editors. CNN driven sparse multi-level b-spline image registration. Proceedings of the IEEE Conference on Computer Vision and Pattern Recognition; 2018.

32. Uzunova H, Wilms M, Handels H, Ehrhardt J, editors. Training CNNs for image registration from few samples with model-based data augmentation. International Conference on Medical Image Computing and Computer-Assisted Intervention; 2017: Springer.

33. Dosovitskiy A, Fischer P, Ilg E, Hausser P, Hazirbas C, Golkov V, et al., editors. FlowNet: Learning optical flow with convolutional networks. Proceedings of the IEEE international conference on computer vision; 2015.

34. Ferrante E, Oktay O, Glocker B, Milone DH, editors. On the adaptability of unsupervised CNN-based deformable image registration to unseen image domains. International Workshop on Machine Learning in Medical Imaging; 2018: Springer.

35. Yamada A, Oyama K, Fujita S, Yoshizawa E, Ichinohe F, Komatsu D, et al. Dynamic contrast-enhanced computed tomography diagnosis of primary liver cancers using transfer learning of pretrained convolutional neural networks: Is registration of multiphasic images necessary? International Journal of Computer Sssisted Radiology and Surgery. 2019;**14**(8):1295-301.

36. Zhu N, Najafi M, Han B, Hancock S, Hristov D. Feasibility of Image Registration for Ultrasound-Guided Prostate Radiotherapy Based on Similarity Measurement by a

Convolutional Neural Network. *Technology in Cancer Research & Treatment*. 2019;**18**:1533033818821964.

37. Shan S, Yan W, Guo X, Chang EI, Fan Y, Xu Y. Unsupervised end-to-end learning for deformable medical image registration. *arXiv preprint arXiv:171108608*. 2017.

38. Zhu W, Myronenko A, Xu Z, Li W, Roth H, Huang Y, et al. Neureg: Neural registration and its application to image segmentation. *The IEEE Winter Conference on Applications of Computer Vision*. 2020:3617-26.

39. Kavitha K, Rao BT. Evaluation of distance measures for feature based image registration using AlexNet. *arXiv preprint arXiv:190712921*. 2019.

40. Zhang J, Ma W, Wu Y, Jiao L. Multimodal remote sensing image registration based on image transfer and local features. *IEEE Geoscience and Remote Sensing Letters*. 2019;**16**(8):1210-4.

41. Hu Q, Whitney HM, Giger ML. A deep learning methodology for improved breast cancer diagnosis using multiparametric MRI. *Scientific Reports*. 2020;**10**(1):1-11.

42. Han X. MR-based synthetic CT generation using a deep convolutional neural network method. *Medical Physics*. 2017;**44**(4):1408-19.

43. Yang Z, Dan T, Yang Y. Multi-temporal remote sensing image registration using deep convolutional features. *IEEE Access*. 2018;**6**:38544-55.

44. Ye F, Su Y, Xiao H, Zhao X, Min W. Remote Sensing Image Registration Using Convolutional Neural Network Features. *IEEE Geoscience and Remote Sensing Letters*. 2018;**15**(2):232–6.

45. Otsu N. A Threshold Selection Method from Gray-Level Histograms. *IEEE Transactions on Systems, Man, and Cybernetics*. 1979;**9**(1):62–6.

46. Marr D. Vision. A Computational Investigation into the Human Representation and Processing of Visual Information. Cambridge, MA: The MIT Press; 1982. 54-78 p.
47. Belongie S, Malik J, editors. Matching with Shape Contexts. 2000 Proceedings Workshop on Content-based Access of Image and Video Libraries; 2000; Head Island, SC, USA.
48. Kuhn HW. The Hungarian Method for the assignment problem. Naval Research Logistics Quarterly. 1955;**2**:83–97.
49. Jonker R, Volgenant A. A shortest augmenting path algorithm for dense and sparse linear assignment problems. Computing. 1987;**38**(4):325-40.
50. Glasbey CA, Mardia KV. A review of image-warping methods. Journal of Applied Statistics. 1998;**25**(2):155-71.
51. Powell MJD. A Thin Plate Spline Method for Mapping Curves into Curves in Two Dimensions. Computational Techniques and Applications (CTAC '95). 1995.
52. Bunch JR, Hopcroft J. Triangular factorization and inversion by fast matrix multiplication. Mathematics of Computation. 1974;**28**(125):231–6.
53. Ferreira DPL, Ribeiro E, Barcelos CAZ. A variational approach to non-rigid image registration with bregman divergences and multiple features. Pattern Recognit. 2018;**77**:237–47.
54. Zhou W, Bovik AC, Sheikh HR, Simoncelli EP. Image Quality Assessment: From Error Visibility to Structural Similarity. IEEE Transactions on Image Processing. 2004;**13**(4):600–12.
55. Zhang Z, Han D, Dezert J, Yang Y. A new image registration algorithm based on evidential reasoning. Sensors. 2019;**19**(5):1091.

56. DeepDreaming with TensorFlow.

<https://github.com/tensorflow/tensorflow/blob/master/tensorflow/examples/tutorials/deepdream/deepdream.ipynb>. Accessed on July 04, 2020.

## CHAPTER 6

### CONCLUSIONS

In this thesis, I developed reactive transport models that provides mechanistic understanding of EET in two sets of microbial communities: 1). anaerobic methane oxidizing consortia and 2). *G. sulfurreducens* biofilms grown on electrode in setting of microbial fuel cells. Our models produces metabolic activity patterns matching those observed in the  $^{15}\text{N}$  FISH-nanoSIMS experiments. We have shown that direct EET is a viable pathway for interspecies electron transport between archaea and bacteria within AOM consortia. It is evident that direct EET provides bioenergetic advantages over the mediated EET. Our work also highlighted that there are inevitable cost associated with direct EET with increasing spatial distance between the electron donating microbe and electron accepting partners. We have identified critical factors include total redox active molecules ( $M_{tot}$ ), number of conductive connections ( $N_{nw,cell}$ ), conductivity ( $\sigma$ ) and cell redox active factor ( $k_{act} \times A_{act}$ ). Our work on large-size AOM aggregate also revealed advantages of a hybrid DIET-MIET mechanism, allowing for balanced microbial energetics for both syntrophic partners, but opening up the potential for decoupling of the sulfate-reducing bacterial partner from the methanotrophic archaea by utilizing electron donors from environment.

In our work on electroactive *G. sulfurreducens* biofilm we showed that our model is able to reproduce high-resolution activity measurements of biofilms grown under high (+0.24 V) and low (-0.1 V) anode potentials. Three major features of the metabolic activity patterns in the experimental data are captured in our model: 1) the maximum activity occurs near the anode surface in both high and low potential

simulations, 2) at high potential a second activity peak occurs near the surface of the biofilm, and 3) a slight decrease in metabolic activity occurs right at the surface of the high potential anode. Central to these model results are potential losses and the accumulation of protons that in concert regulate the observed metabolic stratifications. Potential losses cause cells to experience lower effective potential than the value at which the anode is poised. These effects become more significant the further cells are from the anode surface causing the maximum metabolic activity to occur near the anode in both high and low potential simulations. Shifting between two redox-active systems allows *G. sulfurreducens* cells to respond to the decreasing external electric potential, leading to the secondary metabolic peak at  $\sim 12 \mu\text{m}$  from the electrode. No such secondary peak appears when the anode is poised at low potential because under these conditions the low potential redox-active system is the only one operative throughout the entire biofilm. At high anode potential our model reveals that  $\text{H}^+$  accumulation close to the electrode limited *G. sulfurreducens* metabolism, leading to a slight decrease in metabolic activity at the electrode surface. This effect is not observed at low anodic potentials because the pH does not fall to values low enough to inhibit metabolic activity. Our model simulations also demonstrate how the redox gradients and electric fields that developed within *G. sulfurreducens* biofilms drive extracellular electron transfer through the biofilms to the electrode. Further analysis of simulation results shows that electrons can be temporarily stored as reduced redox-active molecules (i.e.  $\text{Cyt}_{red}$ ) with a higher fraction of  $\text{Cyt}_{red}$  at locations farther away from the electrode, suggesting that for a short time, *G. sulfurreducens* cells may take advantage of the developed direct electron transport network even without external electron acceptors.

Our work reveals some fundamental connections underlying interspecies EET within syntrophic AOM consortia and EET between *G. sulfurreducens* biofilm and electrode. Although our implementation for EET within AOM consortia is different from anode-respiring *G. sulfurreducens* biofilm in many ways, both of our models show direct EET is viable for long-range electron transport over a spatial distance greater than 10  $\mu\text{m}$  beyond diffusion limit. Both models show significant loss of metabolic activity may occur with increasing spatial distance from the electron-donating cells due to the existence of ohmic resistance loss and activation loss associated with direct EET. In another words, there is a spatial limitation on how large active biofilms or microbial consortia can grow. Moving forward there is a need to synthesize direct EET models across broader microbial communities. Our efforts have shown that reactive transport modeling can be powerful tool to capture the physical, chemical and biological aspects of the EET phenomenon with a systematic, careful evaluation of model parameters, and with single-cell resolved experimental validations.

## APPENDIX A

### CHAPTER 2 SUPPLEMENTARY MATERIAL

#### A1. Model schematic

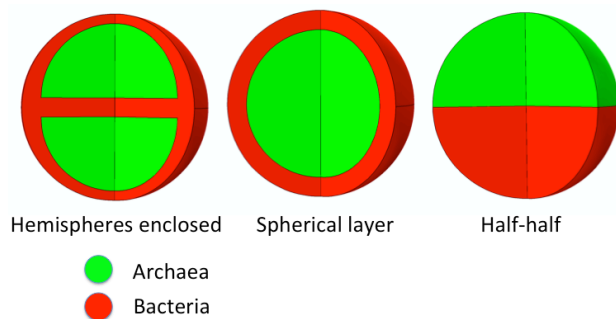


Fig. A1. Schematic of the spatial distribution of archaea (green) and bacteria (red) with open-view (225°) 3D mesh representation in COMSOL. From left to right: two hemispheres enclosed archaea surrounded by bacteria (hemispheres enclosed), a sphere of archaea surrounded by bacteria (spherical layer), and a half sphere of bacteria and archaea each (half-half).

## A2. AOM rate simulation and patterns

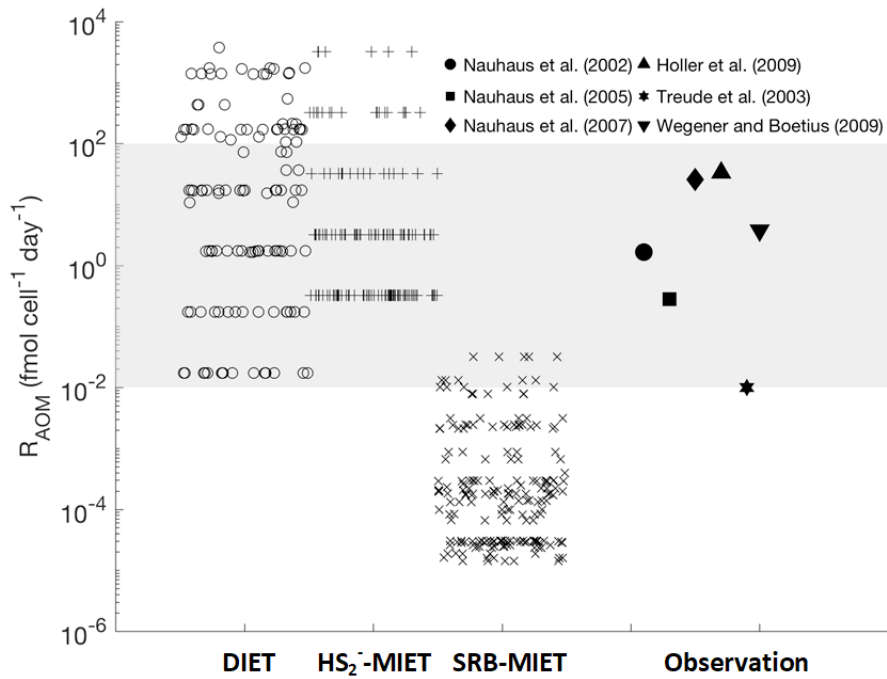


Fig. A2: Simulation results for DIET (o),  $\text{HS}_2^-$ -MIET (+) and SRB-MIET ( $\times$ ) models. Each symbol indicates an individual model realization, differing in size, arrangement or rate parameterization. The estimated range of environmental cell-specific rates is indicated by the gray shaded area. Estimated environmental cell-specific AOM rates are indicated by the filled black symbols (see section 3.3 and Table 3.1).

### A3. Reduced model estimations

In order to assess the spatial gradients in resource concentration (and by extension the likelihood of spatially varying cellular activities) we consider a simple geometry of two concentric spheres each composed of either archaea or bacteria. If the inner sphere produces a metabolic intermediate at a constant rate and the outer sphere consumes that intermediate at a constant rate, then the concentration dynamics are given by

$$\frac{\partial C}{\partial t} = \frac{D}{r^2} \frac{\partial}{\partial r} \left( r^2 \frac{\partial C}{\partial r} \right) - \gamma$$

where  $C$  is the concentration of the intermediate,  $r$  is the radial distance,  $D$  is the diffusivity of the intermediate, and  $\gamma$  is the consumption rate of the intermediate. Solving for the steady state concentration of  $C$ , with a no-flux boundary condition at the outer boundary,

$\frac{\partial C}{\partial r} \Big|_{r=r_{ou}} = 0$ , and a constant value of  $C_{in}$  at the surface of the inner sphere gives

$$C = C_{in} + \frac{\gamma(2r_{in}r_{ou}^3 - r(r_{in}^3 + 2r_{ou}^3) + r_{in}r^3)}{6Dr_{in}r}$$

where  $r_{in}$  and  $r_{ou}$  are the inner and outer sphere radii respectively, and  $C_{in}$  is the concentration at the surface of the inner sphere.

We solved for the concentration profile using typical AOM rates for  $\gamma$  (5 fmol cell<sup>-1</sup> d<sup>-1</sup>), diffusivities of  $2.4 \times 10^{-10}$  m<sup>2</sup> s<sup>-1</sup> and  $1 \times 10^{-7}$  m<sup>2</sup> s<sup>-1</sup> for chemical diffusion and electron conduction, respectively, and an aggregate radius of 3  $\mu$ m (Fig. A3) to illustrate the impact of transport constraints on substrate distribution. Same substrate concentration (Fig. A3A: H<sub>2</sub>; Fig. A3B: HS<sub>2</sub><sup>-</sup>) at the edge of inner sphere ( $r = r_{in}$ ) and different diffusivities are used to calculate the substrate concentration across the outer sphere ( $C/C_{in}$ ). The steady state concentration of HS<sub>2</sub><sup>-</sup> at the edge of inner sphere ( $r = r_{in}$ ) is set to be 0.055 mol m<sup>-3</sup> (faster AOM rates allow higher producing rate and thus higher concentration of HS<sub>2</sub><sup>-</sup>) based on

the simulation results from  $\text{HS}_2^-$ -MIET models with no gradient boundary condition. The concentration of  $\text{H}_2$  at the steady state at the edge of inner sphere ( $r = r_{in}$ ) is set to be  $2.4 \times 10^{-4} \text{ mol m}^{-3}$ ) based on the simulation results from DIET models with no gradient boundary condition.

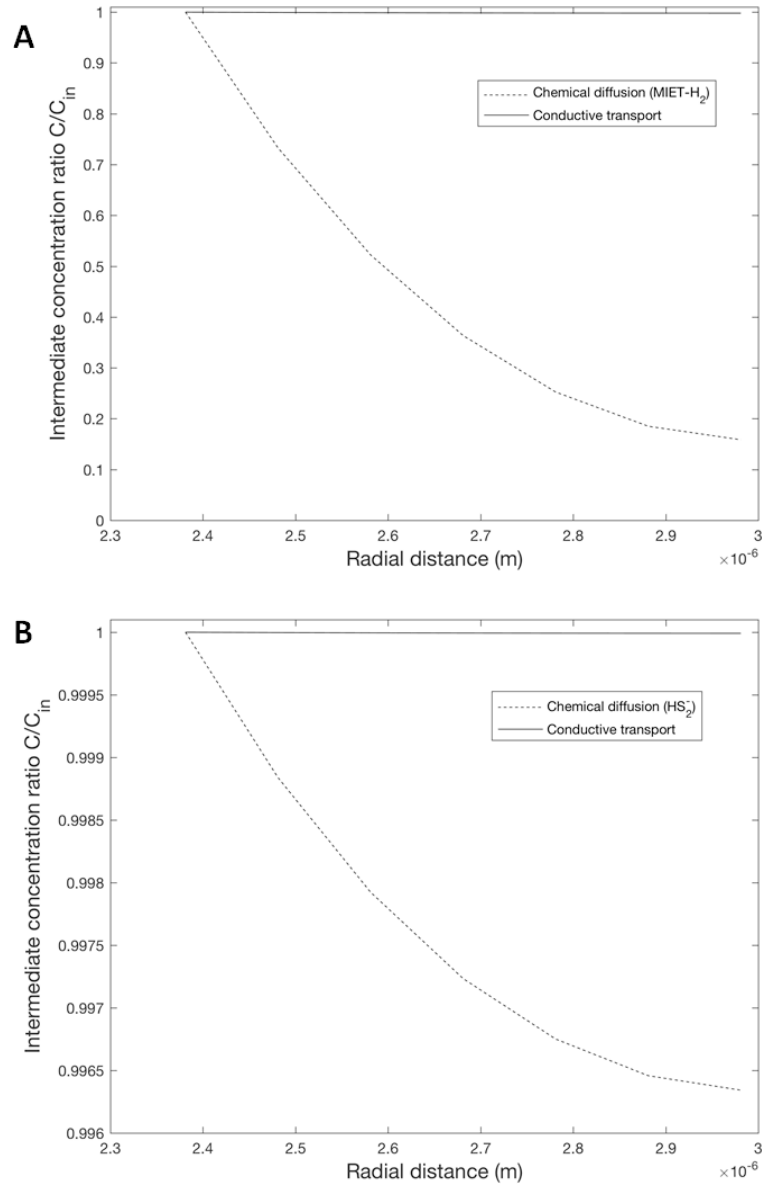


Fig. A3. Substrate concentration across the outer sphere ( $C/C_{in}$ ). (A). Transportation of  $\text{H}_2$  via chemical diffusion vs conductive transport. (B). Transportation of  $\text{HS}_2^-$  via chemical

diffusion vs conductive transport. Note the difference in scale of the y-axes in the two panels.

#### A4. Standard Gibbs Free Energy of Reaction

The standard Gibbs Free Energies of reaction for are given as follows:

The energetics of reactions 6 and 7 involving methane, water, bicarbonate, sulfate, sulfide, hydrogen, and considering the oxidized and reduced form of cytochrome c as redox molecules M, MH (Korth et al. 2015), are:

$$\Delta G^0 \text{ (reaction 6)} = G_{\text{HCO}_3^-}^0 + G_{\text{H}^+}^0 + f_D G_{\text{H}_2}^0 + f_M G_{\text{MH}}^0 - G_{\text{CH}_4}^0 - 3G_{\text{H}_2\text{O}}^0 - f_M G_{\text{M}}^0$$

with  $\Delta G^0 = 36.8 \text{ kJ mol}^{-1} \text{ CH}_4$  for  $f_D$  and  $f_M$  equal to 0.4 and 7.2

$$\Delta G^0 \text{ (reaction 7)} = G_{\text{HS}^-}^0 + 4G_{\text{H}_2\text{O}}^0 + f_M G_{\text{M}}^0 - G_{\text{SO}_4^{2-}}^0 - G_{\text{H}^+}^0 - f_M G_{\text{MH}}^0$$

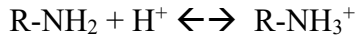
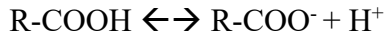
with  $\Delta G^0 = -69.7 \text{ kJ mol}^{-1} \text{ SO}_4^{2-}$  for  $f_D$  and  $f_M$  equal to 0.4 and 7.2

#### A5. Acid-base reactions

We consider the dissolved inorganic carbon and borate system, using the kinetic implementation described in Zeebe and Wolf-Gladrow (2005) and DOE (1994), involving the following acid-base reactions:



The effect of cell surface acid-base reactions is approximated as:



Equilibrium constants were estimated for carboxy and amino surface groups from Phoenix et al. (2002), Voet and Voet (2004). The protonation rate constant is set to  $10^9 \text{ m}^3 \text{ s}^{-1} \text{ mol}^{-1}$  (Burgess et al. 2006) and the deprotonation rate constant is set to  $1 \text{ s}^{-1}$  for carboxy. This gives equilibrium constant for carboxy surface groups to be  $10^{-5} \text{ M}$  ( $\text{pK}_a = 5$ ), consistent with equilibrium constants given in Phoenix et al. (2002) and Voet and Voet (2004). In addition, protonation constant for amino groups is set to  $10^6 \text{ m}^3 \text{ s}^{-1} \text{ mol}^{-1}$  and deprotonation rate constant is set to  $1 \text{ s}^{-1}$ . The second-order rate constant for reaction of the unprotonated amino group was estimated based on values reported in Kaplan et al. (1971). This results in equilibrium constant for amino surface groups to be  $10^{-9} \text{ M}$  ( $\text{pK}_a = 9$ ), consistent with equilibrium constants given in Phoenix et al. (2002) and Voet and Voet (2004).

The reaction rates ( $\text{mol}/(\text{m}^3 \cdot \text{s})$ ) for each species involved in these acid-base reactions then are (see Table A1 for rate constants):

$$d\text{CO}_2/dt = k_{1-} \cdot \text{HCO}_3^- \cdot \text{H}^+ - k_{1+} \cdot \text{CO}_2 + k_{3-} \cdot \text{HCO}_3^- - k_{3+} \cdot \text{CO}_2 \cdot \text{OH}^-$$

$$d\text{HCO}_3^-/dt = -d\text{CO}_2/dt + k_{2-} \cdot \text{CO}_3^{2-} \cdot \text{H}^+ - k_{2+} \cdot \text{HCO}_3^- + k_{4+} \cdot \text{CO}_3^{2-} - k_{4-} \cdot \text{HCO}_3^- \cdot \text{OH}^- - k_{5-} \cdot \text{BOH}_4^- \cdot \text{HCO}_3^- + k_{5+} \cdot \text{CO}_3^{2-} \cdot \text{B(OH)}_3$$

K4a: Forward Equilibrium Rate constant for  $\text{HCO}_3^- + \text{OH}^- \rightarrow \text{CO}_3^{2-} + \text{H}_2\text{O}$

$$d\text{H}^+/dt = -k_{1-} \cdot \text{HCO}_3^- \cdot \text{H}^+ + k_{1+} \cdot \text{CO}_2 - k_{2-} \cdot \text{CO}_3^{2-} \cdot \text{H}^+ + k_{2+} \cdot \text{HCO}_3^- - k_{w-} \cdot \text{H}^+ \cdot \text{OH}^- + k_{w+} \cdot \text{H}^+ \cdot \text{OH}^- - k_{\text{COOH}} \cdot \text{RCOO}^- \cdot \text{H}^+ + k_{\text{COOH}} \cdot \text{RCOOH} + k_{\text{NH}_2} \cdot \text{RNH}_3^+ - k_{\text{NH}_2} \cdot \text{RNH}_2 \cdot \text{H}^+$$

$$d\text{R-NH}_2/dt = k_{\text{NH}_2} \cdot \text{RNH}_3^+ - k_{\text{NH}_2} \cdot \text{RNH}_2 \cdot \text{H}^+$$

$$dR\text{-COOH}/dt = k_{\text{COOH}}R\text{-COO}^- \cdot H^+ - k_{\text{COOH}^+}R\text{-COOH}$$

$$dOH^-/dt = k_3\text{-HCO}_3^- - k_{3+}\text{CO}_2 \cdot OH^- + k_B\text{-BOH}_4^- - k_{B+}B(OH)_3 \cdot OH^- + k_{4+}\text{CO}_3^{2-} \cdot OH^- - k_4\text{-HCO}_3^- - k_w\text{-H}^+ \cdot OH^- + k_w+$$

$$d\text{CO}_3^{2-}/dt = -k_2\text{-CO}_3^{2-} \cdot H^+ + k_{2+}\text{HCO}_3^- - k_4\text{-CO}_3^{2-} + k_{4+}\text{HCO}_3^- \cdot OH^- + k_5\text{-B(OH)}_4^- \cdot \text{HCO}_3^- - k_{5+}\text{CO}_3^{2-} \cdot B(OH)_3$$

$$d\text{BOH}_4^-/dt = -k_5\text{-B(OH)}_4^- \cdot \text{HCO}_3^- + k_{5+}\text{CO}_3^{2-} \cdot B(OH)_3 - k_B\text{-B(OH)}_4^- + k_{B+}B(OH)_3 \cdot OH^-$$

1 Table A1. Parameter list for acid-base reactions

Symbol	Value at T=8°C, S= 35	Description	Reactions	References
<b>Environmental conditions</b>				
pH	8.2	Initial pH		(DOE 1994)
T <sub>B</sub>	0.427 mol m <sup>-3</sup>	Total Boron		
T <sub>DIC</sub>	2.36 mol m <sup>-3</sup>	Total DIC		
ρ <sub>sw</sub>	1.03×10 <sup>3</sup> kg m <sup>-3</sup>	Density of seawater. Calculated		(Chester and Jickells 2012)
[RCOOH] <sub>T</sub>	10 <sup>-3</sup> mol (g dry cell) <sup>-1</sup>	Concentration of total surface carboxy groups		(Konhauser 2006)
[RNH <sub>2</sub> ] <sub>T</sub>	10 <sup>-3</sup> mol (g dry cell) <sup>-1</sup>	Concentration of total surface amino groups		
<b>Kinetic reactions</b>				
K <sub>1</sub>	9.9×10 <sup>-4</sup> mol m <sup>-3</sup>	Equilibrium constant	CO <sub>2</sub> + H <sub>2</sub> O → HCO <sub>3</sub> <sup>-</sup> + H <sup>+</sup>	(DOE 1994)
k <sub>1+</sub>	6.07×10 <sup>-3</sup> s <sup>-1</sup>	Forward rate constant		(Zeebe and Wolf-Gladrow 2005)
k <sub>1-</sub>	6.13 m <sup>3</sup> s <sup>-1</sup> mol <sup>-1</sup>	Backward rate constant		
K <sub>2</sub>	2.17×10 <sup>-7</sup> mol m <sup>-3</sup>	Equilibrium constant	HCO <sub>3</sub> <sup>-</sup> → CO <sub>3</sub> <sup>2-</sup> + H <sup>+</sup>	(DOE 1994)
k <sub>2+</sub>	10.5 s <sup>-1</sup>	Forward rate constant		(Zeebe and Wolf-Gladrow 2005)
k <sub>2-</sub>	4.87×10 <sup>7</sup> m <sup>3</sup> s <sup>-1</sup> mol <sup>-1</sup>	Backward rate constant		
K <sub>3</sub>	7.99×10 <sup>4</sup> m <sup>3</sup> mol <sup>-1</sup>	Equilibrium constant	CO <sub>2</sub> + OH <sup>-</sup> → HCO <sub>3</sub> <sup>-</sup>	(DOE 1994)
k <sub>3+</sub>	2.24 m <sup>3</sup> s <sup>-1</sup> mol <sup>-1</sup>	Forward rate constant		(Zeebe and Wolf-Gladrow 2005)
k <sub>3-</sub>	2.8×10 <sup>-5</sup> s <sup>-1</sup>	Backward rate constant		
K <sub>4</sub>	17.9 m <sup>3</sup> mol <sup>-1</sup>	Equilibrium constant	HCO <sub>3</sub> <sup>-</sup> + OH <sup>-</sup> → CO <sub>3</sub> <sup>2-</sup> + H <sub>2</sub> O	(DOE 1994)
k <sub>4+</sub>	5.84×10 <sup>6</sup> m <sup>3</sup> s <sup>-1</sup> mol <sup>-1</sup>	Forward rate constant		(Zeebe and Wolf-Gladrow 2005)
k <sub>4-</sub>	3.34×10 <sup>5</sup> s <sup>-1</sup>	Backward rate constant		
K <sub>5</sub>	7.43	Equilibrium constant	CO <sub>3</sub> <sup>2-</sup> + B(OH) <sub>3</sub> + H <sub>2</sub> O → B(OH) <sub>4</sub> <sup>-</sup> + HCO <sub>3</sub> <sup>-</sup>	(DOE 1994)
k <sub>5+</sub>	4.06×10 <sup>3</sup> m <sup>3</sup> s <sup>-1</sup> mol <sup>-1</sup>	Forward rate constant		(Zeebe and Wolf-Gladrow 2005)
k <sub>5-</sub>	5.46×10 <sup>2</sup> m <sup>3</sup> s <sup>-1</sup> mol <sup>-1</sup>	Backward rate constant		
K <sub>w</sub>	1.24×10 <sup>-8</sup> mol <sup>2</sup> m <sup>-6</sup>	Equilibrium constant	H <sub>2</sub> O → H <sup>+</sup> + OH <sup>-</sup>	(DOE 1994)
k <sub>w+</sub>	1.44 mol m <sup>-3</sup> s <sup>-1</sup>	Forward rate constant		(Zeebe and Wolf-Gladrow 2005)
k <sub>w-</sub>	1.16×10 <sup>8</sup> m <sup>3</sup> s <sup>-1</sup> mol <sup>-1</sup>	Backward rate constant		
K <sub>B</sub>	1.61×10 <sup>-6</sup> mol m <sup>-3</sup>	Equilibrium constant	B(OH) <sub>3</sub> + H <sub>2</sub> O → H <sup>+</sup> + B(OH) <sub>4</sub> <sup>-</sup>	(DOE 1994)
k <sub>B+</sub>	6.09×10 <sup>3</sup> m <sup>3</sup> s <sup>-1</sup> mol <sup>-1</sup>	Forward rate constant		(Zeebe and Wolf-Gladrow 2005)
k <sub>B-</sub>	46.9 s <sup>-1</sup>	Backward rate constant. Calculated		
K <sub>NH2</sub>	10 <sup>6</sup> m <sup>3</sup> mol <sup>-1</sup>	Equilibrium constant	R-NH <sub>2</sub> + H <sup>+</sup> → R-NH <sub>3</sub> <sup>+</sup>	(Kaplan et al. 1971, Voet and Voet 2004)
k <sub>NH2+</sub>	10 <sup>6</sup> m <sup>3</sup> s <sup>-1</sup> mol <sup>-1</sup>	Forward rate constant		(Kaplan et al. 1971)
k <sub>NH2-</sub>	1 s <sup>-1</sup>	Backward rate constant. Calculated.		
K <sub>COOH</sub>	10 <sup>-8</sup> mol m <sup>-3</sup>	Equilibrium constant	R-COOH → R-COO <sup>-</sup> + H <sup>+</sup>	(Phoenix et al. 2002, Voet and Voet 2004)
k <sub>COOH+</sub>	1 s <sup>-1</sup>	Forward rate constant. Calculated.		(Burgess et al. 2006)
k <sub>COOH-</sub>	10 <sup>9</sup> m <sup>3</sup> s <sup>-1</sup> mol <sup>-1</sup>	Backward rate constant		

2

## A6. Model governing equations

Fixed concentration boundary conditions are imposed for all chemical species at the outer domain boundary except for  $HS_2^-$  for which a no flux condition is imposed at the outer domain boundary, and for MH, R-COOH, R-NH<sub>2</sub>, for which no flux condition is imposed at the aggregate surface. Boundary conditions are set to:  $10^{-4}$  M  $HS^-$ ,  $10^{-3}$  M  $HCO_3^-$ , pH=8.2,  $10^{-2}$  M  $SO_4^{2-}$ ,  $10^{-3}$  M  $CH_4$ ,  $10^{-7}$  mM acetate. The acid-base reactions for  $HCO_3^-$ ,  $H^+$ ,  $CO_2$ ,  $CO_3^{2-}$ ,  $OH^-$ ,  $BOH_4^-$ , R-NH<sub>2</sub>, and R-COOH, as described in Supporting Information Appendix A5.

### A6.1 Mediated interspecies electron transfer

$$\frac{\partial \phi CH_4}{\partial t} = -\phi R_A + \nabla \cdot (\phi \mathbf{D}_{CH_4} \nabla CH_4)$$

$$\frac{\partial \phi Ac}{\partial t} = \phi R_A - \phi R_B + \nabla \cdot (\phi \mathbf{D}_{Ac} \nabla Ac)$$

$$\frac{\partial \phi SO_4^{2-}}{\partial t} = -\phi R_B + \nabla \cdot (\phi \mathbf{D}_{SO_4^{2-}} \nabla SO_4^{2-})$$

$$\frac{\partial \phi HCO_3^-}{\partial t} = \phi R_A - 2\phi R_B + \nabla \cdot (\phi \mathbf{D}_{HCO_3^-} \nabla HCO_3^-)$$

$$\frac{\partial \phi HS^-}{\partial t} = \phi R_B + \nabla \cdot (\phi \mathbf{D}_{HS^-} \nabla HS^-)$$

$$R_A = k_A B_A \frac{CH_4}{K_m^{CH_4} + CH_4} \max \left( 0, 1 - \exp \left( -\frac{-(\Delta G_A^0 + R_{gas} T \ln Q_A) - \Delta G_{ATP}}{\chi R_{gas} T} \right) \right),$$

$$R_B = k_B B_B \frac{SO_4^{2-}}{K_m^{SO_4^{2-}} + SO_4^{2-}} \frac{Ac}{K_m^{Ac} + Ac} \max \left( 0, 1 - \exp \left( -\frac{-(\Delta G_B^0 + R_{gas} T \ln Q_B) - \Delta G_{ATP}}{\chi R_{gas} T} \right) \right),$$

where  $B_A$ ,  $B_B$  are the cell densities of archaea and bacteria as a function of space, respectively,

$$\Delta G_A^0 = 14.8 \text{ kJ (mol } CH_4)^{-1}, \quad \Delta G_B^0 = -47.7 \text{ kJ (mol } SO_4)^{-1}, \quad Q_A = \frac{a_{Ac}}{a_{CH_4} a_{HCO_3}}, \quad Q_B = \frac{a_{HS} a_{HCO_3}^2}{a_{Ac} a_{SO_4}},$$

with  $a$  denoting activities, computed as the product of concentrations and activity coefficients as given in Orcutt and Meile (2008).

### A6.2 Disulfide pathway

$$\frac{\partial \phi CH_4}{\partial t} = -\phi R_A + \nabla \cdot (\phi \mathcal{D}_{CH_4} \nabla CH_4)$$

$$\frac{\partial \phi SO_4^{2-}}{\partial t} = -\frac{8}{7} \phi R_A + \frac{1}{7} \phi R_B + \nabla \cdot (\phi \mathcal{D}_{SO_4^{2-}} \nabla SO_4^{2-})$$

$$\frac{\partial \phi HCO_3^-}{\partial t} = \phi R_A + \nabla \cdot (\phi \mathcal{D}_{HCO_3^-} \nabla HCO_3^-)$$

$$\frac{\partial \phi HS^-}{\partial t} = \phi R_B + \nabla \cdot (\phi \mathcal{D}_{HS^-} \nabla HS^-)$$

$$\frac{\partial \phi HS_2^-}{\partial t} = \frac{4}{7} \phi R_A - \frac{4}{7} \phi R_B + \nabla \cdot (\phi \mathcal{D}_{HS_2^-} \nabla HS_2^-)$$

$$\frac{\partial \phi H^+}{\partial t} = -\frac{5}{7} \phi R_A + \frac{5}{7} \phi R_B + \nabla \cdot (\phi \mathcal{D}_{H^+} \nabla H^+)$$

where

$$R_A = k_A B_A \frac{CH_4}{K_m^{CH_4} + CH_4} \frac{SO_4^{2-}}{K_m^{SO_4^{2-}} + SO_4^{2-}} \max(0, 1 - \exp\left(-\frac{-(\Delta G_A^0 + R_{gas} T \ln Q_A) - \Delta G_{ATP}}{\chi R_{gas} T}\right)),$$

$$R_B = k_B B_B \frac{HS_2^-}{K_m^{HS_2^-} + HS_2^-} \max(0, 1 - \exp\left(-\frac{-(\Delta G_B^0 + R_{gas} T \ln Q_B) - \Delta G_{ATP}}{\chi R_{gas} T}\right)),$$

where  $B_A$ ,  $B_B$  are the cell densities of archaea and bacteria as a function of space, respectively,

$$\Delta G_A^0 = -62.6 \text{ kJ rxn}^{-1}, \Delta G_B^0 = 29.7 \text{ kJ rxn}^{-1}, Q_A = \frac{a_{HS_2}^{4/7} a_{HCO_3}}{a_{CH_4} a_{SO_4}^{8/7} a_H^{5/7}}, Q_B = \frac{a_{HS_2} a_{SO_4}^{1/7} a_H^{5/7}}{a_{HS_2}^{4/7}}, \text{ with } a$$

denoting activities, computed as the product of concentrations and activity coefficients as given in

Orcutt and Meile (2008).

### A6.3 Direct interspecies electron transfer

$$\frac{\partial \phi CH_4}{\partial t} = -\phi R_A + \nabla \cdot (\phi \mathcal{D}_{CH_4} \nabla CH_4)$$

$$\frac{\partial \phi HCO_3^-}{\partial t} = \phi R_A + \nabla \cdot (\phi \mathcal{D}_{HCO_3^-} \nabla HCO_3^-)$$

$$\frac{\partial \phi SO_4^{2-}}{\partial t} = -\phi R_B + \nabla \cdot (\phi \mathcal{D}_{SO_4^{2-}} \nabla SO_4^{2-})$$

$$\frac{\partial \phi_{H_2}}{\partial t} = f_D \phi_{R_A} - f_D \phi_{R_B} + \nabla \cdot (\phi \mathcal{D}_{H_2} \nabla H_2)$$

$$\frac{\partial \phi_{H^+}}{\partial t} = \phi_{R_A} - \phi_{R_B} + \nabla \cdot (\phi \mathcal{D}_{H^+} \nabla H^+)$$

$$\frac{\partial \phi_{HS^-}}{\partial t} = \phi_{R_B} + \nabla \cdot (\phi \mathcal{D}_{HS^-} \nabla HS^-)$$

$$\frac{\partial \phi_{MH}}{\partial t} = \phi f_M R_A - \phi f_M R_B + \nabla \cdot (\phi \mathcal{D}_{MH} \nabla MH) + \phi \nabla \cdot (k^0 M \cdot MH \left( \frac{nF\delta}{R_{gas}T} \right) \frac{\partial \phi}{\partial x})$$

In the case where  $R_A$  and  $R_B$  are independent of the concentration of the redox-active molecules fixed on conductive pili or matrix (reduced: MH; oxidized: M):

$$R_A = k_A B_A \frac{CH_4}{K_m^{CH_4} + CH_4} \max \left( 0, 1 - \exp \left( - \frac{-(\Delta G_A^0 + R_{gas}T \ln Q_A) - \Delta G_{ATP}}{\chi R_{gas}T} \right) \right),$$

$$R_B = k_B B_B \frac{SO_4^{2-}}{K_m^{SO_4^{2-}} + SO_4^{2-}} \max \left( 0, 1 - \exp \left( - \frac{-(\Delta G_B^0 + R_{gas}T \ln Q_B) - \Delta G_{ATP}}{\chi R_{gas}T} \right) \right),$$

In the case where  $R_A$  and  $R_B$  are dependent on M and MH (see Eqns. 11 and 12):

$$R_A = k_A B_A \frac{CH_4}{K_m^{CH_4} + CH_4} M \cdot \max \left( 0, 1 - \exp \left( - \frac{-(\Delta G_A^0 + R_{gas}T \ln Q_A) - \Delta G_{ATP}}{\chi R_{gas}T} \right) \right),$$

$$R_B = k_B B_B \frac{SO_4^{2-}}{K_m^{SO_4^{2-}} + SO_4^{2-}} MH \cdot \max \left( 0, 1 - \exp \left( - \frac{-(\Delta G_B^0 + R_{gas}T \ln Q_B) - \Delta G_{ATP}}{\chi R_{gas}T} \right) \right),$$

where  $B_A$ ,  $B_B$  are the cell densities of archaea and bacteria as a function of space, respectively.

$\Delta G_A^0$  and  $\Delta G_B^0$  vary with  $f_D$  and  $f_M$  (see Supporting Information Appendix A3),  $Q_A =$

$$\frac{a_{H_2}^{f_D} a_{HCO_3} a_{MH}^{f_D} a_{H^+}}{a_{CH_4} a_M^{f_D}}, \quad Q_B = \frac{a_{HS} a_M^{f_D}}{a_{H_2}^{f_D} a_{SO_4} a_{MH}^{f_D} a_{H^+}},$$

with  $a$  denoting activities, computed as the product of concentrations and activity coefficients as given in Orcutt and Meile (2008). Note also

that the diffusion term for MH results from electron hopping, rather than diffusion of the molecule

(see section 2.1.3).

Model implementations are available on bitbucket at

[https://bitbucket.org/MeileLab/xiaojia\\_em/src](https://bitbucket.org/MeileLab/xiaojia_em/src)

## A7. Intra-aggregate cell-specific activity distribution and sensitivity analysis

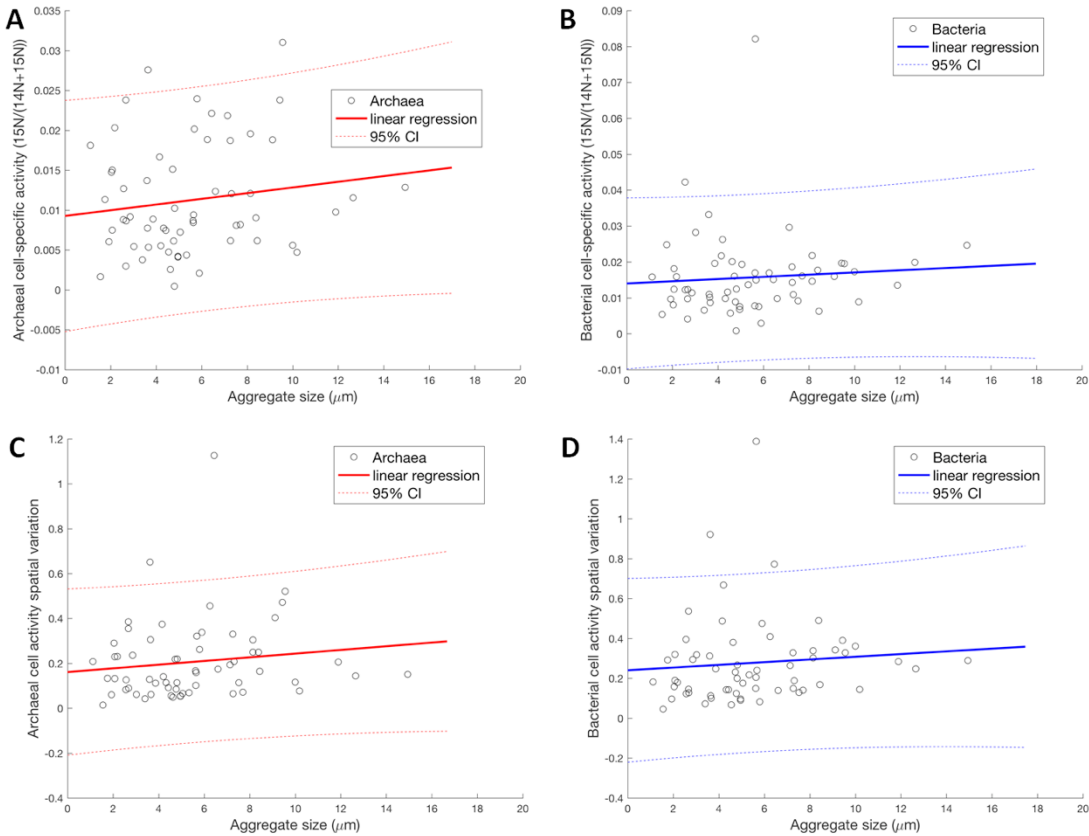


Fig. A4. Average cell-specific activity for archaeal cells (A) and bacterial cells (B) vs. aggregate radius. Intra-aggregate variation in cell-specific activity for archaeal cells (C) and bacterial cells (D) vs. aggregate radius. Dotted lines are for 95% confidence interval (CI) for the regression line.

Spatial activity variation is calculated as  $\left(\frac{\int (R - \bar{R})^2 dV}{V}\right)^{1/2} / \bar{R}$ , where  $R$  and  $V$  denote the rates and volumes, of the archaeal and bacterial regions, respectively, and  $\bar{R}$  is the volume averaged reaction rate.

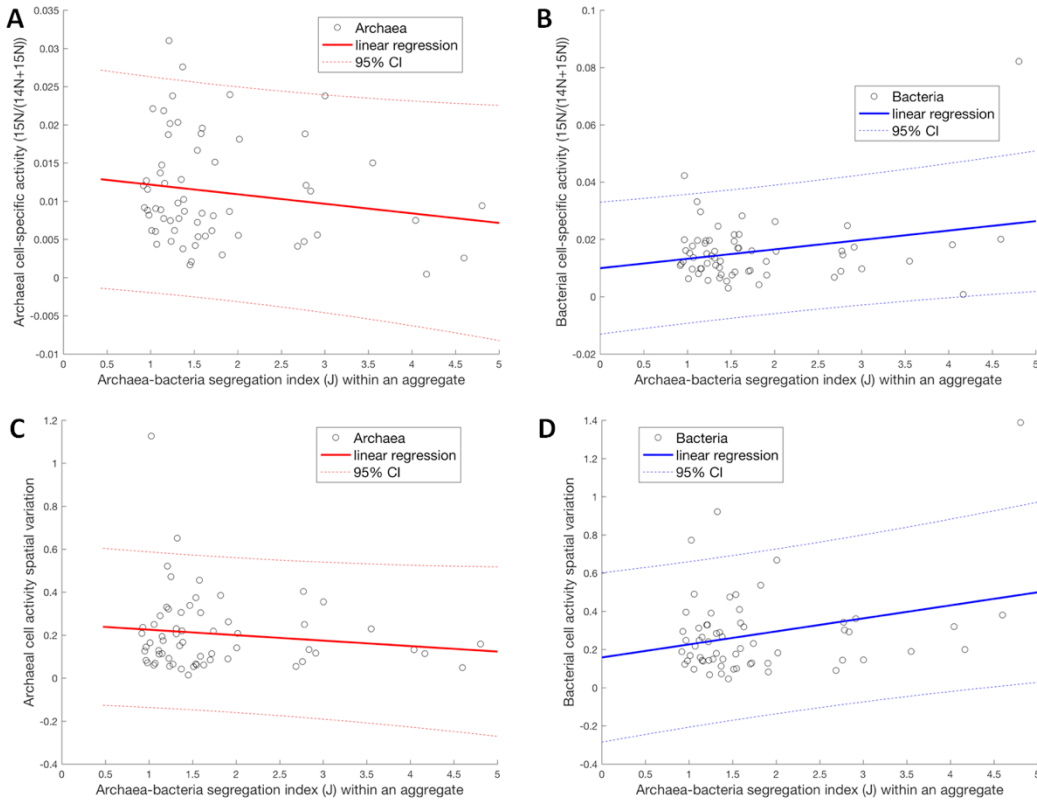


Fig. A5. Average cell-specific activity for archaeal cells (A) and bacterial cells (B) vs. archaea-bacteria segregation index (J) within an aggregate as defined in McGlynn et al. (2015). Intra-aggregate variation in cell-specific activity for archaeal cells (C) and bacterial cells (D) vs. archaea-bacteria segregation index (J) within an aggregate. Dotted lines are for 95% confidence interval (CI) for the regression line. Spatial activity variation is calculated as  $\left(\frac{\int (R-\bar{R})^2 dV}{V}\right)^{1/2} / \bar{R}$ , where  $R$  and  $V$  denote the rates and volumes of the archaeal and bacterial regions, respectively, and  $\bar{R}$  is the volume averaged reaction rate.

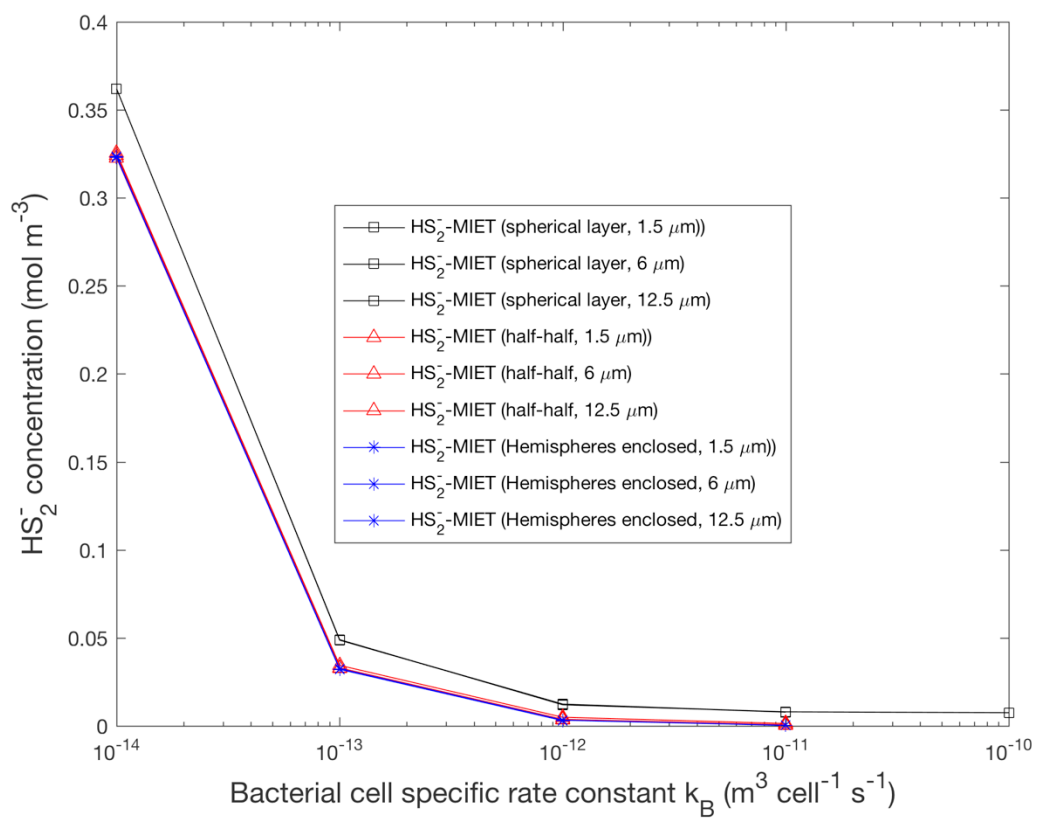


Fig. A6. Average concentration of  $\text{HS}_2^-$  in environment vs. bacterial cell specific rate constant  $k_B$ .

Archaeal cell specific rate constant  $k_A$  is fixed at  $10^{-14} \text{ mol cell}^{-1} \text{ d}^{-1}$ .

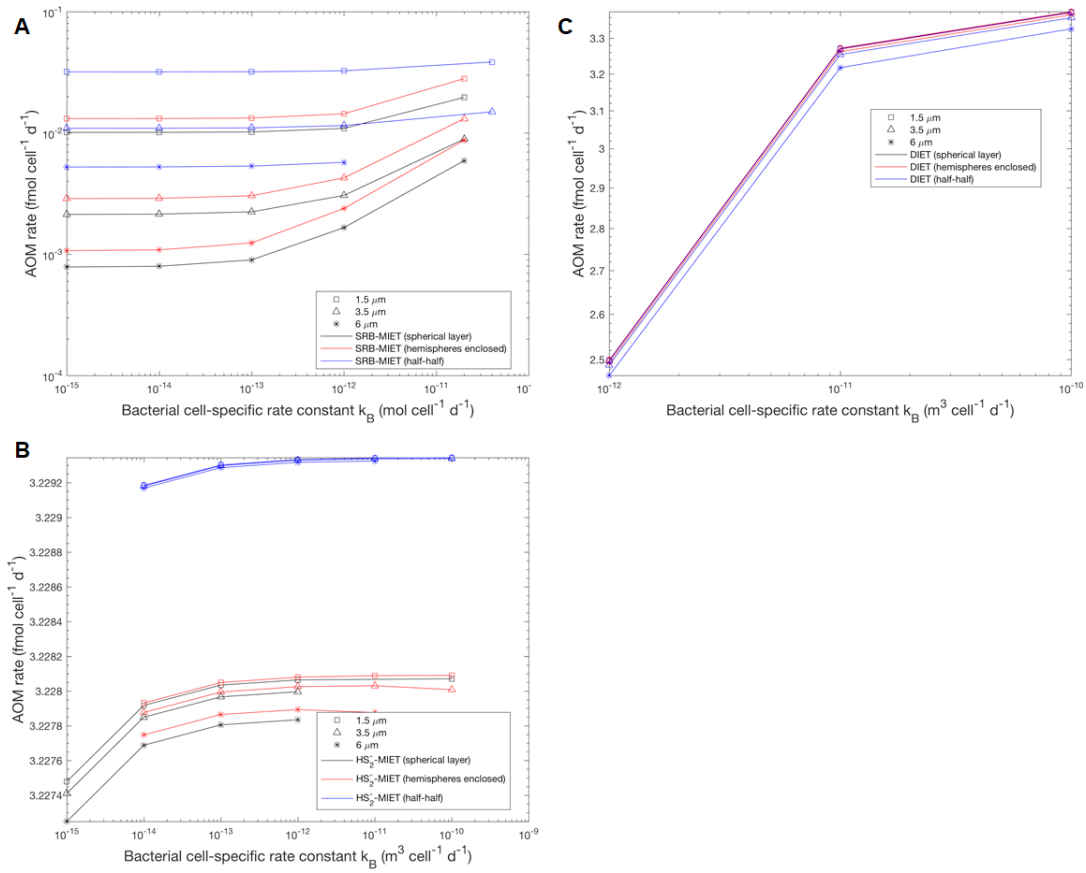


Fig. A7. AOM rate vs. bacterial cell-specific rate constant ( $k_B$ ). The archaeal cell specific rate constants are fixed at A)  $k_A = 10^{-15}$  mol cell<sup>-1</sup> d<sup>-1</sup>, SRB-MIET; B)  $k_A = 10^{-14}$  mol cell<sup>-1</sup> d<sup>-1</sup>, HS<sub>2</sub><sup>-</sup>-MIET; and C)  $k_A = 10^{-12}$  m<sup>3</sup> cell<sup>-1</sup> d<sup>-1</sup>, DIET.

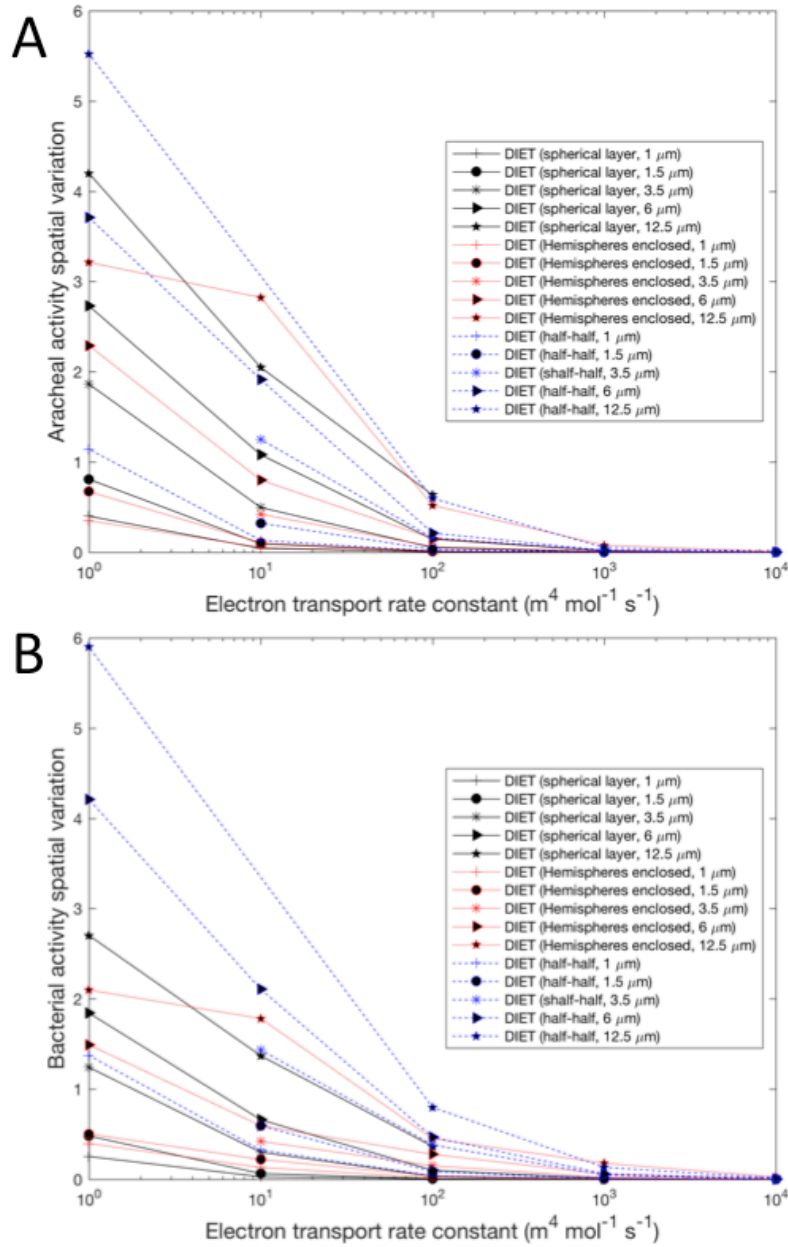


Fig. A8. Intra-aggregate variation in archaeal (A) and bacterial (B) activity vs. electron transport rate constant for models with DIET pathway. Simulation parameters:  $k_A$  and  $k_B = 10^{-12} \text{ m}^3 \text{ cell}^{-1} \text{ d}^{-1}$ .

<sup>1</sup>. Spatial activity variation is calculated as  $\left(\frac{\int (R - \bar{R})^2 dV}{V}\right)^{1/2} / \bar{R}$ , where  $R$  and  $V$  denote the rates and volumes, of the archaeal and bacterial regions, respectively, and  $\bar{R}$  is the volume averaged reaction rate.

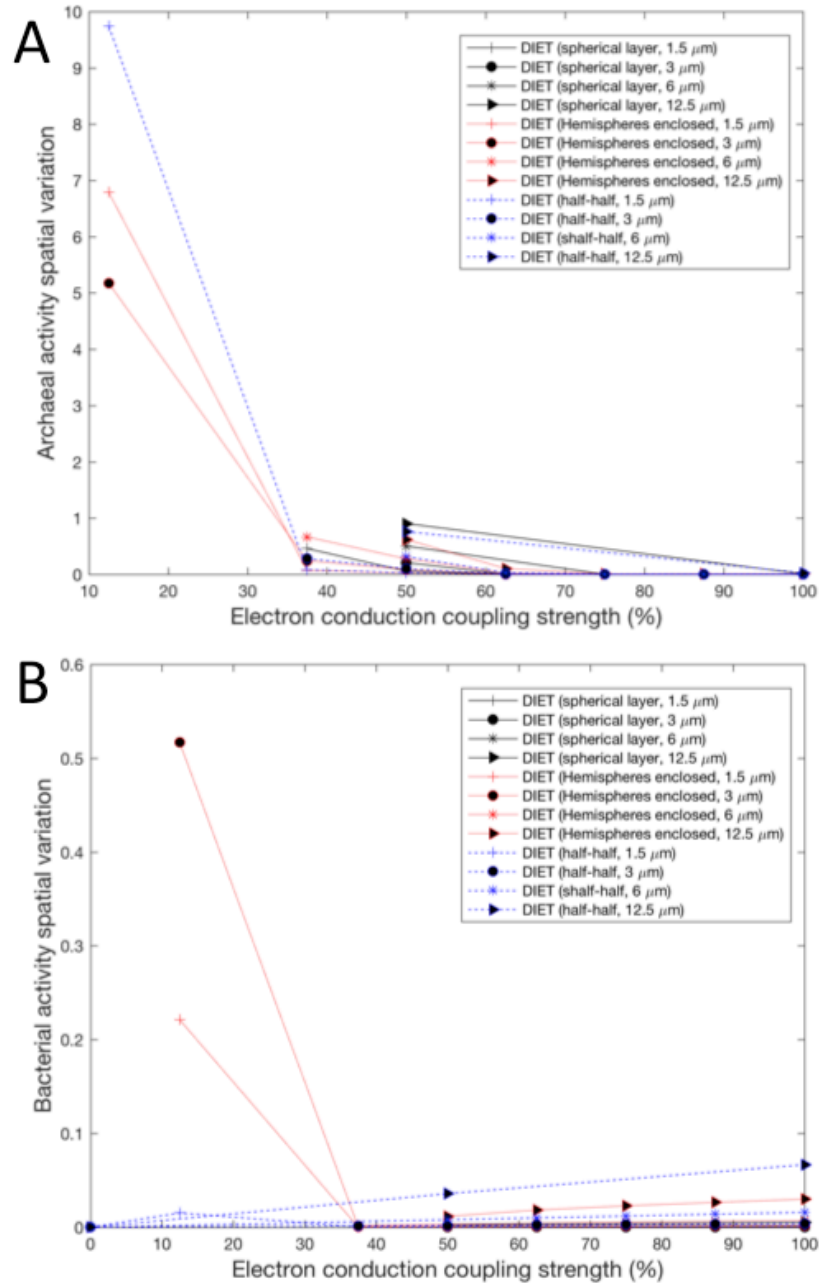


Fig. A9. Intra-aggregate variation in archaeal (A) and bacterial (B) activity vs. electron conduction coupling strength (%), defined as  $f_M/8 \times 100$ , Reaction 6) for models with DIET pathway. Simulation parameters:  $k_A$  and  $k_B = 10^{-12} \text{ m}^3 \text{ cell}^{-1} \text{ d}^{-1}$ . Spatial activity variation is calculated as

$$\left( \frac{\int (R - \bar{R})^2 dV}{V} \right)^{1/2} / \bar{R},$$

where  $R$  and  $V$  denote the rates and volumes of the archaeal and bacterial

regions, respectively, and  $\bar{R}$  is the volume averaged reaction rate.

## References

Burgess, I., Seivewright, B., and Lennox, R. B. (2006) Electric field driven protonation/deprotonation of self-assembled monolayers of acid-terminated thiols. *Langmuir*, **22(9)**: 4420–4428.

Chester, R., and Jickells, T. (2012) Chapter 7. Descriptive Oceanography: water column parameters. In *Marine Geochemistry* (3<sup>rd</sup> ed). Wiley-Blackwell, pp. 125-153.

DOE (1994) Handbook of methods for the analysis of the various parameters of the carbon dioxide system in sea water. Version 2, A. G. Dickson & C. Goyet, eds. ORNL/CDIAC-74.

Kaplan, H., Stevenson, K.J., and Hartley, B.S. (1971) Competitive labelling, a method for determining the reactivity of individual groups in proteins. The amino groups of porcine elastase. *Biochem J* **124**: 289-299.

Konhauser, K. (2006) Chapter 3. Cell surface reactivity and metal sorption. In *Introduction to geomicrobiology*. Konhauser, K. (ed): Blackwell Publishing.

Korth, B., Rosa, L.F.M., Harnisch, F., and Picioreanu, C. (2015) A framework for modeling electroactive microbial biofilms performing direct electron transfer. *Bioelectrochemistry* **106**: 194–206.

Nauhaus, K., Albrecht, M., Elvert, M., Boetius, A., and Widdel, F. (2007) In vitro cell growth of marine archaeal-bacterial consortia during anaerobic oxidation of methane with sulfate. *Environ Microbiol* **9**: 187-196.

Nauhaus, K., Boetius, A., Krüger, M., and Widdel, F. (2002) In vitro demonstration of anaerobic oxidation of methane coupled to sulphate reduction in sediment from a marine gas hydrate area. *Environ Microbiol* **4**: 296–305.

Nauhaus, K., Treude, T., Boetius, A., and Krüger, M. (2005) Environmental regulation of the anaerobic oxidation of methane: a comparison of ANME-I and ANME-II communities. *Environ Microbiol* **7**: 98-106.

Phoenix, V.R., Martinez, R.E., Konhauser, K.O., and Ferris, F.G. (2002) Characterization and implications of the cell surface reactivity of *Calothrix sp.* strain KC97. *Appl Environ Microbiol* **68**: 4827-4834.

Zeebe, R.E., and Wolf-Gladrow, D. (eds) (2005) CO<sub>2</sub> in seawater: equilibrium, kinetics, isotopes. Elsevier, Amsterdam, the Netherlands.

APPENDIX B

CHAPTER 3 SUPPLEMENTARY MATERIAL

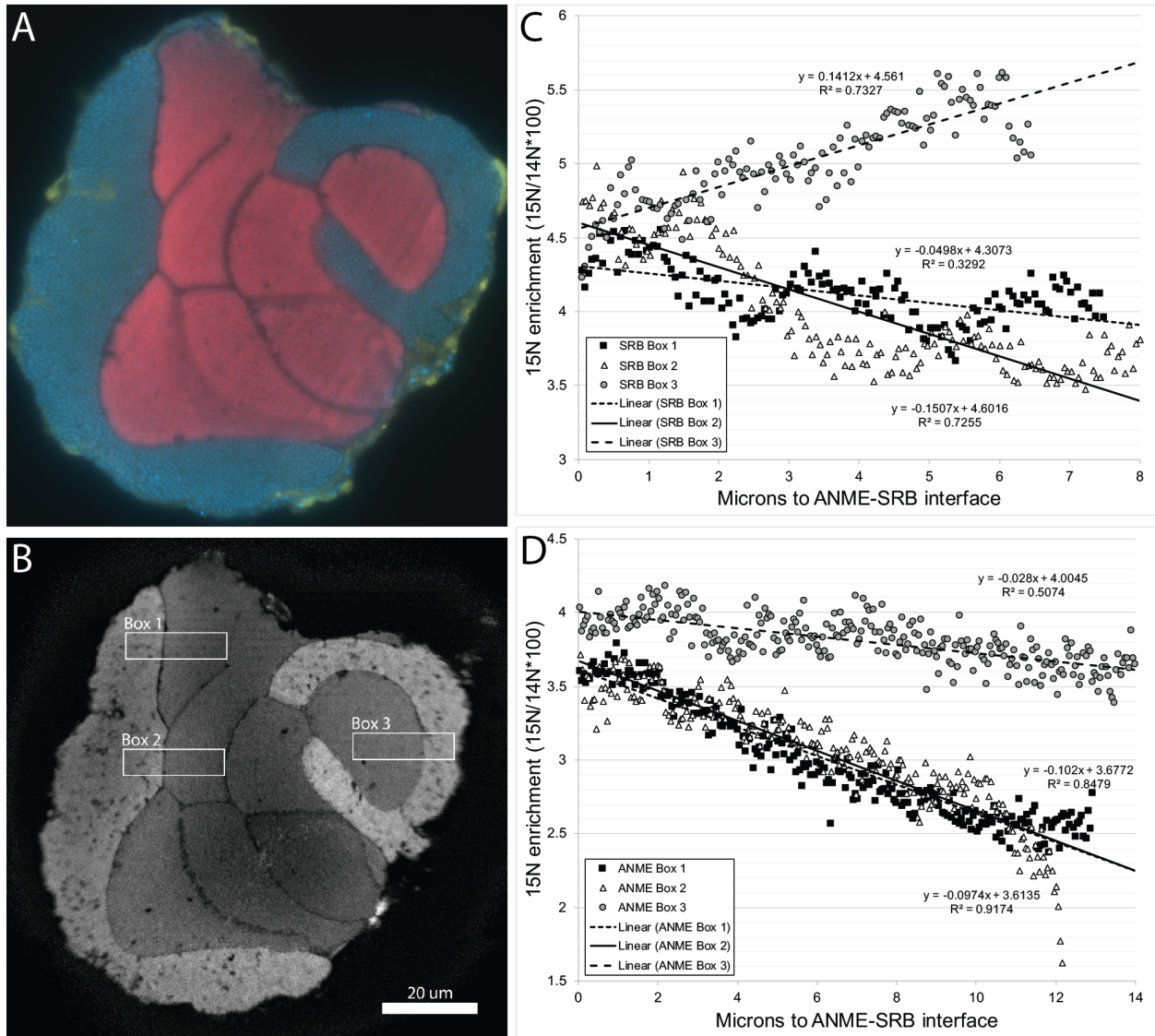


Fig. B1. Previous observations of significant correlations between the activity of cells and their distances to their syntrophic partners. This exceptionally large ANME-SRB aggregate was observed in the  $^{15}\text{N}$  ammonium incubation of a previous study (see Scheller et al 2016 for details).

A) Fluorescent microscopy image showing overview of aggregate structure. B)  $^{15}\text{N}$  fractional

abundance image. Boxes represent selected areas where  $^{15}\text{N}$  incorporation data was quantified (average value of each pixel column in the box). C-D) Average values for SRB and ANME  $^{15}\text{N}$  incorporation values at one pixel increments away from the ANME-SRB interface (each pixel corresponds to 50nm). The magnitude of these correlations varies based on the location in the aggregate, likely due to our uncertainty about the true distances to the ANME-SRB interface in this aggregate's complex three-dimensional structure.

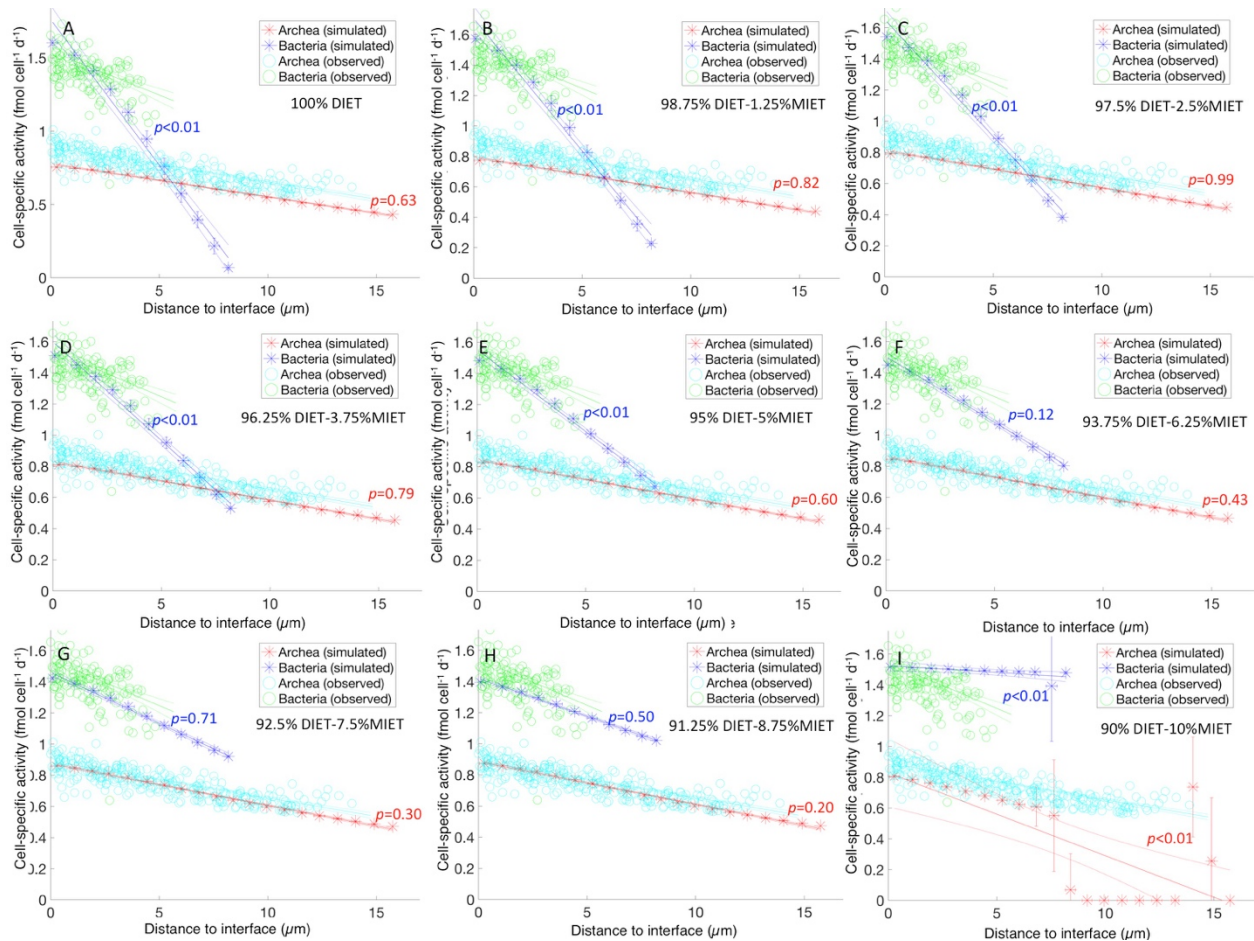


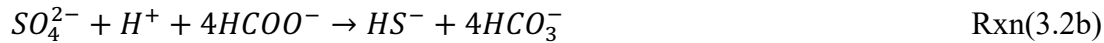
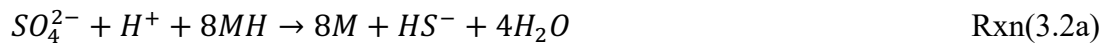
Fig. B2. Cell-specific activity with varying DIET to MIET ratio for an aggregate radius of 20 μm (base model parameter). (A) 100% DIET, (B) 98.75% DIET, (C) 97.5% DIET, (D) 96.25% DIET, (E) 95% DIET, (F) 93.75% DIET, (G) 92.5% DIET, (H) 91.25% DIET, (I) 90% DIET. ANCOVA:

$p$  values for the statistical significance of the difference between the slopes and intercepts of the two regressions, with *blue* and *red* for Archaea and Bacteria respectively.

## B2. Partial decoupling of archaeal methanotrophy and bacterial sulfate-reduction

A hybrid DIET-MIET mechanism would require additional metabolic capabilities, and hence carries a cost, but it also provides an opportunity for support externally supported bacterial metabolism decoupled from archaeal activity. It is noteworthy to mention that the addition of MIET mechanism that allows for the uptake of an external electron donor largely relieves the energetic constraint in DIET for bacteria (Fig. 3.6 and Fig. B4). Recently, several studies have shown that the HotSeep-1 cluster (*Desulfosarcina/Desulfococcus*) can grow solely on external source (H<sub>2</sub>) without ANME partner (Wegener et al. 2015; Krukenberg et al. 2016).

To investigate the relative contribution of decoupled bacterial metabolisms we separate Rxn(2) in our model into



where Rxn(3.2a) and Rxn(3.2b) represent the decoupled DIET and MIET mechanism for bacteria, respectively. Reaction rates for Rxn(3.2a) and Rxn(3.2b) are described by

$$R^{Rxn(2a)} = k_{B,DIET} B_B \frac{SO_4}{K_m^{SO_4} + SO_4} MH \cdot F_T^{Rxn(2a)} \quad \text{Eq (3.11)}$$

$$R^{Rxn(2b)} = k_{B,MIET} B_B \frac{SO_4}{K_m^{SO_4} + SO_4} HCOO^- \cdot F_T^{Rxn(2b)} \quad \text{Eq (3.12)}$$

where  $k_{B,MIET}$  and  $k_{B,DIET}$  represent the bacterial cell specific constant, respectively.  $F_T^{Rxn(2a)}$  and  $F_T^{Rxn(2b)}$  represent the thermodynamic constraint for bacteria under each reaction condition.

Without changing  $k_{B,MIET}$  and  $k_{B,DIET}$  from the default value given by  $k_B$ , model simulations (Fig. B3 and Fig. B4A) show that bacteria suffer from energetic constraints as discussed earlier (Fig. 3.6). It is noted that the fraction of the formate reaching the bacteria that originates from the environment drastically changed from 100% at pure DIET (i.e. no formate is generated within the

aggregate, and any formate used by the bacteria is obtained from the environment) to a flux from the aggregate to the environment with decreasing archaeal DIET/MIET ratio (Fig. B4C), due to the increased production but relatively constant consumption of formate (Fig. B4B).

Considering that cell-specific rate constants may differ for different electron donors, a 100-fold increase of  $k_{B,MIET}$  could eventually lead to rates of Rxn(3.2b) on the same magnitude as those of Rxn(3.2a), with higher activity at the outer aggregate surface (Fig. B5) where the formate supply to bacteria was 100% from environment. Corresponding fluxes and formate levels are shown in Fig. B6. With formate supply from environment alone (simulated by deactivating the ANME and Rxn(1) and hence any DIET-driven bacterial activity), bacteria could potentially be very active near the aggregate surface (first 2  $\mu\text{m}$ ), but completely inactive farther away (Fig. B7A). Responses to different formate level in the environment are shown in Fig. B8, with the effect of aggregate size illustrated in Figs. B9 and B10. Figs. B11-B15 show the patterns of factors that potentially control cell activity.

Cell activity increases as cell-specific rate constant  $k_A$  and  $k_B$  increases, as reflected in Eqs. 3.1-3.3. As shown in Fig. B16E, cell activity is relatively homogenous at smaller  $k_A$  and  $k_B$ , and changes more drastically at higher  $k_A$  and  $k_B$ . The change of  $k_A$  and  $k_B$  has a dominant impact on activation loss (Fig. 3.5A), which subsequently led to a sharper decrease of metabolic activity at the distance close to the archaea-bacteria interface (Fig. 3.4). Lastly, activation loss constant  $k_{act}$  exhibits a significant impact on the metabolic activity at the distance close to the archaea-bacteria interface as well. With increasing  $k_{act}$ , cell activity is more homogenous at the distance closer to archaea-bacteria interface due to a smaller activation loss (Fig. 3.5A).

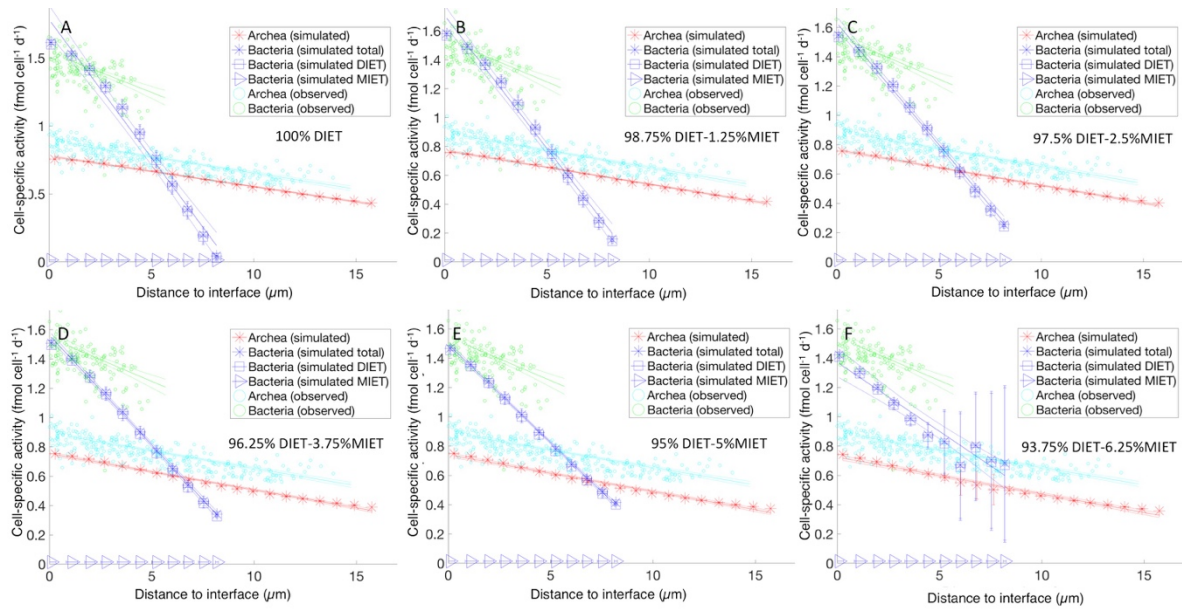


Fig. B3. Decoupled bacterial metabolism that utilizes DIET and MIET independently. (A) to (F) show cell-specific activity with varying archaeal DIET to MIET ratio for an aggregate with a 20  $\mu\text{m}$  radius (base model parameter). (A) 100% DIET, (B) 98.75% DIET, (C) 97.5% DIET, (D) 96.25% DIET, (E) 95% DIET, (F) 93.75% DIET.

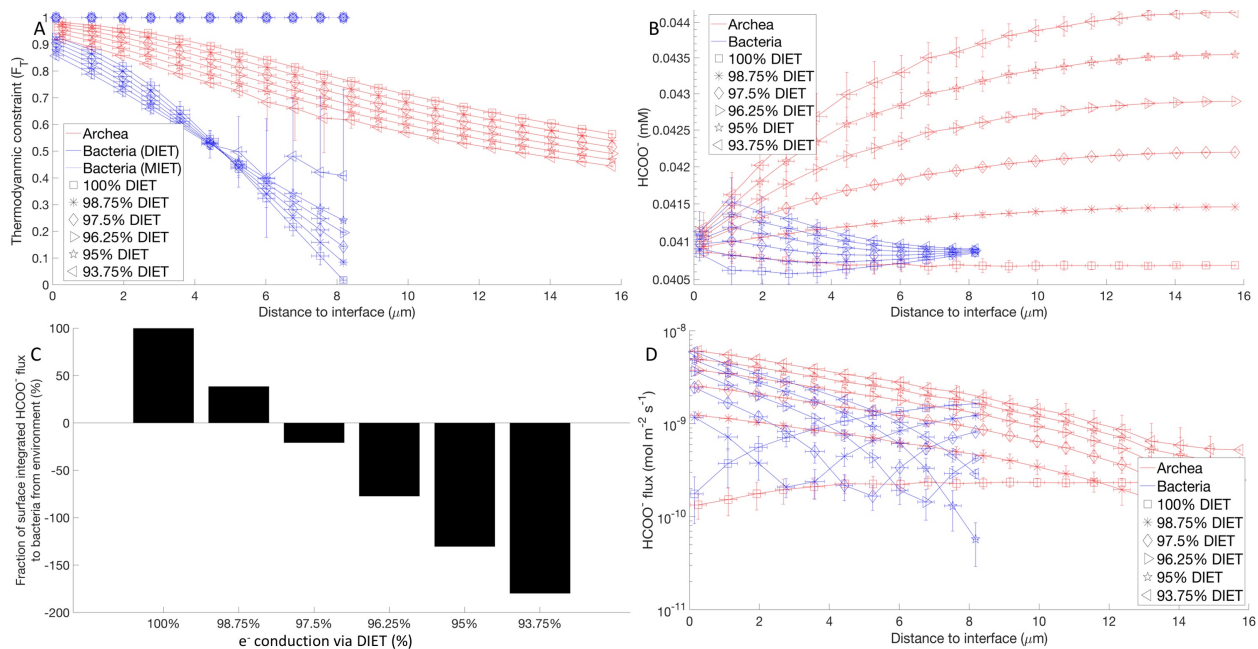


Fig. B4. Decoupled bacterial metabolism that utilizes DIET and MIET independently, with varying archaeal DIET to MIET ratio for an aggregate with a 20  $\mu\text{m}$  radius (baseline parameters). (A) thermodynamic constraint, (B)  $\text{HCOO}^{-}$  concentration field, (C) fraction of the total  $\text{HCOO}^{-}$  flux metabolized by the bacteria obtained from the external environment and (D)  $\text{HCOO}^{-}$  flux at various environmental  $\text{HCOO}^{-}$  concentrations.

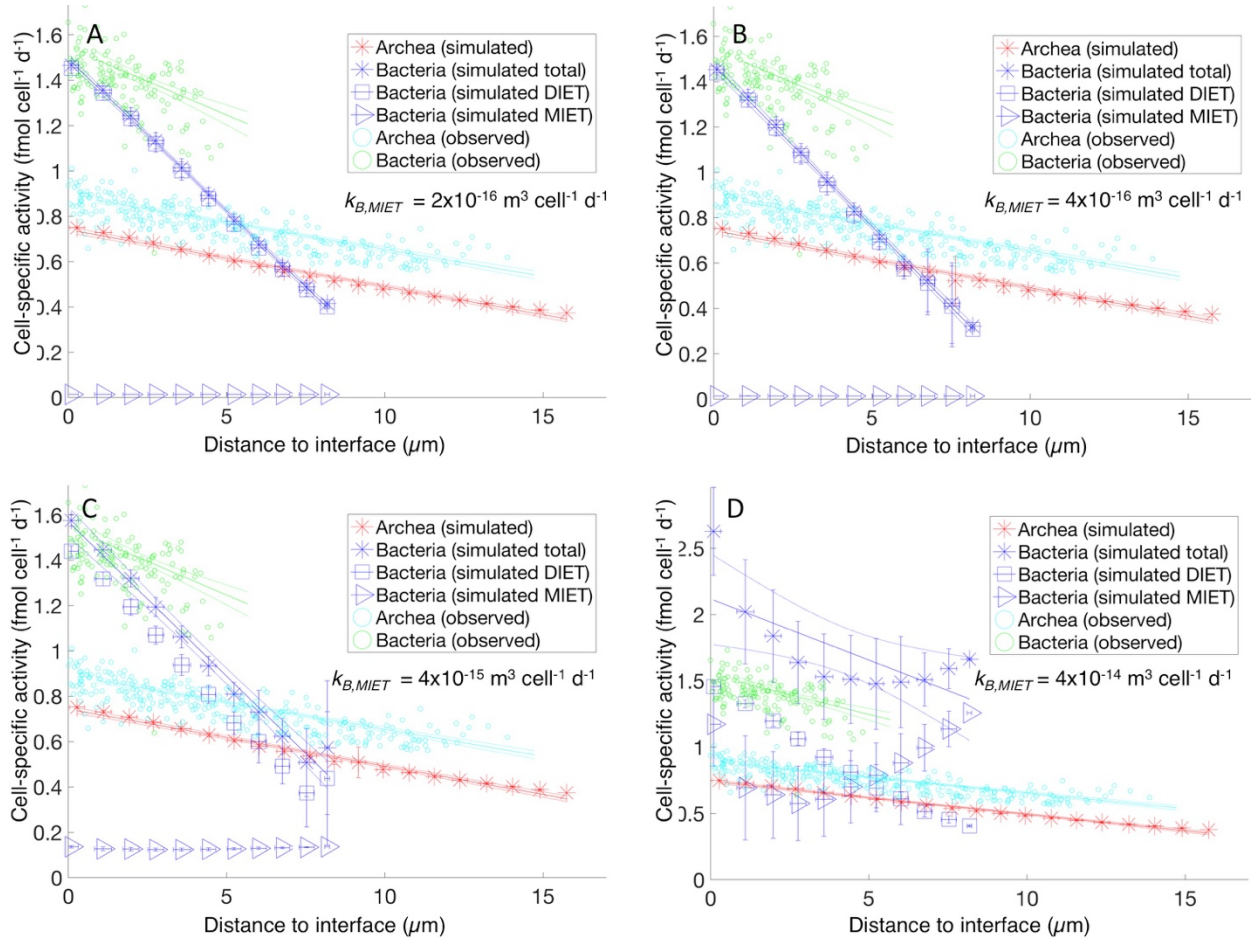


Fig. B5. Decoupled bacterial metabolism that utilizes DIET and MIET independently. (A) to (D) show cell-specific activity with varying bacterial rate constant associated with MIET ( $k_{B,MIET}$ ). (A)  $k_{B,MIET} = 2 \times 10^{-16} \text{ m}^3 \text{ cell}^{-1} \text{ d}^{-1}$ , (B)  $k_{B,MIET} = 4 \times 10^{-16} \text{ m}^3 \text{ cell}^{-1} \text{ d}^{-1}$ , (C)  $k_{B,MIET} = 4 \times 10^{-15} \text{ m}^3 \text{ cell}^{-1} \text{ d}^{-1}$ , (D)  $k_{B,MIET} = 4 \times 10^{-14} \text{ m}^3 \text{ cell}^{-1} \text{ d}^{-1}$ . These are simulations for an aggregate with a  $20 \text{ } \mu\text{m}$  radius with 92.5% DIET and baseline parameters.

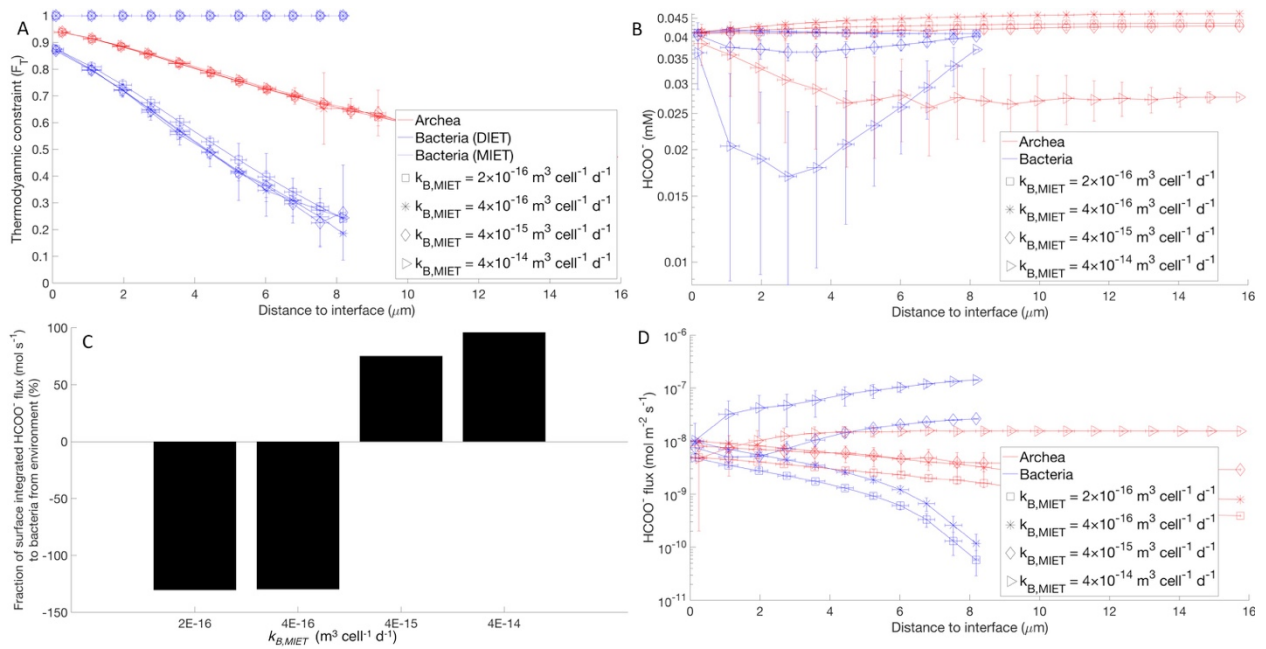


Fig. B6. Decoupled bacterial metabolism that utilizes DIET and MIET independently, with varying bacterial rate constant associated with MIET ( $k_{B,MIET}$ ) for an aggregate with a 20  $\mu\text{m}$  radius (baseline parameters). (A) thermodynamic constraint, (B) HCOO<sup>-</sup> concentration field, (C) fraction of the total HCOO<sup>-</sup> flux metabolized by the bacteria obtained from the external environment and (D) HCOO<sup>-</sup> flux at various environmental HCOO<sup>-</sup> concentrations.

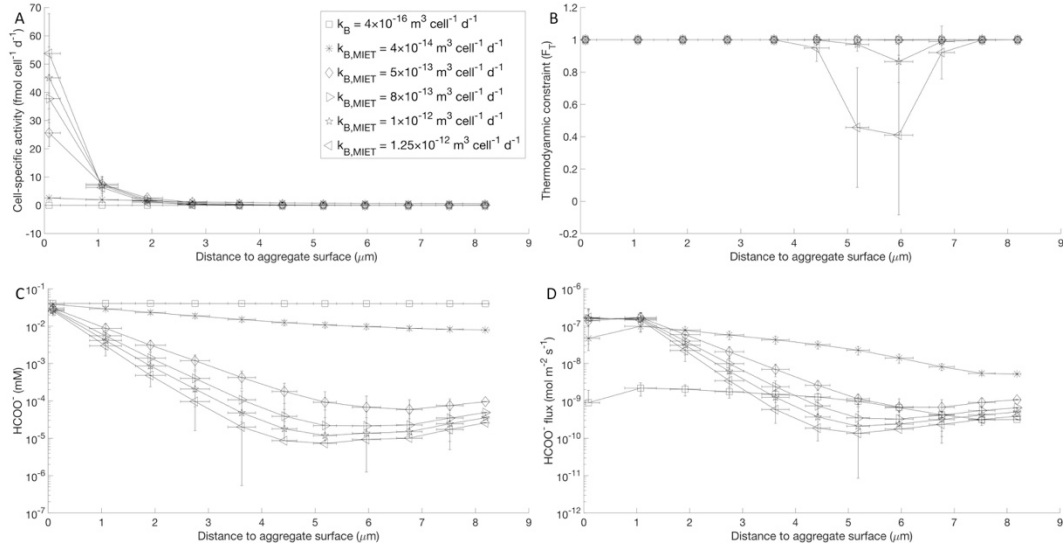


Fig. B7. Decoupled bacterial metabolism that utilizes MIET only, with inactive archaeal metabolism for an aggregate with a 20  $\mu\text{m}$  radius (baseline parameters). (A) bacterial cell-specific activity, (B) thermodynamic constraints, (C)  $\text{HCOO}^-$  concentration field and (D)  $\text{HCOO}^-$  flux at various cell-specific rate constants ( $k_B$ ).

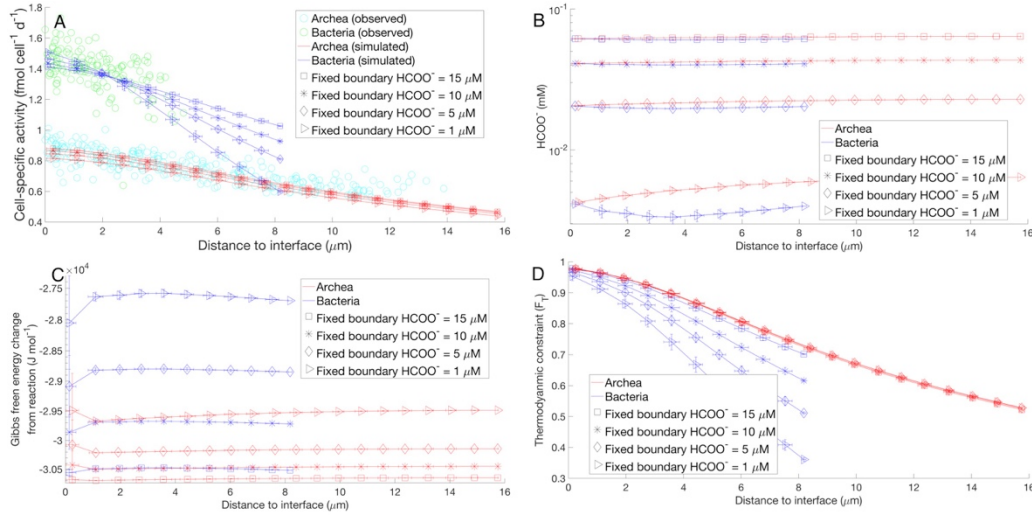


Fig. B8. (A) Impact of intermediate species on archaeal and bacterial activities; (B)  $\text{HCOO}^-$  concentration at various environmental  $\text{HCOO}^-$  concentrations; (C) Gibbs free energy of bacterial reaction and (D) thermodynamic constraint at various environmental  $\text{HCOO}^-$  concentrations. These are simulations for an aggregate with a  $20 \mu\text{m}$  radius with baseline parameters.

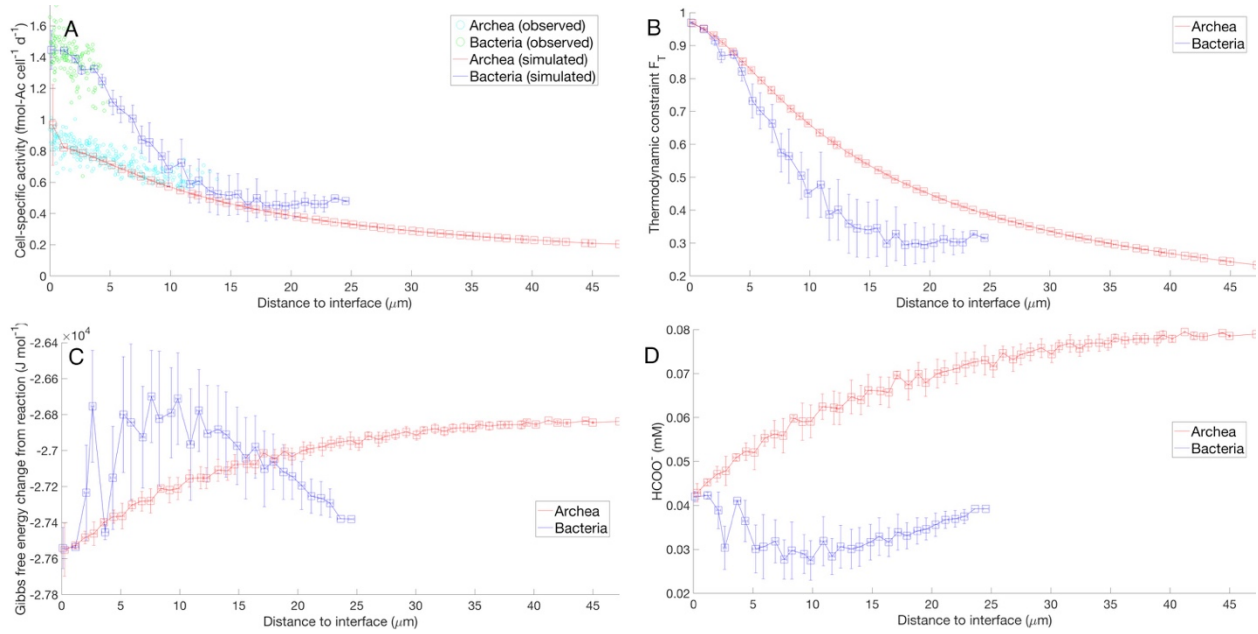


Fig. B9. Simulation with aggregate size at 60 μm radius, showing the transport of formate can limit bacterial activity (A), as reflected by the thermodynamic factor (B), Gibbs free energy change of reaction (C), and concentration of HCOO<sup>-</sup> (D). These are simulation results with 92.5% DIET and base model parameters.

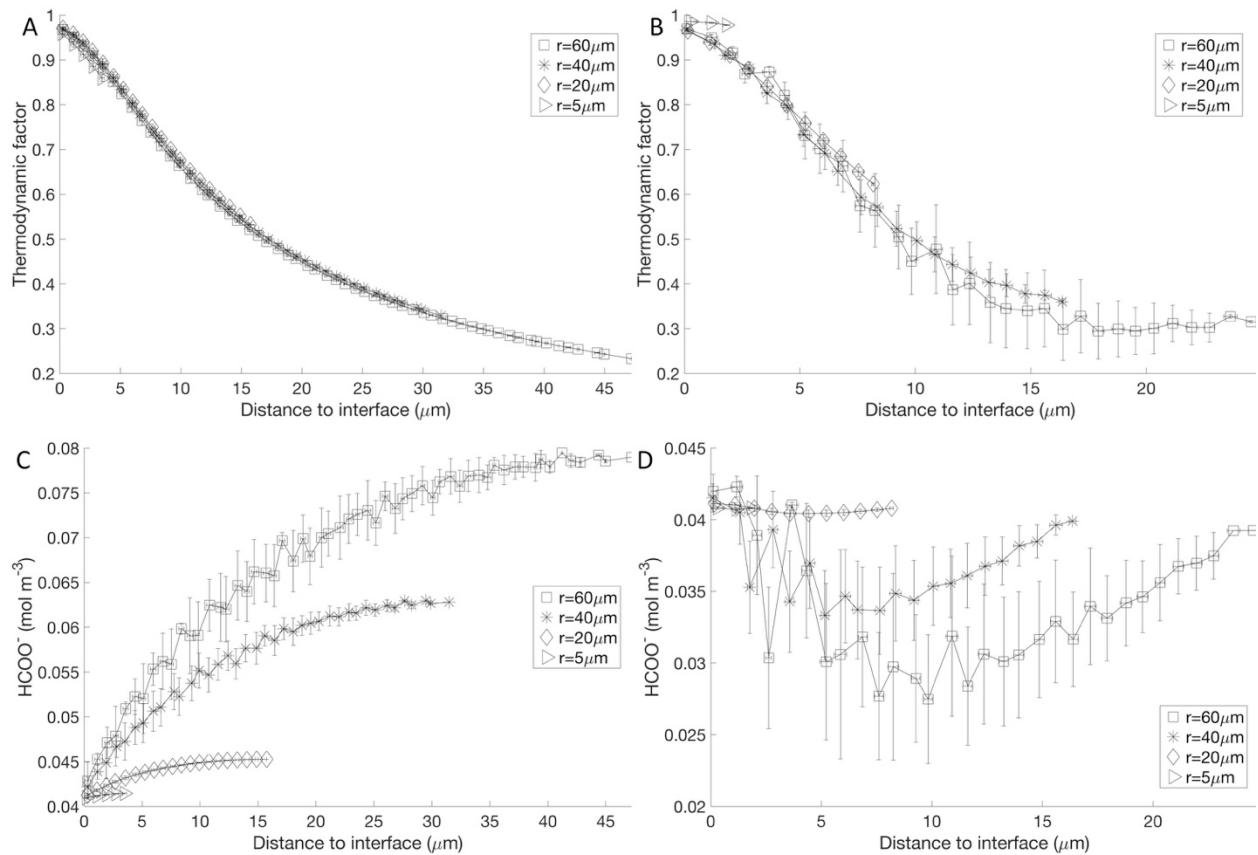


Fig. B10. After a specific aggregate size is reached ( $\sim 60\ \mu\text{m}$ ), the diffusion of formate started to limit bacterial activity, as reflected by the thermodynamic factor (A), concentration of  $\text{HCOO}^-$  in archaea (B) and bacteria (C).

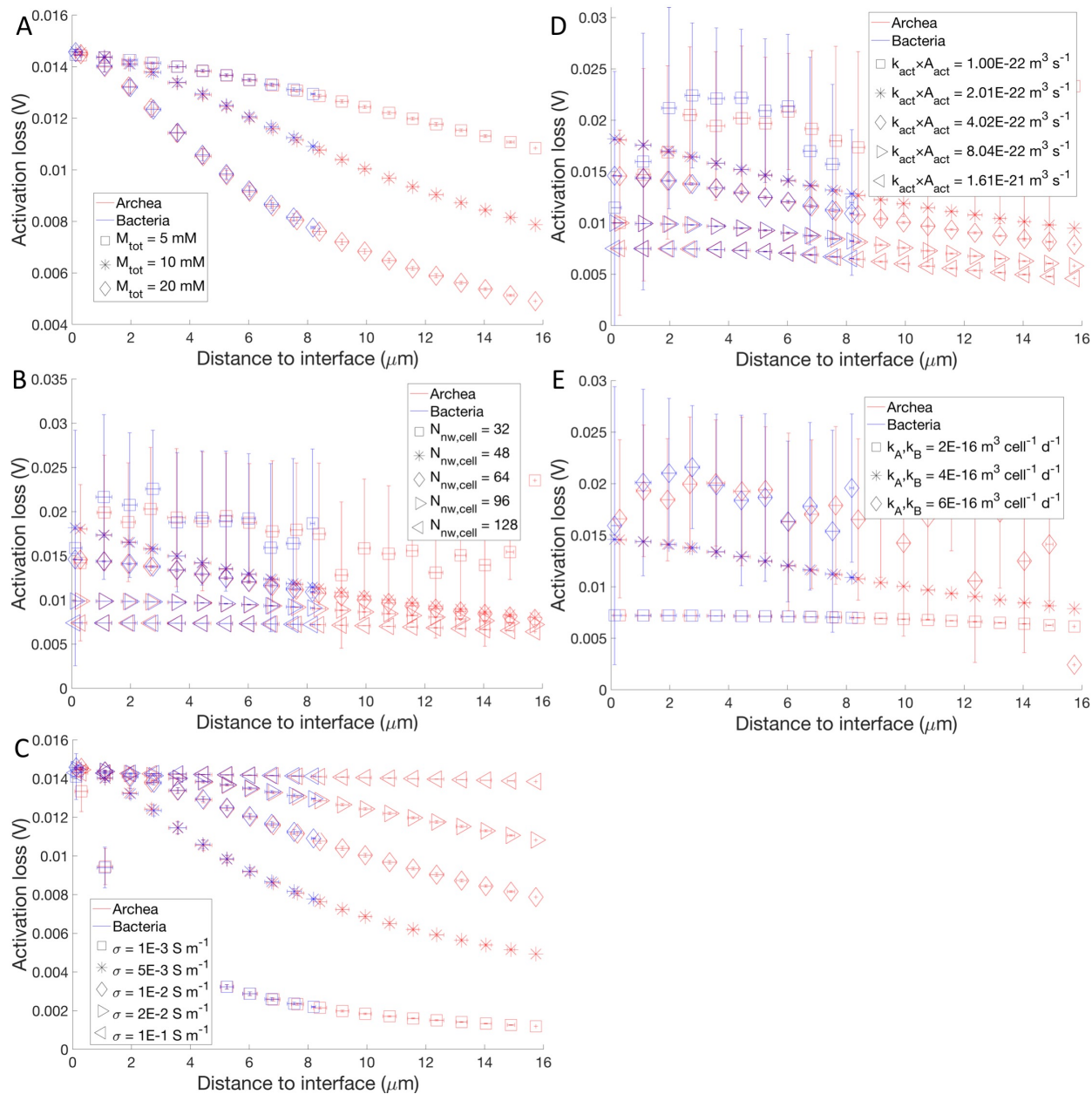


Fig. B11. Activation loss profile for archaea and bacteria with various parameter values. (A) concentration of redox active molecules ( $M_{tot}$ ), (B) conductive network density ( $N_{nw,cell}$ ), (C) their conductivity ( $\sigma$ ), (D) cell redox active factor ( $k_{act} \times A_{act}$ ) and (E) associated cell-specific constants ( $k_A, k_B$ ). These are simulations at aggregate radius of  $20 \mu\text{m}$  with baseline parameters unless otherwise noted.

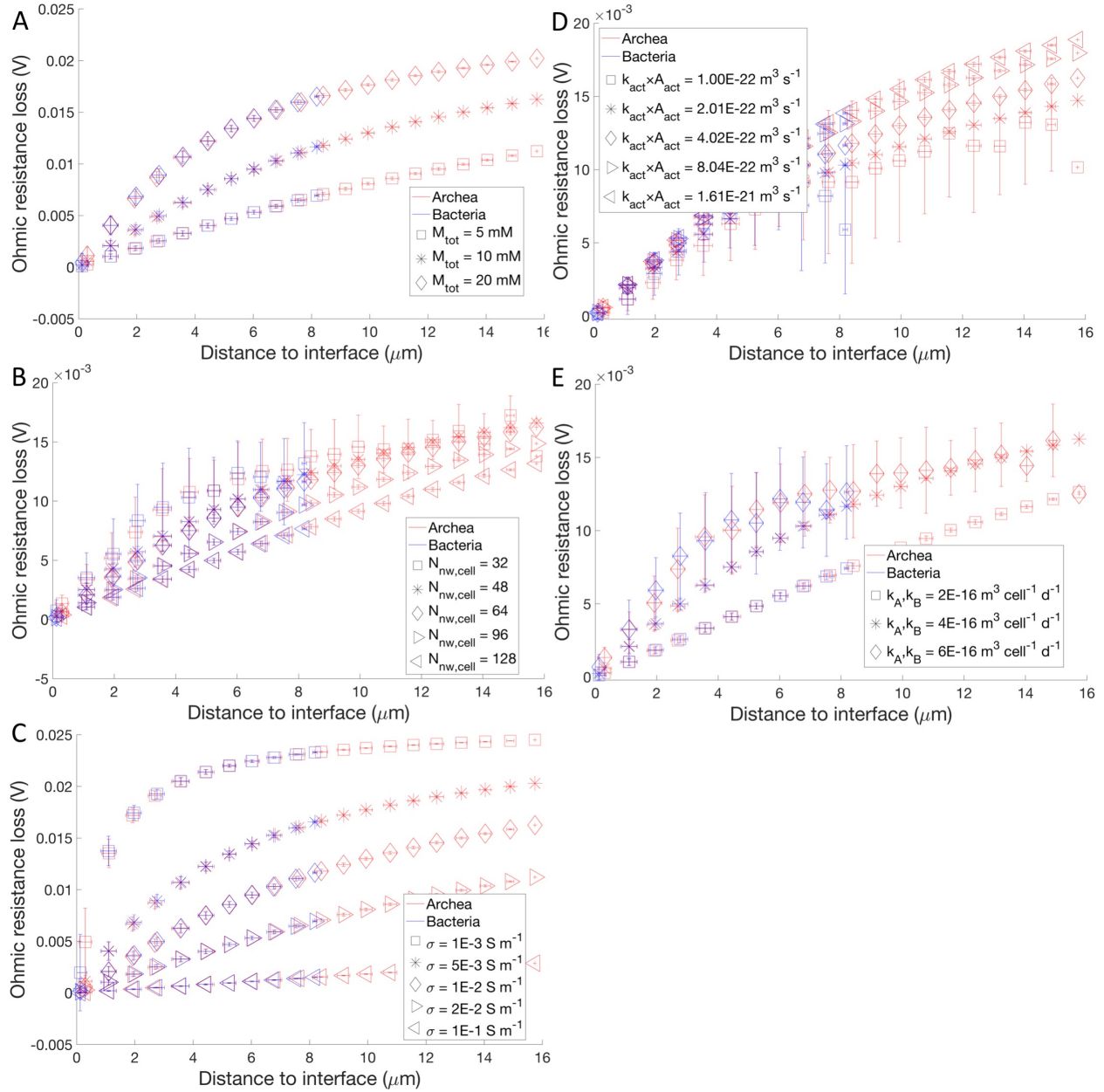


Fig. B12. Ohmic resistance loss profile for archaea and bacteria with various parameter values. (A) concentration of redox active molecules ( $M_{tot}$ ), (B) conductive network density ( $N_{nw,cell}$ ), (C) their conductivity ( $\sigma$ ), (D) cell redox active factor ( $k_{act} \times A_{act}$ ) and (E) associated cell-specific constants ( $k_A, k_B$ ). These are simulations at aggregate radius of 20  $\mu\text{m}$  with baseline parameters unless otherwise noted.

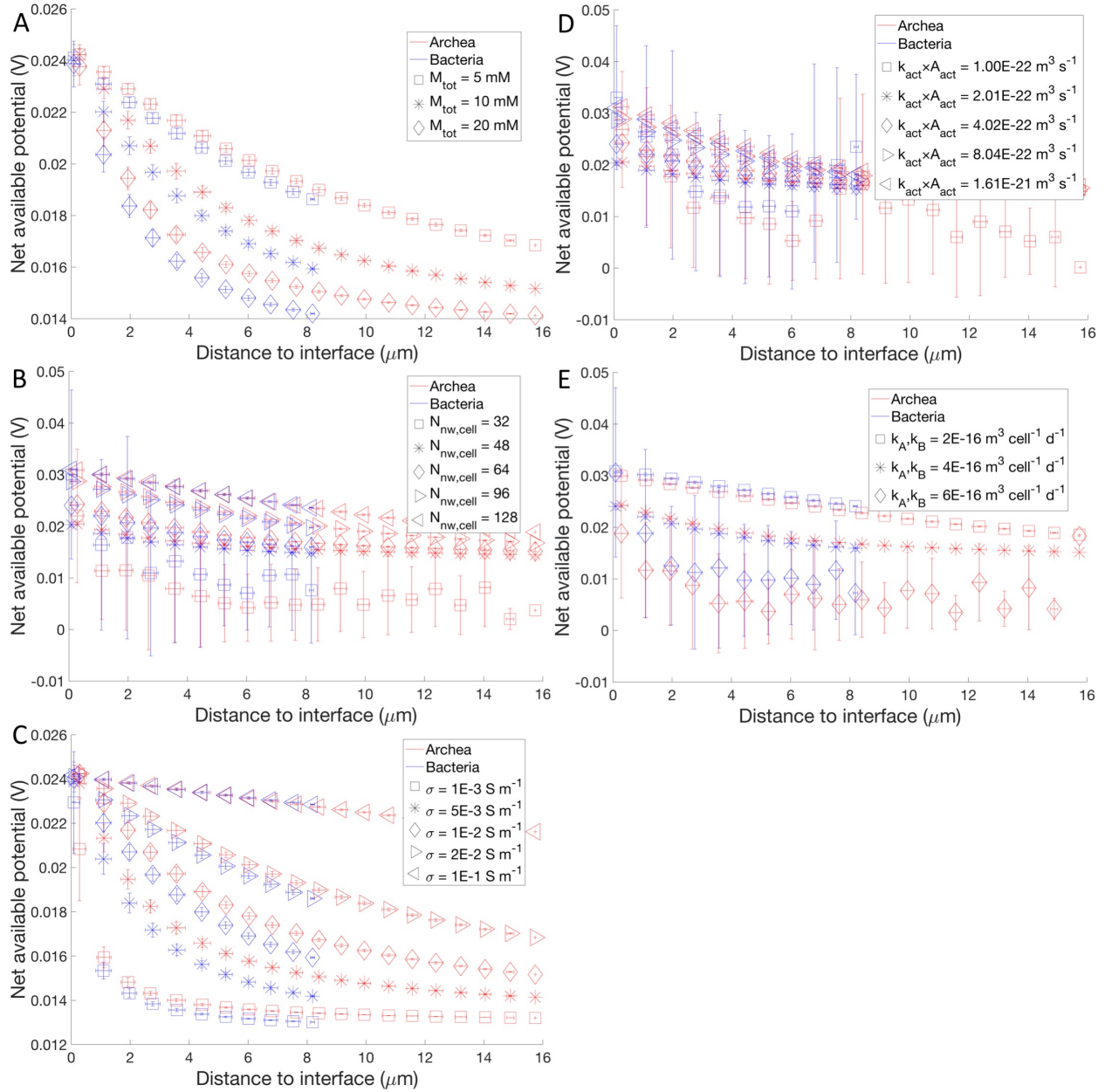


Fig. B13. Net available potential profile for archaea and bacteria with various parameter values. (A) concentration of redox active molecules ( $M_{tot}$ ), (B) conductive network density ( $N_{nw,cell}$ ), (C) their conductivity ( $\sigma$ ), (D) cell redox active factor ( $k_{act} \times A_{act}$ ) and (E) associated cell-specific constants ( $k_A, k_B$ ). These are simulations at aggregate radius of  $20\ \mu\text{m}$  with baseline parameters unless otherwise noted.

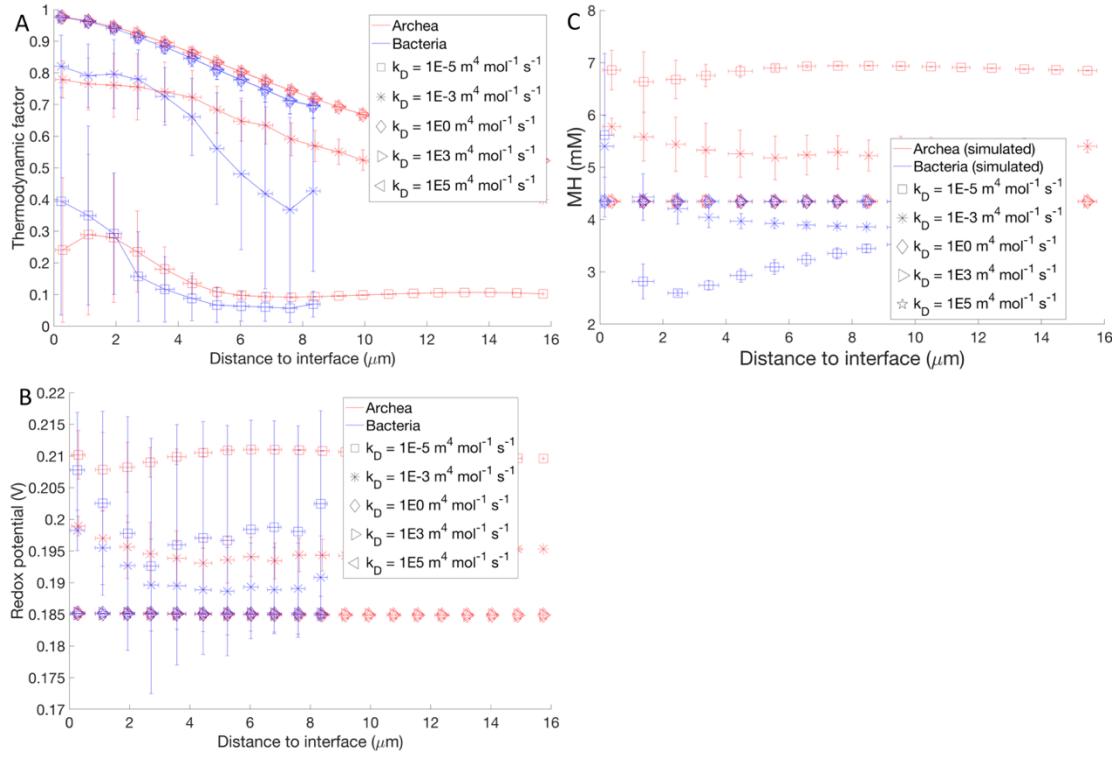


Fig. B14. Thermodynamic factor (A) and consortia redox potential (B) started to change at  $k_D < 1$   $\text{m}^4 \text{mol}^{-1} \text{s}^{-1}$ . The transport of redox molecules MH is not limited at  $k_D \geq 1$   $\text{m}^4 \text{mol}^{-1} \text{s}^{-1}$  (C). These are simulations at aggregate radius of  $20 \mu\text{m}$  with baseline parameters unless otherwise noted.

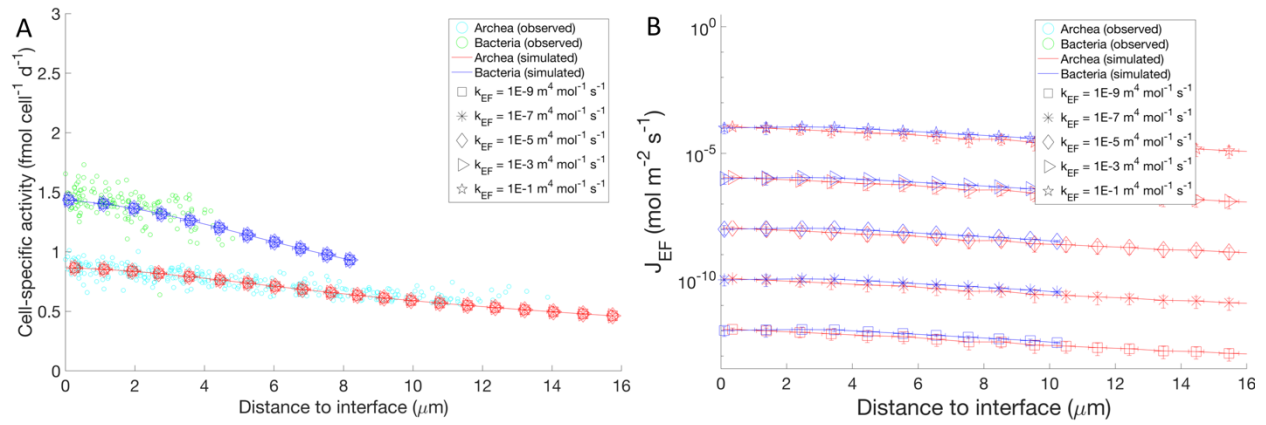


Fig. B15. Electric field does not impact cell-specific activity at fast  $k_D$  (default value of  $10^5 \text{ m}^4 \text{ mol}^{-1} \text{ s}^{-1}$ ) (A). Electric field driven flux of MH linearly changes along with electric field constant  $k_{EF}$  (B). These are simulations at aggregate radius of  $20 \text{ } \mu\text{m}$  with baseline parameters unless otherwise noted.

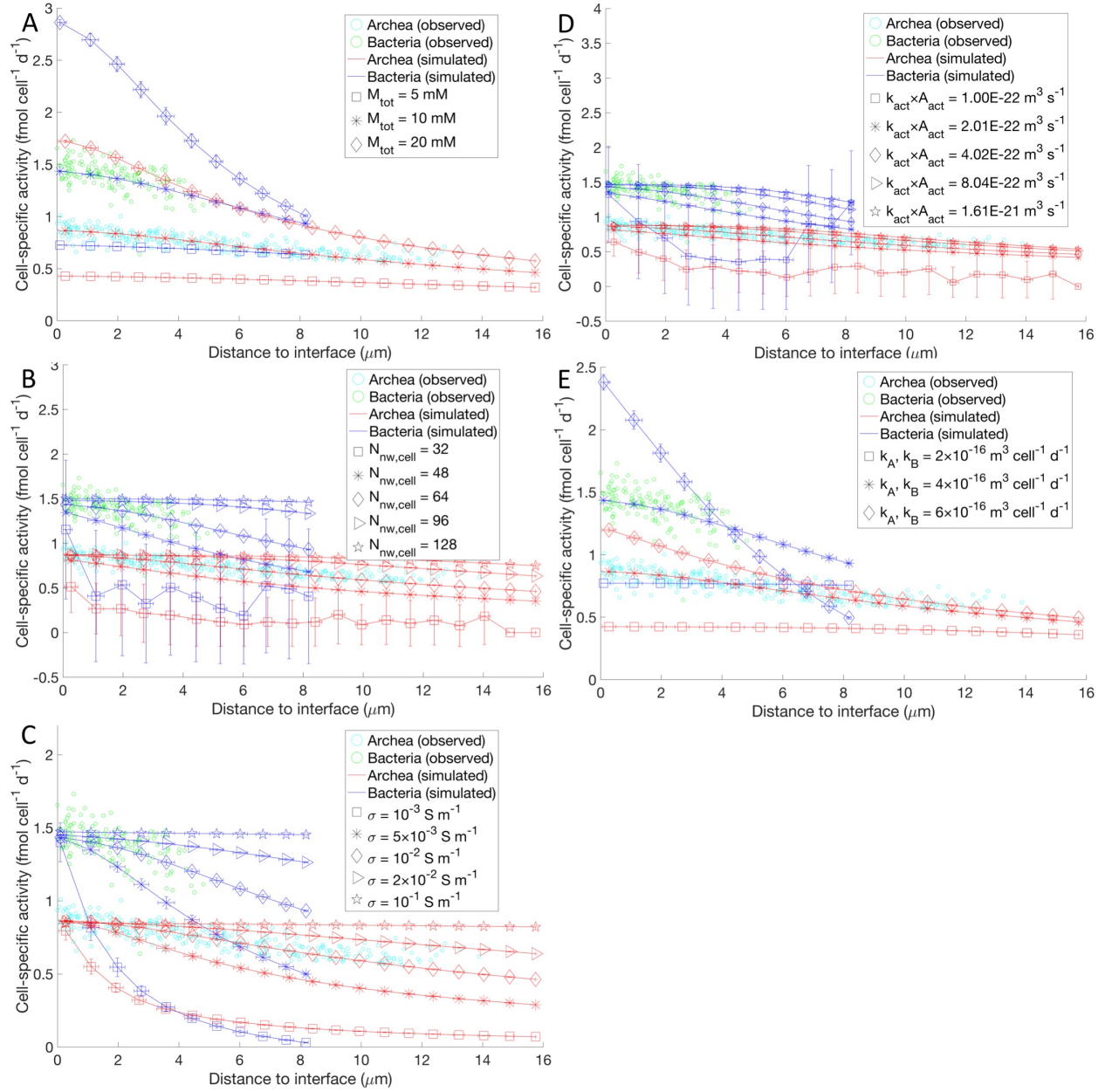


Fig. B16. Sensitivity towards key model parameters, including (A) concentration of redox active molecules ( $M_{tot}$ ), (B) conductive network density ( $N_{nw,cell}$ ), (C) their conductivity ( $\sigma$ ), (D) cell redox active factor ( $k_{act} \times A_{act}$ ) and (E) associated cell-specific constants ( $k_A, k_B$ ). These are simulations at aggregate radius of  $20 \mu\text{m}$  with baseline parameters unless otherwise noted.

## References

Krukenberg V, Harding K, Richter M, Glöckner FO, Gruber-Vodicka HR, Adam B, Berg JS, Knittel K, Tegetmeyer HE, Boetius A, Wegener G. *Candidatus Desulfofervidus auxilii*, a hydrogenotrophic sulfate-reducing bacterium involved in the thermophilic anaerobic oxidation of methane. *Environ. Microbiol.* 2016; 18:3073–3091.

Scheller S, Yu H, Chadwick GL, McGlynn SE, Orphan VJ. Artificial electron acceptors decouple archaeal methane oxidation from sulfate reduction. *Science* 2016; 351:703-707.

Wegener G, Krukenberg V, Riedel D, Tegetmeyer HE, Boetius A. Intercellular wiring enables electron transfer between methanotrophic archaea and bacteria. *Nature* 2015; 526:587–590.

## APPENDIX C

### CHAPTER 4 SUPPLEMENTARY MATERIAL

#### C1. Acetate uptake, growth yield and metabolism

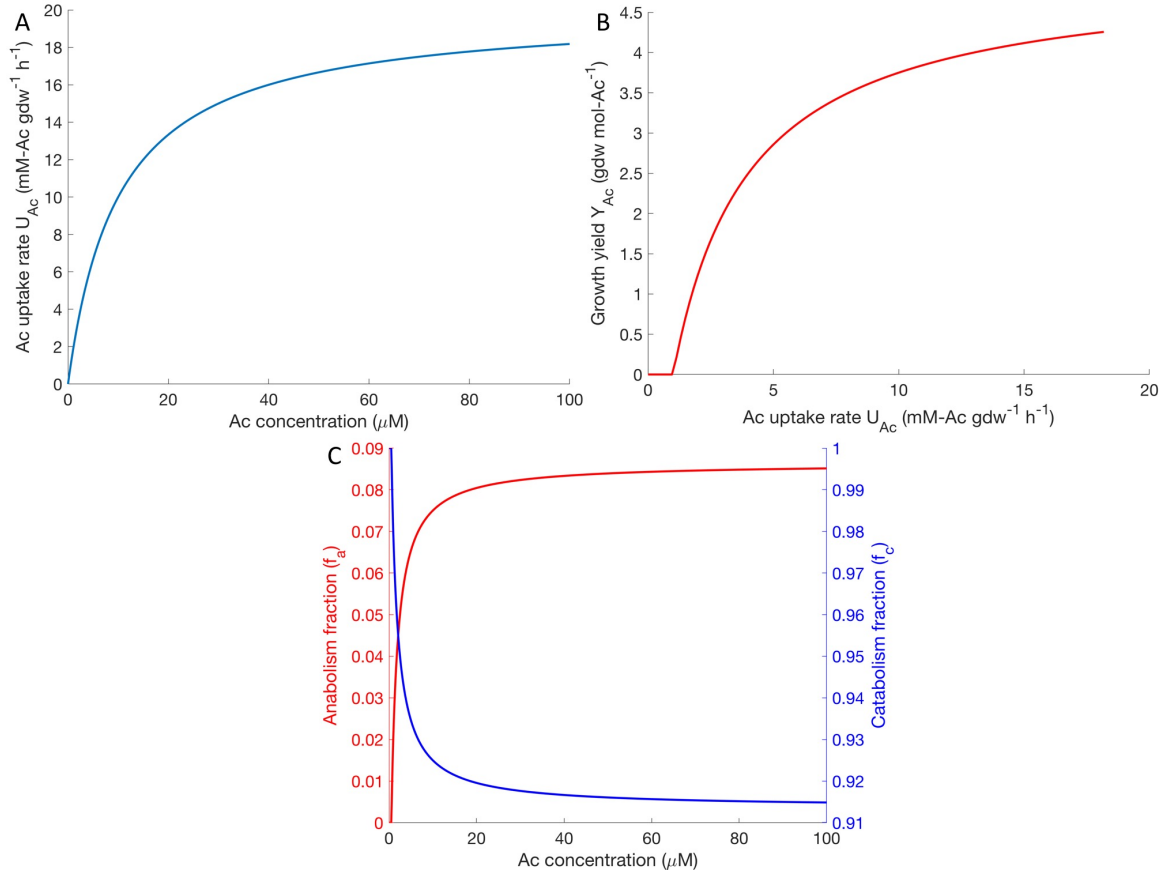


Fig. C1. Acetate (Ac) uptake (A) and growth yield (B) used in our simulations. Curves are based on fitting the relationships developed in King et al. 2009. The fraction of acetate oxidation goes to anabolism and catabolism is derived from the growth yield and acetate uptake (C).

Here we can give a simple example to show how the fraction of Ac oxidation used for anabolism  $f_a$  is calculated in Fig. C1C. First, the total biomass was converted in mole using a

molecular formula of  $\text{CH}_{1.8}\text{O}_{0.5}\text{N}_{0.2}$  (24.6 g/mol). Assuming 4 gdw ( $Y_{Ac}$ ) biomass synthesis per mol Ac oxidized, resulting in 0.163 mol  $\text{CH}_{1.8}\text{O}_{0.5}\text{N}_{0.2}$ . Therefore  $\sim 0.08$  mol carbon goes to biomass ( $\text{CH}_{1.8}\text{O}_{0.5}\text{N}_{0.2}$ ) per mol C assimilated, which gives anabolism fraction  $f_a \sim 8\%$ . This is close to the value reported for acetate-oxidizing *Geobacter sulfurreducens* growth with Fe(III)-citrate, in which 93.6% acetate transported into the cell was utilized for oxidation and ATP generation via the TCA (Mahadevan et al., 2006).

## C2. Shift of redox-active center mid-potential and Impact of critical shift potentials on metabolic activity and pH

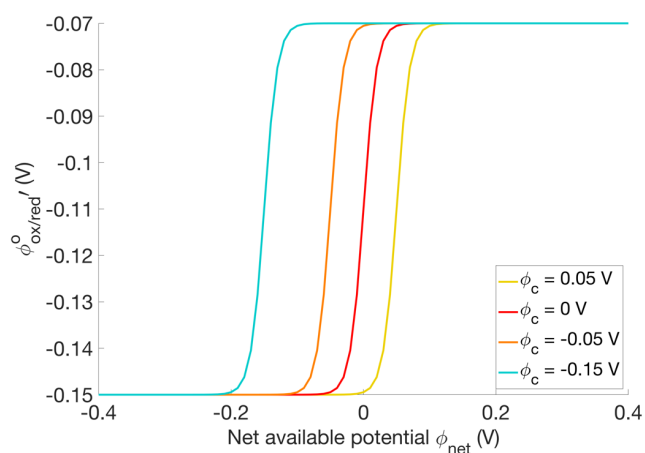


Fig. C2. Impact of critical shifting potential ( $\phi_c$ ) on mid-potential of redox-active center.

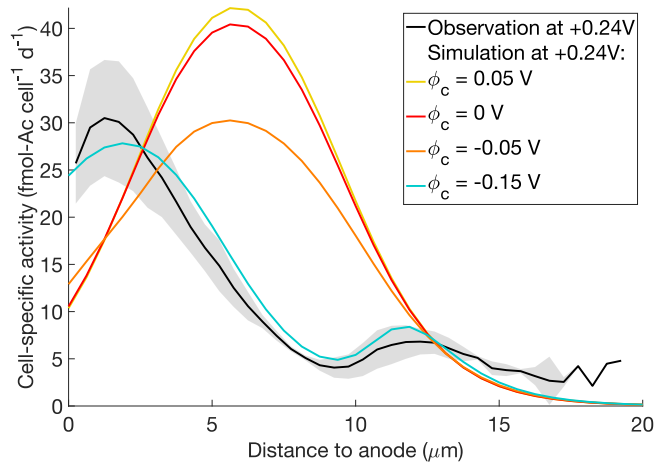


Fig. C3. The impact of critical shifting potential ( $\phi_c$ ) on metabolic activity patterns in simulated *G. sulfurreducens* biofilms. The shaded area represents the 95% confidence interval for the observations.

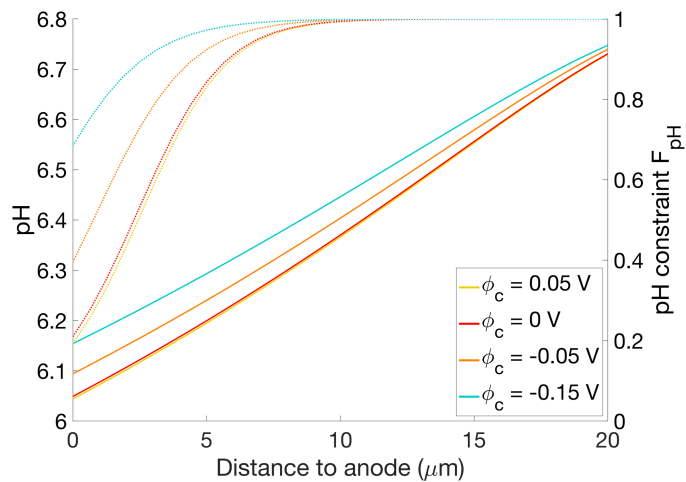


Fig. C4. The change of pH and pH constraint ( $F_{pH}$ ) for different critical shift potentials.

### C3. External constraints on acetate oxidation rate

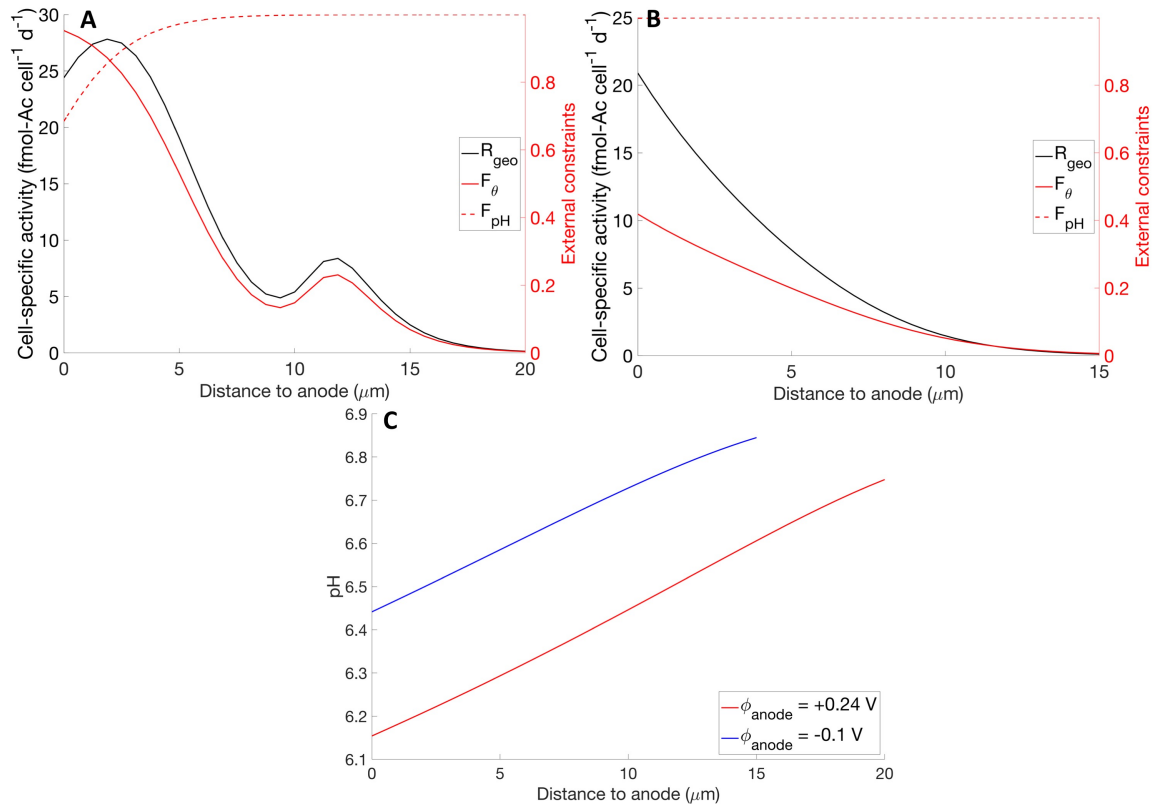


Fig. C5. External constraints on acetate oxidation rate ( $R_{geo}$ ) at high anode potential (A) and low anode potential (B): external potential constraint ( $F_{\theta}$ ) and pH constraint ( $F_{pH}$ ).  $F_{pH}$  and  $F_{\theta}$  control the first and second cell-specific activity shown in (A), respectively. (C) shows the simulated pH at high anode potential and low anode potential.

#### C4. Simulated acetate concentration and acetate uptake

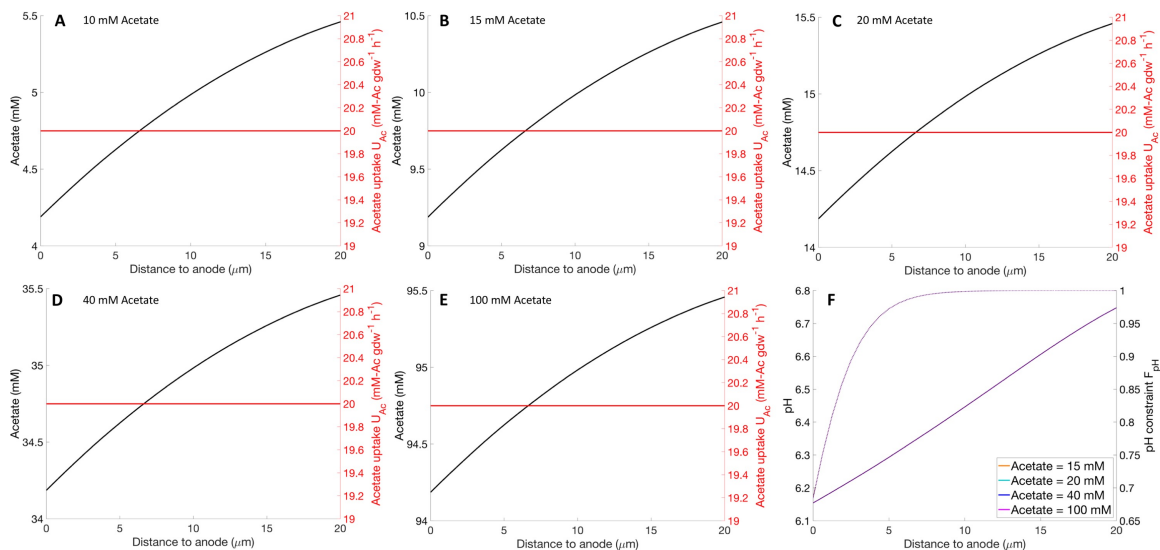


Fig. C6. Simulated acetate concentrations within biofilms at high anode potential with baseline parameters: A-10 mM acetate, B-15 mM acetate, C-20 mM acetate, D-40 mM acetate, E-100 mM acetate. (F) shows the pH and its impact on activity ( $F_{pH}$ ).

### C5. Impact of critical pH ( $C_{pH}$ ) on metabolic activity

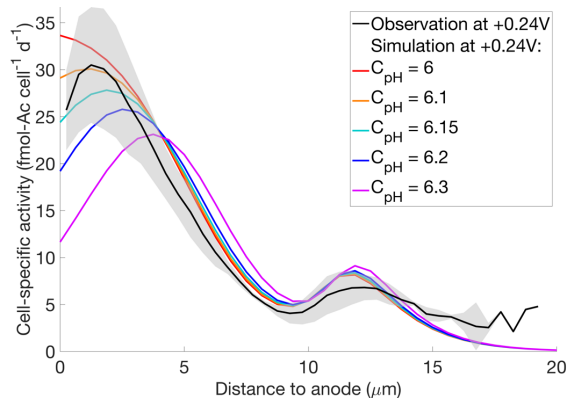


Fig. C7. The impact of critical pH ( $C_{pH}$ ) on activity patterns at high anode potential for the early activity peak near electrode. Shaded area represents 95% confidence interval for observations.

### C6. Impact of bicarbonate buffering capacity on pH

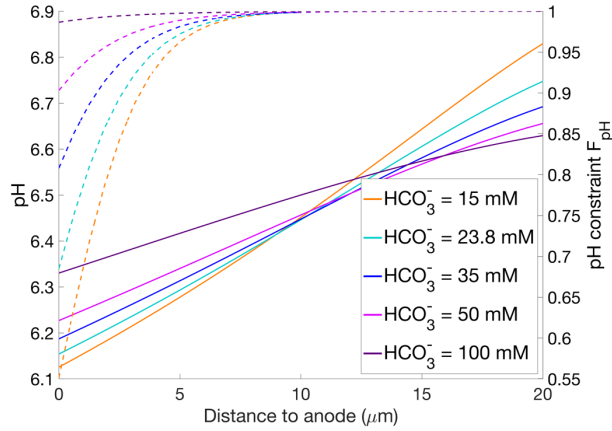


Fig. C8. Impact of bicarbonate buffering capacity on pH and the pH dependency  $F_{pH}$ . Solid and dash lines represent pH and  $F_{pH}$ , respectively.

### C8. Cell-specific current, redox potential, and fraction of $Cyt_{red}$ in biofilms

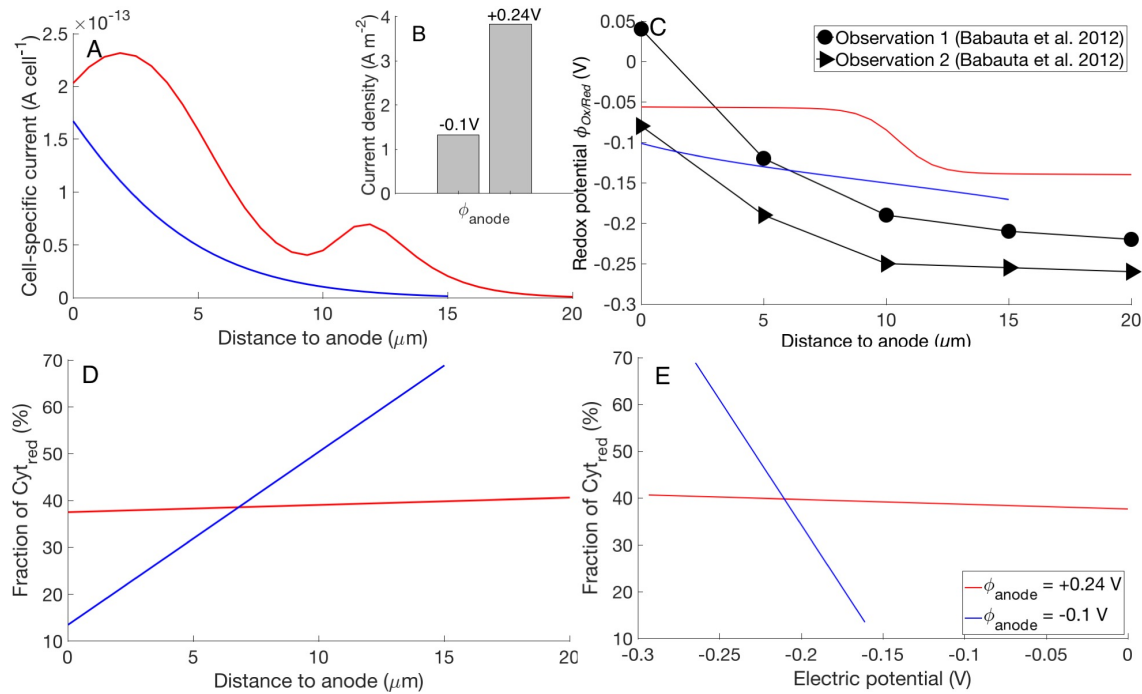


Fig. C9. (A) Cell-specific current, (B) current density, (C)  $\phi_{Ox/Red}$ , and (D,E) fraction of  $Cyt_{red}$  vs. distance to anode (D) and electric potential (E) at high and low anode potential. Filled circles and triangles in (C) show observations from Babauta et al. (2012).

### C9. Impact of effective diffusion coefficient and electric field on electron conduction

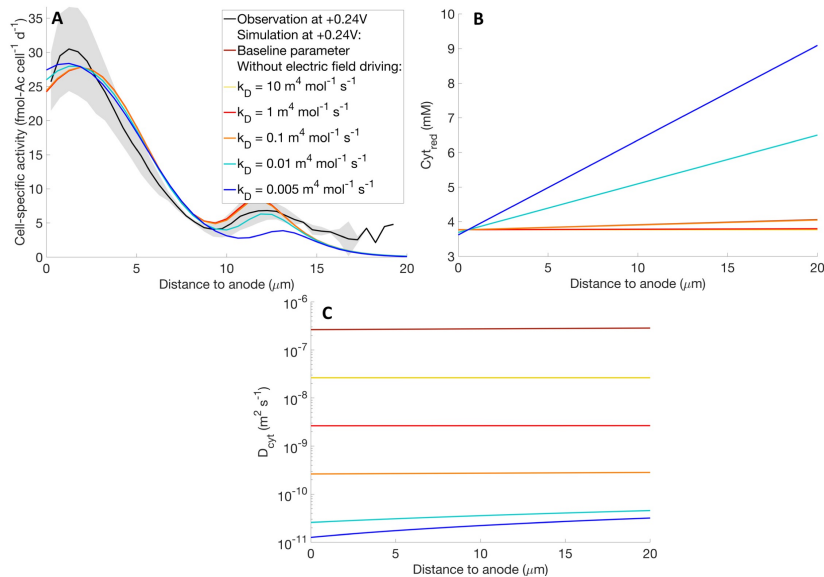


Fig. C10. Impact of electron transfer rate constant  $k_D$  without electric field as additional driving force. (A) cell-specific activity; (B) Cyt<sub>red</sub>; (C) effective diffusion coefficient  $D_{\text{Cyt}}$ .

### C10. Sensitivity analysis of model parameters

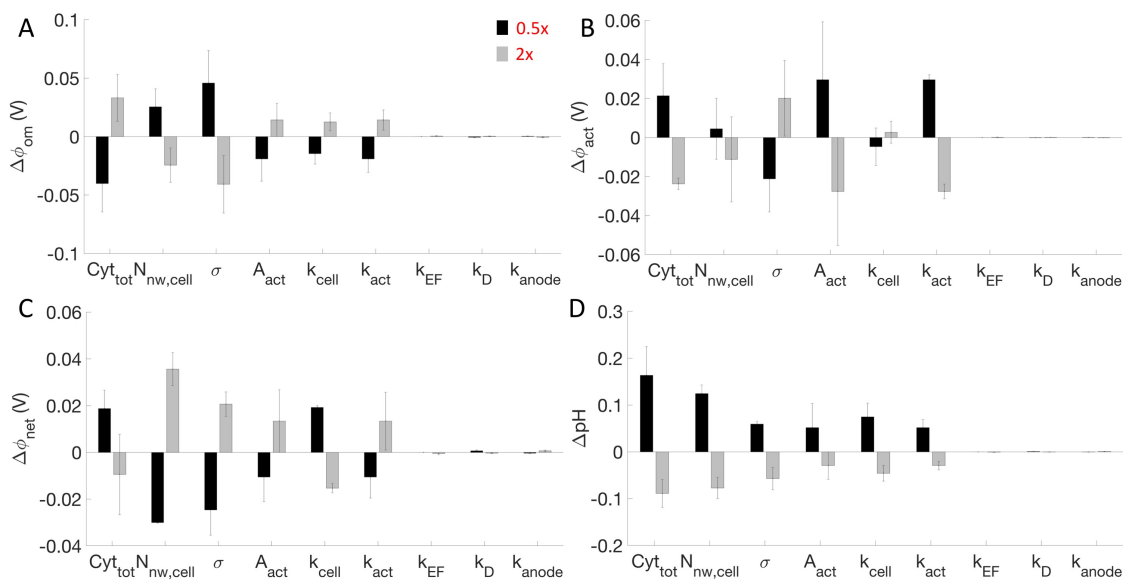


Fig. C11. Sensitivity analysis of model parameters and its effects on ohmic resistance loss (A), activation loss (B), net electric potential (C), and pH (D).

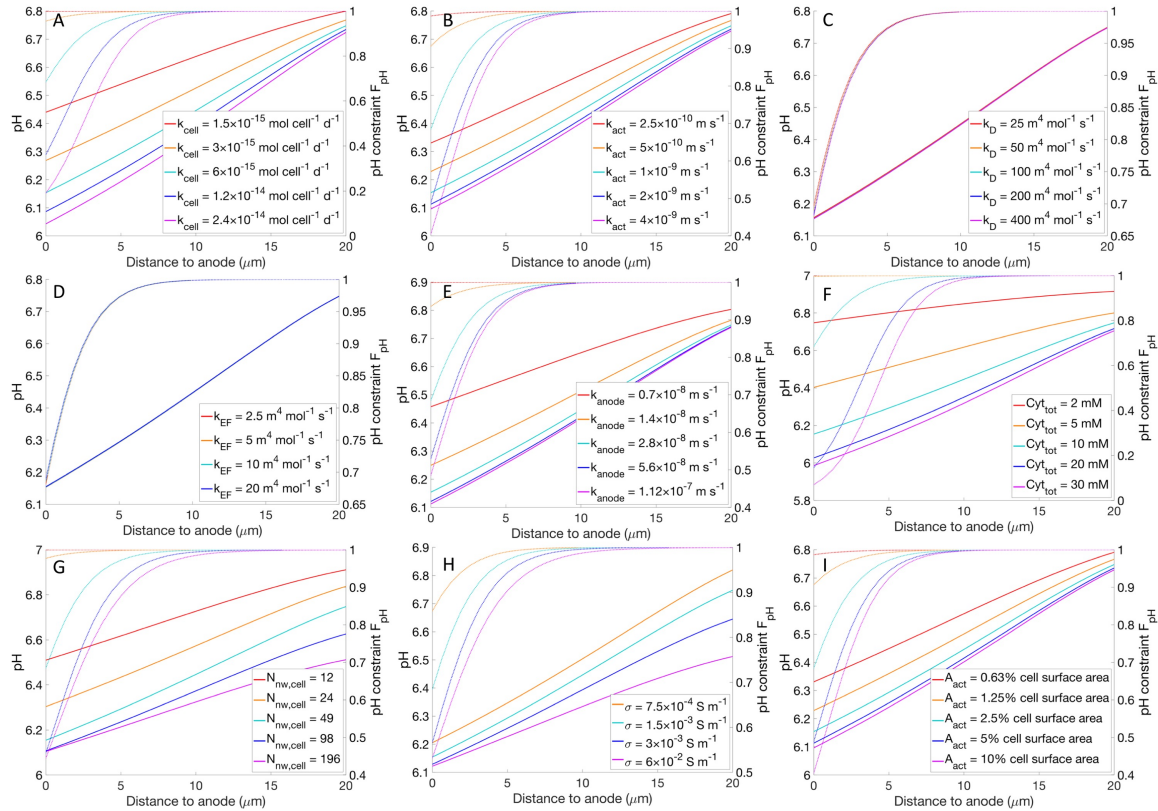


Fig. C12. pH and pH constraint ( $F_{pH}$ ) for different (A) cell-specific rate constant; (B) activation constant; (C) electron transport rate constant; (D) electric field driven rate constant; (E) electrode discharge constant; (F) the abundance of redox-active molecules; (G) the density of conductive network connections; (H) conductive biofilm conductivity; (I) redox-active cell surface area.

## Reference

Babauta, J. T.; Nguyen, H. D.; Harrington, T. D.; Renslow, R.; Beyenal, H., pH, Redox Potential and Local Biofilm Potential Microenvironments Within *Geobacter sulfurreducens* Biofilms and Their Roles in Electron Transfer. *Biotechnol Bioeng.* **2012**, *109*, (10), 2651–2662.

Mahadevan, R.; Bond, D. R.; Butler, J. E.; Esteve-Núñez, A.; Coppi, M. V.; Palsson, B. O.; Schilling, C. H.; Lovley, D. R., Characterization of metabolism in the Fe (III)-reducing organism *Geobacter sulfurreducens* by constraint-based modeling. *Appl. Environ. Microbiol.* **2006**, *72*, (2), 1558-1568

## APPENDIX D

### CHAPTER 5 SUPPLEMENTARY MATERIAL

#### **D1. Impact of fine-tuning on final registration**

Fine-tuning is a technique by taking weights of a pretrained convolutional neural network (CNN) and applying it as initialization for a new CNN model being trained on new data (Tajbakhsh et al. 2016). Registration using fine-tuned CNN produced almost the same registration results using binary images as input (Fig. D1-D4). It did improve a little for registration using raw (RGB) images as input; however, registration results were still far from satisfactory. Moreover, fine-tuning process consumes significantly more computing power and takes substantially longer to finish. Examples are given here using VGG16 and VGG19 networks.

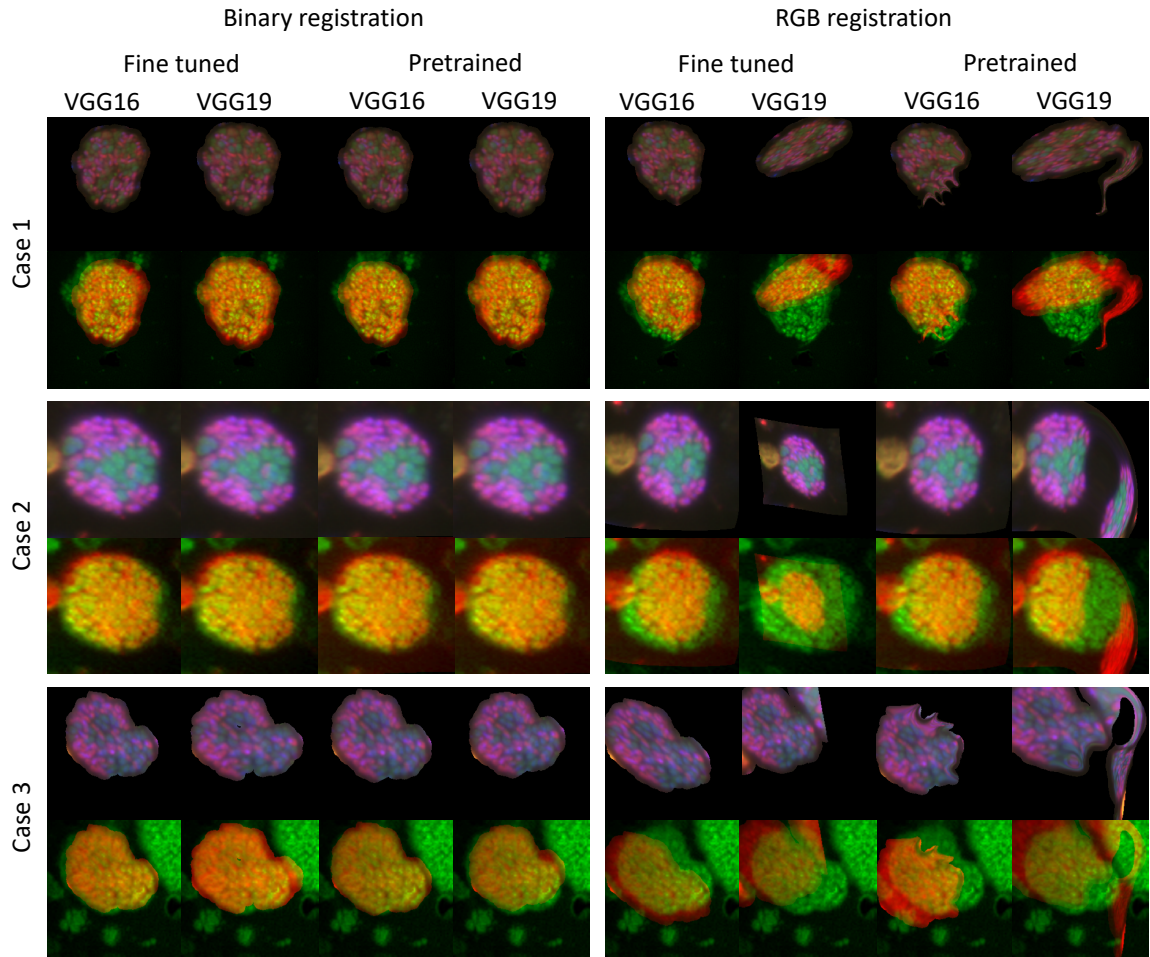


Fig. D1. Image registration for a modestly deformed (case 1, upper panel), a significantly deformed (case 2, middle panel), and a deformed FISH image with multiple components (case 3, lower panel) onto nanoSIMS image.

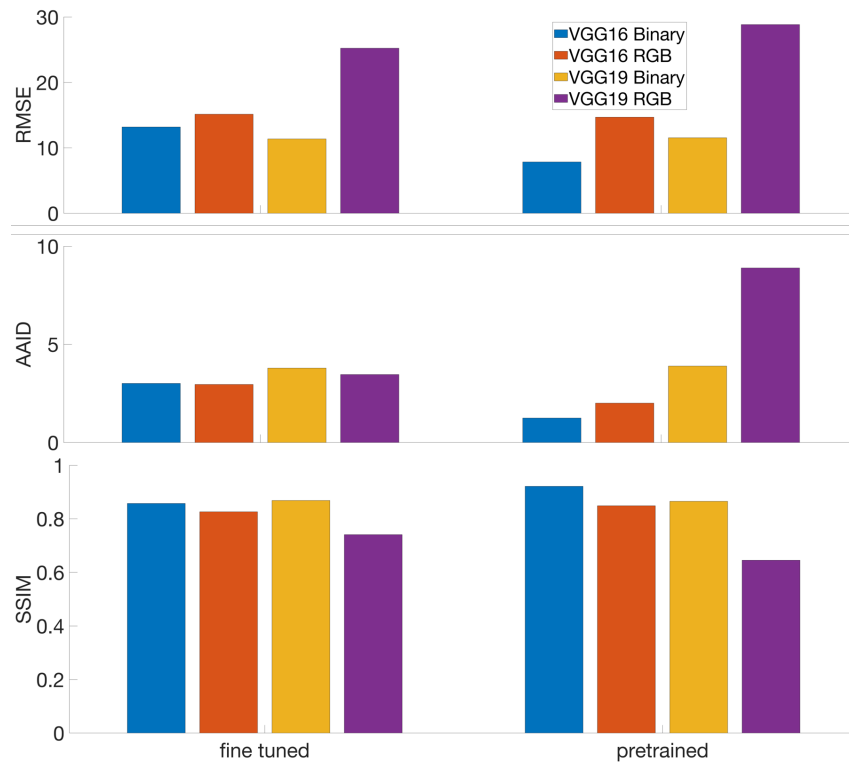


Fig. D2. Image registration accuracy for modestly deformed FISH images (case 1): RMSE (upper panel), AAID (middle panel), and SSIM (lower panel).

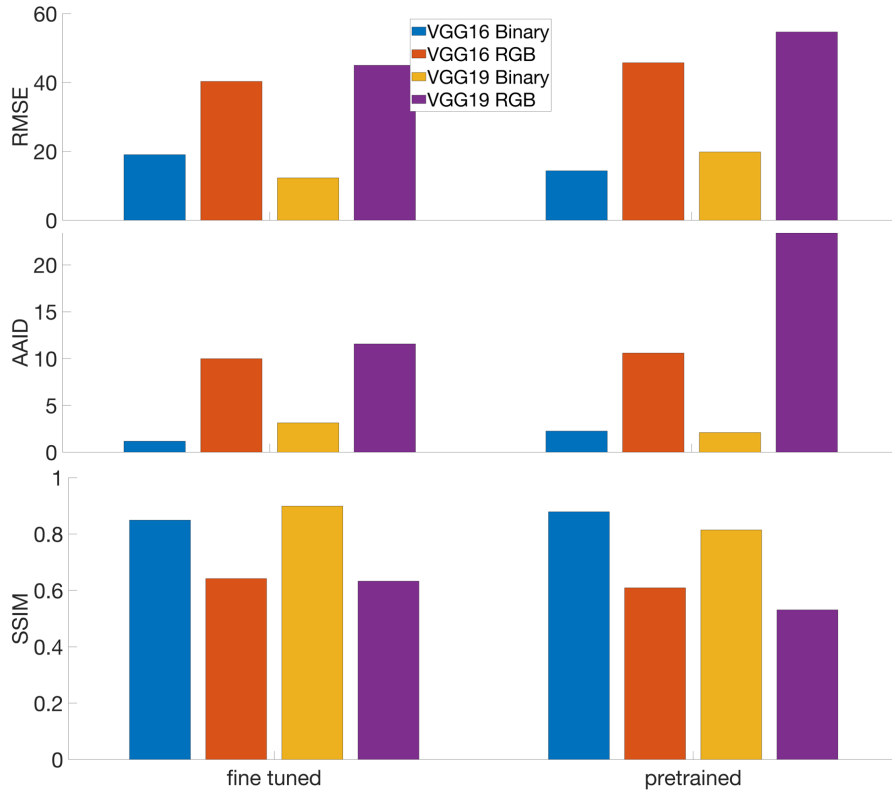


Fig. D3. Image registration accuracy for significantly deformed FISH images (case 2): RMSE (upper panel), AAID (middle panel), and SSIM (lower panel).

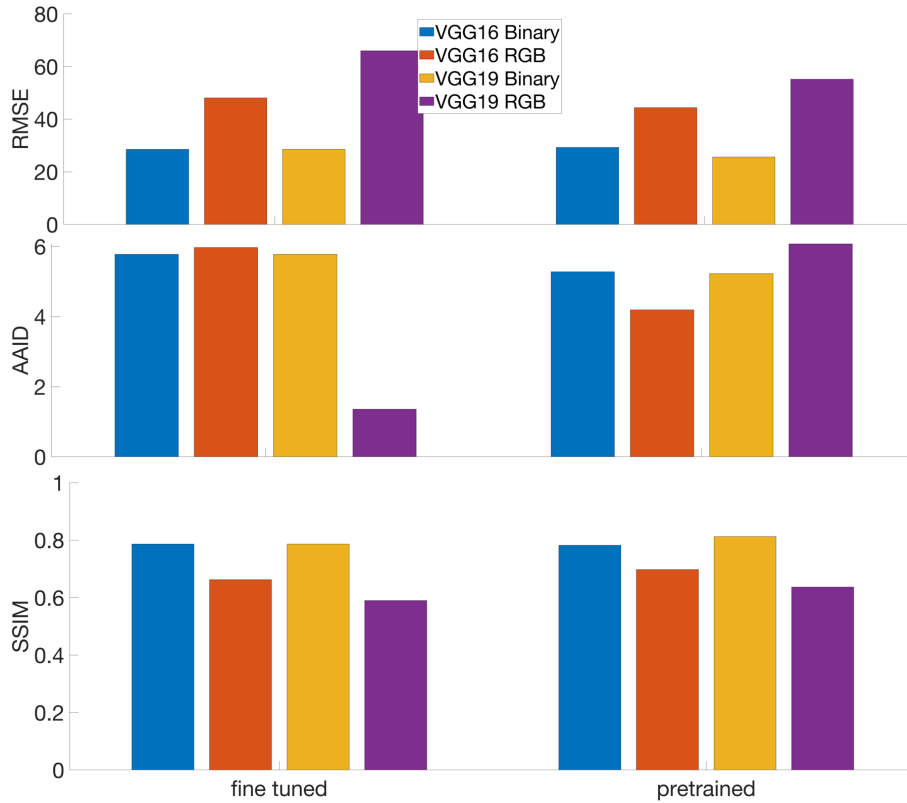


Fig. D4. Image registration accuracy for a deformed FISH image with multiple components (case 3): RMSE (upper panel), AAID (middle panel), and SSIM (lower panel).

## D2. Using standard features other than CNN for registration

We also tested on registration using standard features. Examples are given here for SURF (Speeded Up Robust Features, Bay et al. 2008), KAZE (Alcantarilla et al. 2012), BRISK (Binary Robust Invariant Scalable Keypoints, Leutenegger et al. 2011), Harris (Harris et al. 1988), and FAST (Features from Accelerated Segment Test, Rosten et al. 2005) features (Fig. D5 and Fig. D6). SURF is a similarity invariant, fast and robust algorithm for local feature extraction (Bay et al. 2008). KAZE is a scale and rotation invariant, fast multiscale feature detection and description approach for nonlinear scale spaces (Alcantarilla et al. 2012). BRISK is also a scale and rotation invariant, fast feature point extraction algorithm (Leutenegger et al. 2011). Instead, Harris (Harris

et al. 1988) and FAST (Rosten et al. 2005) are corner detection algorithms that are commonly used to extract corners and infer features of an image. None of them produced satisfactory results in our tests. Using RGB images as input all failed to register FISH images due to insufficient features extracted and matched.

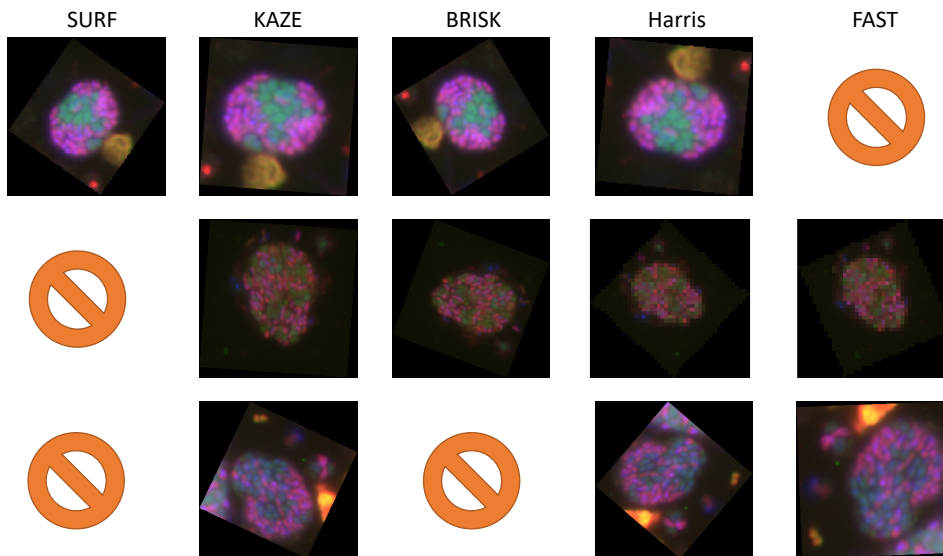


Fig. D5. Image registration for a modestly deformed (upper panel), a significantly deformed (middle panel), and a deformed FISH image with multiple components (lower panel) onto nanoSIMS image. Binary images were used as input. Colored symbols indicate failed registration.

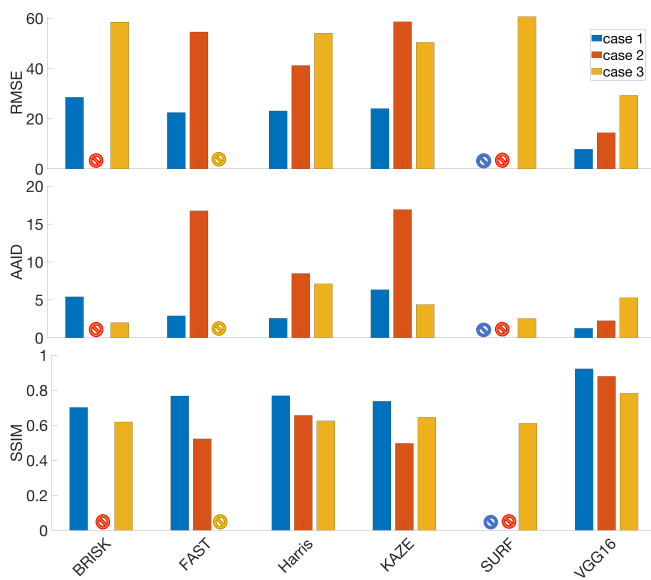


Fig. D6. Image registration accuracy for three FISH images (case 1: modestly deformed; case 2: significantly deformed; case 3: deformed FISH image with multiple components): RMSE (upper panel), AAID (middle panel), and SSIM (lower panel). Colored symbols indicate failed registration.

#### Referneces

Alcantarilla, P.F.; Bartoli, A.; Davison, A.J., KAZE Features. In: Fitzgibbon A., Lazebnik S., Perona P., Sato Y., Schmid C. (eds) *Computer Vision – ECCV 2012*. ECCV 2012. Lecture Notes in Computer Science, 7577. Springer, Berlin, Heidelberg.

Bay, H.; Ess, A.; Tuytelaars, T.; Van Gool, L., SURF:Speeded Up Robust Features. *Computer Vision and Image Understanding (CVIU)* **2008**, 110(3), 346–359.

Harris, C.; Stephens, M., A Combined Corner and Edge Detector. *Proceedings of the 4th Alvey Vision Conference* **1988**, 147-151.

Leutenegger, S.; Chli, M.; Siegwart, R., BRISK: Binary Robust Invariant Scalable Keypoints. *2011 International Conference on Computer Vision*, Barcelona, 2011, 2548-2555.

Rosten, E.; Drummond, T., Fusing Points and Lines for High Performance Tracking. *Proceedings of the IEEE International Conference on Computer Vision* **2005**, 2, 1508–1511.

Tajbakhsh, N.; Shin, J.Y.; Gurudu, S.R.; Hurst, R.T.; Kendall, C.B.; Gotway, M.B.; Liang, J., Convolutional neural networks for medical image analysis: Full training or fine tuning? *IEEE Transactions on Medical Imaging* **2016**, 35(5),1299-1312.